

**Characterisation and In-Orbit
Demonstration of a Heterodyne
Spectrometer for Atmospheric Research
from Small Satellites**



**BERGISCHE
UNIVERSITÄT
WUPPERTAL**

Oliver Wroblowski

Fakultät für Mathematik und Naturwissenschaften

Bergische Universität Wuppertal

Dissertation

vorgelegt zur Erlangung des Grades

Doktor der Naturwissenschaften (Dr. rer. nat.)

Wuppertal, 2023

Acknowledgements

First of all, I would like to express my sincere gratitude to my supervisors Prof. Martin Riese and Prof. Ralf Koppmann for providing the opportunity to conduct my research in a cooperation between the Research Centre Jülich and the University of Wuppertal. Without your continuous support, guidance and invaluable advice, this work would have not been possible. It was a great pleasure being part of your research groups.

I would like to say a special thank you to my academic supervisor Dr. Martin Kaufmann. Your insights in this field of research led to a lot of interesting discussions and made this research project an inspiring experience for me.

A lot of help was received from Friedhelm Olschewski and Dr. Klaus Mantel regarding experimental work. I will not forget the countless hours we spent together in the lab, figuring out what works best. Your advice and contributions to this research project were always greatly appreciated.

In person, I would like to thank Dr. Johannes Stehr for a lot of helpful discussions about spatial heterodyne spectroscopy and Konstantin Ntokas for providing sound data processing algorithms. Special thanks belong to Dr. Heinz Rongen, Tom Neubert, Georg Schardt and Dennis Fröhlich for your continuous support regarding the instrument electronics and software.

To conclude, I cannot forget to thank my family and friends for all their unconditional support over the past years.

Abstract

This work presents the development of a new limb-sounder for temperature exploration of the upper atmosphere, the Atmospheric Limb Interferometer for Temperature Exploration (AtmoLITE). It is a miniaturized satellite instrument based around the technique of spatial heterodyne spectrometers. This class of spectrometers is well suited for miniaturization which allowed to design AtmoLITE within the form factor of a 6U CubeSat. The observable of AtmoLITE is the rotational spectral distribution of the day- and night-time oxygen atmospheric band emission, which is particularly suited for temperature exploration from the lower most mesosphere towards the ionosphere. In addition, this work proposes a novel calibration concept suited to accurately characterise the AtmoLITE spectrometer's spectral response. Major milestones achieved in this work were (1) the development of the optical system of AtmoLITE, (2) design of an appropriate calibration light stimulus, (3) experimental verification of AtmoLITE in-front of the calibration source, and (4) a first estimate of expected AtmoLITE temperature retrieval uncertainty.

Contents

List of Figures	ix
List of Tables	xiii
List of Abbreviations	xv
1 Introduction	1
1.1 Gravity waves in the upper atmosphere	3
1.2 Objectives of this work	5
1.3 Outline	6
1.4 Remarks about AtmoLITE optics simulations	7
2 Observation of the O₂ A-Band by Spatial Heterodyne Spectroscopy	13
2.1 The Oxygen Atmospheric Airglow	16
2.2 The Spatial Heterodyne Spectrometer	21
2.3 Spectrometer Design for the AtmoLITE Instrument	24
2.4 Definition of interferogram fringe visibility	27
2.5 The AtmoLITE SHS under Space Conditions	30
2.6 SHS Tolerance & Alignment Considerations	36
3 Instrument Optics Design	43
3.1 AtmoSHINE - In-Orbit Demonstrator	46
3.2 AtmoSHINE - Imaging Quality and Wavefront Errors	47
3.3 AtmoSHINE - Line-Of-Sight Calibration	58
3.4 AtmoSHINE - In-Field Ghost Reflections	62
3.5 AtmoLITE - A new optical System	69
3.6 AtmoLITE - Tolerance Budget	77
3.7 Low Pressure Compensation of Optics	79
3.8 Tolerances of the camera optics locking mechanism	81
3.9 SHS optimization within the full optical system	81
3.10 Expected O ₂ A-band Radiances In-Orbit	84

4	The AtmoLITE Calibration Unit	91
4.1	AtmoLITE Calibration Unit - Design Concept	93
4.2	AtmoLITE Calibration Unit - Requirements	95
4.3	AtmoLITE Calibration Unit - Optical Design	100
4.4	AtmoLITE Calibration Unit - Mechanical Design	103
4.5	AtmoLITE Calibration Unit - Alignment	105
4.6	Verification of the ACU prototype(s)	119
4.7	Impact of a ACU non-uniformity on visibility	132
5	The AtmoLITE Prototype - An experimental verification of performance	137
5.1	SHS assembly	138
5.2	Characterisation of PSF, MTF & FOV	139
5.3	First interferograms of AtmoLITE	149
5.4	Expected temperature retrieval uncertainty	158
6	Summary and final remarks	165
Appendices		
A	AtmoSHINE & AtmoLITE addon	185
A.1	Zernike Polynomials	186
A.2	LOS Calibration - Propagation of Uncertainties	188
A.3	Characterisation of PSF and spot size - continued	189
A.4	Instrument and ACU Info Sheets	191
A.5	Oxygen A-band emission lines	193
A.6	AtmoLITE - Simulated Spectra continued	194
A.7	AtmoLITE - ILS formulas	195
B	Additional information about ACU characterisation	197
B.1	View factor between two rectangular, parallel plates	198
B.2	Preparations of ACU Wavefront Curvature Estimation	199
B.3	Impact of ACU chromatic focal shift	202
B.4	Aperture stop design of test equipment	204
B.5	ACU scan head design details	206
B.6	Power monitoring of ACU	212
C	AtmoLITE alignment guide	215
C.1	Step-By-Step guide to SHS alignment	215
C.2	Step-by-Step Alignment of Front and Camera Optics	219

List of Figures

1.1	AtmoLITE EM after integration and first optics alignment	5
2.1	Overview of O ₂ A-band emission production and loss mechanisms	17
2.2	Concept of the spatial heterodyne spectrometer	22
2.3	O ₂ A-band emission spectrum	25
2.4	Estimation of required SHS resolving power	26
2.5	AtmoLITE bandpass for different grating groove densities	28
2.6	Expected SHS pressure dependence	31
2.7	SHS Thermal analysis - stress and deformation	32
2.8	Temperature dependence of the Littrow wavenumber	35
2.9	Impact of SHS arm imbalances on PSF including interference	37
2.10	Wavelength dependent fringe rotation caused by SHS arm imbalances	40
3.1	AtmoLITE optical layout	45
3.2	AtmoSHINE Flight Model	47
3.3	Experimental setup during the AtmoSHINE wavefront aberration measurements	48
3.4	Overview of AtmoSHINE opto-mechanical lens mounts	49
3.5	Wavefront quality of AtmoSHINE front optics A1	51
3.6	Reduction of first order coma in front optics B2	52
3.7	AtmoSHINE MTF based on measured wavefront aberrations - front optics	54
3.8	Wavefront quality of AtmoSHINE camera optics C1	55
3.9	AtmoSHINE MTF based on measured wavefront aberrations - camera optics	56
3.10	Experimental setup to characterise the AtmoSHINE LOS	59
3.11	Experimental setup used to test the AtmoSHINE point spread response	63
3.12	Evaluation of AtmoSHINE ghost reflections across the detector array	64
3.13	Simulation of the ghost origin within the AtmoSHINE optics	67
3.14	AtmoSHINE in-orbit interferograms including ghost artefacts	68
3.15	AtmoLITE opto-mechanics CAD cross-section	71
3.16	AtmoLITE MTF curves including different materials.	72

3.17	Example of a single simulated interferogram at 759.83 nm - on-axis	74
3.18	Example of a single simulated interferogram at 759.83 nm - off-axis	75
3.19	Simulated mean visibility for different AtmoLITE configurations . .	76
3.20	AtmoLITE MTF curves correlated to simulated visibility	76
3.21	Mean RMS and PV wavefront aberrations of the final AtmoLITE system	78
3.22	Limb viewing geometry of the AtmoSHINE and AtmoLITE missions	85
3.23	Simulated O ₂ A-band radiance as seen by the satellite instrument .	88
4.1	Conceptual design of the ACU	94
4.2	AtmoLITE optical performance in dependence on source-to-instrument distance	97
4.3	ACU non-uniformity - impact on relative spectral response	98
4.4	ACU optical layout in ZEMAX	100
4.5	ACU tolerances - mean RMS and PV wavefront aberrations	102
4.6	Simulated ACU aperture illumination	103
4.7	CAD illustration of the ACU mechanics without optics	104
4.8	Detailed view of the ACU mechanics between lens doublet and integration sphere	105
4.9	ACU lens alignment and wavefront measurement in front of Zygo interferometer	107
4.10	ACU wavefront quality measured in front of Zygo interferometer . .	108
4.11	Setup during the ACU focal plane determination	109
4.12	Processing of measured shearogram data	110
4.13	ACU alignment - wavefront ROC in dependence on point source position	111
4.14	ACU alignment - uncertainty estimation of ACU wavefront curvature	112
4.15	ACU alignment - diffuser disc alignment	114
4.16	ACU non-uniformity - radiative transfer between diffuser disc and integration sphere	115
4.17	ACU non-uniformity - impact on apodization	116
4.18	Impact of finite diffuser thickness	117
4.19	ACU alignment - shift of point source after insertion of diffuser disc	118
4.20	ACU scan head - overview of aperture masks	120
4.21	ACU verification - setup manual	121
4.22	ACU verification - setup motorised	121
4.23	ACU verification - angular scans of 1st ACU	123
4.24	ACU verification - aperture illumination of 1st ACU	123
4.25	ACU angular scan - horizontal	125
4.26	ACU angular scan - vertical	125

4.27	ACU angular scan - shifted scan head	126
4.28	ACU angular scan - full field	127
4.29	ACU aperture illumination - measured uniformity	129
4.30	Expected change of visibility due to non-uniform aperture illumination	133
4.31	Interferogram fringe visibility change due to ACU misalignment . .	134
5.1	Improved SHS alignment jig	139
5.2	Experimental setup of PSF, MTF and FOV measurements	141
5.3	AtmoLITE EM PSF during front optics alignment	142
5.4	AtmoLITE EM PSF scan across full field of view	144
5.5	Experimentally derived MTF curve	147
5.6	Demonstration of AtmoLITE SHS performance	150
5.7	Evaluation of AtmoLITE EM visibility	151
5.8	Interferogram crosssection at 764.80 nm obtained with the AtmoLITE EM prototype	153
5.9	Derived AtmoLITE EM modulation efficiency.	154
5.10	Derived phase distortion of the AtmoLITE EM.	154
5.11	AtmoLITE EM polychromatic flat field description at different wave- lengths.	155
5.12	Expected atmospheric spectrum based on the measured AtmoLITE EM instrumental lineshape.	159
5.13	Expected AtmoLITE temperature retrieval uncertainty due to cali- bration of the ILS	162
5.14	AtmoLITE EM noise contribution to temperature retrieval uncertainty.	164
A.1	AtmoLITE spot sizes at 759.83 nm	189
A.2	Example of a single simulated interferogram at 764.74 nm	194
B.1	View factor of two plane parallel rectangles	198
B.2	Verification of the shearing plate wedge	199
B.3	Expected shearogram fringe tilt at different shears and wavefront radii of curvature	201
B.4	ACU chromatic focal shift	202
B.5	Simulated shearogram tilt at different wavelengths	203
B.6	ACU aperture mask and definition of correction factors.	205
B.7	CAD view of the ACU scan head setup	209
B.8	On-axis raytrace of a collimated wavefront through the ACU scan head	210
B.9	Simulation of the pinhole aperture diffraction pattern as seen by the photo diode	210
B.10	Vignetting expected within the ACU scan head due to the finite aperture size of the pinhole	211

B.11 Spectral responsivity of a typical photo diode of type SM05PD3A 211

B.12 ACU verification - correlation of measured laser power by internal
photo-diode and external powermeter 213

C.1 Overview of DoFs during SHS assembly 216

List of Tables

2.1	Results of the SHS arm imbalance analysis	38
3.1	Data obtained during the LOS calibration of the AtmoSHINE EM instrument	59
3.2	Design requirements of the new AtmoLITE system	69
3.3	AtmoLITE optics performance under vacuum	80
3.4	AtmoLITE optics performance under vacuum - locking mechanism .	82
3.6	Expected in-orbit flux per detector pixel	87
4.1	Optical, mechanical and calibration design requirements of the ACU	99
4.2	Lens prescription data of finite-infinite ACU optics	100
4.3	ACU tolerances - simulation parameters	102
A.1	Zernike Polynomials	187
A.2	AtmoSHINE PSF measurements at different field points	190
A.3	Summary of ACU design	191
A.4	Summary of instrument design	192
A.5	HITRAN O ₂ A-band emission line data	193
B.1	ACU verification - radii and correction factors for ACU scan head aperture masks	205

List of Abbreviations

ACU	AtmoX Calibration Unit
AOI	Angle Of Incidence
ARCADE	Atmospheric Coupling and Dynamics Explorer
AtmoHIT	Atmospheric Heterodyne Interferometer Test
AtmoLITE	Atmospheric Limb Interferometer for Temperature Exploration
AtmoSHINE	Atmospheric Spatial Heterodyne Interferometer - Next Explorer
BUW	University of Wuppertal
COTS	commercial-of-the-Shelf
CRISTA	Cryogenic Infrared Spectrometers and Telescopes for the Atmosphere
DISSECT	Development Initiative of Small Satellites for Exploration of Climatology by Tomography
DoF, DoFs	Degree(s)-of-Freedom
EM	Engineering Model
ESA	European Space Agency
ESF	Edge Spread Function
FFT	Fast Fourier Transformation
FTS	Fourier Transform Spectrometer
FOV	Field Of View
FWHM	Full Width Half Maximum
FWP	field-widening prism
GRIPS	Ground Based P-branch Infrared Spectrometer
GWMF	Gravity Wave Momentum Flux
INSPIRE	International Satellite Program in Research and Education
IIST	Indian Institute of Space Science and Technologies
ISF	Interferogram Scaling Factor

LASP	Laboratory for Atmospheric and Space Physics
LOS	Line of Sight
LSP	Line Spread Function
LTE	(rotational) Local Thermal Equilibrium
MATS	Mesospheric Airglow/Aerosol Tomography and Spectroscopy instrument
MTF	Modulation Transfer Function
MISU	Department of Meteorology at Stockholm University
MLA	Micro Lens Array
MLT	Mesosphere and Lower Thermosphere
NA	numerical aperture
NDMC	Network for the Detection of Mesospheric Change
OSIRIS	Swedish Optical Spectrograph and InfraRed Imaging System
OTF	Optical Transfer Function
PV	Peak-to-Valley wavefront aberration
PCC	plano-concav
PCX	plano-convex
PSF	Point Spread Function
RMS	Residual Mean Squared value
ROI	Region Of Interest
SCIAMACHY	Scanning Imaging Absorption Spectrometer for Atmospheric Cartography
SHS	Spatial Heterodyne Spectrometer
SNR	signal-to-noise ratio
TCE	coefficient of thermal expansion
TOTR	Total Track length
VER	volume emission ratio
QE	Quantum Efficiency
WINDII	Wind Imaging Interferometer
ZARM	Zentrum für angewandte Raumfahrttechnologie und Mikrogravitation
ZC	Zernike Coefficient
ZEMAX	Zemax Optical Studio

1

Introduction

Contents

1.1 Gravity waves in the upper atmosphere	3
1.2 Objectives of this work	5
1.3 Outline	6
1.4 Remarks about AtmoLITE optics simulations	7

In view of understanding global climate change, the upper atmosphere has become increasingly interesting over the past decades. Since the discovery of the coupling between lower and upper atmospheric properties by propagating waves, in particular temperature trends within the mesosphere, thermosphere and up to the ionosphere have been extensively studied [Beig et al., 2003; Beig, 2011]. One objective was to derive long term trends in atmospheric temperature. First trend results were reported by Kokin and Lysenko [1994] based on rocket and radiosonde measurements. Based on data obtained from 1964 to 1990, they derived a cooling of the lower mesosphere of up to 0.3 – 1.0 K/yr and a warming of the lower stratosphere and troposphere of up to 0.1 – 0.2 K/yr. Following studies soon extended observations towards the ionosphere [Taubenheim et al., 1990; Serafimov and Serafimova, 1992; Bremer, 1998] which revealed a dependence on latitude of temperature trends [Beig et al., 2003]. Based on observations of different airglow layers, long-term trends were found to depend on altitude as well [Reisin and Scheer, 2002]. Hence, new instrumentation at different latitudinal sides was required to extent temperature monitoring beyond regional studies and to establish temperature observation over several decades.

One such instrument was the Ground Based P-branch Infrared Spectrometer (GRIPS). It derives atmospheric temperatures from observation of the OH airglow layer at an altitude of about 87 km and was setup at the University of Wuppertal (BUW) in 1980. Since then, the continuous temperature data recorded was used to investigate decadal variations [Bittner et al., 2002] and a long-term trend of -0.23 K/yr after correction for solar cycle influences was deduced Offermann et al. [2010]. An updated study considering GRIPS data obtained up to 2008 indicated that the long-term temperature trend could also inhibit strong seasonal variations if monthly averaged data is considered [Kalicinsky et al., 2016].

Over time, satellite instrumentation has greatly advanced temperature sounding capabilities of the upper atmosphere. This allowed to perform comparison to ground-based measurement approaches and to obtain temperature data on a global scale. With respect to activities at the BUW regarding the observation of mesospheric temperature change at an altitude of about 87km, multiple satellite instruments were found suitable for a comparison. These were the Wind Imaging Interferometer (WINDII) [Shepherd et al., 1993], the Cryogenic Infrared Spectrometers and Telescopes for the Atmosphere (CRISTA) instrument [Offermann et al., 1999], the Scanning Imaging Absorption Spectrometer for Atmospheric Cartography (SCIAMACHY) [Bovensmann et al., 1999] and the Atmosphere Using Broadband Emission Radiometry (SABER) payload [Remsberg et al., 2008]. GRIPS was consistently showing higher temperatures, up to 3.7 K compared to CRISTA [Scheer et al., 2006], up to 2.7 K compared to SCIAMACHY [von Savigny, 2004] and up to 3.4 K compared to SABER [Kalicinsky et al., 2016]. But, considering an accuracy of ± 4 K representative for satellite instrument data for an altitude of 87 km as derived for SABER in Remsberg et al. [2008], good agreement was found and the GRIPS instrument quickly became one of the standard instruments for ground-based temperature sounding of the mesosphere. Nowadays, GRIPS is part of the Network for Detection of Mesospheric Change (NDMC) and continues to extent one of the longest data series of mesospheric temperature available.

Recently, the decision to further extent measurement capabilities of mesospheric temperature at the BUW was made. In a joint co-operation between the BUW, the Max-Planck institute for the Science of Light, the York University and led by the Research Centre Jülich development of a novel limb-sounder fitting in the form factor of a CubeSat was started. The scientific objective is to derive atmospheric temperature by observation of the rotational distribution of the O₂ A-band emission and, featuring an angular field-of-view (FOV) of $\pm 0.65^\circ$, to deduce temperature variations across altitudes between 60 km and 120 km. Taking advantage of the

manoeuvrability of a CubeSat sized instrument will enable tomographic temperature retrieval in along-track slices [Ungermaun et al., 2010; Song et al., 2018], especially, when multiple instruments are deployed for simultaneous observation. This 3-D temperature data will then provide new insights in atmospheric dynamics. For instance, inspired by studies of absolute gravity wave momentum flux derived from limb-sounding of the stratosphere [Ern, 2004; Alexander et al., 2008; Preusse et al., 2009], improvements to our general understanding of gravity wave sources and propagation are expected from upcoming limb-scanning observations [Preusse et al., 2009, 2014]. First simulations concerning gravity wave properties expected to be inferred from the instrument considered in this work are evaluated by Chen et al. [2022]. In particular, Chen et al. [2022] mention that limb-scanning observations can enhance understanding and description of wind reversal above the summer MLT, the recovery phase of sudden stratospheric warming or gravity wave interaction with the background atmosphere in the thermosphere. These phenomena are currently not well resolved by models relying on current gravity wave parametrization schemes.

But, what are gravity waves, why is global observation of upper atmospheric temperature key to understand their sources and how does their propagation influence atmospheric dynamics?

1.1 Gravity waves in the upper atmosphere

Gravity waves belong to the group of buoyancy waves and transport momentum as well as energy through the whole atmosphere. The restoring force is the gravitational pull of the earth, thus, any disturbance of background atmospheric flow can excite gravity waves by local displacement of atmospheric air masses. Their primary sources are flow over topography and convective systems in the troposphere. In addition, strong wind fields such as the jet streams excite gravity waves. While propagating from the lower to the upper atmosphere, the amplitude of gravity waves continuously increases as the air density decreases until the waves finally break. This causes the gravity wave momentum and energy to be deposited into the background atmosphere. This quantity is commonly referred to as gravity wave momentum flux (GWMF). The net effect of GWMF is the creation of turbulence or driving of large scale circulations [Fritts and Alexander, 2003; Alexander et al., 2010]. Of particular importance are seasonal changes of the global-scale circulation within the mesosphere over polar regions. Here, a reversal of up-welling and down-welling transport occurs during summer or winter time, respectively [Lindzen, 1981; Holton, 1982]. The induced turbulence and large-scale circulation further cause a change

of atmospheric background temperature due to the adiabatic heating and cooling of displaced air masses. This allows to infer gravity waves from 3D datasets of observed temperature fluctuations as demonstrated by Ern et al. [2011].

Coupling to the background flow further imprints properties of the lower atmosphere onto gravity waves, thus, linking lower and upper atmospheric dynamics. Besides altitude-dependent filtering of the gravity wave spectrum by wind fields [Fritts and Alexander, 2003], the generation of secondary waves is of importance. Known effects include zonally non-uniform dissipation [Holton, 1984] and baroclinic instabilities near jets [Sato and Nomoto, 2015], both exciting planetary waves. In addition, breaking gravity waves often excite secondary gravity waves due to flow imbalances caused by locally deposited momentum [Vadas et al., 2003; Becker and Vadas, 2018]. Modelling efforts are still being extended to include these coupling effects, with one of the main challenges being a wave-resolved simulation scheme all the way from the lower to the upper atmosphere [Becker, 2011]. Notable advances were made by self-consistent gravity wave resolving general circulation models [Watanabe et al., 2015; Becker and Vadas, 2018] and ray-tracing studies of wave events [Preusse et al., 2006; Kalisch et al., 2014]. The challenge becomes even more apparent if three dimensional gravity wave propagation and refraction is considered. Refraction is expected by interaction with strong wind fields in the mesosphere [Sato et al., 2009; Ern et al., 2011] or sudden stratospheric warmings [Thurairajah et al., 2014; Ern et al., 2016]. All these effects further lead to gravity waves propagating not only vertically but horizontally throughout the atmosphere.

While aforementioned studies mostly address gravity wave propagation only from the troposphere towards the mesosphere, occurrence of gravity waves also impacts thermospheric and ionospheric dynamics [Siskind et al., 2012; Park et al., 2014; Forbes et al., 2016]. Especially, secondary and higher order gravity waves are of importance [Zhou, 2002]. For example, Trinh et al. [2018] demonstrated that gravity wave momentum fluxes observed at altitudes between 30 km and 90 km correlate with gravity wave induced perturbations of the thermosphere/ionosphere system at 250 km. Trinh et al. [2018] specifically mention sparse knowledge about the wavelength spectrum of horizontally propagating gravity waves as one limiting factor of their current research.

Now, the goal of the AtmoLITE mission is to develop a limb sounding instrument capable of providing 3D temperature data. Covering in particular the transition region between mesosphere and thermosphere, this data is expected to yield new insights about sources and propagation of gravity waves currently not accurately modelled. With the goal to build a CubeSat sized instrument, this project further aims at providing low-cost access to such observations.

1.2 Objectives of this work

The first objective of this work is the development of the latest iteration of the proposed limb-sounder, the Atmospheric Limb Interferometer for Temperature Exploration (AtmoLITE). It takes part in the international satellite program in research and education (INSPIRE) and will be launched on INSPIRESat-4 as part of the atmospheric coupling and dynamics explorer (ARCADE) mission. INSPIRESat-4 is jointly developed by LASP at the university of Colorado, IIST, NCU in Taiwan and the research centre Juelich in Germany and aims to provide ion temperature, velocity, density and electron temperature measurements of the equatorial ionosphere [Chandran et al., 2019]. The payload AtmoLITE will provide temperature information, in particular in the equatorial MLT region. A photo of the first AtmoLITE prototype is shown in Figure 1.1.

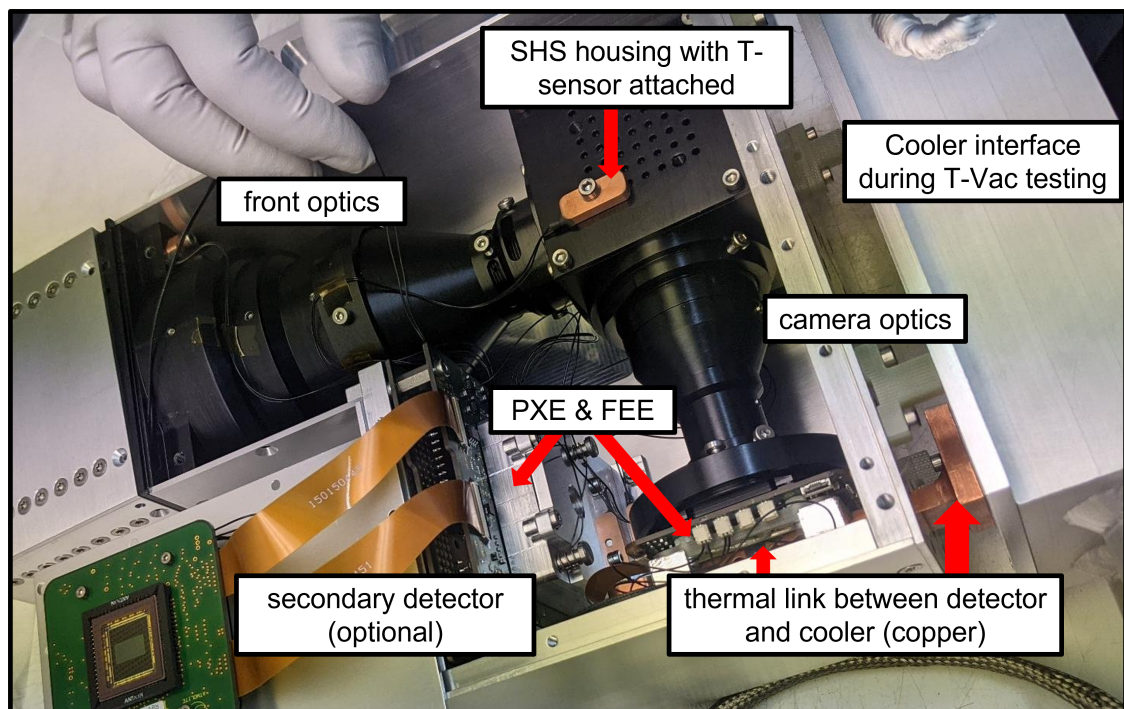


Figure 1.1: AtmoLITE EM after integration and first optics alignment. All parts were manufactured and successfully integrated. The second detector is currently not used but provides the readout for future integration of a nadir viewing cloud camera.

The second objective of this work is the development of a calibration device suitable to characterise the AtmoLITE spectral response, called the AtmoLITE Calibration Unit (ACU). A full description of the design requirements, mechanical and optical layout, and experimental verification of an ACU prototype are included. All developments concerning AtmoLITE and the ACU are also part of the MetEOC-3 and MetEOC-4 projects with the overall goal to provide traceable temperature

measurements of the mesosphere and to compare on-ground measurements, for instance obtained by GRIPS, to space-borne observations.

Lastly, a set of measurements of the combined system of AtmoLITE and ACU was obtained. Analysis shows that expected instrument performance in terms of interferogram fringe visibility is achieved. Although a few measurements had to be delayed due to COVID-19, an uncertainty budget for the instrument calibration based on ACU characterisation, expected instrument noise and expected O₂ A-band radiances in-orbit is derived.

1.3 Outline

The present study is now divided into the following parts. Closing the introduction in section 1.4, remarks are made about definitions and conventions used throughout this thesis regarding optical simulations. Discussed are the interferogram simulations and general mathematical concepts relevant to the analysis of the optical systems in the following chapters. Discussion of the O₂ A-band airglow layer formation follows in section 2.1 whereby the spatial heterodyne spectrometer (SHS) is introduced as a suitable type of spectrometer for its observation. General properties of SHS in first order are covered in section 2.2 which yield analytical expressions for the expected interferogram fringe patterns and are used to derive the baseline geometric design. Adding performance requirements of the AtmoLITE mission, especially, in due consideration of size constraints and the AtmoLITE optical layout, allows a more detailed discussion in section 2.5 with respect to the expected thermal environment and the impact of the low pressure in-orbit conditions. The importance of manufacturing and alignment tolerances of SHS components is covered in section 2.6 which includes expected performance degradations in terms of interferogram fringe visibility if tolerances are exceeded. Discussion of the instrument optics is covered in chapter 3. The chapter starts with a discussion of drawbacks discovered during the on-ground and in-orbit verification of the Atmospheric Spatial Heterodyne Interferometer Next Explorer (AtmoSHINE) instrument, the AtmoLITE predecessor, which ultimately required a new optical layout. The discussion includes results of optical characterisation of separated front- and camera optics in section 3.2 and unexpected stray light reflections between optical elements discovered during the LOS characterisation of AtmoSHINE in section 3.3 and section 3.4. Updated requirements for AtmoLITE and the new optical layout are presented in section 3.5. A modelling study is presented which covers expected interferogram fringe visibility with respect to field angle and wavelength of observation. Additional details are

summarized in section 3.7 and section 3.8 regarding operation in low pressure environments and the optics' performance sensitivity to alignment, respectively. The chapter closes with an estimation of expected atmospheric radiance levels as observed by the AtmoLITE instrument in section 3.10. This estimation is later used in the derivation of an overall temperature retrieval uncertainty for the AtmoLITE instrument. In chapter chapter 4 the calibration concept is introduced which for the first time features a new calibration light source developed specifically for the AtmoLITE instrument. The first sections cover performance requirements and optical design of the new light source from section 4.1 onwards, a first proof-of-concept alignment test in section 4.5 and the general concept of its verification in section 4.6.

In order to verify all proposed alignment and assembly strategies in an as-build scenario, an experimental verification of performance based on the AtmoLITE prototype instrument has been conducted which is covered in chapter chapter 5. Featured are improvements made to the SHS alignment jig in section 5.1, the general approach of PSF, MTF and FOV extent measurements in section 5.2 and the first interferograms obtained with the AtmoLITE instrument under ambient conditions in section 5.3. For the first time, these experimental results are used to derive a temperature retrieval uncertainty for the AtmoLITE instrument with respect to its calibration only which highlights important constraints of the AtmoLITE instrument not considered in previous studies. Most notably, the currently expected AtmoLITE temperature retrieval standard uncertainty, based on standard uncertainties of the calibration only, is derived which yields $u_{\text{AtmoLITE}} = \pm 1.4 \text{ K}$.

The main part of this work closes with a summary of all major improvements made to the science payload, its calibration concept and achieved experimental milestones. It also provides an outlook and a few guidelines for upcoming studies covering experimental tests still required to assess the full temperature retrieval standard uncertainty but delayed due to the COVID19 pandemic.

1.4 Remarks about AtmoLITE optics simulations

Already knowing that AtmoLITE becomes a limb sounder which shall provide spatially resolved 3D temperature data, metrics to evaluate or quantify its imaging performance are necessary. Moreover, because the temperature information is inferred from the rotational spectral distribution of observed O₂ A-band airglow, a method to predict the expected AtmoLITE SHS interferogram shape is necessary. Therefore, this chapter introduces the general concept of point spread function (PSF)

and modulation transfer (MTF) in advance to the optical design and analysis of the AtmoLITE instrument. The given definition of PSF also provides a convenient way to simulate the interferogram of the combined system of AtmoLITE SHS and AtmoLITE optics.

Definition of PSF and MTF

Concerning the AtmoLITE imaging performance, the primary interest is the optics resolution, in particular the resolution of individual altitude layers. Resolution describes the ability of optical systems to distinguish small details of objects at finite conjugates or to separate their angular extent when focused at infinity. Here the best known limit, Equation 1.1, is considered when photons are used to produce an image under incoherent illuminations and assuming diffraction limited imaging. It is called Abbe criterion and relates the smallest resolved feature size d , the numerical aperture NA of the optical system and the wavelength of observation [Abbe Hon., 1881]. Commonly, the numerical aperture is expressed by the refractive index n of the medium between object or image plane and the optical systems aperture, and the optics' cone angle α as $\text{NA} = n \cdot \sin \alpha$. Including unit magnification and projection onto a two-dimensional imaging plane, the distance d is referred to as the Airy radius or disc of an optical system.

$$d \geq \frac{\lambda}{2 \cdot \text{NA}} \quad (1.1)$$

A more practicable definition yields the limit expressed in Equation 1.1 based on the Fourier transform of a circular and aberration free pupil function of an imaging system where the Airy disc corresponds to the first minimum of the resulting point-spread function [Goodman, 2005]. Notations of the theoretical derivation used in the following are based on the lecture notes of Norbert Lindlein (Simulationsmethoden in der Optik, personal communication with Klaus Mantel, 2018) and derived from the free-space propagation of plane waves. At first, the general description of a complex plane wave $u(x, y, z_0)$ at a distance z_0 away from its source and propagating strictly in positive z-direction is considered which is expressed by Equation 1.2. This expression is the mathematical description of the well known superposition of elementary waves h of radius r according to the Huygens-Fresnel principal. Note that the notation in Equation 1.2 and 1.3 differs from Goodman [2005, p. 52, equation 3-51] in that the direction cosine of propagation is expressed by the wave vector component k_n and the radial intensity drop of the wave is explicitly given.

$$u(x, y, z_0) = \int \int u_0(x', y', 0) \underbrace{\left(-\frac{1}{2\pi} \left(ik_n - \frac{1}{r} \right) \frac{z_0}{r} \frac{e^{ik_n r}}{r} \right)}_h dx' dy' \quad (1.2)$$

In order to evaluate Equation 1.2 including an optical system, the effective transmission function of an optical system in thin lens approximation Equation 1.3 is introduced which includes the effective focal length f and wavefront aberrations $W(x', y')$ in case of real systems.

$$t_{lens}(x', y') = e^{-ik\left(f\sqrt{1+\frac{x'^2+y'^2}{f^2}}-f\right)} + e^{ikW(x', y')} \quad (1.3)$$

Multiplying the integrand of Equation 1.2 by Equation 1.3 allows to evaluate the complex wave $u(x, y, z_0)$ near the paraxial focus at $(0, 0, f)$. Neglecting terms of second and higher orders in x, y, x' and y' and evaluating the integral over the optics' aperture area A yields Equation 1.4. Note the difference in notation to Goodman [2005, p. 67, formula 4-17] is an explicit expression of the wave front aberrations by $\exp[ikW(x', y')]$.

$$u(x, y, z_0) = \frac{-i}{\lambda z_0} e^{ikz_0} e^{ik\frac{x^2+y^2}{2z_0}} \iint_A u(x', y', 0) e^{ikW(x', y')} e^{ik\frac{\Delta z}{z_0 f} \frac{x'^2+y'^2}{2}} e^{-ik\frac{xx'+yy'}{z_0}} dx' dy' \quad (1.4)$$

Typically, Equation 1.4 is evaluated at the focal plane of an optical system at $\Delta z = 0$ and the quantity of interest is the intensity distribution $|u^2|$ which is called PSF. Note that within the focal plane $z_0 = f$. Therefore, the final expression for the PSF is given in Equation 1.5 as the Fourier transform of the complex wave function evaluated over the system's exit aperture.

$$PSF(x, y) = \frac{1}{\lambda^2 f^2} \left| \iint_A u(x', y', 0) e^{ikW(x', y')} e^{-ik\frac{xx'+yy'}{f}} dx' dy' \right|^2 \quad (1.5)$$

In addition, performing a second Fourier transform of the PSF allows to recover the frequency spectrum corresponding to a given PSF distribution. The magnitude given in Equation 1.6 is commonly referred to as MTF and is the measure of transferred image contrast between object and image plane.

$$MTF(\nu_x, \nu_y) = |OTF(\nu_x, \nu_y)| = \left| \iint PSF(x, y) e^{2\pi i(\nu_x x + \nu_y y)} dx dy \right| \quad (1.6)$$

Evaluation of the MTF yields a direct measure of the altitude resolution. For instance, the desired altitude separation of 1.5 km corresponds to a spatial frequency of $\nu_x = 4.2$ lp/mm for the AtmoLITE optics. Thus, evaluation of the AtmoLITE optics MTF at this frequency yields a direct metric whether desired altitude resolution is achieved or not. Therefore, MTF values obtained by Equation 1.6 are normalized to the interval $[0; 1]$. Values of 0 correspond to no altitude resolution of the desired spacing and a more coarse altitude sampling would need to be used. MTF values of 1 express perfect imaging of the source without any loss of contrast.

Interferogram simulation

The keen reader might have noticed that the wavefront aberration $W(x', y)$ in Equation 1.5 is only restricted to a single source point. In particular, splitting and recombination of the wavefront between source point and exit aperture of the imaging optics allow to simulate interference effects of SHS systems as follows.

Assume a single atmospheric source point in-front of the AtmoLITE instrument. In limb-viewing geometry of AtmoLITE, waves originating from this source point appear as plane waves to the instrument, hence, Equation 1.2 and Equation 1.5 apply. Using ray-tracing to propagate the wavefront, the additional wavefront aberration added by the AtmoLITE optics and evaluated at the exit aperture of the system is obtained. Conducting this ray-trace for both SHS arms separately and adding the result coherently, allows to estimate the effective wavefront aberration including splitting and recombination of the wavefront at the SHS beam splitter:

$$\exp [ikW(x', y')] = \exp [ikW_{\text{arm } 1}(x', y')] + \exp [ikW_{\text{arm } 2}(x', y')] \quad (1.7)$$

The image of the single source point including the interference effects caused within the SHS is then obtained by substitution of Equation 1.7 into Equation 1.5. Incoherent summation over all source points across the AtmoLITE field-of-view (FOV) yields the final interferogram.

Conventions regarding the AtmoLITE FOV

The AtmoLITE instrument is designed to cover an angular field of $\pm 0.65^\circ$ along vertical and horizontal viewing direction. Hereby, vertical and horizontal direction correspond to different altitude layers and the spectral axis of interferogram recording, respectively. For convenience, a normalized coordinate system is used throughout this work. The normalized coordinates are denoted H_x , H_y and are defined on the interval between $[-1; 1]$ which corresponds to the detector edges. In particular, $H_x = \pm 1$ denotes the interferogram edges corresponding to an observation angle of $\pm 0.65^\circ$ in altitude direction whereas H_y denotes coordinates along the dispersion direction. It is noteworthy that this FOV definition implies that the maximum field point at $(H_x, H_y) = (1, 1)$ encloses up to 0.92° with respect to the optical axis.

Software used to evaluate simulations

Interferogram simulations are performed with a combination of Zemax Optical Studio (ZEMAX) and Python 3.5+. The official ZOSAPI interface of ZEMAX is used to send input and output commands to ZEMAX via Python. Next, ray-tracing of a plane wavefront through the AtmoLITE optics is performed in ZEMAX to obtain aforementioned wavefront aberration. The obtained wavefront aberrations are then passed to Python for evaluation of Equation 1.7 and Equation 1.5. For convenience, wavefront aberration data is represented by fringe Zernike polynomials if explicitly presented. A short overview of the definition of fringe Zernike polynomials is appended in section A.1.

All algorithms are implemented based on the official Python modules of Numpy and Scipy and visualizations of results is done with Matplotlib. No other or proprietary software tools are used to evaluate the optical performance of the AtmoLITE instrument in this work.

Remarks about Fourier transformation

The evaluation of Equation 1.5 and 1.6 requires computation of the Fourier transform. In this work, the discrete Fourier transform proposed by Cooley and Tukey [1965] is used as implemented in the Numpy.fft module. In order to smooth simulation results, 8-fold zero padding is applied.

In addition to zero padding, the evaluation of simulated and measured interferograms by means of Fourier transformation includes apodisation. Apodisation is commonly applied in signal processing of periodic signals such as interferograms if a sharp cut-off of the signal occurs. By multiplication with the apodisation function, the signal is continuously decreased to zero at the considered window edge, thus, allowing for a continuous continuation beyond the simulated or measured interferogram edge. If not applied, the sharp signal boundary leads to so called ringing or side lobes in spectral domain. In the well known case of Fourier transformation of a rectangular (boxcar) function, a sinc function of the form $\text{sinc}(x) = \sin(\pi x)/(\pi x)$ is obtained which was first discussed by Woodward and Davies [1952]. To suppress these ringing effect, this work considers the blackman apodization window [Blackman et al., 1960] in all following discussions.

This comprises the introduction to the optical simulations of AtmoLITE. Further details are now provided in chapter 2 where the AtmoLITE SHS properties are discussed and its expected performance is evaluated. In addition, first results of the interferogram simulation are presented to highlight the importance of

manufacturing tolerances and a fault tolerant assembly. Further simulation results follow in chapter 3 where the AtmoLITE optics performance is evaluated under different environmental conditions, namely varying temperature and pressure. The interferogram simulation is also used to define baseline requirements for the design of the AtmoLITE Calibration Unit in chapter 4.

2

Observation of the O₂ A-Band by Spatial Heterodyne Spectroscopy

Contents

2.1	The Oxygen Atmospheric Airglow	16
2.2	The Spatial Heterodyne Spectrometer	21
2.3	Spectrometer Design for the AtmoLITE Instrument .	24
2.4	Definition of interferogram fringe visibility	27
2.5	The AtmoLITE SHS under Space Conditions	30
2.6	SHS Tolerance & Alignment Considerations	36

The atmospheric oxygen A-band emission, in short O₂ A-band, is an airglow phenomenon generated by excited oxygen molecules. It is mostly excited by solar irradiation during day-time but also apparent at night-time due to collisional excitation processes. Having a rather long-lived excited state, atmospheric background temperature is imprinted in the O₂ A-band rotational fine structure. Hence, observation of the O₂ A-band emission allows for retrieval of temperature information in the mesosphere and lower thermosphere (MLT).

In the following discussion, the envisaged device to conduct spectrally resolved O₂ A-band observations is the SHS selected for the Development Initiative of Small Satellites for Exploration of Climatology by Tomography (DISSECT) framework [Deiml et al., 2014] with major changes implemented for the AtmoLITE missions as described in section 2.2 and section 2.3. In comparison, another instrument currently in development at the Department of Meteorology at Stockholm University (MISU)

in Stockholm is the Mesospheric Airglow/Aerosol Tomography and Spectroscopy (MATS) instrument which does not resolve the spectral fine-structure of the O₂ A-band [Gumbel et al., 2020]. In fact, it relies on comparison of the total transmitted radiance across four different spectral channels to derive temperature information. Further examples of other well known satellite instruments are the scanning imaging absorption spectrometer for atmospheric cartography SCIAMACHY onboard ENVISAT-1 [Hoogeveen et al., 1994], NASA’s Orbiting Carbon Observatory OCO-2 [Pollock et al., 2010; Basilio et al., 2014] or the Swedish Optical Spectrograph and InfraRed Imaging System (OSIRIS) onboard ODIN [Llewellyn et al., 2004; Frisk et al., 2003; Olberg et al., 2003]. The common observable of these instruments is the spectral rotational fine structure of the O₂ A-band emission, although, the optics are quite different between all of these instruments. In general, the O₂ A-band fine structure is Boltzmann distributed in dependence on temperature which is further discussed in section 2.1. Therefore, temperature information can be retrieved by fitting an atmospheric forward model to the measured spectra and scenery.

The concept of a spatial heterodyne spectrometer was first proposed by Connes [1958] and called *Spectromètre interférentiel à selection par l’amplitude de modulation*. Its main advantage compared to the traditional measurement techniques of Michelson or Fabry-Pérot interferometers is its ability to record multiple wavelength spectra within a single 2D-image without requiring any scanning mechanism. Thus, the SHS incorporates the Fellgett or multiplex advantage of FTS instruments [Fellgett, 2006] at a great reduction of opto-mechanical steering mechanisms by design. Unfortunately, experimental setups could not take full advantage of the 2D-imaging property prior to the early 70s, until two-dimensional imaging detectors became readily available. SHS applications in atmospheric science took even longer. Based on early works of Harlander [1990] the SHS technology was further adapted to observations onboard sounding rockets [Harlander et al., 1995]. Following continuous development allowed to manufacture miniaturised and monolithic SHS instruments [Harlander et al., 2003], paving the way for research from space [Harlander et al., 2004]. To this day, different applications were developed involving observations of mesospheric wind and temperature [Harlander et al., 2010], water vapour [Langille et al., 2019a] and emission spectra ranging from UV [Watchorn et al., 2001, 2010] to IR [Smith et al., 1999a]. In addition, ongoing research will soon extend these observations towards mesospheric temperature based on measurements in the VIS/NIR wavelength range which is discussed in the following. The SHS technology is also applied in other fields of research. For instance, spectral analysis of material

compositions commonly based on observation of Raman spectra [Gomer et al., 2011] and/or laser induced breakdown spectroscopy [Gornushkin et al., 2014].

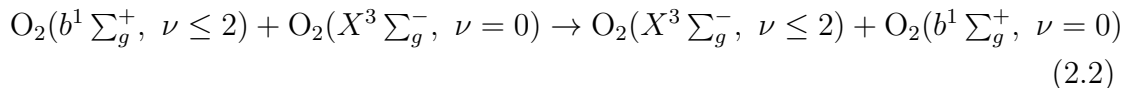
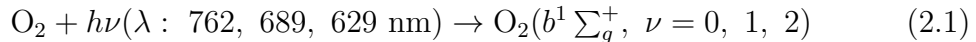
When instrumentation is brought into space, it has to cope with harsh environmental conditions during launch and in-orbit operation. During the design process, compensators were considered for fluctuating instrument temperature and surrounding ambient pressure. Corresponding simulations and derived guidelines for the SHS procurement are presented in section 2.6 and section 2.5. Additional considerations involving the optics surrounding the SHS are presented in chapter 3. Finally, evaluation of data from space missions requires a thorough calibration strategy. Where large satellite platforms can rely on build-in calibration sources and re-calibrate themselves in-orbit, the instrumentation for the AtmoLITE mission has to fit into the small form factor of a CubeSat. Thus, space is not available for a build-in calibration source and the calibration has to be performed on-ground prior to the satellite launch. The developed calibration strategy and necessary tools are introduced in chapter 4.

2.1 The Oxygen Atmospheric Airglow

The molecular emission introduced in this section is the oxygen atmospheric band which is also known as the O₂ A-band airglow. The following brief overview includes the photo-chemical reactions leading to the population and deactivation of the excited state O₂($b^1 \Sigma_g^+$, $\nu = 0$). Further, the temperature dependence of the fine structure on rotational temperature is discussed which is the basis for the AtmoLITE instrument design, the next generation instrument of AtmoSHINE. The complete atmospheric model is not covered here as it has already been covered in great detail in previous studies. A comprehensive model overview is provided by Sheese [2011] who greatly extended earlier works of Bucholtz et al. [1986]. Deiml [2017] and Song [2018] used this model to develop the first optical design and an in-orbit observation strategy for AtmoSHINE, respectively. Airglow during night time was further covered in Chen [2020] including estimations of OH and O₂ along interpretation of measured satellite data from GOMOS, SABER and compared to first measurements of AtmoSHINE.

Excitation of the O₂ A-band airglow

Typically, three excitation processes are distinguished which end up in the O₂ A-band emitting state O₂($b^1 \Sigma_g^+$, $\nu = 0$). Firstly, the direct absorption of solar irradiance during daytime excites oxygen molecules at the three different wavelengths of $\lambda = 629, 689$ and 762 nm which are named γ -, B- and A-band, respectively. By quenching, the energetically higher vibrational excitation levels of O₂($b^1 \Sigma_g^+$, $\nu = 1, 2$) transition to O₂($b^1 \Sigma_g^+$, $\nu = 0$) via intra-molecular near resonance electronic-electronic exchange (EE)[Yankovsky, 1991]. This process transfers the electronic excitation from the initially excited oxygen molecule to its collisional partner while conserving the vibrational excitation $\nu = 1, 2$ [Yankovsky and Manuilova, 2006] and is given by Equation 2.2. Note that the direct absorption of solar irradiation in the infra-red atmospheric band indicated in Figure 2.1 does not contribute to the emitting state O₂($b^1 \Sigma_g^+$, $\nu = 0$). Due to self-absorption the atmosphere becomes optically thick below 80 km in limb view, thus, observations of the atmospheric band emissions and retrieval of e.g. temperatures and number densities are preferably conducted from satellite platforms.



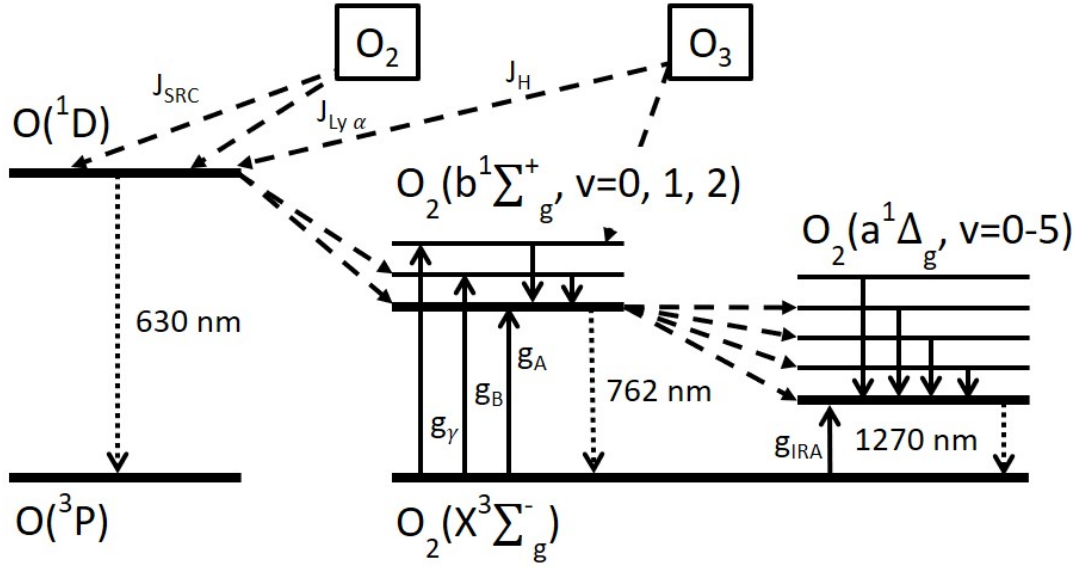
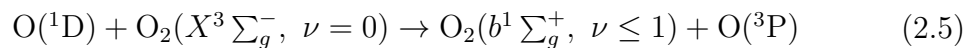
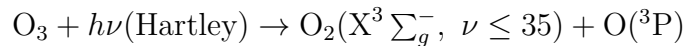
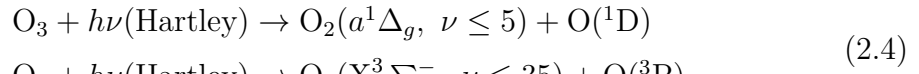
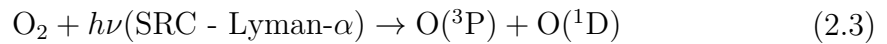
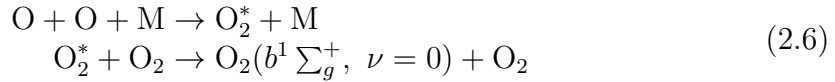


Figure 2.1: Overview of O₂ A-band emission production and loss mechanisms.

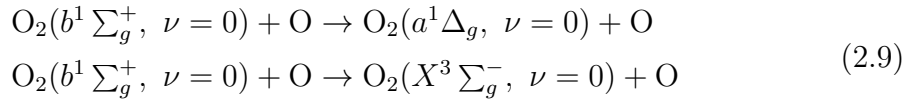
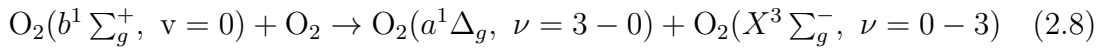
Secondly, deactivation of O(¹D) by quenching with oxygen molecules populates the lowermost two vibrational levels of O₂(b¹Σ_g⁺, ν = 0, 1) by collisional excitation as given in Equation 2.5 [Streit et al., 1976; Lee and Slanger, 1978; Green et al., 2000]. The source of O(¹D) is photo-dissociation of ozone and oxygen due to solar irradiation with the governing reactions in Equation 2.3. At altitudes above 80 km, photo-dissociation of oxygen becomes the dominant source of O(¹D) as the concentration of ozone decreases much more rapidly when compared to oxygen. For instance, based on initial noon-time concentrations at 80 km of $n_{O_2} \approx 10^{14} \text{ cm}^{-3}$ and $n_{O_3} \approx 10^9 \text{ cm}^{-3}$, the relative ratio of n_{O_2}/n_{O_3} already increases by four orders of magnitude towards an altitude of 120 km [Rodrigo et al., 1986] ($n_{O_2} \approx 10^{11} \text{ cm}^{-3}$ and $n_{O_3} \approx 10^2 \text{ cm}^{-3}$ at 120 km). The photo-dissociation of ozone in the Hartley band yields O₂(a¹Δ_g, ν ≤ 5) as a by-product which is of interest for the formation of the oxygen atmospheric infra-red emission [Michelsen et al., 1994; Sparks et al., 1980; Valentini et al., 1987; Ball et al., 1995; Klais et al., 1980]. The second possible by-product of ozone photo-dissociation is vibrationally excited ground state oxygen covered in Equation 2.4 which does not produce O(¹D) [Svanberg et al., 1995].



Finally, a third process proposed by Barth and Hildebrandt [1961] describes the three-body recombination of atomic oxygen forming excited O_2^* . These molecules form $O_2(b^1 \Sigma_g^+, \nu = 0)$ by collisional relaxation with other oxygen molecules which is indicated in Equation 2.6 which yields an significant increase of the O_2 A-band emission near 90 km. Historically, an alternative reaction has been proposed by Wallace and Hunten [1968]. However, following studies by e.g. Campbell and Gray [1973] or Slanger and Black [1977] soon favoured the Barth process. Until today and despite the importance of this process in the absence of solar irradiation during night, the rate constants and possible branching ratios are still poorly understood [Kalogerakis, 2019] and approximations based on airglow observation introduced by McDade et al. [1986] see persistent use.



Apart from spontaneous emission of the O_2 A-band at $\lambda = 762$ nm the excited state $O_2(b^1 \Sigma_g^+, \nu = 0)$ is deactivated by quenching with different partners. This includes quenching with N_2 , O_2 , O_3 and CO_2 into $O_2(a^1 \Delta_g, \nu = 0)$. Hereby, quenching with O_2 may also excite the reaction partner to $O_2(X^3 \Sigma_g^-, \nu \leq 3)$ along varying vibrational levels of $O_2(a^1 \Delta_g, \nu \leq 3)$ as given in Equation 2.8 [Klingshirn and Maier, 1985]. At altitudes above 80 km, the strongly increasing concentration of molecular oxygen yields two further quenching reactions 2.9 [Atkinson et al., 1992; Hadj-Ziane et al., 1992] which completes the overview of activation and deactivation processes involved in the formation of $O_2(b^1 \Sigma_g^+, \nu = 0)$.



A typical contribution of each reaction pathway to the total airglow within the narrow altitude range relevant for this study was covered in [Deiml et al., 2014] based on the model of [Sheese, 2011]. Starting at 50 km, reaction pathways are dominated by contribution of photo-dissociation of ozone. Between 50 km and 90 km resonant scattering and self-absorption of photons in the atmospheric bands is the largest contribution Equation 2.1. At higher altitudes, where the concentration of ozone diminishes rapidly and the overall density of the atmosphere decreases, the photo-dissociation of molecular oxygen Equation 2.3 remains the only significant contribution to the airglow layer.

Temperature signature within the O₂ A-band

Equilibrium of all presented photo-chemical pathways is another critical assumption commonly made in order to derive atmospheric temperature from O₂ A-band airglow observations. The most direct reasoning that equilibrium is valid on small scales for mesospheric O₂ A-band airglow, relies on the continuity equation 2.10 as formulated by (Brasseur and Solom, 2005). This relation describes a balance between (1) the temporal variation of the number density of excited molecules $[x]$, (2) the mass flow through the volume of consideration and (3) any production or loss mechanisms $S_x = P_x - L_x[x]$ of the excited species.

$$\frac{\delta[x]}{\delta t} + \nabla \cdot ([x] \vec{v}) = S_x \quad (2.10)$$

Given the radiative life time τ of O₂($b^1 \Sigma_g^+$, $v = 0$) can be expressed by the reciprocal band Einstein coefficient, $\tau = 1/A \approx 12$ s, two assumptions are made as follows. On the one hand, τ is sufficiently short such that transport processes have negligible impact on $[x]$, on the other hand, τ is sufficiently long such that reactant concentrations of local chemical reactions can be assumed in equilibrium, $\frac{\delta[x]}{\delta t} = 0$. Thus, the left side of Equation 2.10 is commonly set equal to zero and the number density $[x]$ becomes equal to the ratio of production and loss processes. This is an advantageous simplification which allows to derive temperature information directly from O₂ A-band spectra, relying on local chemistry rather than large scale circulation models Sheese [2011].

In addition, rotational local thermal equilibrium (LTE) is assumed. This allows to represent the rotational fine structure of the emission spectrum by the Boltzmann distribution given in Equation 2.11 under the assumption that all excited states of interest are thermalized. The normalisation is defined by the partition sum $Q(T)$ of the upper-state rotational energies E_u including statistical weights g_u . The individual emission lines are further scaled by their respective Einstein coefficients of spontaneous emission $A_{u,e}$ and normalised to the band Einstein coefficient A_{762} .

$$f_{\text{Boltzmann}}(\nu)_{u,e} = \frac{g_u(\nu)}{Q(T)} \cdot \exp\left(-\frac{hcE_u(\nu)}{k_B T}\right) \cdot \frac{A_{u,e}(\nu)}{A_{762}} \quad (2.11)$$

$$Q(T) = \sum_u \left[g_u \cdot \exp\left(-\frac{hcE_u}{k_B T}\right) \right] \quad (2.12)$$

This description is sufficient for the present study and included simulations of expected instrument performance. However, a few more steps are required if atmospheric spectra are observed where multiple volumes of emitting molecules at different temperatures are superimposed. Commonly, studies start with an estimate

of the altitude dependent volume emission rate (VER) expressed as deactivated molecules of the emitting state per unit volume and time interval where an a priori temperature distribution in the atmosphere is initially assumed. Afterwards, integration of the VER along the instrument LOS yields the radiance levels observed by the instrument [He et al., 2019]. Next, an iterative retrieval scheme estimates a best fit temperature distribution such that observed and simulated radiance levels match. Within the AtmoHITE project such modelling efforts were started by Deiml [2017] and Song [2018] which were later advanced for the AtmoLITE project by Chen [2020]. The original model of all these studies was based on Sheese [2011].

2.2 The Spatial Heterodyne Spectrometer

Harlander [1990] was one of the first working on scientific instrumentation based on symmetric and asymmetric SHS designs. Mainly focusing on the field-widening and throughput characteristics, he developed expressions for the general SHS description. Following his conventions, this section introduces the symmetric SHS design shown in Figure 2.2 which is utilised throughout this thesis. Manufacturing defects and resulting interferometer arm imbalances are neglected for now. Strategies to handle these such as flat-fielding [Englert and Harlander, 2006a] and phase correction [Englert et al., 2005] are discussed in chapter 5.

The symmetric SHS is similar to a Michelson interferometer. It divides the incident light of intensity I into two wave fronts utilising a beam splitter. However, the propagating wave fronts are refracted at two inclined diffraction gratings $G_{1,2}$ instead of mirrors. These diffraction gratings are fixed in position and no scanning has to be performed which greatly simplifies the overall design and allows for a monolithic approach where all SHS parts are bonded together. Due to the diffraction, a small phase offset is added to each propagating wave front which is indicated by tilted wavefronts exiting the beam splitter in Figure 2.2. After recombination of the wave fronts at the beam splitter, the so called Fizeau interference fringe pattern is recorded at the exit aperture of the SHS. This exit aperture is typically visualized as localisation plane of highest interferogram fringe contrast and corresponds to the virtual position of the grating surface as seen by the camera optics [Harlander et al., 2002]. In this work, the corresponding visualization is presented once the AtmoLITE optics are introduced in Figure 3.1.

In the following, the beam splitting is considered ideal and polarisation effects $\epsilon_{1,2}$ are neglected which is only applicable if material properties are identical and alignment is ideal across both SHS arms. In practice, such polarisation effects or material non-uniformities (e.g. anti-reflection coatings, refractive index non-uniformities, mechanical stress or impurities) manifest as phase distortions of the interferogram or an imbalance of individual arm transmission. For the corresponding mathematical description of the interferogram refer to chapter 5 and section A.7. Here, the propagating wavefronts in each arm are of same intensity $I_1 = I_2 = I_0/2$ and the general fringe pattern is defined by Equation 2.13 if plane waves are considered.

$$\begin{aligned} I &= I_1 + I_2 + 2\sqrt{I_1 I_2} \cos[(\vec{k}_1 - \vec{k}_2)\vec{r} + \epsilon_1 - \epsilon_2] \\ &= I_0(1 + \cos[(\vec{k}_1 - \vec{k}_2)\vec{r}]) \end{aligned} \quad (2.13)$$

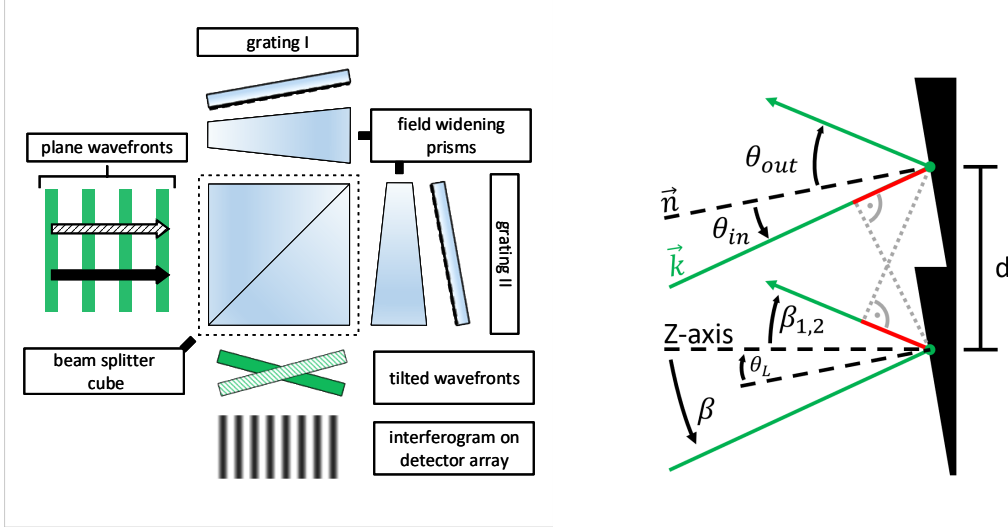


Figure 2.2: Concept of the spatial heterodyne spectrometer including all essential parts (left) and detailed view of a plane wave refraction at a typical saw tooth type grating surface (right). The angle definitions are referenced to the nominal optical axis (Z -axis) and the grating surface normal \vec{n} . The total optical path difference after refraction between two points is shown as projection from the dispersion plane onto the beam path (red).

The wave vectors $\vec{k}_{1,2}$ of the incident wavefronts are given by Equation 2.14. The wave number is denoted σ and Φ_i is the angle between the wave vectors $\vec{k}_{1,2}$ and the dispersion plane of the gratings. The angle β_i describes the outgoing wave vectors angle after diffraction.

$$\begin{aligned} k_{x,i} &= 2\pi\sigma \cos \Phi_i \sin \beta_i \\ k_{y,i} &= 2\pi\sigma \sin \Phi_i \\ k_{z,i} &= 2\pi\sigma \cos \Phi_i \cos \beta_i \end{aligned} \quad (2.14)$$

Defining the grating equation in terms of the incoming angles and outgoing angles yields Equation 2.15, whereby G denotes the grating groove density and m is the diffraction order.

$$\begin{aligned} mG &= \sigma \cos \Phi (\sin(\theta_{out}) + \sin(\theta_{in})) \\ &= \sigma \cos \Phi (\sin(\theta_L \mp \beta_{1,2}) + \sin(\theta_L \mp \beta)) \end{aligned} \quad (2.15)$$

The angle θ_L is called Littrow angle. It defines the Littrow wave number σ_L at which the incident and outgoing wave vector directions are identical and yields the Littrow condition in Equation 2.16.

$$mG = 2\sigma_L \sin \theta_L \quad (2.16)$$

Combining the Littrow condition and grating equation, the first order approximation, Equation 2.17, for the outgoing angles $\beta_{1,2}$ is derived.

$$\begin{aligned} \frac{2\sigma_L \sin \theta_L}{\sigma \cos \Phi} - \sin(\theta_L \mp \beta) &= \sin(\theta_L \mp \beta_{1,2}) \\ &= \sin \theta_L \mp \beta_{1,2} \cos \theta_L + \mathcal{O}(\beta_{1,2}^2) \end{aligned} \quad (2.17)$$

Considering wave fronts exclusively propagating on-axis ($\Phi = 0$, $\beta = 0$) expression 2.18 for the outgoing wave vector is obtained.

$$\beta_{1,2} = \pm 2 \frac{\sigma_L - \sigma}{\sigma} \tan \theta_L \quad (2.18)$$

Combining Equation 2.14 and Equation 2.18, the analytical Fizeau fringe pattern is derived for first order in $\beta_{1,2}$. Note that the interference pattern is only evaluated along the dispersion plane by substitution of $\vec{r} = (x, 0, 0)$.

$$I = I_0(1 + \cos(2\pi \cdot [4 \tan \theta_L (\sigma_L - \sigma)]x)) \quad (2.19)$$

Based on Equation 2.19, three important SHS properties are evident. Firstly, the spatial frequency of the fringes is the linear difference of the incident light's to the Littrow wave number scaled by the tangent of the Littrow angle. Therefore, the range of recorded frequencies can be tuned by proper choice of the Littrow wave number during the design process. For instance, small interferogram fringe frequencies can be obtained by minimizing the difference $\sigma_L - \sigma$ between the Littrow wave number and the spectral features of interest. This is the heterodyne component. Secondly, the scaling factor $\tan \theta_L$ is tuned by variation of the grating groove density G while keeping a fixed Littrow wave number. This allows to narrow or widen the total bandpass between minimum and maximum desired frequencies by increasing or reducing G , respectively, according to Equation 2.16. Thus, a fine tuning of the spectral resolution during the SHS design is possible. The third property can be derived by substituting wave numbers above and below the Littrow wave number into Equation 2.19. Choosing wave numbers at equal distances around the Littrow wave number yields the same frequency. This ambiguity has to be accounted for to avoid spectral leakage from outside the expected emission. The easiest solution is a well defined bandpass filter around the spectral features of interest with the Littrow wave number placed near one of the filter edges. This will be further illustrated in section 2.3 where the design changes from the AtmoHIT/AtmoSHINE SHS towards the AtmoLITE SHS are discussed.

Applications of the SHS often require to disperse wave fronts which do not exclusively propagate on axis but are incident at a certain angle. Fortunately, field-widening techniques of Michelson interferometers can be applied to the SHS by including a prism in each interferometer arm as demonstrated by Harlander [1990]. Hereby, the field-widening effectively introduces three boundary constraints for the SHS angles between beam splitter, field-widening prism and grating surface which are given in Equation 2.20, 2.21 and 2.22.

$$\frac{n^2-1}{n^2} \tan \beta \frac{2n^2-\sin^2 \beta}{n^2-\sin^2 \beta} = \tan \theta_L \quad (2.20)$$

$$n \sin \frac{\alpha}{2} = \sin \beta \quad (2.21)$$

$$\eta = \theta_L - \arcsin[n \sin(\alpha - \arcsin(\frac{1}{n} \sin \beta))] \quad (2.22)$$

The angles α , β and η describe the relative orientations of the SHS parts. An overview is given in Table A.4. Note that the refractive index dependence in Equation 2.22 makes the SHS sensitive to temperature and pressure changes of the environment which is further discussed in section 2.5.

2.3 Spectrometer Design for the AtmoLITE Instrument

The starting point of every SHS design is the selection of the target emission lines and their corresponding required spectral resolution. Here, the AtmoLITE instrument targets emission lines between 13057 cm^{-1} and 13160 cm^{-1} if the bandpass filter is considered as explained in the following. Based on section 2.1 the corresponding spectral intensity distribution can be evaluated which is shown in Figure 2.3. The typical separation between Q- and R-branch of linear molecules appears around $\sigma = 13127 \text{ cm}^{-1}$.

Initially, the resolving power required to separate every single emission line is estimated according to Equation 2.23. The difference $\Delta\sigma$ is defined between adjacent lines which have a relative emission intensity of greater than one percent at an atmospheric background temperature of 200 K.

$$R = \frac{\sigma}{\Delta\sigma} \quad (2.23)$$

Both O₂ A-band branches are separated at $\sigma = 13127 \text{ cm}^{-1}$ in order to highlight the more demanding resolving power required to fully resolve individual emission lines at $\sigma > 13127 \text{ cm}^{-1}$ and an overview of the estimated resolving powers is given in Figure 2.4. Note that a spectral resolution of $\Delta\lambda < 0.1 \text{ nm}$ is already sufficient to fully resolve all individual emission lines below $\sigma = 13127 \text{ cm}^{-1}$ which corresponds to a resolving power of $R = 7300$. At $R = 28000$ a spectral resolution better than $\Delta\lambda = 0.03 \text{ nm}$ would be required to fully resolve all emission lines included in the upper branch. Luckily, the temperature retrieval precision goal of $\Delta T = \pm 1.5 \text{ K}$ does not require such high resolving powers. Preliminary estimations by Chen (personal communication with Q. Chen, 2018) showed that an effective spectral resolution of

$\Delta\lambda = 0.17$ nm corresponding to $R = 4500$ is sufficient if both branches are included in the observed spectra. Thus, the designed resolving power is chosen at $R = 9000$ in order to allow later usage of apodization windows which typically degrade the spectral resolution by a factor of up to two. Thereby, the AtmoLITE SHS does no longer resolve individual emission lines by design, contrary to the AtmoSHINE SHS.

Next, a suitable grating has to be selected where the grating groove density and usable illuminated area are the first parameters to be chosen. COTS available grating groove densities range from $G = 3000$ cm⁻¹ to $G = 12000$ cm⁻¹ for applications working in first order of diffraction and around a wavelength of $\lambda = 760$ nm. The usable illuminated grating area is limited by two boundary conditions. Firstly, the AtmoLITE mission requires back-compatibility of its GSENSE detector array to the older HWK1910 sensor. Therefore, the usable detector area is limited to $A = 1 \times 1$ cm² during the design process, in particular the area is limited to the full width of the HWK1910 sensor. Secondly, the camera optics magnification from the grating surface to the detector array is designed around a target value of $M = 0.6$. Thus, the corresponding illuminated grating area is $A = 1.6 \times 1.6$ cm². Combining the illuminated grating area width $W = 1.6$ cm and the grating groove density, the SHS resolving power is rewritten in Equation 2.24

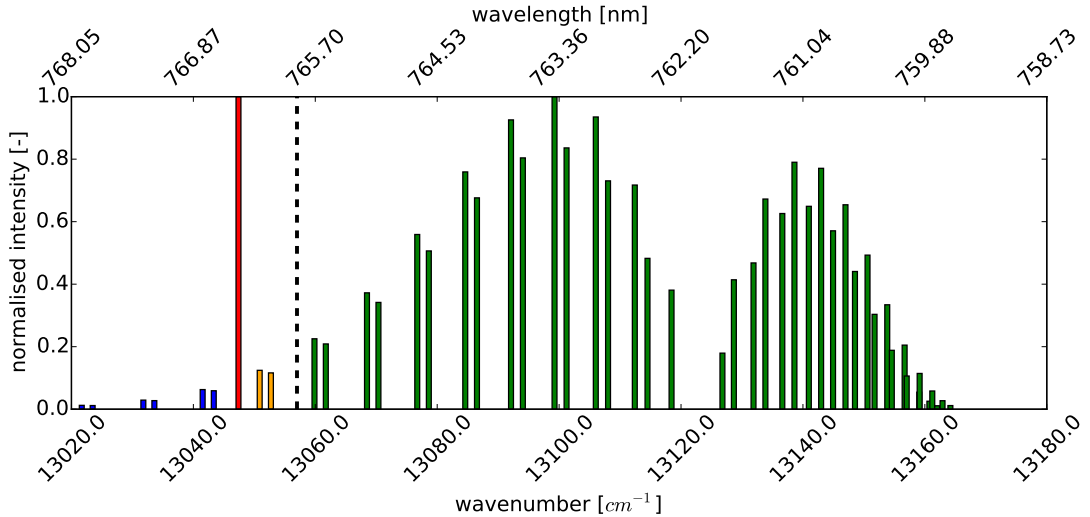


Figure 2.3: O₂ A-band emission spectrum. Shown are the expected emission line intensities at $T_{rot} = 200$ K without considering the finite resolution of the SHS. For reference, the design Littrow wavenumber $\sigma_L = 13047$ cm⁻¹ (red) and the filter edge (dashed) at low wavenumbers are indicated. Emission lines at wavenumbers below σ_L are not observed by AtmoLITE (blue). Dependent on final SHS assembly and bandpass filter manufacturing tolerances, emission lines between the design filter edge and σ_L may be observed (orange).

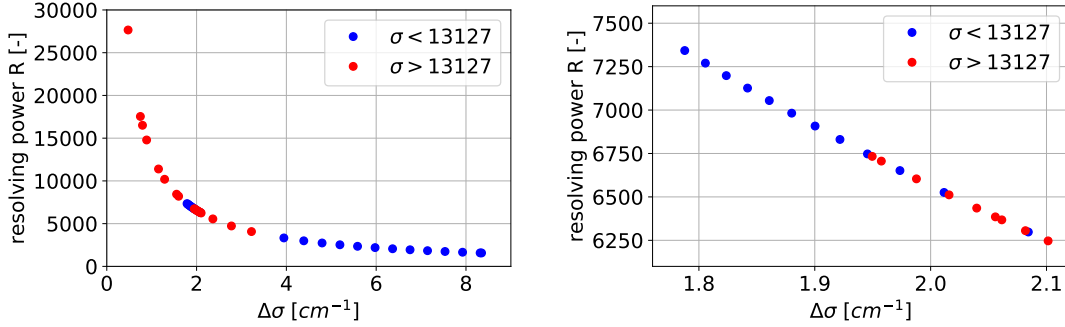


Figure 2.4: Estimation of required SHS resolving power. O_2 A-band emission lines separate in Q- and R-branch around $\sigma = 13127 \text{ cm}^{-1}$ and require a much higher resolving power at higher wavenumbers to be fully resolved (left). The lower branch caps out at a maximum required resolving power of $R = 7300$ (right).

according to Deiml [2017]. Consequently, all available grating groove densities are viable options as $G = 3000 \text{ cm}^{-1}$ corresponds to $R = 9600$ which already exceeds the required design resolving power. Higher grating groove densities would further increase the resolving power.

$$R = 2 \cdot W \cdot G \quad (2.24)$$

Nevertheless, one additional boundary condition has to be considered. The combined system of optics and SHS will record varying fringe patterns across the detector array. Due to the heterodyne property of the SHS, these fringes vary in frequency forming a beat signal, thus, an upper limit exists at which the finite pixel number within the illuminated detector area becomes insufficient to record higher frequencies. This phenomenon is known as the Nyquist-Shannon sampling theorem in spectral analysis and restricts the recovered maximum frequency corresponding to half the maximum pixel number along the illuminated detector array. During the AtmoLITE mission the GSENSE detector provides close to 900 pixel at a pixel pitch of 0.011 mm across the illuminated area which corresponds to a Nyquist frequency of 450 cm^{-1} . In FTS systems where the interferogram is captured on an imaging detector, the highest frequency of observation is usually chosen well below the Nyquist frequency in order to avoid loss of contrast and aliasing due to a finite pixel pitch. Here, the margin is chosen by a factor of three below the Nyquist frequency which will be further motivated once the concept of interferogram contrast and its implications on temperature retrieval precision is introduced. Selecting a second spatial frequency at the lower frequency limit now allows to set the spectral range or bandpass for the AtmoLITE mission. In Figure 2.5 the bandpass

width for different pairs of minimum and maximum spatial frequencies is shown separately for the two design options of $G = 3000 \text{ cm}^{-1}$, 6000 cm^{-1} . Note that $\Delta\lambda = 3 \text{ nm}$ corresponds to the old bandpass width considered during AtmoSHINE [Kaufmann et al., 2018]. The newer design for the AtmoLITE mission is designed to record up to $\Delta\lambda = 7 \text{ nm}$ which restricts the grating groove density to $G = 3000$. The maximum frequency is given by $f_{max} = f_{\text{Nyquist}}/3 = 150. \text{ cm}^{-1}$ whereas the minimum frequency is yet to be chosen. Based on the expected radiance and noise levels presented in section 3.10 and section 5.4, relative line strengths below 1 % do not provide additional temperature information and are neglected. However, a high interferogram fringe contrast (denoted *visibility* in the following section) is desirable which becomes increasingly important at high fringe frequencies due to the gradual drop of the camera optics MTF towards higher frequencies as discussed in section 3.5. Thus, the Littrow wavenumber is chosen as close as possible to the emission lines of interest at $\sigma_L = 13047 \text{ cm}^{-1}$ and centred between the two line pairs at $\sigma = 13043 \text{ cm}^{-1}$ and $\sigma = 13052 \text{ cm}^{-1}$. These mark the relative line intensity threshold of 5 % at a rotational temperature of 200 K. The additional offset of $\Delta\sigma = 10 \text{ cm}^{-1}$ is chosen towards the bandpass filter edge in order to effectively exclude frequency components close to the background signal or zero frequency component after FFT in the spectral domain. A closer look upon this problem is taken in chapter 3 and chapter 5 based on simulated and measured spectra, respectively. The resulting range of expected frequencies including the already mentioned camera optics magnification is between 9.6 cm^{-1} and 87.8 cm^{-1} for the emission lines at $\sigma = 13059.5 \text{ cm}^{-1}$ and $\sigma = 13160.8 \text{ cm}^{-1}$, respectively.

2.4 Definition of interferogram fringe visibility

Before discussion of SHS characteristics continues, the concept of interferogram fringe visibility and its impact on instrument performance are introduced. Mathematically, the interferogram fringe visibility V is defined by the ratio of the modulated to the non-modulated interferogram parts. Referring to Equation 2.13, this is expressed by the difference between minimum and maximum of the recorded interferogram divided by their sum, or simplified, by the modulation amplitude divided by the interferogram mean as expressed in Equation 2.25. Note that the modulation amplitude introduced here is later extended to $A_{\text{mod}} = 2t_A t_B \epsilon$ in chapter 4 which includes transmission losses $t_{A|B}$ of the individual SHS arms and an effective modulation efficiency ϵ . Values of the visibility are always within

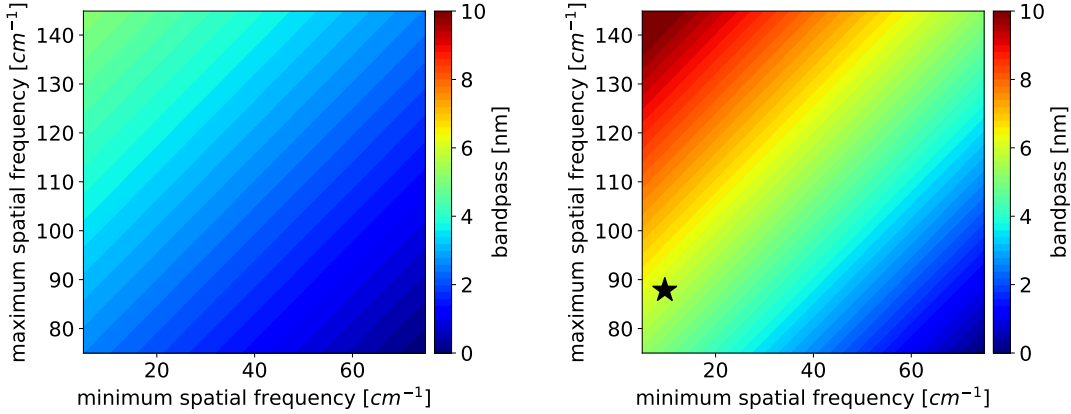


Figure 2.5: AtmoLITE bandpass for different grating groove densities. Shown is the required bandpass which depends on the choice of minimum and maximum spatial frequencies. The two cases distinguish between grating groove densities of $G = 3000 \text{ cm}^{-1}$ (left) and $G = 6000 \text{ cm}^{-1}$ (right). All frequencies are estimated including the camera optics' magnification $M = 0.6$. The final selected configuration is marked by a star.

the half open interval $[0; 1)$ for real systems and are commonly reported relative to the theoretical maximum of 1.

$$V = \frac{I_{\max} - I_{\min}}{I_{\max} + I_{\min}} = \frac{A_{\text{mod}}}{I_0} \quad (2.25)$$

By definition, the visibility is a direct measure of instrument performance because after Fourier transformation of the measured interferograms only the modulated part contributes to the rotational spectral distribution of the observed emission lines. The non-modulated part is added up in the zero frequency component of the spectra and becomes inaccessible, although it still contributes to the overall noise level as follows. Consider N photons measured at the focal plane array in the ideal scenario of negligible detector readout or thermal noise contributions. Then, the signal-to-noise ratio (SNR) is limited by shot noise only. Assuming a typical shot noise contribution of $u_{\text{shot}} = \sqrt{N}$ and assuming an effective signal level equal to the modulated interferogram part $S = V \cdot N$ yields $\text{SNR} = S/u_{\text{shot}} = V \cdot \sqrt{N}$. Thus, the instrument SNR is directly proportional to the visibility, e.g. a reduction of the visibility from the ideal case of $V = 1.0$ to $V = 0.5$ would reduce the SNR by half. Considering that the only other options to regain high SNR after instrument assembly and during the AtmoLITE mission in-orbit are an increased integration

time or binning of interferogram rows, both at the cost of reduced spatial resolution, high visibility is the most important instrument properties. Therefore, the following discussion relates changes of the optical system or SHS wherever possible to their respective impacts on interferogram fringe visibility. It is further distinguished whether changes in visibility are expected near the detector edge or its centre due to the non-uniformity of the visibility across the focal plane introduced in chapter 3.

2.5 The AtmoLITE SHS under Space Conditions

So far, all considerations about the SHS are made neglecting changes in its environment. However, the final satellite instrument will be exposed to the harsh environmental conditions in space. Mostly the temperature changes expected between -30°C and $+20^{\circ}\text{C}$ at instrument level and varying pressure levels during instrument assembly, laboratory testing and later mission operation have to be accounted for. Instrument performance deteriorations caused by environmental changes occur at different optical components. Changes within the SHS affecting the refraction at the FWP and grating are of interest in this section. Changes related to the front and camera optics are discussed in section 3.5 and section 3.7 once the full instrument is introduced.

SHS Performance dependent on Pressure

The SHS encloses two air volumes in each arm between the beam splitter, field-widening prism and grating. Due to the difference in refractive indices at the boundaries between glass parts and environment, the Littrow angle varies between vacuum and air at ambient pressure levels of $p = 1013 \text{ hPa}$. This change may be estimated by substitution of the non-unity refractive index of air in Equation 2.22 by $n = n_{\text{FWP}}/n_{\text{air}}$. Afterwards, the Littrow angle θ_L is estimated in dependence on pressure and the shift of spatial frequencies is evaluated based on Equation 2.19. Note that all other angles are fixed by design and only subject to manufacturing uncertainties. In particular, they do not change in dependence of ambient pressure. The new Littrow wavelength in air is now defined by Equation 2.16. It evaluates to $\lambda_L = 766.15 \text{ nm}$ in air which is 0.29 nm shorter than in vacuum. An overview of the Littrow angle decrease with increasing ambient pressure and its induced shift of spatial frequencies to shorter wavelength is given in Figure 2.6. The wavelength axis is scaled to vacuum wavelengths as the wavelength monitoring during assembly is automatically provided in terms of vacuum wavelength. Further, the expected Littrow angle change of about ten arc-seconds between an air and vacuum environment highlights the importance to consider the SHS pressure dependence as its effect is of similar magnitude when compared to the angle tolerances mentioned in section 2.6 and chosen for manufacturing. In terms of wavenumbers, this change corresponds to an expected increase of the Littrow wavenumber from $\sigma_L = 13047 \text{ cm}^{-1}$ to $\sigma_L = 13052 \text{ cm}^{-1}$. Note the tendency of the Littrow wavenumber to change towards the bandpass filter edge. This effect is of great importance during SHS assembly with respect to the expected minimum spatial frequency and further discussion follows in section 5.1.

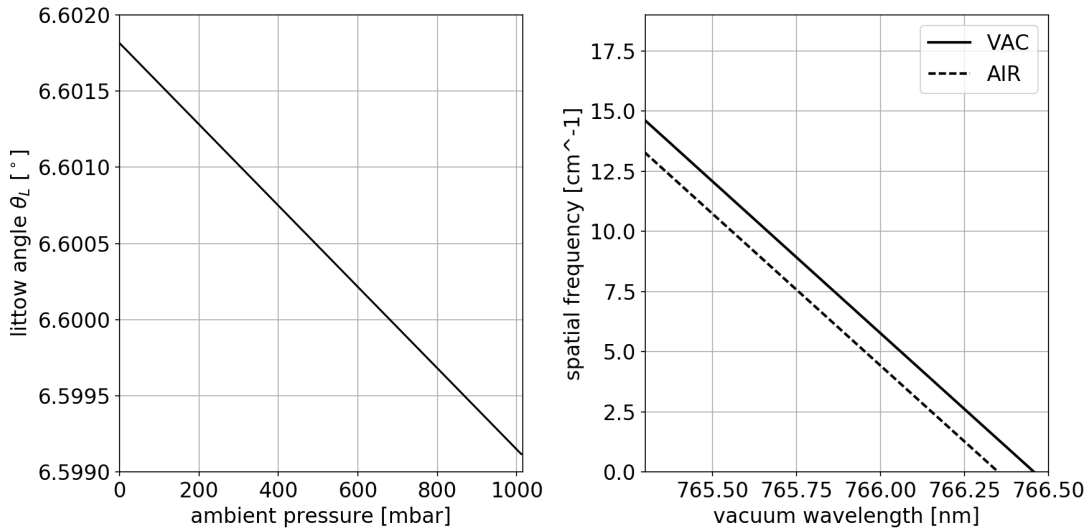


Figure 2.6: Expected pressure dependence of the SHS during assembly and testing. The Littrow angle decreases with increasing ambient pressure due to the non-negligible difference in refractive index between air and vacuum (left). In addition, the laser test wavelength is shorter in air than in vacuum which corresponds to a shift in spatial frequency and Littrow wavelength (right). The Littrow wavelength shifts from $\lambda_L = 766.46$ nm under vacuum to $\lambda_L = 766.15$ nm at an ambient pressure of $p = 1013$ hPa. The corresponding desired wavelength is $\lambda_{L, \text{vac}} = 766.35$ nm as monitored and displayed in units of vacuum wavelengths by the spectrum analyser during assembly.

SHS Performance dependent on Temperature

One major obstacle of instrumentation on satellites are thermal drifts due to the rapidly changing environment along the orbital track [Gilmore, 2002]. Such thermal drifts may degrade or alter performance of optical systems due to thermal deformation and induced stress or change of the refractive index within optical components. While continuous radiative heat transfer towards deep space cools down all instrument parts, the heat uptake of outgoing infra-red radiation from Earth's surface and the heat dissipated from the instrument electronics itself may yield an equilibrium state over a broad temperature range. The expected temperature range assumed in the following study lies between $T = -30$ °C and $T = +20$ °C which is based on the simulations and in-orbit demonstrations of the AtmoSHINE demonstrator mission. The upper temperature limit of $+20$ °C corresponds to the expected temperature during integration and laboratory testing on-ground prior to the satellite launch.

The previous study of the AtmoSHINE SHS has shown the importance to consider changes of the grating groove density, field-widening prism refractive index and small angular changes of the SHS components with temperature [Deiml,

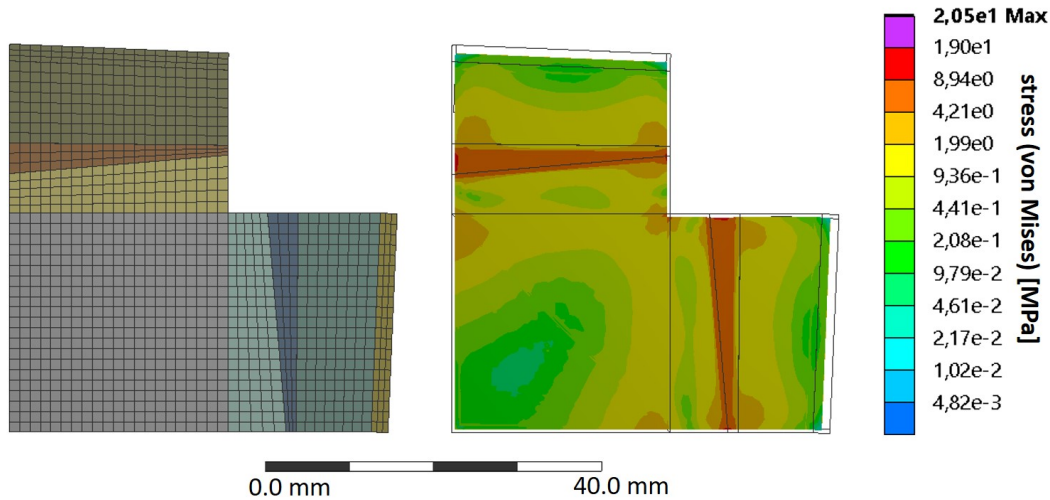


Figure 2.7: Thermal static stress model of the AtmoLITE SHS. The SHS is divided into hexahedra including individual mesh settings for every component. The adhesive layers between all components are divided into five equally thick layers and a bonded contact is chosen at each surface interfacing to the glass components (left). The shown stress is obtained at a temperature difference of $\Delta T = -50$ K relative to the nominal design conditions (right). Note that the maximum stress values above 10 MPa correspond to single element singularities at the edges near contacted surfaces which are not modelled with sufficient accuracy. The overlapped black outline indicates the non-deformed SHS which shows an overall contraction of the SHS with a maximum deformation of $15 \mu\text{m}$. For illustration purposes only, this contraction is magnified by a factor of 100. All results were obtained in ANSYS R18.0.

2017]. In addition, this section will include an estimation of the induced stress due to thermal deformation and discuss its implications on the stress induced change of refractive index. Therefore, minor differences to the previous study are introduced. A small $5 \mu\text{m}$ thick adhesive layer is now included between bonded SHS components and the mechanical dimensions are changed in accordance to section 2.3 to represent the new SHS design. All components are strictly modelled with hexahedra type elements and a size constrain of 1 mm element edge length is chosen to keep the maximum element number within ANSYS licence limits. A side view of the resulting mesh is shown in Figure 2.7.

Two boundary conditions are chosen in the stress free state. The first one constrains the reference temperature at $T_{\text{ref}} = +20$ °C and equal steps of $\Delta T = -10$ °C are chosen for the load cases down to $T = -30$ °C. The second one yields a fixation at the silicone interface to the SHS housing. This effectively restricts the analysis to the SHS only and does not account for external forces which may be introduced due to deformations of the SHS housing, optics housing or the interface to the satellite structure. All glass materials are modelled based on the online

versions of the SCHOTT AG [2022b] and Ohara Corp. [2022] glass catalogues. Mechanical and thermal properties of the adhesives NOA-88 and MasterSIL-SO are taken from the respective data-sheets. Due to the low thermal mass of the SHS compared to its surrounding housings, temperature gradients across the SHS are neglected and a single temperature across all parts is assumed.

In each load case von Mises stresses and thermal deformations of the SHS are estimated. An example of the resulting stress at $T = -30$ °C and corresponding deformations is presented in Figure 2.7. The largest stress occurs at the boundaries between the field widening prisms and both spacers as expected due to the large difference of TCE at the part boundaries. Note that single node singularities above $S > 10$ MPa occur only at the edges of the adhesive layer structures which are not modelled with sufficient accuracy. Therefore, compared to the tensile strength of the adhesive NOA88 utilised during the SHS procurement of about 2000 psi (13.8 MPa), failure of the bond is not expected. Based on the stresses within the glass surface ranging from 2.5 MPa to 6.9 MPa over the bonded area, failure of the glass components is not expected, as well, when compared to the common rule-of-thumb safety threshold of 1000 psi (6.9 MPa) [Yoder, 2008]. The same safety level is also recommended by SCHOTT AG [2022a]. This result is further compared to a more sophisticated FEA analysis approach published by Kaufman et al. [2017]. Their study finds the general Equation 2.26 for the thermal stress induced near the centre bond-line between two glass pieces. It combines the difference of the thermal expansion coefficients ΔTCE , the average elastic modulus E_{avg} and the temperature change ΔT where $C_\sigma = 0.96$ is a dimensionless constant recommended for a conservative estimate of the induced stress. Applied to the AtmoLITE SHS, Equation 2.26 evaluates to $\sigma_{\text{glass}} = 4.2$ MPa $<$ 6.9 MPa in good agreement with the FEA analysis presented here, once more, indicating a low risk of glass failure within the SHS during cooling .

$$\sigma_{\text{glass}} \approx C_\sigma \cdot \Delta TCE \cdot \Delta T \cdot E_{\text{avg}} \quad (2.26)$$

Another important property of the SHS is the refractive index dependency of the Littrow angle on temperature introduced in section 2.2. By fitting a plane through both field-widening prism and the grating top surfaces, the relative orientations α , β and η are estimated at each load step. This allows to estimate a temperature dependent Littrow angle according to Equation 2.22. Hereby, the refractive index change due to temperature changes and thermal stress is also considered. Next, the design Littrow angle in Equation 2.16 is replaced by the newly found temperature dependent Littrow angle which gives the temperature dependent

Littrow wavenumber. In this step, the contraction of the grating is considered which causes an increase of the grating groove density defined by Equation 2.27 where N_{grooves} denotes the absolute number of grating grooves and W_{gratings} is the width of the grating along the dispersion direction. The coefficient of thermal expansion is called TCE and describes the linear expansion proportional to the temperature difference ΔT with respect to the deformation free state at 20 °C.

$$G(T) = N_{\text{grooves}} / (W_{\text{gratings}} \cdot [1 + TCE \cdot \Delta T]) \quad (2.27)$$

The resulting Littrow wavenumber shift is shown in Figure 2.8 for two different grating substrates. When a low thermal expansion substrate such as the fused silica type LITHOSIL-Q glass from SCHOTT is considered, a total increase of $\Delta\sigma_L \approx +1.0 \text{ cm}^{-1}$ is expected over the full temperature range. This is precisely the SHS temperature stabilisation proposed by Deiml [2017] which partly compensates the dominant angular change between field-widening prism and grating by an increase of the grating groove density. However, this stabilisation is no longer valid if the grating substrate is swapped to commonly available float glasses. In case of a grating substrate made of N-BK7 an increase of at least $\Delta\sigma_L \approx +5.0 \text{ cm}^{-1}$ is expected. Note that the shift always occurs towards the bandpass filter edge, reducing observed interferogram fringe frequencies and the number of spectral bins between zero frequency and the first emission line within the bandpass filter transmission range.

Direct aliasing in spectral domain between the zero frequency bin and the first emission line within the bandpass filter is not expected because the shift of $\Delta\sigma_L \approx +5.0 \text{ cm}^{-1}$ is smaller than the designed offset between Littrow wavenumber and filter edge of $\Delta\sigma \approx +10 \text{ cm}^{-1}$. However, as the Littrow wavenumber is the reference point of the spectral axis, its temperature dependence has to be considered during calibration. In particular, the instrumental line shape function has to be recorded at each operational temperature of AtmoLITE, respectively. Although not demonstrated explicitly in this work, the instrumental line shape description appended in section A.7 can simply be redefined to include the temperature dependence by substitution of $\nu \rightarrow \nu(T)$.

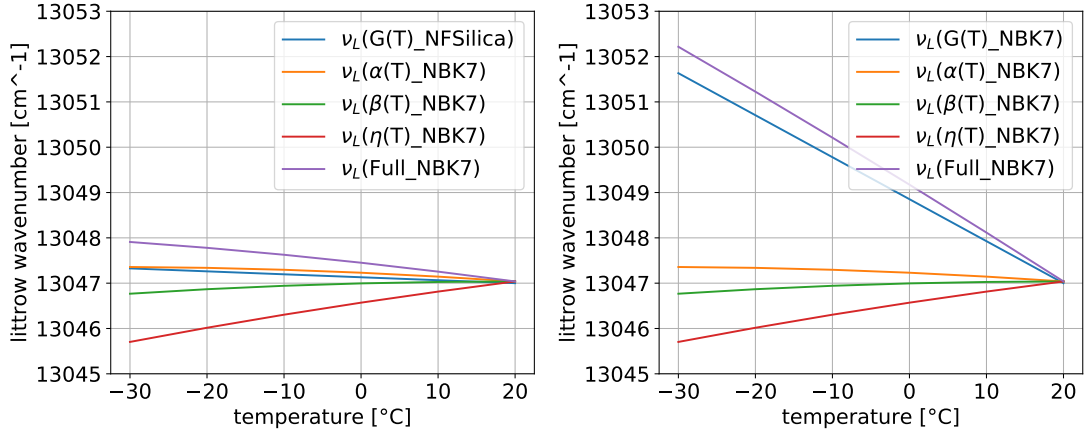


Figure 2.8: Temperature dependent drift of the Littrow wavenumber. Considering small deformations of the AtmoLITE SHS during operation at different temperatures, an overall increase of the Littrow wavenumber with decreasing temperature is expected. The major contribution is coming from the diffraction grating groove density change. This change may be minimized if the gratings are made of a low thermal expansion substrate similar to fused silica. In that case, the SHS deformations and grating groove density change almost compensate each other and the expected Littrow wavenumber shift is below $\Delta\sigma = +1.0 \text{ cm}^{-1}$ (left). However, COTS gratings, largely available on float glass substrates, are similar to NBK7 which leads to a Littrow wavenumber drift of at least $\Delta\sigma = +5.0 \text{ cm}^{-1}$ (right).

2.6 SHS Tolerance & Alignment Considerations

In this section, a closer look is taken on the SHS assembly, involved manufacturing tolerances and the alignment procedure. Initially, a few degrees of freedom are considered in the analysis of SHS arm imbalances in order to get a qualitative measure of their impact on the interferogram visibility. The analysis includes the three SHS angles and the thickness of the spacers and field-widening prism. In total, 22 configurations are tested which correspond to 3×4 angles, 3×3 thicknesses chosen over range of loose opto-mechanical tolerances and one reference run without tolerances. Here, the worst case being one SHS arm in nominal configuration whereby the second arm remains subject to tolerances is assumed. Based on the discussion in section 3.5, two small regions are selected for the visibility evaluation on-axis at $H_x = 0.0$ and off-axis at $H_x = 0.9$ which correspond to regions of low and high expected visibility within the FOV. Here, H_x denotes the relative full field angle perpendicular to the dispersion direction of the gratings. Choosing the wavelength beyond any emission line of interest at $\lambda_{SIM} = 759.0$ nm, effectively tests the SHS tolerance sensitivity at the very boundaries of the optical design due to the high spatial frequency of $\nu = 95.0$ cm⁻¹. Results of the simulated visibility are summarized in Table 2.1. Here, visibility values $V > 50$ % are considered acceptable. This threshold corresponds to half the signal-to-noise ratio when compared to an ideal system at $V = 100$ % with respect to the modulated interferogram portion. The reference simulation run yields $V = 61.6 \pm 0.5$ and $V = 90.5 \pm 0.7$ for on-axis and off-axis, respectively.

The simulated visibility shows a general decrease with increasing SHS arm imbalances as expected. The most pronounced visibility degradation occurs when thickness tolerances are introduced. Here, the spacer thickness tolerance virtually inclines the localization plane of the imbalanced arm. This produces a best focus over the intermediate image at the intersection of both localization planes which yields a localized increase of visibility on-axis. However, the diffraction at the gratings perpendicular to the dispersion direction yields a lateral mismatch of the centroids of both SHS arm images when off-axis fields are considered. Thus, the off-axis visibility is already decreased by a factor of 1.7 at the small thickness imbalance of 25 μ m. Introducing a thickness imbalance normal to the first surface of the field-widening prism has a different effect. The footprints' overlap of the on-axis centroids, defined by the intersection of the individual ray-fans of both SHS arms and the localization plane, decreases due to a slight defocus within the imbalanced SHS arm. This effectively shifts the centroids apart. Here, a more intuitive visualization

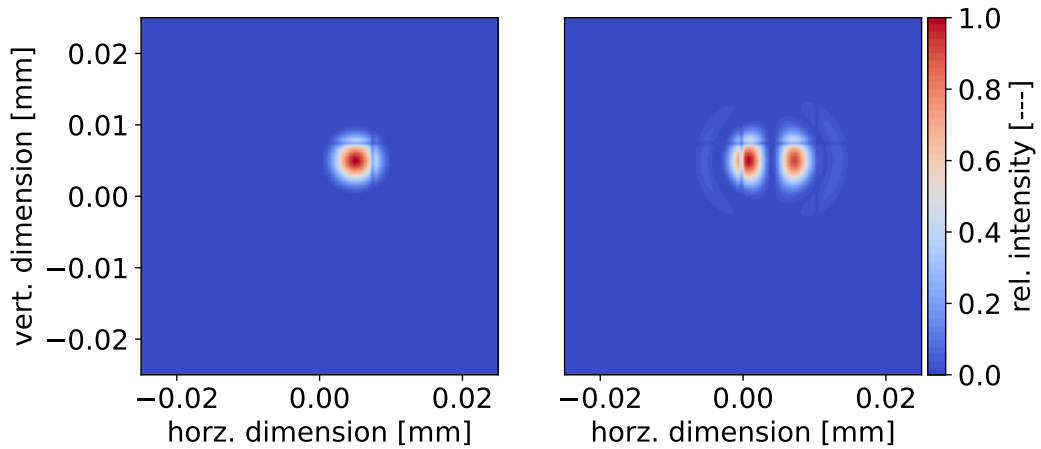


Figure 2.9: Impact of SHS arm imbalances on PSF and including interference from both SHS arms. The PSF distribution of the designed system shows a single PSF peak (left). When FWP thickness imbalances are introduced into the SHS the interference PSF splits and shows two separated peaks (right). The arm imbalance is set to 100 μm and causes a separation of the PSF peaks by about 6.3 μm within the dispersion plane.

is obtained based on the interference PSF. When a single on-axis field point is simulated, the interference PSF shown in Figure 2.9 exhibits two distinct maxima separated by about 6.3 μm which is in good agreement with the effective centroid displacement of 7.0 μm estimated based on direct ray tracing through both SHS arms. As the full interferogram is the incoherent sum of all interference PSFs across the considered FOV, this splitting or, in general, broadening of the interference PSF causes a reduction of visibility. Note that the field-widening prism's thickness imbalance was set to 100 μm in order to visualise a clear separation of the maxima but imbalances larger than 10 μm already reduce the on-axis visibility to below 50 %. The visibility reduction is less pronounced at off-axis field points which can be explained by the decreased ratio between centroid displacement to centroid diameter. Further quantitative details are summarized in Table 2.1.

The SHS comprises three important angular tolerances related to the angle β of spacer SP1 between beam splitter and field-widening prism, the field-widening prism apex angle α and its angle η towards the grating surface. The range of simulated angular arm imbalances starts at one arc-minute and extends to 0.15°. Based on the results in Table 2.1, angular arm imbalances of α and η have a similar impact on interferogram visibility. At the off-axis field point $Hy = 0.9$ the visibility decreases slightly and is still at reasonable high values ranging from $V_\eta = (73.5 \pm 1.6) \%$ to $V_\alpha = (77.8 \pm 0.8) \%$ at the maximum arm imbalance of 0.15°. However, the on-axis visibility is already below the threshold of $V = 50 \%$ at an angular arm

imbalance of 0.05° . This indicates that angular tolerances shall not exceed $1'$. A quite interesting ambiguity occurs when imbalances of the angle β are considered. Here, an angular arm imbalance of 0.5° almost exactly inverts the visibility when compared to the reference runs. It turns out that the centroid displacement actually decreases on-axis from $0.6 \mu\text{m}$ to $0.3 \mu\text{m}$ and increases off-axis from $0.1 \mu\text{m}$ to $0.3 \mu\text{m}$. Centroid displacements at diagonal field points do not change. Thus, an overall radial drop-off in visibility would be expected in this type of imbalanced SHS. However, assembling an SHS including precisely this angular arm imbalance might prove difficult in practice as the assembling and alignment procedure currently did not allow to monitor the interferogram contrast while bonding the beamsplitter, SP1 and the field-widening prism which is further discussed in section 5.1.

Next, the discussed SHS arm imbalances and their impact on visibility shall be related to tolerance values suitable for manufacturing. The main difference between the tolerances specified for manufacturing and the simulated SHS arm imbalances can be related to the thin adhesive layer used to bond individual SHS parts during assembly. The UV curing optical adhesive NOA-88 is used as the bonding agent during the AtmoLITE SHS assembly. Before hardening the adhesive by UV irradiation, this allows for adjustment of the SHS arms and tuning of the Littrow wavenumber while simultaneously optimizing the interferogram contrast. Details of the alignment procedure are appended in section C.1. In the following tolerance estimations, a conservative estimate of the adhesive layer thickness between $5 \mu\text{m}$ to $15 \mu\text{m}$ is used which can serve as a compensator of part-to-part differences after manufacturing. Thus, a maximum angular compensation between 0.01° and 0.03° is achievable over the full beam splitter edge length of 26 mm. Note that the

Table 2.1: Results of the SHS arm imbalance analysis. Given is the mean visibility after introducing either an angular or thickness imbalance in one SHS arm. The modified SHS parts are the two spacers SP1 and SP2, and the field-widening prism FWP. Each simulation is evaluated at two field coordinates on-axis at $H_x = 0.0$ (top row) and at $H_x = 0.9$ (bottom row). When no tolerances are introduced the reference visibilities evaluate to $(61.6 \pm 0.5) \%$ and $(90.5 \pm 0.7) \%$, respectively.

	angular tolerance [$^\circ$]				thickness tolerance [μm]		
	0.017	0.05	0.10	0.15	25	50	100
SP1	76.0 ± 0.5	88.4 ± 0.6	66.3 ± 0.6	25.3 ± 0.6	59.5 ± 4.9	55.3 ± 9.2	43.3 ± 13.7
	89.5 ± 0.5	61.3 ± 1.1	8.7 ± 0.9	4.2 ± 0.7	53.2 ± 1.1	13.0 ± 0.2	8.0 ± 0.2
SP2	54.2 ± 0.5	39.5 ± 0.5	18.9 ± 0.6	4.0 ± 0.5	59.4 ± 4.9	55.4 ± 9.1	43.2 ± 13.7
	88.8 ± 0.6	85.6 ± 0.6	80.0 ± 0.8	73.5 ± 1.6	52.9 ± 1.1	13.1 ± 0.2	8.2 ± 0.2
	angular tolerance [$^\circ$]				thickness tolerance [μm]		
	0.017	0.05	0.10	0.15	10	25	50
FWP	65.0 ± 0.5	44.5 ± 0.3	27.6 ± 0.4	12.9 ± 0.3	54.0 ± 10.1	32.8 ± 10.0	12.1 ± 3.1
	89.4 ± 0.7	86.8 ± 0.6	82.5 ± 0.8	77.8 ± 0.8	88.0 ± 0.7	77.0 ± 0.8	45.1 ± 1.2

beam splitter edge length is interchangeable with spacer or field-widening prism edge lengths due to the narrow angles used in the SHS design. Comparing the achievable compensation to the SHS arm imbalances discussed previously, one recognizes a potential problem. The compensation may only be sufficient to adjust either the angular or thickness tolerance and, in particular, not both at the same time. Thus, after consultation with different manufacturers the following approach is taken. Angular tolerances can be chosen four times smaller at values as low as 15'' without additional effort on the side of manufacturing when an absolute thickness tolerance of 20 μm is accepted. By polishing a long glass block to the desired apex angle and cutting it into multiple pieces of required length, the spacers and field-widening prisms can be produced with relatively small part-to-part thickness deviations corresponding to the discussed SHS arm imbalances. In the more critical case of the FWP, assuming a pyramidal error of 15'' along the glass block two prisms produced as a pair may deviate by up to 6 μm . An additional simulation run including the combined tolerances at all three angles and thicknesses yields $(68.5 \pm 2.7) \%$ and $(76.0 \pm 0.5) \%$ for on- and off-axis visibility, respectively.

The tolerances discussed above do not guarantee a perfectly aligned SHS in an as-built scenario where manually introduced misalignments may not be neglected. In Figure 2.10 two simulation runs are shown where the grating in one arm is misaligned. The misalignment is simulated either by rotation of the grating around its surface normal or by tilt of the grating perpendicular to the dispersion direction. Simulations only consider the phase change of a plane wave transmitted through the SHS which allows for evaluation over the full interferogram and speeds up simulations considerably. In particular, changes in interferogram fringe visibility are not expected if one compares the scale of previously mentioned imbalances to imbalances introduced by rotation or tilt of the grating. On the one hand, rotation of the grating is done around its surface normal, thus, does not introduce SHS arm imbalances and no visibility degradation is expected. On the other hand, grating tilts are considered up to 0.015° . This corresponds to an SHS arm thickness imbalance of $\pm 1.3 \mu\text{m}$ if projected along the illuminated grating area which is much smaller than the previously mentioned thickness tolerance of SP2 of 25 μm . If one linearly extrapolates the estimated worst case visibility drop (off-axis, $\Delta V = 37.6 \%$) across this difference in imbalances of $\Delta \approx 23 \mu\text{m}$, the resulting visibility change is up to $\Delta V = 1.6 \%$, thus, is neglected.

The fringe inclination is evaluated at different wavelengths which yields a wavelength dependent rotation. Tilt of the gratings causes an up to ten times stronger fringe inclination than rotation by the same amount. In addition, evaluation

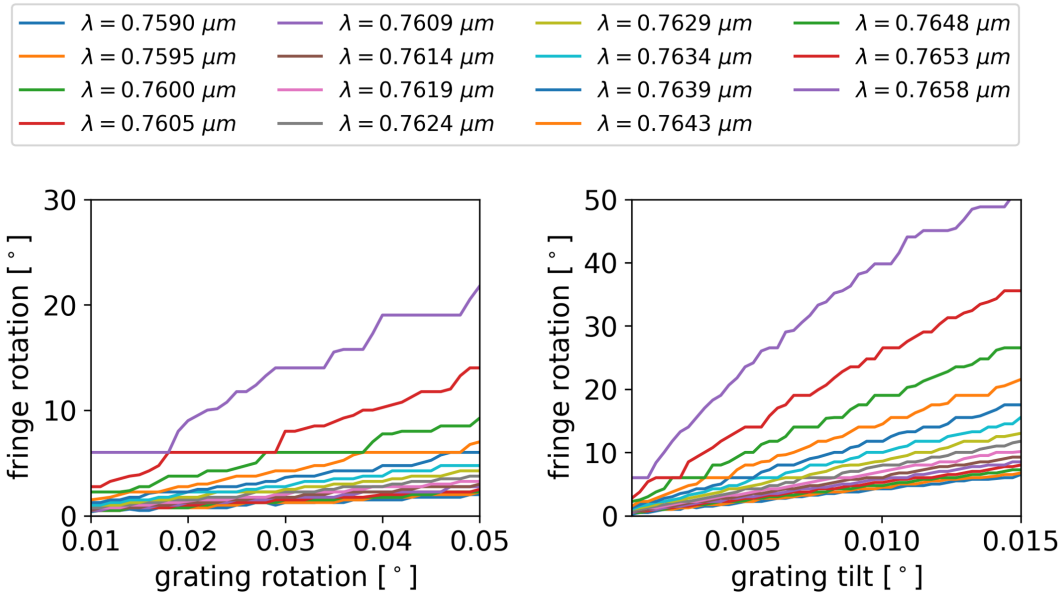


Figure 2.10: Wavelength dependent fringe rotation caused by SHS arm imbalances. During manufacturing of the SHS, the last alignment step involves the grating tilt and rotation with respect to the optical axis. If both gratings are not aligned identically, a secondary wavefront tilt is introduced perpendicular to the nominal dispersion direction which manifests in a wavelength dependent fringe rotation over the detector plane. However, the corresponding spatial frequencies along the dispersion direction remain unaltered.

of the interferograms along the spectral direction by means of FFT does not show any frequency shifts. This indicates that in both cases the net effect is a secondary tilt of the wavefront reflected in the misaligned arm which corresponds to a frequency component perpendicular to the spectral direction. Although, 2D Fourier-transformation allows to recover and separate both frequency components, the satellite application discussed here does not provide sufficient computing capacity to perform this calculation on-board. Moreover, binning has to be performed along the altitude direction ahead of on-ground processing due to the limited downlink bandwidth. Thus, the fringe rotation could cause a reduction of visibility when multiple lines of different fringe rotation are present, consequently, reducing the overall SNR. First experimental tests of the new SHS prototype along a new but yet not-refined assembly strategy discussed in section 5.1 showed that the misalignment between both gratings may be minimized during alignment. However, after curing of the adhesives occurred, misalignments were re-introduced and imbalances of adhesive thickness led to apparent fringe rotation. The discussion of experimental data showing this rotation continues in chapter 5 after the AtmoLITE optics and the AtmoLITE Calibration Unit have been introduced.

Summary of SHS design

The spectral rotational distribution of the O₂ A-band airglow has been introduced as a reasonable proxy for atmospheric temperature. Its excitation by photo-chemical reaction pathways and the necessary assumption of local thermodynamic equilibrium to express the spectral rotational distribution by a Boltzmann distribution were introduced. In addition, a spectrometer design of spatial heterodyne type has been discussed which is suitable to resolve the O₂ A-band airglow spectra. The discussion included the geometric baseline design, the impact of harsh environmental conditions in-orbit on performance and a sensitivity study regarding manufacturing and assembly tolerances. In regard to the SHS sensitivity on its surrounding pressure and the dependence of the interferogram fringe visibility on precise SHS arm alignment, guidelines were presented suitable for manual assembly of a first prototype.

Most importantly, this chapter introduced all necessary changes from the AtmoSHINE SHS towards the AtmoLITE SHS. In particular, these are the extension of the spectral range to wavenumbers between 13047.0 cm⁻¹ and 13160.8 cm⁻¹, an increase of the illuminated grating width from 7.1 mm to 15.2 mm, a reduction of the grating groove density from 1200 lp/mm down to 300 lp/mm and a shift of the Littrow wavenumber from 13127 cm⁻¹ towards 13047 cm⁻¹. In combination, these changes reduced the overall resolving power of the SHS from 16800 down to 9000 while still maintaining the desired temperature retrieval accuracy of below $\Delta T = \pm 1.5$ K.

3

Instrument Optics Design

Contents

3.1	AtmoSHINE - In-Orbit Demonstrator	46
3.2	AtmoSHINE - Imaging Quality and Wavefront Errors	47
3.3	AtmoSHINE - Line-Of-Sight Calibration	58
3.4	AtmoSHINE - In-Field Ghost Reflections	62
3.5	AtmoLITE - A new optical System	69
3.6	AtmoLITE - Tolerance Budget	77
3.7	Low Pressure Compensation of Optics	79
3.8	Tolerances of the camera optics locking mechanism . .	81
3.9	SHS optimization within the full optical system	81
3.10	Expected O₂ A-band Radiances In-Orbit	84

The general idea of temperature sounding by observation of the O₂-A band emission and the design of a suitable SHS is outlined in chapter 2. However, the importance and purpose of the additional involved optics has not been discussed yet. The main problems solved by these optics are the image acquisition of the interferograms at a high interferogram fringe visibility, the simultaneous separation of different altitude layers and provision of sufficient signal intensity to enable altitude resolved temperature retrieval at high signal-to-noise ratios (SNR).

Collecting a large number of photons to achieve a high SNR is the first problem to be solved for remote sensing instruments, especially, if faint phenomena such as the O₂ A-band airglow are observed. For the instrument optics described in the following, the approach of a telescope type collector optics is adapted which has already been implemented successfully in previous variations of SHS instruments

[Englert et al., 2010; Langille et al., 2019b; Englert et al., 2017]. Given the imaging of the atmospheric scene onto the gratings and subsequently onto the systems image plane, the maximum SNR per pixel is only limited by the ratio between the overall optics etendue and the total number of available pixel. Higher SNR can be obtained by increases of the etendue via enlargement of the entrance aperture, an increase of the total FOV angle or by decreasing the total number of pixel. However, the latter two options yield a decreased spatial resolution as less detection elements are used per solid angle which is not desired. Instead, the classical approach to maximize the effective aperture is taken whereby current limitations are only imposed by the launch vehicle's capacity as demonstrated by the folded primary mirror of the James Webb Space Telescope [Contreras and Lightsey, 2004]. However, the present work discusses an optical system suitable for integration to a CubeSat, thus, relies on an all refractive telescope with the entrance aperture undersized to $\emptyset = 75$ mm of the available $\emptyset = 100$ mm or 1U-CubeSat cross-section envelop. The interested reader may also refer to the studies of Snell et al. [2020] and Ditto et al. [2020] where ongoing research on novel approaches of additively manufactured reflective optics suitable for CubeSats or space telescopes entirely build without lenses and mirrors is presented. Lastly, continuous advances of modern sensor technology enable higher SNR due to continuously decreasing levels of readout noise which enabled continuous advances in the field of remote sensing [Campbell, 1987; Toth and Józków, 2016]. For the AtmoLITE instrument a back-side illuminated GSENSE440BSI detector is used. Back-compatibility to the HWK1910 sensor, which has successfully been demonstrated in space during the AtmoSHINE mission, is required as risk mitigation.

The work presented here requires the SHS to be integrated in between the front optics telescope and the imaging camera optics in order to imprint the spectral information onto the atmospheric scene as discussed in section 2.2. Therefore, the optics is split into front and camera optics. The infinite-finite conjugate front optics images the atmospheric scenery onto the virtual localization plane corresponding to the grating surfaces. This localization plane corresponds to the object plane of highest interferogram visibility when observed by a finite-finite camera optics [Harlander et al., 2002]. By imaging the localization plane onto the detector array by the finite-finite camera optics, the heterodyned image of the atmospheric scenery is obtained and different altitude layers are separated along the vertical direction. A schematic example based on the AtmoLITE optical design is given in Figure 3.1. Included are the nominal ray paths for on-axis and off-axis field angles and a back-trace which shows the virtual position of the localization plane as seen from the detector. The bandpass filter in front of lens L1 is not included

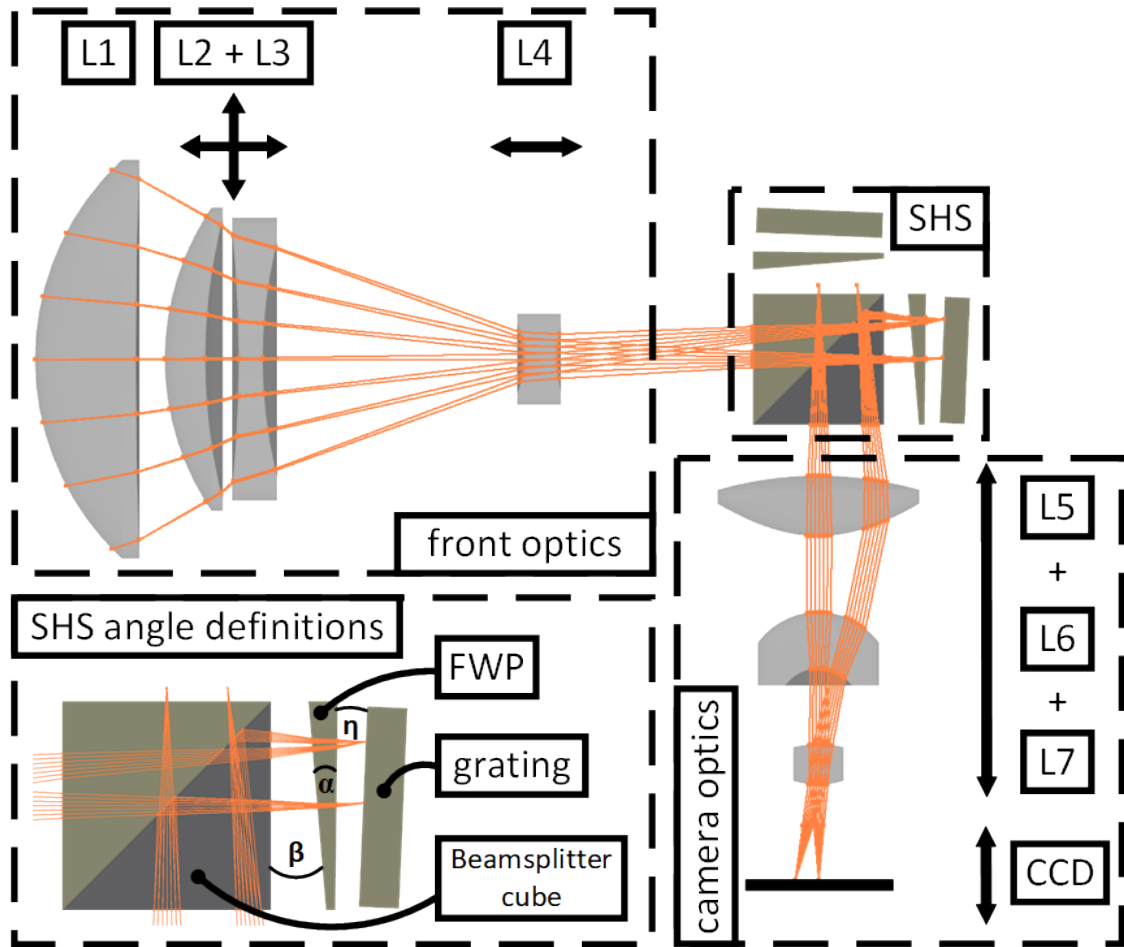


Figure 3.1: AtmoLITE optical layout. Two ray traces for the on- and outermost off-axis field angles are included. The lenses are enumerated starting at the entrance aperture and the SHS angles are labelled for further reference. The four compensation mechanisms considered during the tolerance analysis are indicated by arrows spanning the involved components per compensator. The virtual position of the localization plane in object space of the camera optics is indicated by a back-trace of the shown ray bundles towards the upper SHS arm. Note that the back-trace does not consider the refractive index of the beam splitter.

in Figure 3.1. The simple approach of two optics in an all refractive configuration provides an easy way to include multiple compensation mechanisms necessary during the alignment of the optics as well. The direction of movement due to these compensation mechanisms is indicated by arrows.

Details about the optical design of front and camera optics are now provided in the following sections. These sections start with an overview of the AtmoSHINE in-orbit demonstrator mission and discuss the problems discovered during the AtmoSHINE qualification tests. Measurements of the wave front aberrations of front- and camera optics are presented in section 3.2. The line-of-sight calibration

necessary for alignment of AtmoSHINE to the Chinese satellite interface is discussed in section 3.3. It revealed a general problem of the AtmoSHINE optics due to stray light and led to the development of the new AtmoLITE instrument optics. Analysis of first calibration data obtained for the AtmoSHINE instrument [Liu, 2019] and application of retrieval algorithms to satellite data [Chen, 2020] has already been done and is not repeated here. The design changes made towards the AtmoLITE optical design are discussed in section 3.5 and include a separate tolerance estimation in section 3.6. Performance degradation and preparatory measures before bringing the system into vacuum are discussed in section 3.7. The optics etendue is estimated in section 3.10.

3.1 AtmoSHINE - In-Orbit Demonstrator

After the successful proof-of-concept demonstration of the AtmoHIT optics and instrument on a REXUS (Rocket EXperiments for University Students) rocket in 2017 [Deiml et al., 2017], development of the AtmoSHINE instrument started with the goal of a first in-orbit technology demonstration. In a joined co-operation between the Research Centre Jülich, the Bergische Universität Wuppertal, the Max-Planck institute for the Science of Light and the York University the first ready-to-flight instrument shown in Figure 3.2 was assembled. The instruments final envelope measured $400 \text{ mm} \times 112 \text{ mm} \times 141 \text{ mm}$ including all optics, electronics and a radiator required to cool the HWK1910 detector during operation. Its final mass was below 4.7 kg with a total heat capacity of 3880 J/K which was well within specifications given by the Chinese satellite provider and was already close to compatible with current CubeSat specifications [California Polytechnic State University, 2022].

The flight model also enabled first measurements of the temperature dependent Littrow wavenumber drift after thermal-cycling test were conducted at the ZARM in Bremen in 2018. These tests extended the temperature range tested during earlier AtmoHIT experiments [Deiml, 2017] down to $-30 \text{ }^\circ\text{C}$ and a higher than expected temperature drift was found with the Littrow wavenumber at $-0.11 \text{ cm}^{-1}/^\circ\text{C} \cdot T + 13131 \text{ cm}^{-1}$ compared to the designed drift of $\Delta\sigma_L = -0.018 \text{ cm}^{-1}/^\circ\text{C}$.

AtmoSHINE was launched on 22nd of December 2018 onboard the Chinese Hongyun satellite. Following a dawn/dusk sun-synchronous orbit at an inclination of 99.88° , the instrument successfully delivered first in-orbit measurements of the O_2 A-band emission layer during night-time between December 2018 and August 2019 on multiple occasions. Despite missing a thorough on-ground calibration, first temperature retrieval algorithms could be tested [Chen, 2020]. Further, the

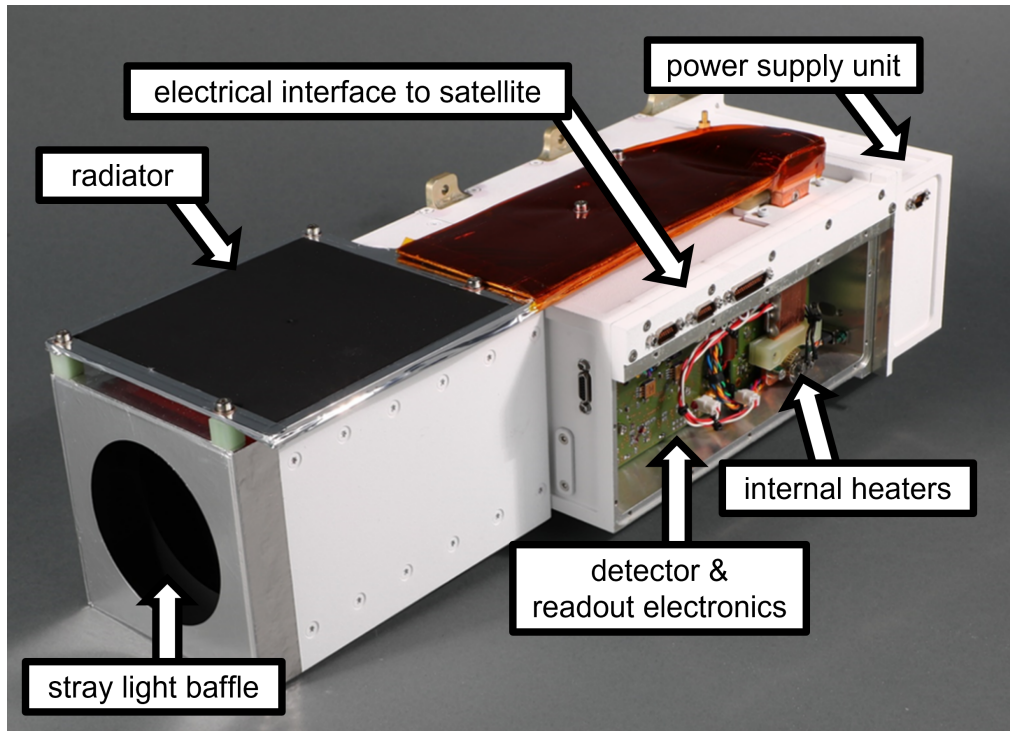


Figure 3.2: Shown is the final AtmoSHINE model before final integration to the satellite. The electronics housing was left open for illustration purposes only, providing a view on the PXE and FEE. The detector is directly connected to the radiator via a cold-finger made out of copper. Heating elements were placed on top of the cold-finger. Photo provided by ZEA-2, Research Centre Jülich.

thermal concept including heating elements at the connection between electronics and radiator was verified.

However, despite this successful in-orbit demonstration, changes had to be made to the overall instrument's optics design [Deiml, 2017] which are described in the following. This decision was mostly motivated based on the observation of a stray light ghost within the AtmoLITE optics (cf. section 3.4) which would restrict observations during future missions to night-time only. Here, the stray light ghost refers to a double-bounce reflection between lens elements of the AtmoSHINE optics which created a secondary image of the observed source on the detector.

3.2 AtmoSHINE - Imaging Quality and Wavefront Errors

The discussion in section 1.4 introduced the mathematical framework to simulate and describe optics imaging performance. Its application to evaluate real systems against their simulated performance is now demonstrated based on wavefront aberration

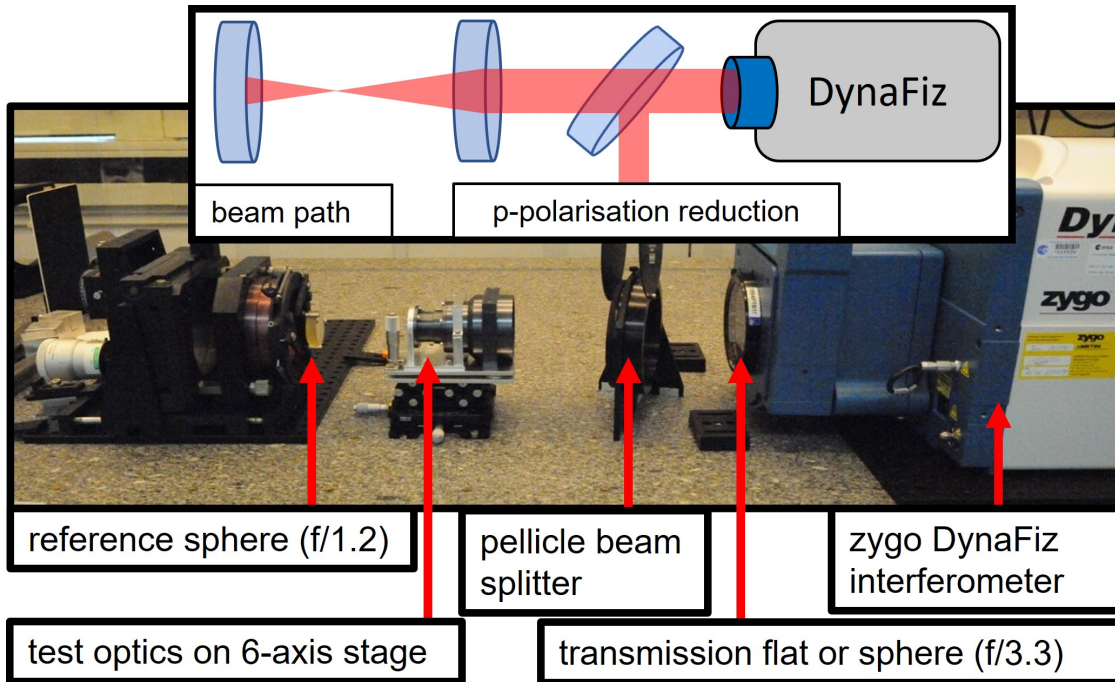


Figure 3.3: Experimental setup during the wavefront aberration measurements of AtmoSHINE. A dual path interferometric setup is shown including the zygo DynaFiz interferometer as source and detection device. The p-polarisation was reduced by including a pellicle beam splitter which increased the interferogram contrast. The front optics under test and reference sphere were mounted separately on 6-axis alignment stages. Exchanging the transmission flat with a transmission sphere allowed to test the camera optics of AtmoSHINE.

measurements performed on the AtmoSHINE optics. Before the final AtmoSHINE flight model optics' integration was started, an experimental evaluation of the system's wavefront aberrations was attempted. The front and camera optics were separately tested and first results are discussed here. The goal was to find the *best performing* optics for the AtmoSHINE flight model.

All wavefront measurements were performed with the Zygo Dynafiz interferometer available at the facilities of the project partner ESA at ESTEC. In particular, the laboratory equipment of the Optics Section (TEC-MMO) within the Mechatronics and Optics Division (TEC-MM) of the Mechanical Engineering Department (TEC-M) of the Directorate of Technical and Quality management (D/TEC) of ESA at ESTEC in Noordwijk was used. The reflective sphere and its mount, the transmission flat and the pellicle beam splitter shown in Figure 3.3 were available on-site. The test sample holder had to be procured in advance. It was build up as a stack of a Z-STAGE and XYR-Stage provided by Thorlabs and a custom-build tip/ tilt stage. The tip/ tilt stage provided interfaces to secure the front and camera optics in place which were adapted from the SHS housing interface of the full instrument.

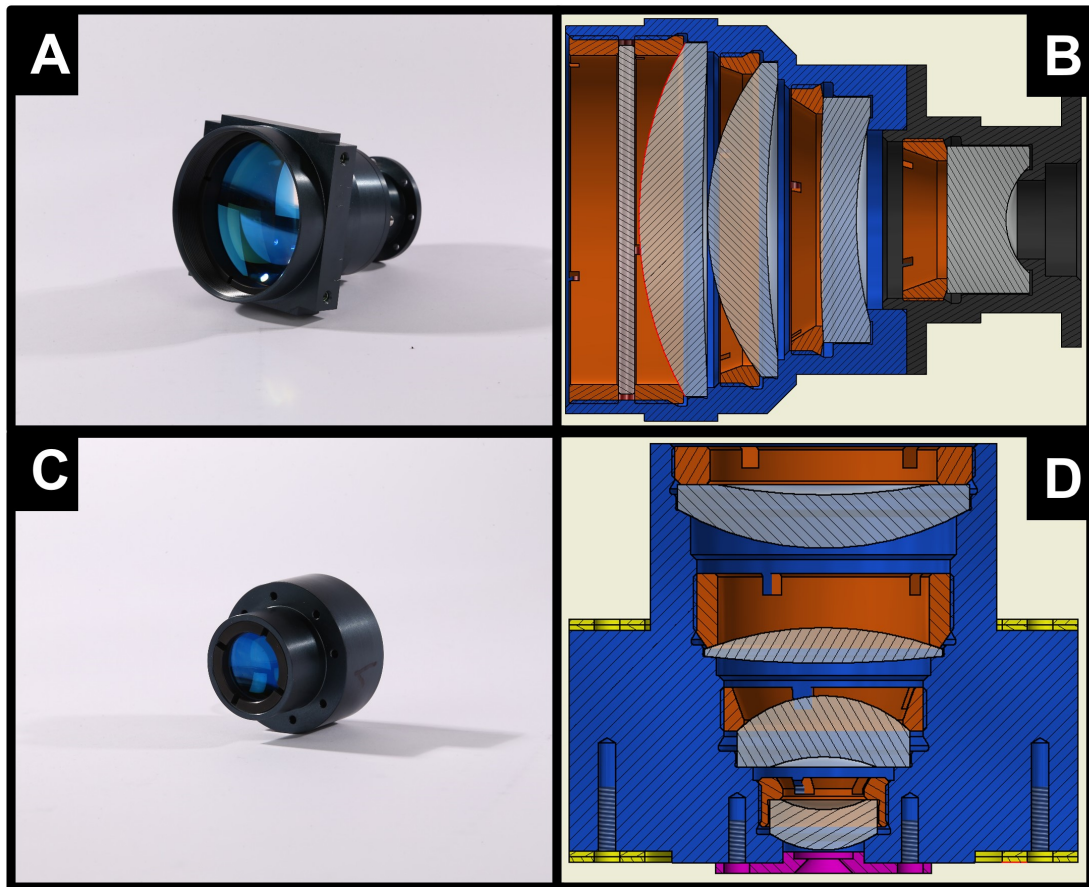


Figure 3.4: Overview of AtmoSHINE opto-mechanical lens mounts. Images of the integrated lens mounts are shown (left) next to the corresponding CAD cross-section views (right). The AtmoSHINE front optics (A + B) and camera optics (C + D) were separately tested. The bandpass filter as first element of the front optics was removed prior to the measurements due to its blocking characteristic at the interferometer test wavelength. The stray light reducing aperture stop of the camera optics is indicated in purple behind the last lens element (D).

The horizontal translation and the tip/ tilt could be controlled by micrometers. In preparation for the camera optics evaluation, the measurement setup had to be modified. The shown transmission flat was replaced by a transmission sphere and the flat reference mirror replaced by a concave one. Both parts were adapted to the camera optics object and image space NA, respectively.

A total of six optics comprising three front and three camera optics were evaluated. A cross-section through the optics is shown schematically in Figure 3.4 alongside images of the as-built optics prior to testing. The bandpass filter within the front optics was removed prior to the measurements because the test wavelength provided by the Dynafiz was 632.8 nm, thus, lying outside the nominal transmission range of the narrow AtmoSHINE bandpass filter with a FWHM of 4 nm centred

around 763 nm. Further, the following three changes were introduced diverging from the nominal opto-mechanical design. The mount of the last front optics' lens was centre-turned in the first front optics. The second front optics' last lens was centred by including spacers between the lens side and the mount. The third front optics remained unaltered and was assembled similar to previous AtmoHIT front optics. All three optics were labelled A1, B1 and B2 for further reference. Two camera optics remained unaltered but the stop of the third one was removed. These optics were labelled C1, C2 and C3. It was noted that the front optics B1 was contaminated by dark dust particles from the inside, presumably caused by abrasion within the black-anodized threads during assembly.

An example of the obtained wavefront data is shown in Figure 3.5 for the front optics A1. Zernike polynomials were fitted to the measurement in order to distinguish different types of aberrations according to the definition of fringe Zernike polynomials introduced in section A.1. Including the first 36 Zernike polynomials and computing the residuum of measured and fitted wavefront, over 98 % of the measured wavefront could be described. The first order aberrations of focus, astigmatism, coma and spherical aberration described by the Zernike polynomials 4 – 9 are shown as well. This highlighted the dominant contribution of coma within the front optics which appeared to be at least an order of magnitude stronger than the remaining aberrations. Note that piston and tilt could not be separated from the measurement setup because the setup does not disuingish whether piston/tilt is introduced by the Dynafiz or the optics under test. The estimated P-V and RMS wavefront aberration is shown without accounting for the dual-path geometry of the measurement. Considering the ISF of 0.5 appropriate in this case, total wavefront aberrations of P-V= 0.57λ and RMS= 0.18λ were obtained for front optics A1.

After identification of coma as the major contribution to the overall wavefront aberration and to test if proper alignment of the front optics could reduce aberrations, a set of measurements was conducted on front optics B2. It was suspected that aforementioned centring of lens four of the front optics could introduce unwanted tilt of lens four which could impact the optics performance. Consequently, lens four was rotated in 60° steps around the optical axis in order to investigate the change of measured wavefront aberrations, in particular a change of coma. At each position of lens four, two interferograms were recorded whereby the full front optics was rotated by 180° around the optical axis during the second measurement. This allowed to subtract the two measured wavefronts in order to cancel out even wave aberrations of focus, spherical aberration, piston and to isolate the coma contribution. The evaluation of the field-independent first order coma is shown

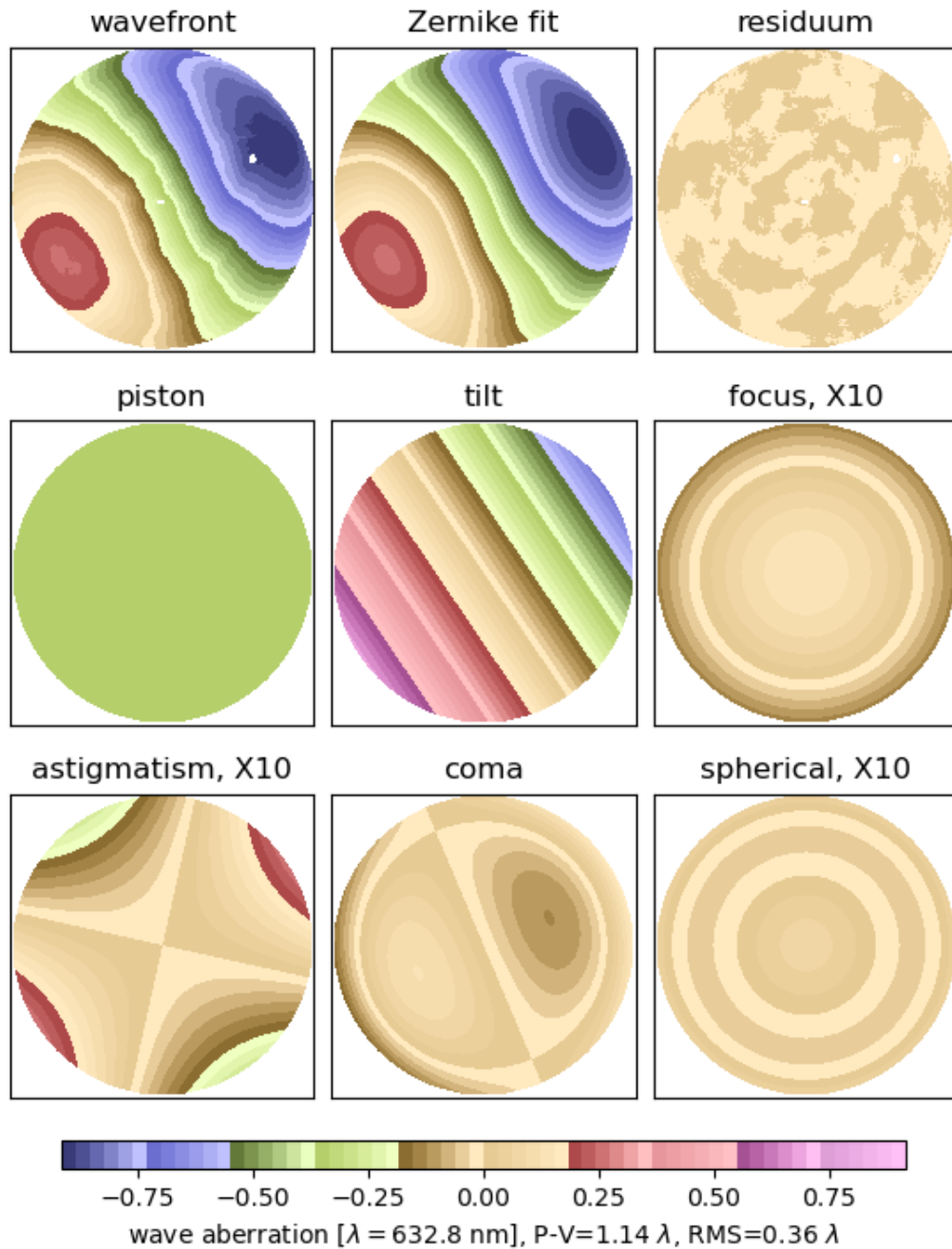


Figure 3.5: Wavefront quality of AtmoSHINE front optics A1. Measured wavefront aberrations were fitted based on the first 36 Zernike polynomials. The first 9 Zernike polynomials describing first order piston, tilt, focus, astigmatism, coma and spherical aberration were separately plotted which showed the dominant contribution of coma within the front optics. Shown data did not consider the ISF.

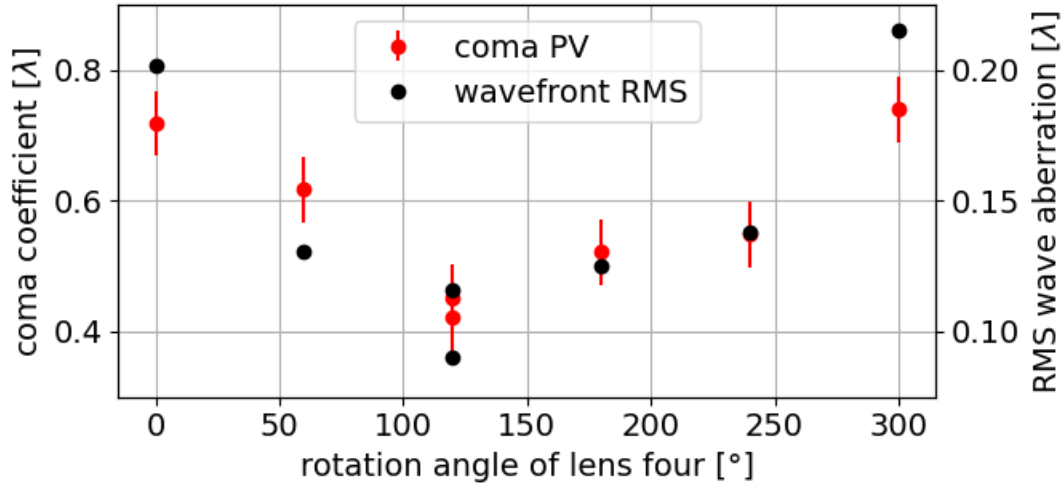


Figure 3.6: Reduction of first order coma in front optics B2. Shown is the field-independent first order coma wavefront aberration at different rotations of lens four and the corresponding wavefront RMS. The uncertainties of the estimated coma coefficient represent the repeatability of individual wavefront aberration measurements. A reduction of first order coma was found at a rotation of 120° relative to the starting position. The measurement at a lens rotation of 120° was repeated with the full front optics rotated by 90° around the optical axis and yielded agreement by up to 0.03λ .

in Figure 3.6. At a rotation of 120° relative to the starting position, a significant reduction in coma from $ZC_{coma} = 0.72 \lambda$ down to $ZC_{coma} = 0.42 \lambda$ was found with a repeatability of $\Delta ZC_{coma} = 0.03 \lambda$. The absolute uncertainty of the measurements was better than 0.05λ including the ISF. The measurement was repeated once the assembly with smallest coma was found with the whole optics rotated by another 90° around the optical axis and no significant additional aberrations larger than the measurement uncertainty were found.

Next, the measured wavefront data was substituted into 1.5 and 1.6 including correction by the $ISF = 0.5$ in order to compare the as-build front optics and their simulated performance. The resulting PSF is shown in Figure 3.7. A clear asymmetry could be identified following the first minimum of the PSF which is typical for coma-dominated systems. The MTF was evaluated through the peak of the PSF distributions. Expected values of on-axis and $(0.6^\circ, 0.6^\circ)$ off-axis MTF curves obtained in ZEMAX were indicated by the dashed boundaries showing the field-angle dependent drop in MTF. Two remarks have to be made here about the accuracy of this evaluation. Firstly, the overall alignment accuracy between the optical axis of the AtmoSHINE optics and the interferometer during measurement was estimated to be $\pm 0.2^\circ$ in vertical and horizontal direction. Thus, the derived MTF curves could not be precisely related to a specific field angle. Secondly, the

alignment procedure minimized contributions of focus and spherical aberrations. In the nominal design, the front optics showed contributions of $ZC_{focus} = 0.483 \lambda$ and $ZC_{spherical} = 0.015 \lambda$ which are significantly smaller in the measured data which showed values of $ZC_{focus, A1} = -0.014 \lambda$ and $ZC_{spherical, A1} = 0.007 \lambda$. Replacing the measured coefficients by the simulated once shifted the derived MTF curves closer to the expected off-axis MTF curve, indicating measurements were most likely conducted at a small inclination between optics and the Dynafiz optical axis. Nevertheless, the MTF values of all three front optics being above 0.7 at a frequency of 5.7 cycles/mm for any configuration of measured or simulated Zernike coefficients indicated that a vertical resolution of 1.5 km was possible. At such a low frequency component the difference in MTF between all three optics was negligible as well. In conclusion, all three optics were found suitable for integration to the flight model with B2 being the least favourable due to the mentioned dust contamination.

Wavefront aberration measurements were repeated for the camera optics C1 and C2. The individual camera optics showed similar MTF performance despite their PV and RMS wavefront aberrations being slightly different at $(0.52 \pm 0.10)\lambda$ and $(0.37 \pm 0.06)\lambda$, respectively, when measured in nominal configuration. The major contributions were focus and spherical aberration which is shown in Figure 3.8 for camera optics C1. However, the alignment required adjustment of the two foci in-front and behind the camera optics which was done manually based on nominal design parameters of the front and back focal lengths. Distances were measured by a ruler placed near the camera optics which most likely caused a misalignment of the order of millimetres. This introduced a strong compensation of focus and spherical aberration, in particular measured aberrations were dependent on alignment. Thus, a test was made for C2 to adjust to the least amount of visible interferogram fringes instead of relying on nominal positions of the foci. By shifting the camera optics along the optical axis and introducing a difference to expected foci positions of up to 3 mm, an increase in total aberrations of up to 31.5 % was found which now matched the PV and RMS values of C2 and C1. A significant change in MTF at frequencies below 22 cycles/mm corresponding to the highest interferogram fringe frequency within the AtmoSHINE SHS was not found due to this change in wavefront aberration. This highlights that MTF at such small frequencies was insensitive to the magnitude of observed aberrations. Camera optics C3 showed a strong increase in wavefront aberrations with a total PV and RMS of $(1.18 \pm 0.17)\lambda$ due to the missing aperture stop. The corresponding MTF value at 22 cycles/mm was 0.72. Thus, in comparison to $MTF = 0.88$ of C1 and C2, the removal of the aperture stop reduced the imaging quality of the camera optics significantly.

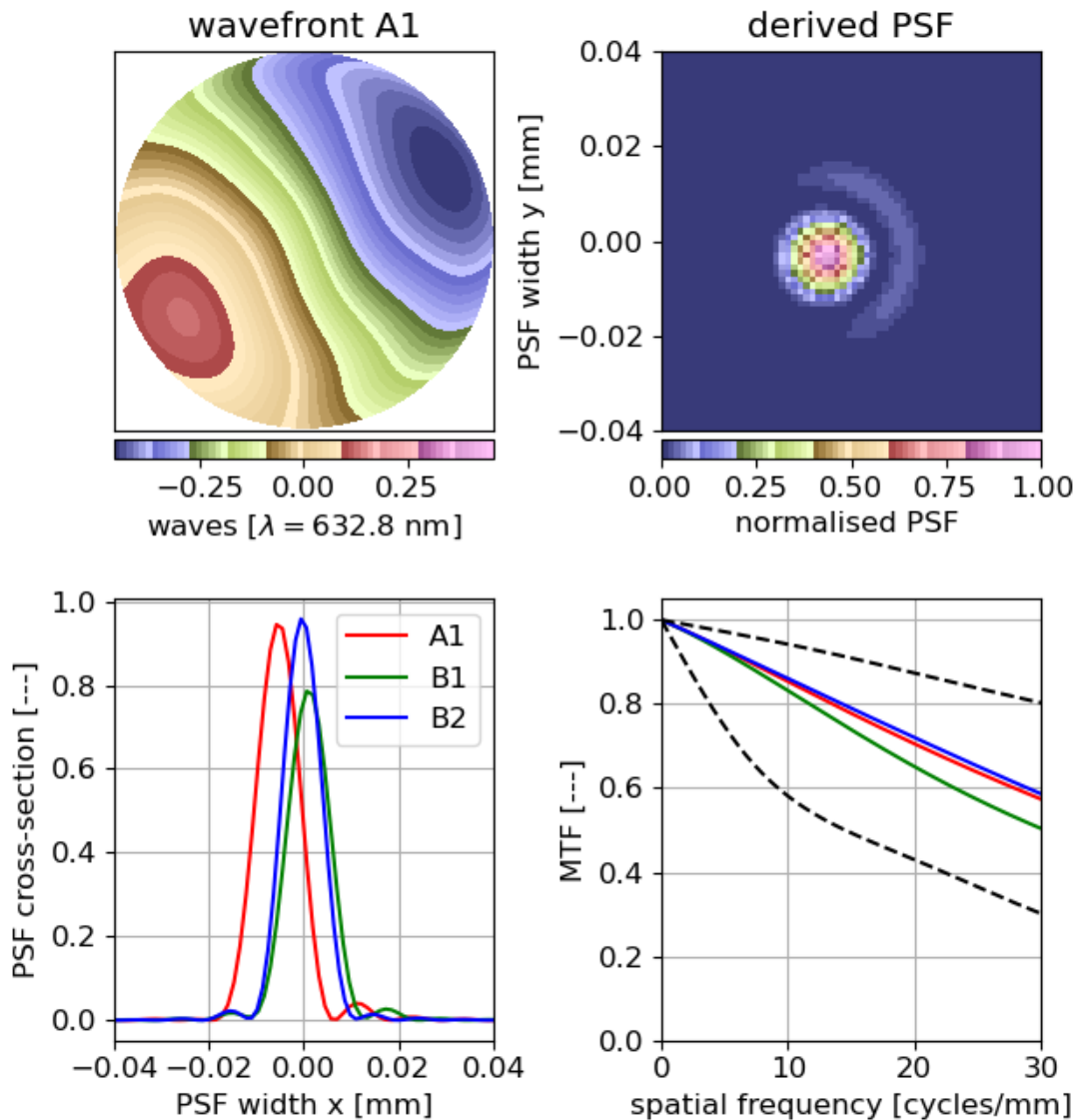


Figure 3.7: AtmoSHINE MTF derived from measured front optics' wavefront aberrations. The obtained wavefront data was utilised to estimate the PSF and corresponding MTF at $\lambda = 632.8$ nm. Shown are the results for the three front optics A1, B1 and B2 which indicated a slightly worse performance of B1. The dashed MTF curves indicate the range of expected values for two field points, on-axis and at $(0.6^\circ, 0.6^\circ)$ off-axis.

Direct comparison of the estimated MTF based on wavefront aberrations and its expected values simulated in ZEMAX yielded no agreement. Even if the three times higher than measured Zernike coefficients of focus and spherical aberration simulated in ZEMAX are substituted into the measured data, a $\Delta\text{MTF} = +4\%$ discrepancy remained. This highlights the limitations of performance evaluation for the camera optics by means of wavefront aberration measurements. For upcoming instrument characterisations it is therefore recommended to only keep the wavefront

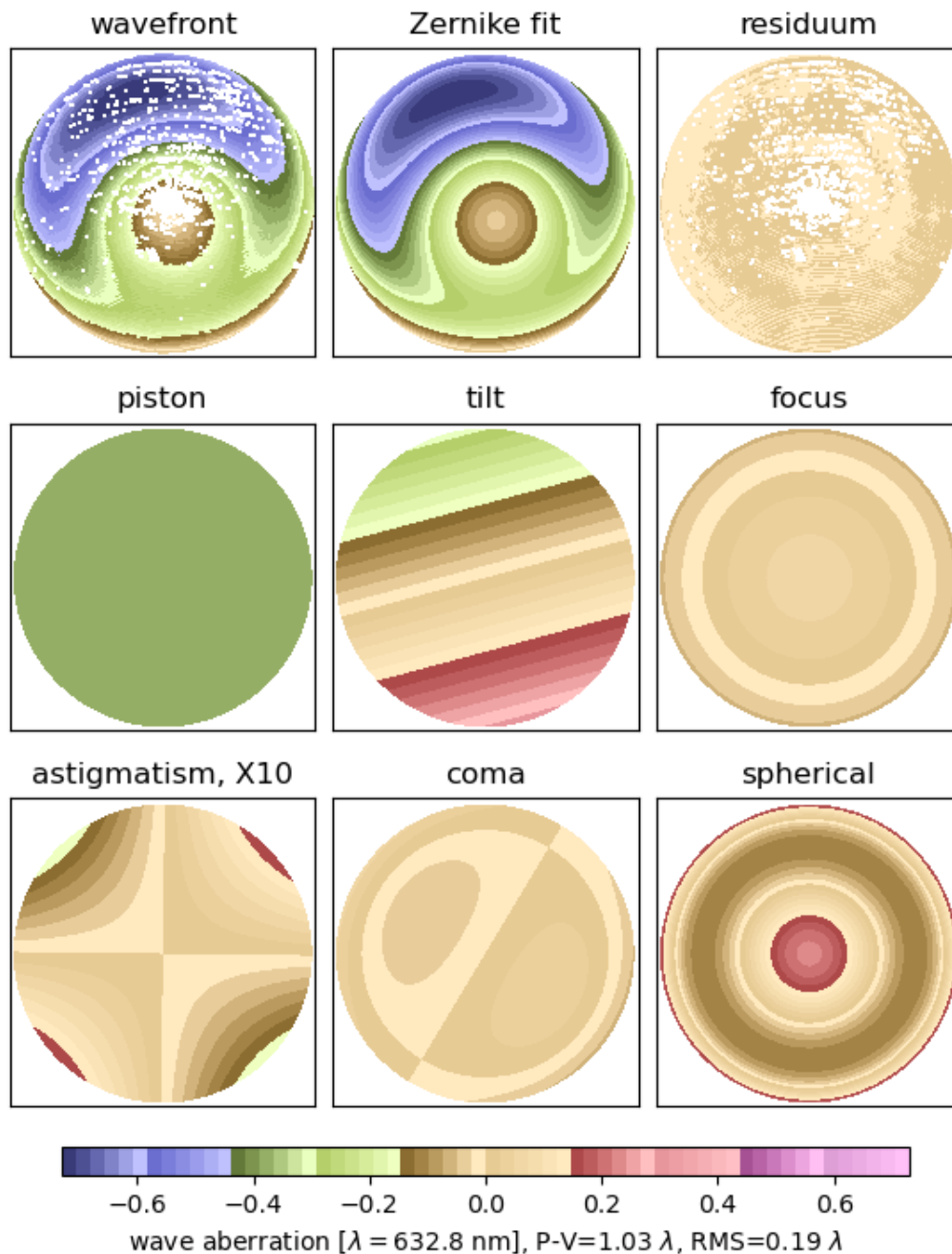


Figure 3.8: Wavefront quality of AtmoSHINE camera optics C1. Measured wavefront aberrations were fitted based on the first 36 Zernike polynomials. The first 9 Zernike polynomials describing first order piston, tilt, focus, astigmatism, coma and spherical aberration were separately plotted which showed the dominant contribution of focus and spherical aberration within the camera optics. Shown data did not consider the ISF.

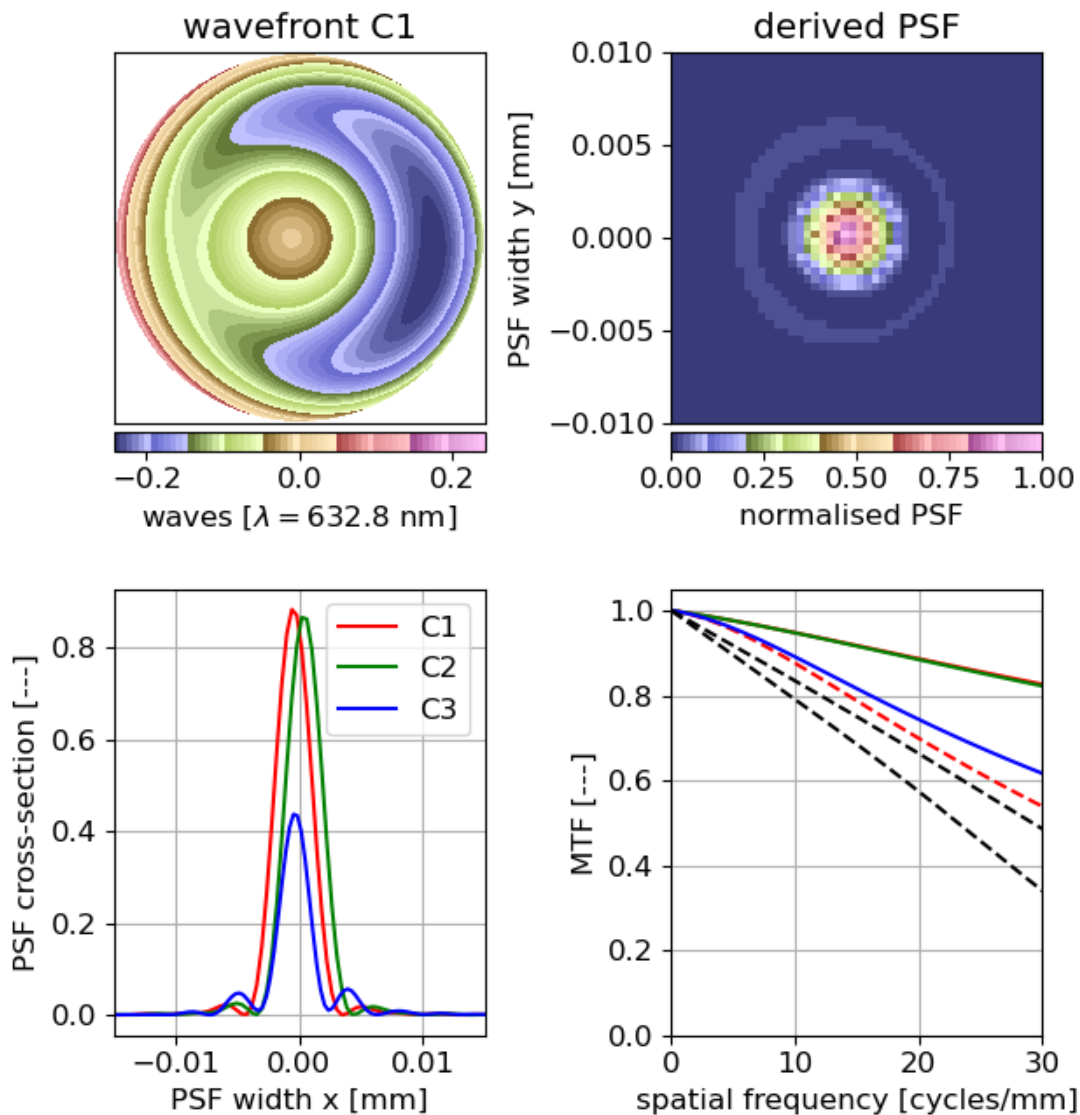


Figure 3.9: Derived MTF curves of the AtmoSHINE camera optics. The obtained wavefront data is utilised to estimate the PSF and corresponding MTF at $\lambda = 632.8$ nm. Shown are the results for the three camera optics C1, C2 and C3. A clear performance degradation of C3 can be seen due to removal of the aperture stop. The black-dashed MTF curves indicate expected values at two field points on-axis and at (2.5 mm, 2.5 mm) off-axis. The red-dashed curve indicates MTF values estimated based on measured wavefront aberrations with focus and spherical aberration replaced by three times higher Zernike coefficients from simulations. Solid red and green MTF curves overlap.

aberration evaluation for the front optics and rely on full system evaluation based on interferogram fringe visibility for evaluation of correct camera optics alignment.

All in all, the wavefront aberration measurements provided a first insight into the relation between wavefront aberrations and imaging quality. Front optics A1

and B2 were selected as candidates for final flight model integration alongside the camera optics C1 and C2. Camera optics C3 may need to be re-evaluated after the aperture stop is re-installed. The optics re-design and analyses of the AtmoLITE system presented from section 3.5 onwards extends the discussion towards the actual interferogram visibility. Further, limitations of measuring the wavefront aberrations of front and camera optics became clear. This highlighted the need for a more sophisticated alignment and verification strategy of the optical system and is covered in chapter 4. Moreover, the results presented here at $\lambda = 632.8$ nm for the front optics, only indicated that imaging performance expressed in terms of MTF was within expectations and that performance as-designed may be expected. However, the absolute values for nominal operation at $\lambda \approx 762$ nm still had to be verified separately.

3.3 AtmoSHINE - Line-Of-Sight Calibration

The LOS orientation is crucial in relating measured spectra and real world coordinates, e.g. altitude, latitude and longitude of the satellite or the tangent point of observation. In general, knowledge about the absolute pointing and its time-dependence is necessary. The absolute pointing or line-of-sight is defined by the vector between the instrument's optical axis and the mean tangent height at the centre of the atmospheric scene of interest. Here, the a-priori orientation between the instrument and satellite interface is less critical and may be corrected during operation by rotation of the whole satellite. However, this step requires that the O₂ A-band emission is already partially within or close to the FOV of AtmoSHINE because a satellite's orientation is typically defined ahead of launch to within a few degrees. A-priori, the orientation is driven by power and thermal considerations involving orientation of solar panels, radiators and communication devices or further secondary payloads [Gilmore, 2002]. Further, the LOS continuously oscillates while the satellite is being stabilised. The stabilisation during AtmoSHINE operation was expected to be better than $0.01^\circ/s$ which corresponds to about 0.7 % of the full FOV. This value was small compared to the expected mechanical alignment tolerance of AtmoSHINE during integration to the satellite bus and could be neglected. Since the integration had to be performed manually, an upper feasible positioning tolerance of ± 1.0 mm was chosen as reference which corresponded to a pointing accuracy of $\pm 0.14^\circ$ when evaluated along the instruments full side length. Therefore, including the expected extent of the O₂ A-band emission during night time of up to 0.2° , the full O₂ A-band emission was expected well within the nominal FOV of 1.3° if characterisation of the deviation between LOS and a reference could be measured better than 0.14° . In the following section, an experimental evaluation of the first LOS characterisation for the AtmoSHINE instrument is covered. The absolute deviation between the LOS pointing and a reference suitable for cross-calibration with the satellite interface is derived. Including the measurement uncertainties, the analysis yielded a deviation of $0.021 \pm 0.007^\circ$ which is well below the required accuracy. Note that only the vertical orientation between LOS and the reference corresponding to the altitude of observation is of interest here. In addition, the LOS characterisation revealed a potential problem due to ghost reflections within the nominal FOV. This problem was further investigated based on simulations and response measurements to a collimated point source and is covered in section 3.4.

The AtmoSHINE instrument was assembled at the BUW but had to be integrated into the larger satellite structure by the satellite provider. Thus, a reference mirror

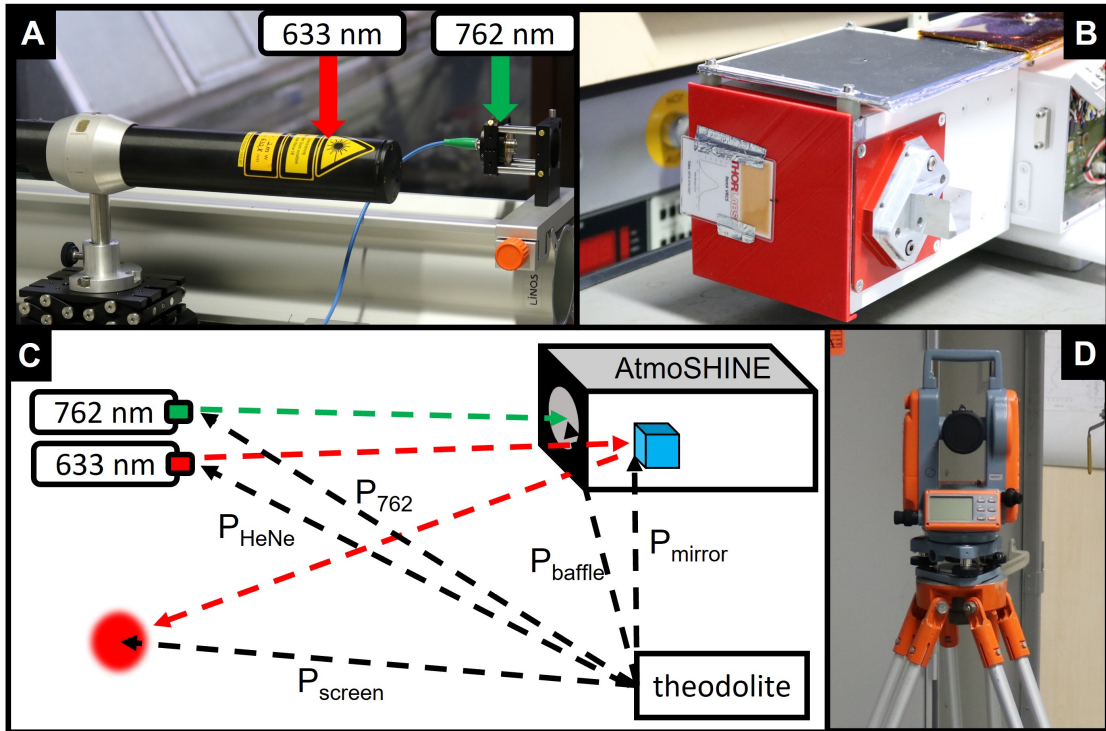


Figure 3.10: Experimental setup to characterise the AtmoSHINE LOS. Two laser sources at 633 nm and 762 nm were utilised (A) and pointed towards the reference mirror and entrance aperture of the AtmoSHINE instrument. A luminescent laser detection card was placed at the AtmoSHINE entrance aperture in order to visualise the 762 nm laser spot (B). The measured reference points were labelled P_i (C) and their relative position was monitored by a theodolite (D).

was installed which allowed for LOS characterisation and later cross-calibration with respect to the satellite interface and coordinate system. The reference mirror was mounted on top of the stray light reducing baffle and its surface normal was oriented parallel to the nominal instrument LOS. In order to measure the deviation between the as-build LOS and the reference mirror surface normal two collimated

Table 3.1: Measured relative positions between laser sources, instrument, reference mirror and screen during the LOS calibration of the AtmoSHINE EM instrument. Data was obtained on 1st of February, 2018. Uncertainties of angular measurements were $\pm 10''$ and distance measurements towards the theodolite were reproducible within ± 30 mm despite a systematic difference between the laser and cords methods.

-	P_{762}	P_{HeNe}	P_{baffle}	P_{mirror}	P_{screen}
vertical	90°00'00''	90°00'00''	90°00'00''	90°00'00''	89°57'46''
horizontal	112°07'35''	111°25'08''	154°21'15''	154°59'33''	101°13'04''
Δ_{cords}	5.810 m	5.700 m	6.825 m	6.775 m	6.095 m
Δ_{laser}	5.809 m	5.710 m	6.847 m	6.850 m	6.095 m

laser sources were utilised. The LOS was defined by aligning one laser directly through the aperture centre of the AtmoSHINE instrument at a wavelength of 762 nm such that a spot formed centred on the detector. A second HeNe laser was aligned to the reference mirror at the visible wavelength of 633 nm. At a small inclination between laser beam and reference mirror, the back-reflection could be monitored at a screen behind the HeNe laser. The relative positions between the source laser apertures P_{762} and P_{HeNe} , the centre of the instrument aperture P_{Baffle} and the laser spot centres on the reference mirror P_{mirror} and on the screen P_{screen} were measured with a theodolite. The theodolite was further utilised as a height reference in order to align all reference points except P_{screen} to the same vertical angular position in order to minimize measurement uncertainties. A schematic overview of these components is given in Figure 3.10 where the vectors \overrightarrow{LOS} and $\overrightarrow{N_{\text{mirror}}}$ were defined by Equation 3.1 and Equation 3.2. Note that the distances between the reference mirror and both laser sources were not equal, hence, division by $\|\dots\|$ denotes normalisation to unity of the respective vectors such that the correct mirror surface normal is obtained. The distances between the theodolite and each reference point were measured independently by either a laser range-finder with an accuracy of ± 2.0 mm or by spanning cords evaluated against a measuring tape. Because the length of the cords exceeded the measuring tape's length, a step-by-step measurement approach was taken with an accumulated uncertainty over all seven steps of ± 7.0 mm. The final measurement results were summarized in Table 3.1 and showed a discrepancy between distance measurements of up to 75 mm between both methods whereas repeated measurements of the individual methods were reproducible within ± 30 mm. The most likely cause of this discrepancy were an unknown sag of the spanned cords or non-ideal measurement conditions with the range-finder pointing onto inclined surfaces.

$$\overrightarrow{LOS} = \overrightarrow{P_{762}} - \overrightarrow{P_{\text{baffle}}} \quad (3.1)$$

$$\overrightarrow{N_{\text{mirror}}} = \frac{1}{2} \left(\frac{\overrightarrow{P_{\text{screen}}} - \overrightarrow{P_{\text{mirror}}}}{\|\dots\|} + \frac{\overrightarrow{P_{\text{HeNe}}} - \overrightarrow{P_{\text{mirror}}}}{\|\dots\|} \right) \quad (3.2)$$

Evaluating Equations 3.1 and 3.2 based on the measured data yielded the final estimation in spherical coordinates (θ, ϕ) presented in Equations 3.3, 3.4 and the deviation $\Delta\theta$ in vertical direction given by Equation 3.5. The uncertainty estimation is based on Gaussian distributed errors assuming $\sigma = \pm 10''$ for all measured angles and ± 30 mm for all length measurements. The corresponding formulas are appended in section A.2.

$$\begin{aligned}\overrightarrow{LOS}_{\text{cords}} &= (90.000^\circ \pm 0.005^\circ, -31.488^\circ \pm 0.374^\circ) \\ \overrightarrow{LOS}_{\text{laser}} &= (90.000^\circ \pm 0.005^\circ, -31.249^\circ \pm 0.374^\circ)\end{aligned}\quad (3.3)$$

$$\begin{aligned}\overrightarrow{N}_{\text{mirror, cords}} &= (89.979^\circ \pm 0.005^\circ, -31.657^\circ \pm 0.331^\circ) \\ \overrightarrow{N}_{\text{mirror, laser}} &= (89.979^\circ \pm 0.005^\circ, -31.037^\circ \pm 0.331^\circ)\end{aligned}\quad (3.4)$$

$$(\overrightarrow{LOS} - \overrightarrow{N}_{\text{mirror}})_\theta = \Delta\theta = 0.021^\circ \pm 0.007^\circ \quad (3.5)$$

It appeared that the systematic difference between both methods did not alter the result when rounded to the first significant digit and evaluated along the altitude direction. However, a horizontal difference of $0.381^\circ \pm 0.706^\circ$ was found which corresponded to an uncertainty of ± 44 km when projected onto the atmospheric scene at the tangent point. The larger uncertainty in horizontal direction was a direct consequence of the alignment strategy. While setting up all equipment, the theodolite was already used to align all reference points to the same height which is also evident from the vertical positions given in Table 3.1. The propagated uncertainty in vertical direction is therefore only relevant in Equation 3.2 whereas uncertainties of the horizontal position already have to be considered in Equation 3.1.

Based on these estimations, AtmoSHINE was integrated at a nominal angle of 29.68° relative to the satellite's reference coordinate system. A final uncertainty estimate from the satellite's integration was not available at the time of writing. Instead, the successfully obtained in-orbit measurements shown later in Figure 3.14 and containing the O₂ A-band emission confirmed that the method described here is sufficiently accurate and may be further used in preparation of follow-up missions.

3.4 AtmoSHINE - In-Field Ghost Reflections

During the AtmoSHINE LOS calibration, a second, unexpected ghost spot was observed on the detector in addition to the expected spot produced by the collimated laser source. The ghost spot appeared mirrored across the optical centre when the instrument's LOS was aligned to the collimated laser source at small inclinations. In particular, the two spots were moving in opposite directions while tip or tilt were introduced between the LOS and the laser source. As both spots could be overlapped in the centre of the detector, no additional measures were taken during the LOS calibration. However, an experimental setup was constructed to further investigate the positional dependency and intensity of this ghost reflection. This setup, the obtained experimental results and simulations used to further understand the origin of this ghost reflection are provided in this section.

An image of the experimental setup used to evaluate the ghost reflections at different positions over the detector is shown Figure 3.11. It comprised a tunable laser source set to 762 nm which was coupled into the setup via an FC/APC fibre collimator. The output was refocused and spatially filtered passing a pinhole with a diameter of $\emptyset 20 \mu\text{m}$. The adjacent $f = 400 \text{ mm}$ achromatic lens re-collimated the laser light and allowed to illuminate the full AtmoSHINE entrance aperture and a spot size of $\emptyset 8.1 \mu\text{m}$ was expected on the detector under ideal conditions. In order to achieve proper collimation the achromatic lens was mounted to a XYZR-stage. Monitoring the transmitted wavefront during alignment with a Hartmann-Shack sensor allowed to minimize the apparent wavefront aberrations. The final alignment yielded a PV wavefront aberration reduction from $10.00 \lambda \pm 2.88 \lambda$ down to $0.20 \lambda \pm 0.03 \lambda$. The uncertainty was based on the measured wavefront RMS. Note that the Hartmann-Shack sensor only covered about 2 % at the centre of the full aperture. This was deemed sufficient because the measurements did not require *best* possible collimation, rather, a small source divergence such that the main and ghost spots are still localized on the detector within a few pixels was accepted. In order to measure the point source response at different locations across the detector, the inclination between the AtmoSHINE instrument and the achromatic lens was manually altered. As this adjustment did not allow for an absolute measurement of the inclination, only the relative positions of main and ghost spots could be determined based on their absolute positions on the detector array during data processing.

An example of two spots and their corresponding ghost reflections is given in Figure 3.12. The ghost reflections always occurred mirrored across the intersection

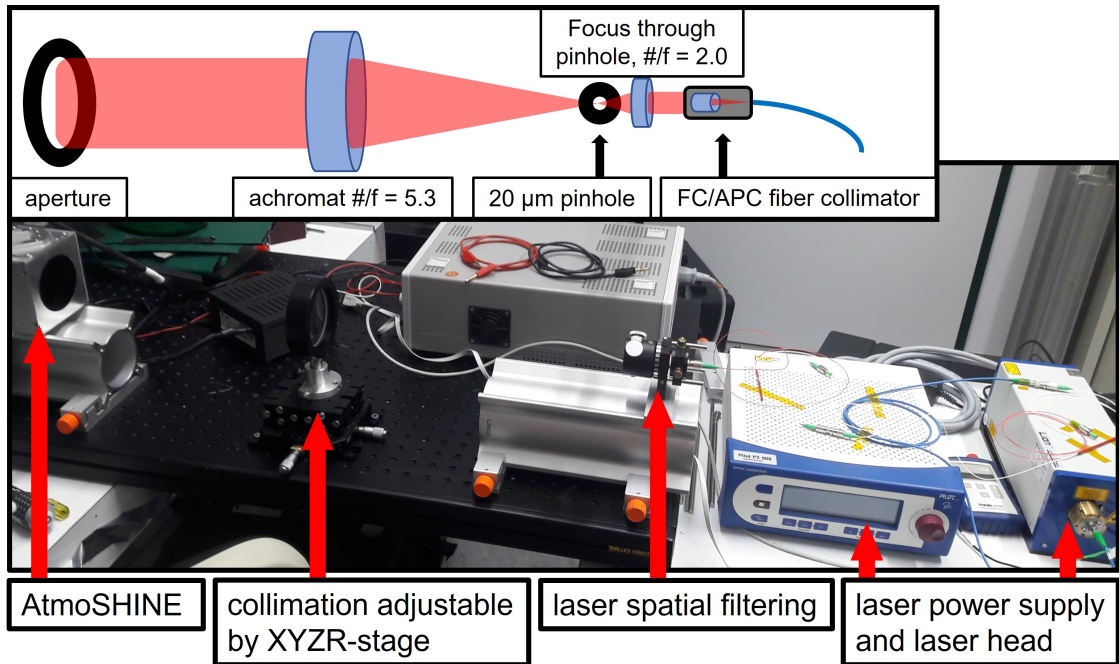


Figure 3.11: Experimental setup used to test the AtmoSHINE point spread response. The laser source is coupled via the FC/APC fiber collimator into the setup. It is spatially filtered by focusing the beam through a $\varnothing = 20 \mu\text{m}$ pinhole and re-collimating the beam towards the AtmoSHINE instrument afterwards. The working f-numbers of the lenses are chosen to yield a full illumination of the AtmoSHINE entrance aperture.

between the optical axis and the detector indicated by the dashed lines. For comparison, 2D Gaussians were fitted through all main and ghost spots where possible and a full summary of all measured spots is appended in Table A.2. Uncertainty estimates of the fitting parameters were based on Gaussian error propagation and were included in the summary. The derived 1σ width was between 1.5 and 10.0 times larger at the ghost spots when compared to the corresponding main spots which made a direct comparison of intensity impossible. Thus, the fitted Gaussians were integrated over a region of 3σ in order to compare the integrated intensities. Evaluation of the ratio between the integrated intensities of the ghost to the main spots showed a general decrease in ghost intensities with increasing radial distance from the optical centre with up to 27 % being distributed into the ghosts reflections near the centre.

In an earlier stray light analysis of the AtmoHIT/AtmoSHINE optics presented in [Deiml, 2017] no ghost reflections were found despite modelling a multitude of potential stray light sources. These included contamination by particles, surface roughness and scatter at mechanical surfaces. However, the simulation considered sources located on-axis only and thereby missed problems related to double reflections cause by off-axis illumination. In the following, a reduced model of the

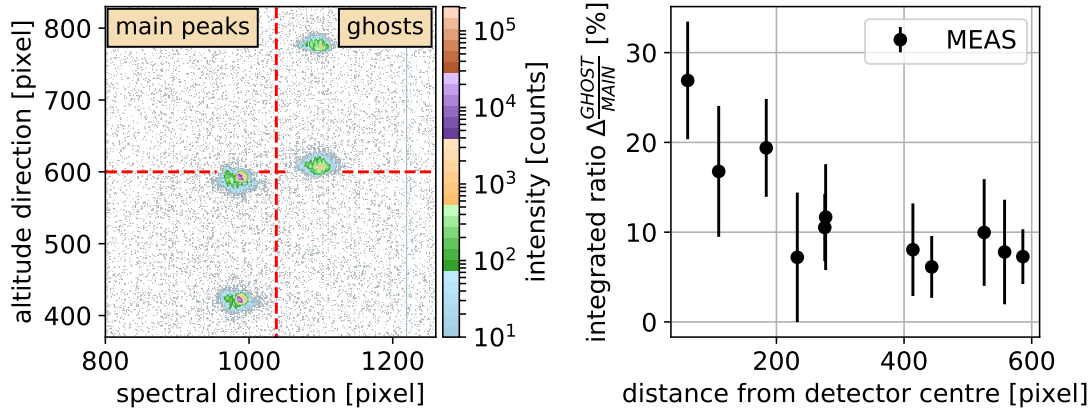


Figure 3.12: Evaluation of AtmoSHINE stray light reflections across the detector array. Shown are main spots as expected from the collimated laser source with their ghost reflections mirrored across the intersection between optical axis and detector at pixel positions $(x, y) = (1038, 600)$ (left). Measured results of two spots are shown as reference with the median background removed. Integration of 2D Gaussians fitted through pairs of main and ghost spots allowed to estimate the relative integrated intensity between ghost and main spot at a radial offset from the optical centre (right).

earlier analysis was used in order to provide fast evaluation of potential sources of ghost reflections. All scatter mechanisms were turned off and mechanical surfaces of the housings and lens mounts were no longer considered with the exception of the stray light reducing stop behind the camera optics. Only direct scatter at the lens surfaces and SHS parts was considered. The magnitude of the scattered rays was chosen based on the specifications of the anti-reflection coatings at 0.5 % of the incident intensity. Reflectivity of the gratings and transmission of all lenses was set to 1.0 and the bandpass filter was replaced by a plan-parallel glass plate. Each simulation run considered a single field point located at a field angle of $(0.35^\circ, 0.35^\circ)$ including a divergence of $\pm 0.0015^\circ$ similar to the idealised experimental setup. The divergence was simulated by distributing $N_{rays} = 30 \times 30 \times 1024$ rays equally around the desired field angle. The 30×30 sub-fields were arranged in a grid spanning $0.35^\circ \pm 0.0015^\circ$ equally. At each grid point 1024 rays with the same orientation were launched uniformly distributed over the entrance aperture. The intensity of a single starting ray was set to $1/N_{rays}$ W.

In total 1 + 12 simulations were conducted. At first, one reference run was made in which all coatings were considered as providing zero back-reflection and a single spot was obtained on the detector as expected. Afterwards, the coatings were implemented alternating between single lens elements which showed the individual contribution of each lens or field-widening prism. This made up a total of 5 + 1 + 1 + 4

simulations for the front optics, beam splitter, field-widening prisms and camera optics, respectively. In the last run all coatings were simultaneously implemented and the overall combined effect was simulated.

Three candidates of ghost reflections were found which are summarized in Figure 3.13. The bandpass filter and third camera lens each yielded an individual ghost reflection with their peak positions located at the same position on the detector. However, the ghost reflection caused by the third camera lens covered almost nine times the area of the one caused by the bandpass filter. But, the integrated intensity was found to be 1.9 times higher when the ghost reflection originated at bandpass filter compared to camera lens three. Another significant but weaker ghost reflection was caused at the field-widening prisms. It appeared as two individual patches about 600 pixels apart and located in spectral direction around the main spot which could not be seen in the measured data, thus, it was disregarded. The combined integrated intensity of the ghost reflections in the simulation run including all coatings and corresponding to the observed problem mirrored across the optical centre was found to be 0.3 % of the main spot's intensity. In contrast to the measured relative intensities in Figure 3.12, this reduced and simplified simulation could not exactly reproduce the magnitude of the observed ghost spot's intensities. However, the key take-away was to include a small inclination of the bandpass filter when placed in front of the optics and to include evaluation of potential off-axis double reflections during the design process of the new optical system.

Lastly, a few remarks about the impact of the mentioned ghosting on measurements of AtmoSHINE are given. First measurements obtained in space indicated that the ghost reflections caused no problem during night-time observation in certain situations. In Figure 3.14 three example images obtained by AtmoSHINE on 21.05.2019 are shown. The region of interest was restricted to 840 pixels in spectral and 1200 pixels in altitude directions. Cross-sections of average signal levels were also provided perpendicular to the spectral direction emphasizing the expected emission layer and its ghost reflection. The lower peak corresponded to the expected emission layer of the O₂ A-band emission which covered up to 500 rows on the detector (second image). A ghost image of the emission layer was observed as a second peak on the upper half of the detector. As the inclination between AtmoSHINE and the peak emission layer changed over time such that the emission layer was imaged closer to the detector center, both peaks appeared closer to each other and their baselines could no longer be clearly separated. It was therefore concluded that an orientation of AtmoSHINE with the apparent emission layer imaged to the lower half of the detector could exclude any biasing with ghost

images. This corresponded to an offset in instrument orientation of 0.45° from the nominal specification in which case the peak emission layer was imaged to rows 350 and below. However, with respect to day-time observations, this solution would not provide any improvements. Due to the continuous extent of the O₂ A-band emission layer across all altitude layers observed by the instrument during day-time, stray light contributions by ghosting were expected in all rows, effectively contributing an unknown bias in all measurements. Therefore, the decision to re-design the instrument optics was made.

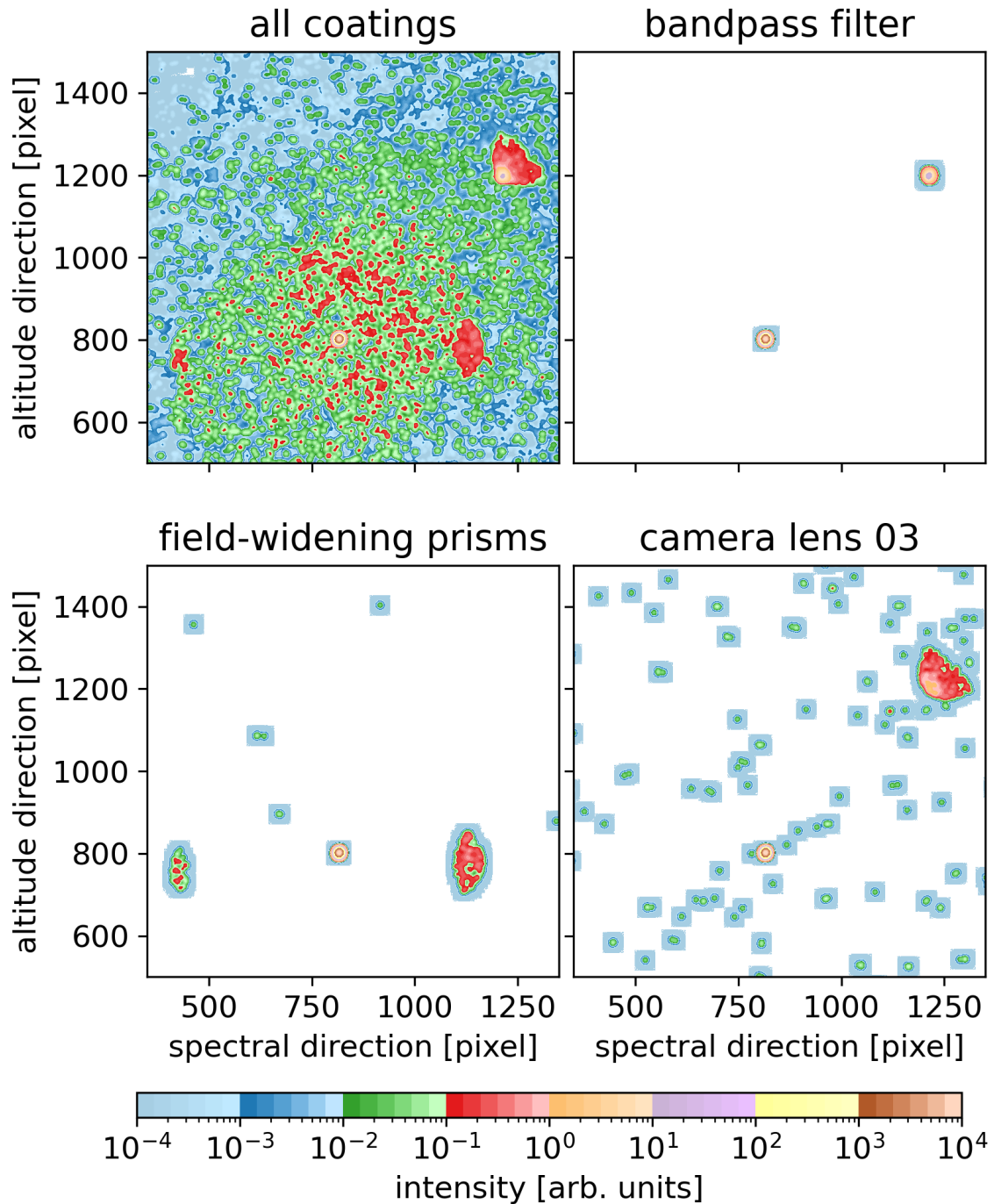


Figure 3.13: Simulation of the ghost origin within the AtmoSHINE optics. An off-axis field point at $(0.35^\circ, 0.35^\circ)$ incidence angle was simulated corresponding to the main peak centred around pixels $x = 802$, $y = 817$. It was split up into 30×30 equally distributed sub-fields spanning a divergence angle of $\pm 0.0015^\circ$. Each sub-field was simulated with 1024 starting rays randomly distributed across the full entrance aperture. Shown are the results including double reflections at single optical elements when evaluated within the detector plane. The three largest contributions of bandpass filter, field-widening prisms and camera lens 03 are separately shown. Scattering at mechanical surfaces, contamination or lens defects was not considered.

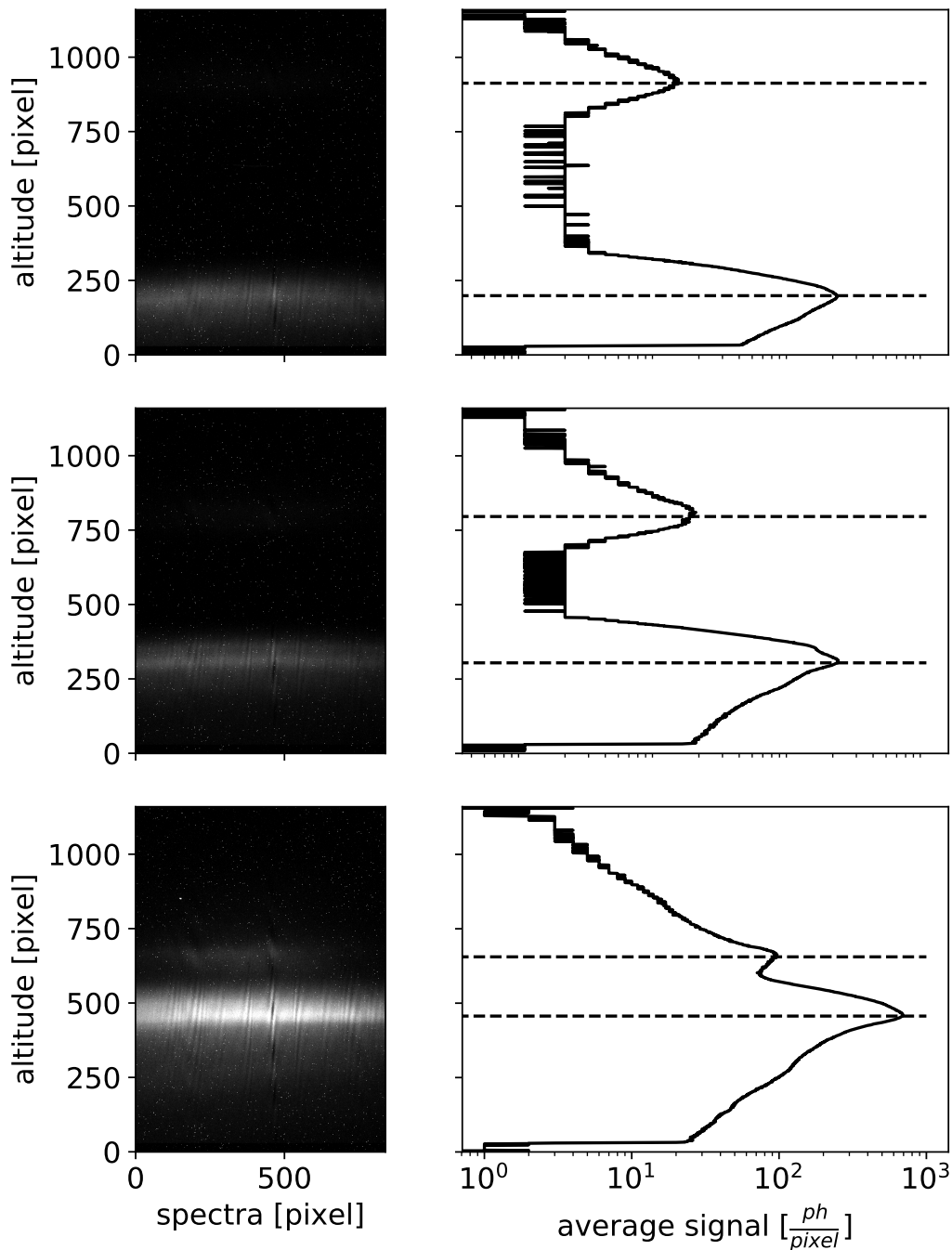


Figure 3.14: AtmoSHINE in-orbit interferograms including ghost artefacts. Data obtained on 21.05.2019 captured the O₂ A-band layer on the lower half of the detector images (left column). Thus, clear ghost images of the observed scenery could be obtained on the upper half of the detector. Taking the median in spectral direction two maxima corresponding to the peak emission layer and its ghost image could be visualised (right column, dashed lines). The average signal strength of the ghost peak relative to the emission layer amounted to approximately 7%, 8% and 14% (top, middle, bottom).

3.5 AtmoLITE - A new optical System

Preparation of the AtmoSHINE instrument and its qualification tests revealed problems which could only be addressed by a re-design of the optical system and preparation of new calibration equipment. Further, the re-design allowed to include performance improvements and mechanical modifications necessary to optimize the as-build performance during assembly and integration. Starting with an overview of requirements and design goals set for the new optical system as summarized in Table 3.2, this section introduces the design changes made for AtmoLITE. A direct comparison of optical and mechanical properties of AtmoSHINE and AtmoLITE is appended in section A.4.

The first calibration of the AtmoSHINE instrument presented in Liu [2019, figures 5.9, 5.10 and 5.17] demonstrated that an interferogram visibility between 80 % and 50 %, dropping from the smallest to the highest observed frequencies, was feasible. It was further recommended to minimize the apparant wavelength dependent fringe rotation to improve the accuracy of tested retrieval algorithms. Thus, it is required to keep or increase the interferogram visibility with the goal set to $V > 50\%$ at the highest frequency for AtmoLITE. In addition, changes of the SHS assembly jig are implemented to better control the grating orientation and minimize the wavelength dependent interferogram rotation. Details and a first experimental verification of this new assembly jig are provided in chapter 5.

The bandpass FWHM is extended from 4.0 nm to 6.5 nm for the AtmoLITE mission, now, including both branches of the O₂ A-band emission spectrum between

Table 3.2: Based on experiments and lessons learnt during the AtmoSHINE preparation and tests, a set of new optical and mechanical design goals was formulated. Presented are the final requirements which include changes made during the re-design. Optical and mechanical requirements are indicated by RO.XX and RM.XX, respectively.

ID	Requirement	Value
RO.01	Spectral range	759.8 – 767.0 nm
RO.02	Entrance aperture size	75 mm
RO.03	Illuminated detector area	$< 10 \times 10 \text{ mm}^2$
RO.04	Illuminated grating area	$> 10 \times 10 \text{ mm}^2$
RO.05	Diffraction limited imaging	MTF $> 80\%$
RO.06	Fringe visibility	$> 50\%$
RO.07	System envelope	$220 \times 120 \times 96 \text{ mm}^3$
RO.08	Operational temperature range	$[-30, +20] \text{ }^\circ\text{C}$
RO.09	Field of View	$\pm 0.65^\circ$
RM.01	Compensation of optics' pressure dependence	
RM.02	Compensation of optics' temperature dependence	

$\nu = 13057 \text{ cm}^{-1}$ and $\nu = 13161 \text{ cm}^{-1}$ (cf. section 2.3). In addition, the Littrow wavenumber is moved from centered between Q- and R-branch to the lower wavenumber $\sigma_L = 13047 \text{ cm}^{-1}$, thus, is placed outside of the bandpass filter range. By design, this avoids the aliasing between Q- and R-branch observed in AtmoSHINE spectra. AtmoLITE features a larger illuminated area on the gratings of $A_{\text{grating, illum.}} \approx 15.2 \times 15.2 \text{ mm}^2$ in order to keep the small fringe frequencies necessary for high interferogram fringe visibility. The trade-off is the increased front optics effective focal length from 273 mm up to 653 mm compared to AtmoSHINE. A GSENSEBSI440 detector is used in the AtmoLITE system due to its expected lower noise and higher quantum efficiency (QE) in comparison to the previous HWK1910 sensor used in the AtmoSHINE instrument. The required back-compatibility of the new optics with the older HWK1910 sensor yields a restriction of the maximum image height of 10 mm. The FOV of $\pm 0.65^\circ$ in altitude and horizontal direction is kept. The new entrance aperture is increased to 75 mm which significantly increases the etendue and further details follow in section 3.10.

The overall optical imaging capabilities are required to resolve at least 40 altitude layers whereby a system $\text{MTF} > 80 \%$ is assumed sufficient at the corresponding frequency of 4.2 lp/mm. Whereas the design of AtmoSHINE purely relied on manufacturing and assembling tolerances, a new approach is developed incorporating manually controlled compensators during integration of the optics which are expected to increase the as-build performance of AtmoLITE. These compensators shall also improve the repeatability of achieved alignments when more instruments are assembled for upcoming projects. The instrument's envelope is further adjusted to meet the specifications of the INSPIRE satellite bus which allocates a maximum volume of $220 \times 120 \times 96 \text{ mm}^3$. Hence, the stray light baffle is shortened. The discussion of simulated radiance levels due to scattered radiation is not covered in this work and was part of an external study conducted by Hembach Photonics GmbH. Ongoing studies are still working on experimental setups to quantify the as-build system stray light characteristics.

Based on these design goals, the new prototype for AtmoLITE shown in Figure 3.15 is developed. Starting on the left, a 75 mm long stray light reducing baffle system includes seven apertures. The adjacent bandpass filter is embedded in rubber rings for further protection against vibrations. It is inclined by 1° in order to avoid potential double reflections as seen by AtmoSHINE. Further, bandpass filter and stray light baffles effectively exclude direct irradiation of the front optics at field angles greater than $> 51^\circ$. The following four lenses constitute the front optics with an effective focal length of 653 mm. Two compensators are included in the front

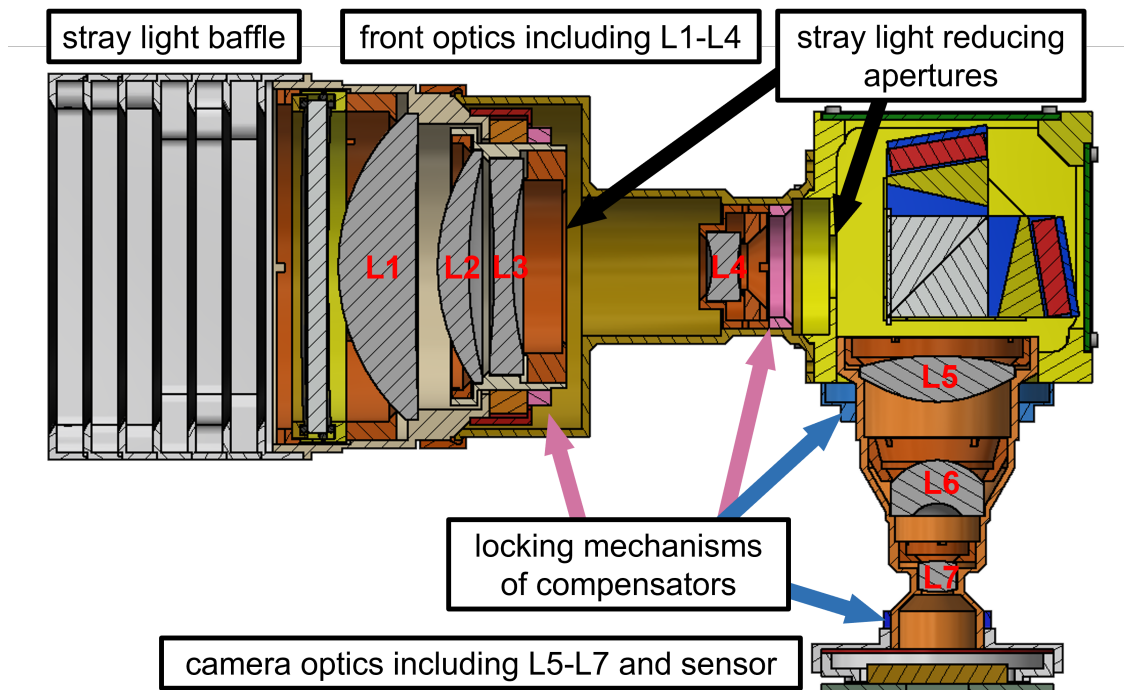


Figure 3.15: AtmoLITE opto-mechanics CAD cross-section. Shown are the front optics and camera optics which include compensators to account for tolerances occurring during manufacturing and assembly. Additional apertures limit the amount of in- and out-of-field stray light reaching the detector.

optics as already indicated in Figure 3.1. Both are required to achieve diffraction limited imaging performance. However, the prototypes analysed in the present study contain only the compensator around L4. The first compensator allows to move lens two and three simultaneously along and perpendicular to the optical axis which compensates tip and tilt tolerances of the first lens. This is achieved by mounting lens two and three combined in one separate lens mount pressed on the mount of lens one and locked in place by an additional locking ring. The second compensator moves lens four along the optical axis. It is used to control the effective focal length of the front optics during integration and enables compensation of the focal length change when the system is exposed to a low pressure environment.

Similar to the AtmoSHINE design, the SHS housing is used as connector of front and camera optics. Here, two major changes are implemented which enable a new assembly strategy. Firstly, the camera optics' distance to the SHS is no longer controlled by shims but a thread is implemented. This allows for continuous adjustment without taking the optics apart. Secondly, a mechanical end top is used to align the SHS beamsplitter cube prior to attaching both SHS arms which reduces the overall number of DoFs during integration. In particular, the SHS

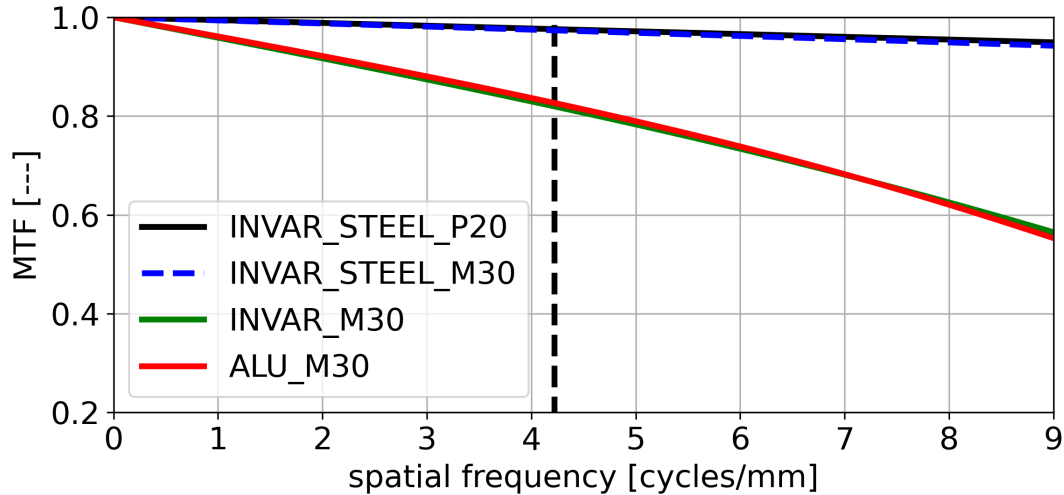


Figure 3.16: AtmoLITE MTF curves including different materials. Shown are the expected MTF curves of the full optical system including parts made of INVAR, aluminium or steel. In comparison to the reference run at ambient conditions, all values are provided at a system temperature of -30°C .

assembly is done while being integrated between both optics which is further discussed in section 5.1. Two ports give lateral access to the SHS. They provide space for two grapplers during SHS assembly and later access during flat-field measurements or inspections.

In the camera optics, the first lens features an aspheric surface which reduces the overall number of lenses by one. The camera optics effective focal length is 85.74 mm and provides a magnification between localization and detector plane of $M = 0.625$. Combined with the front optics, the total image height is 9.472 mm. The threads interfacing from the camera optics towards either the SHS housing or the detector mount enable continuous adjustment during optimization of the interferogram contrast. Note that the three lenses of the camera optics are mounted in a single lens barrel and no fine adjustments between those lenses is used as compensator. Further discussion of experimental data obtained during assembly and laboratory tests of the AtmoLITE prototype is provided in section 5.2 and section 5.3 with respect to measured MTF, FOV and interferogram quality, respectively.

Evaluation of the optical design is based on two figures of merit. The overall imaging capability of the optics is evaluated by means of the MTF which is shown in Figure 3.16 considering four different scenarios. The first two simulations show the diffraction limited and athermal MTF at $+20^{\circ}\text{C}$ and -30°C of the nominal design. These simulations included a lens mount around front optics' lens four made out of steel and the remaining mechanics made out of a low CTE material,

preferably INVAR. However, it is uncertain if a mechanical design incorporating both INVAR and steel is manufacturable and the analysis is repeated for systems entirely made out of INVAR or aluminium. The later two systems show an MTF $> 80\%$ at frequencies below $\nu_{MTF} = 4.2$ cycles/mm when cooled down to -30°C , thus, fulfilling requirement RO.06. Consequently, aluminium is selected as material for fast prototyping and evaluation of the first instrument as demonstrated from chapter 5 onwards. However, the following discussion of instrument performance and tolerance budgets is continued for the as-designed system including the parts made from INVAR.

The expected interferogram visibility is used as second figure of merit. By ray-tracing, the wavefront aberrations of both SHS arms are estimated over the exit pupil and their complex sum is substituted into Equation 1.5. The resulting interference PSF is incoherently added up over all field points along the spectral direction. This simulates the expected interferogram visibility at all wavelengths of interest and examples of the two wavelengths 764.74 nm and 759.83 nm are taken as reference in the following discussion. The later one corresponds to the highest expected interferogram fringe frequency of 87.8 cm^{-1} and smallest expected visibility. Thus, performance degradation simulated at 759.83 nm are expected to be less pronounced at higher wavelengths or smaller frequencies. The simulated interferograms are base-line corrected and the apparent amplitude modulation is estimated based on the analytical signal of the remaining beat frequency similar to the method presented in Liu et al. [2018]. Division of the amplitude by the base-line yields the expected visibility. Results obtained at 759.83 nm are shown in Figure 3.17 and Figure 3.18 at the on-axis and $H_y = 0.9$ off-axis field points, respectively. The same evaluation at 764.74 nm is appended in section A.6. At the on-axis centre of the interferogram a drop in visibility is expected. The magnitude of the drop increases with decreasing wavelength and at 759.83 nm the visibility is as low as $V = 68.5\%$. A similar effect does not occur at the off-axis field point where an almost constant visibility is expected with the smallest value of $V = 92.0\%$ at 759.83 nm. A comparison of average visibility at all O₂ A-band emission wavelengths is provided in Figure 3.19. The comparison includes the two SHS designs of different grating groove densities. The rapid drop in visibility to below $V < 60\%$ at the higher groove density $G = 600\text{ mm}^{-1}$ confirms that including the second branch of the O₂ A-band emission and retaining high visibility, requires a reduction of grating groove density and, consequently, lower spatial frequencies. Conducting the simulation with two different detector settings yields no significant difference in average visibility. Note that those simulations are provided for a vacuum environment.

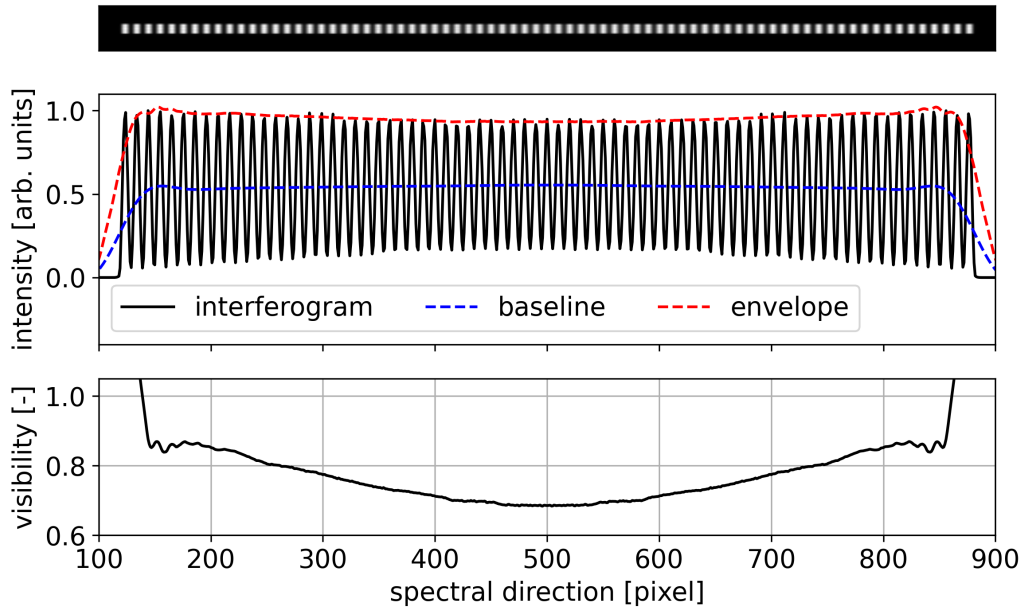


Figure 3.17: Example of a single simulated interferogram at 759.83 nm. Shown are the simulated detector response and the cross-section along the centre row. The estimated visibility was calculated based on a fitted baseline and envelope indicated by dashed lines. Noise and detector artefacts were not simulated.

Because the current interferogram simulation does not support misaligned optics ($\Delta z = 0$) apart from SHS arm imbalances, the impact of misalignments or thermal deformations is now evaluated based on simulated changes of the optics' MTF. In particular, the camera optics MTF is used to evaluate changes in visibility because it is well correlated with simulated visibility. The correlation is shown in Figure 3.20 where the most critical case of on-axis field angle $H\gamma = 0^\circ$ at 759.5 nm is considered which describes the lowest wavelength within the bandpass filter range. The correlation is evaluated at an instrument temperature of $+20^\circ\text{C}$ in an ambient environment and a linear relation is observed. Apparently the visibility decreases twice as fast as the MTF towards the interferogram center where the point of lowest visibility across full detector is expected, $V = 65\%$. Two cases are compared by simulation of the camera optics MTF at ambient conditions during assembly ($+20^\circ\text{C}$, 1013 hPa pressure) and coldest operational condition in-orbit (-30°C , 0 hPa pressure). The simulation results show that a slight increase of camera optics MTF by $+4\%$ is expected when the instrument is moved from ambient into a vacuum environment. Once in vacuum, a continuous decrease of up to -7% is expected while the instrument is cooled down to -30°C . Using the correlation relation of MTF and visibility, the following minimum visibility values are expected

at the detector center: $V = 57\%$ during assembly and $V = 52\%$ in-orbit at coldest point of operation. $V = 60\%$ is expected at the nominal operational temperature of $+0\text{ }^\circ\text{C}$ in-orbit. A noteworthy effect of the thermal SHS deformations discussed in section 2.5 and the corresponding increase of the Littrow wavenumber σ_L with decreasing temperature is a slight increase of visibility due to a decrease of the interferogram fringe frequency. However, an exact estimate is currently beyond simulation capabilities and has to be obtained based on experimental calibration data in upcoming studies. All in all, changes of the instrument temperature are therefore not expected to decrease the interferogram fringe visibility below the required value of $V > 50\%$ at all wavelengths of observed emission lines and under nominal operation conditions (RO.06).

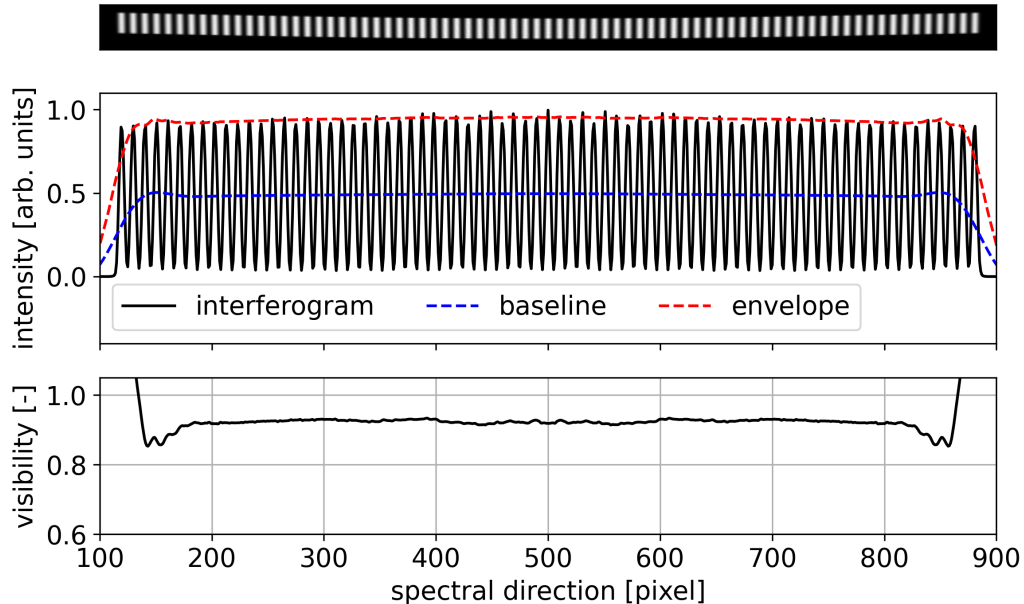


Figure 3.18: Example of a single simulated interferogram at 759.83 nm. Shown is the simulated detector response at the off-axis field point $Hy = 0.9$. The estimated visibility was calculated based on a fitted baseline and envelope indicated by dashed lines. Noise and detector artefacts were not simulated.

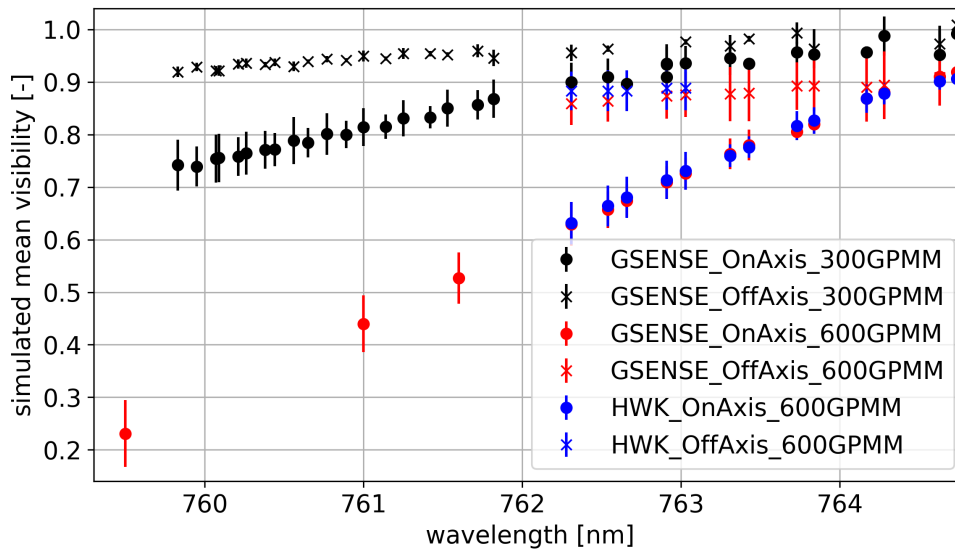


Figure 3.19: Simulated row-wise mean visibility for different AtmoLITE configurations. Shown are simulation results of the final optimised AtmoLITE optical system considering SHS of varying grating groove densities 300 mm^{-1} and 600 mm^{-1} . The given uncertainties are estimated as standard deviation of the non-linear drop of fringe visibility along the spectral axis. The on-axis and off-axis mean values correspond to the row-wise mean visibility at field angles of $H_y = 0.0$ and $H_y = 0.9$, respectively. Results are reported for a vacuum environment ($p = 0 \text{ hPa}$).

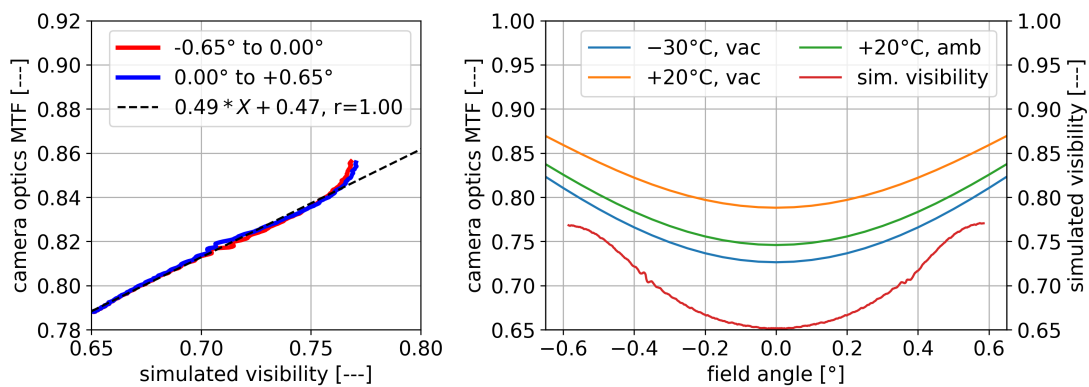


Figure 3.20: A linear correlation of the simulated visibility to the AtmoLITE camera optics MTF along the centre row of the detector is found under ambient conditions, $p = 1013 \text{ hPa}$ (left). The same data is shown along the detector row on the right (MTF green, visibility red). For comparison, expected camera optics MTF under vacuum at the two boundaries of the operational temperature range are shown (blue and orange).

3.6 AtmoLITE - Tolerance Budget

A tolerance analysis of the AtmoLITE instrument is provided with the goal to find suitable estimates for lens manufacturing and assembly tolerances. In addition, the required clearance for all compensators is estimated. The simulation considers 5×3 configurations which correspond to three different wavelengths at five individual field points. The wavelengths are chosen at 761 nm, 765 nm and 768 nm. The high interferogram fringe frequencies at 759.83 nm are not considered because tolerance analysis was performed prior to extension of the AtmoLITE bandpass towards the R-branch of O₂ A-band airglow. Wavefront RMS and PV are selected as the figures of merit and limits are chosen at $\text{RMS} < 0.1 \lambda$ and $\text{PV} < 0.5 \lambda$. These limits guarantee fulfilment of requirement RO.05 such that the desired $\text{MTF} > 80 \%$ can be achieved using aforementioned compensators.

Tolerances of the lens radii, surface figures, lens thickness, refractive index, abbe number, lateral positioning errors and de-centres for all spherical elements are considered. In case of the aspheric lens of the camera optics positional errors due to lens surface tilts and element wedges are considered in addition. SHS angular tolerances are chosen in accordance with the analysis presented in section 2.6 with the thickness tolerances between parts increased to $100 \mu\text{m}$. This ensures proper imaging capabilities of the localisation plane even if the as-build SHS tolerances deviate from expectations.

Starting with a sensitivity analysis, individual values are chosen for the tolerance data at each optical element. Lens element one and its distance to the doublet of lens element two and three are identified as most critical components with respect to positional tolerances and expected overall performance changes. Accordingly, their thickness tolerances are reduced to $\pm 30 \mu\text{m}$ whereas all other thickness tolerances are set to $\pm 50 \mu\text{m}$ or higher values. Surface figure errors are set to ± 3 fringes after consultation with the manufacturer and iteration of available tools. Relying on an auto-centring lens mount design similar to [Lamontagne et al., 2015], achievable lateral positional tolerances are assumed between $\pm 10 \mu\text{m}$ and $\pm 20 \mu\text{m}$. De-centre of spherical surfaces is modelled as surface element tilt and the sensitivity analysis yields acceptable overall performance at values below one arc-minute. Tolerances of the refractive index and abbe numbers are based on the standard glass melt quality of SCHOTT AG [2022b] and Ohara Corp. [2022].

The expected RMS and PV wavefront aberrations are evaluated based on 1000 Monte Carlo simulation runs and results are plotted against the effective field angle in Figure 3.21. In each run, the tolerance data is altered randomly assuming

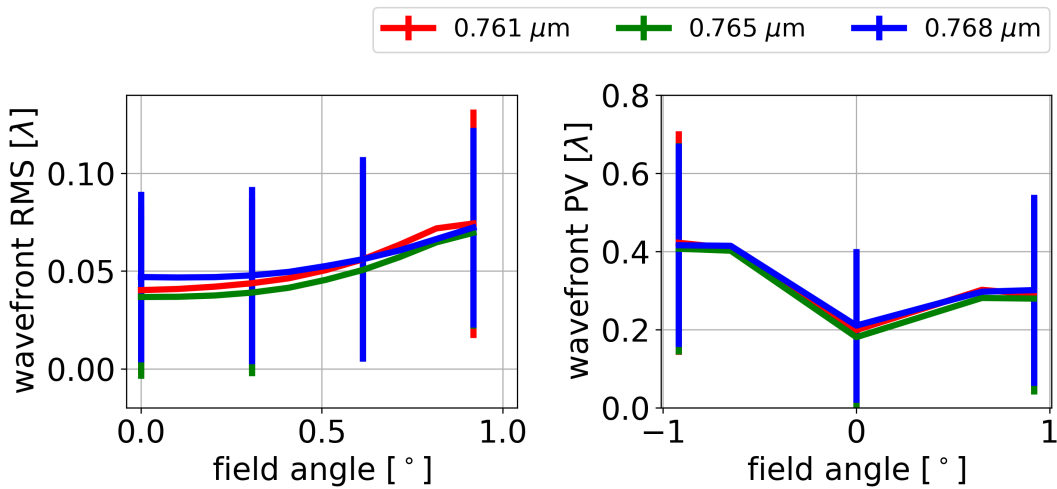


Figure 3.21: Mean RMS and PV wavefront aberrations of the final *AtmoLITE* system including a 3σ tolerance budget. The aberrations were evaluated at three different wavelengths. The statistical mean values were obtained based on 1000 simulation runs.

a uniform distribution. Due to the asymmetry of the SHS, PV mean values are asymmetrically distributed across the full FOV. At all field angles, analysis shows expected mean $\text{RMS} < 0.1 \lambda$ in 95% of the simulated systems. Values of $\text{PV} < 0.5 \lambda$ are found in 84% of the systems, increasing to 97% at $\text{PV} < 0.6 \lambda$. With respect to the compensation mechanisms, this analysis also provides the required distances over which compensation is expected. The found standard deviations correspond to $\pm 28 \mu\text{m}$, $\pm 64 \mu\text{m}$, $\pm 520 \mu\text{m}$ and $\pm 174 \mu\text{m}$ of compensations at the doublet, lens four, camera optics mount to SHS and camera optics mount to detector, respectively. Lateral compensation of the doublet yields standard deviations of $\pm 20 \mu\text{m}$ in both directions.

3.7 Low Pressure Compensation of Optics

Up to now, all considerations are made for a vacuum environment. However, the optics are assembled under ambient conditions involving a much higher ambient pressure of 1013 hPa when compared to a space environment. This pressure difference causes a de-focusing of the front and camera optics due to the non-unity refractive index of the enclosed air volumes between all lenses which effectively changes the optics focal length when compared to later operation under vacuum. Therefore, a mechanism is implemented within the instrument optics which allows to compensate the focal plane shift between ambient pressure and vacuum by additional shift of front optics lens four. The estimations to identify a proper compensator and corresponding performance degradations are discussed here.

Based on simulations of the front and camera optics, differences of their focal lengths are estimated under ambient pressure and in vacuum. Each optics is separately setup in an ambient environment at a pressure level of 1013 hPa. In case of the front optics, the incident fields are chosen with respect to the overall instrument FOV and, with respect to the camera optics, are restricted to the finite object height of the illuminated grating area. The focal plane position is adjusted minimizing the RMS wavefront error. Free apertures as designed for the combined optical system are retained. A multi-configuration is implemented which allows to compare the focal plane positions in dependence on varying ambient pressures. The difference in effective focal lengths is estimated at $\Delta f_{eff} = -23.9$ mm and $\Delta f_{eff} = +0.3$ mm when changing the ambient pressure from $p = 1013$ hPa down to $p = 0$ hPa for the front and camera optics, respectively. These changes correspond to a relative change of 3.8 % and 0.3 % when compared to their absolute effective focal lengths indicating a much stronger pressure dependence within the front optics. Since the estimation of the effective focal length changes does not provide a proper measure of performance degradation, the expected contrast changes are estimated in terms of the modulation transfer function. In case of the front optics, the MTF is evaluated at a spatial frequency of 4.2 mm^{-1} which corresponds to the desired 40 altitude layers commonly utilised in the foreseen atmospheric retrieval model. In case of the camera optics, the largest interferogram fringe frequency of 8.9 mm^{-1} as seen by the detector array at $\lambda = 759.5$ nm and including the camera optics magnification is utilised. A total of three field points is selected for the evaluation centred on-axis, off-axis at the maximum field coordinate in horizontal direction and off-axis at one FOV corner. The corresponding MTF values are listed in Table 3.3 which distinguishes between MTF values at ambient and vacuum environments.

As expected, the front optics is prone to the largest performance degradation. The almost zero MTF values in a vacuum environment without inclusion of compensation indicate that proper imaging of the atmospheric scenery and subsequent retrieval of altitude profiles at desired altitude resolution of 1.5 km would no longer be possible. Conveniently, the already existing compensator at lens four allows to introduce a focal length correction which fully corrects this front optics performance degradation. After shifting lens four away from the SHS by $\Delta = -0.1$ mm, the nominal performance is expected to be restored under vacuum up to MTF rounding errors of ± 0.1 %. The designed rotation compensation of lens four is 36° which allows for an uncertainty of $\pm 7.2^\circ$ to keep the MTF above 50 %. This evaluation assumes a thread pitch of 1 mm per revolution.

The camera imaging capabilities are slightly degraded when changing from an ambient into vacuum environment. A relative change of contrast between 5 % and 10 % is expected when no compensation is considered. Note that an improved performance is expected on-axis despite the overall drop of the MTF towards off-axis field points. Including a shift of the detector array by $\Delta = -0.034$ mm towards the camera optics last lens may reduce the degradation to a relative change of up to 2 %. However, precisely introducing such a small mechanical displacement is not possible with the current mechanical design as pointed out in section 5.1. Thus, a vacuum compensation of the camera optics focal shift is omitted but following a few restrictions are presented concerning the camera optics locking mechanism during integration.

Finally, the MTF evaluation is repeated for the complete optical system including the front and camera optics along the SHS. The same three field points at a

Table 3.3: AtmoLITE optics performance under vacuum. MTF values are evaluated at three different field coordinates given in the normalized field coordinate system (Hx, Hy). Systems are optimized at ambient conditions and evaluated at vacuum with and without an additional focal plane adjustment. This is indicated by f_{eff} adjusted = YES or No. The frequencies of evaluation are 4.2 mm^{-1} , 8.9 mm^{-1} and 8.9 mm^{-1} corresponding to front, camera and combined system optics.

p f_{eff} adjusted Hx, Hy	1013 [hPa]			0 [hPa]			0 [hPa]		
	YES			NO			YES		
	(0, 0)	(0, 1)	(1, 1)	(0, 0)	(0, 1)	(1, 1)	(0, 0)	(0, 1)	(1, 1)
front optics									
MTF [%]	81.6	94.2	86.5	2.5	6.9	8.5	81.5	94.2	86.6
camera optics									
MTF [%]	74.4	92.7	51.5	78.8	91.3	45.5	74.1	92.7	50.8
full system									
MTF [%]	95.3	94.9	94.3	0.1	1.3	2.4	95.2	94.8	94.5

spatial frequency of 8.9 mm^{-1} are considered. The resulting MTF values are in agreement after compensation up to the mentioned rounding error of $\pm 0.1 \%$ which indicates the compensation in the front optics is sufficient to compensate the overall imaging performance as well as the imaging of the atmospheric scenery onto the virtual localisation plane.

3.8 Tolerances of the camera optics locking mechanism

Omitting the camera optics focal length adjustment when exposed to a vacuum environment, raises the question whether tight tolerances of the camera optics locking mechanism are beneficial with respect to the alignment procedure. Similar to the analysis performed in section 3.7, three configurations of the camera optics are tested. At first, the full system is setup and optimized in an air environment corresponding to the environment expected during assembly and alignment. Next, two additional configurations are defined under vacuum with the detector optics locking mechanisms introducing an additional shift of either $\pm 36 \mu\text{m}$ or $\pm 93 \mu\text{m}$ between SHS, camera optics mount and detector array and along the optical axis. These two tolerances are based on manufacturing capabilities available at the inhouse workshop of ZEA-1 of the Research Centre Jülich at the time of analysis. Without further focal length adjustments, the small shift of $\pm 36 \mu\text{m}$ yields an expected change in camera optics MTF of less than $< 3\%$ under vacuum and negligible change of overall performance. Contrary, allowing a shift of $\pm 93 \mu\text{m}$ yields an especially strong MTF decrease on-axis with respect to the camera optics MTF which is expected to degrade visibility significantly by up to -16.2% . Thus, the tighter locking mechanism tolerance is recommended for the mechanics in order to retain high visibility under vacuum. Overall system MTF is less impacted by the choice of tolerance of the camera optics locking mechanism. Largest degradation by up to -5% is expected at the off-axis field point $H_y = 1.0$ which does not reduce overall system MTF below the required 80% (RO.06), thus, is negligible. All simulation results are summarized in Table 3.4.

3.9 SHS optimization within the full optical system

The SHS baseline design is derived based on Equation 2.20, Equation 2.21 and Equation 2.22 and the considerations described in section 2.3. However, final

Table 3.4: AtmoLITE optics performance under vacuum including camera optics lens locking. MTF values are evaluated at three different field coordinates given in tuples of the ZEMAX normalized field coordinate system (Hx, Hy). Systems are optimized at ambient conditions and evaluated at vacuum including the vacuum compensation. The spatial frequency of evaluation is 8.9 mm^{-1} and computed MTF values are given for the two different tolerance classes of locking mechanisms.

p	1013 [hPa]			0 [hPa]			0 [hPa]		
f_{eff} adjusted	YES			NO			NO		
ΔLock	0 [μm]			36 [μm]			93 [μm]		
Hx, Hy	(0, 0)	(0, 1)	(1, 1)	(0, 0)	(0, 1)	(1, 1)	(0, 0)	(0, 1)	(1, 1)
camera optics									
MTF [%]	74.4	92.7	51.5	71.6	93.1	53.5	58.2	92.9	65.8
full system									
MTF [%]	95.3	94.9	94.3	95.2	95.0	94.9	92.3	90.9	92.3

optimization of the optical system requires simultaneous adjustments of front, camera and SHS parameters which requires merit function operands comparable to expected interferogram visibility. Coupling the interferogram simulation and the optimization algorithm in ZEMAX Optical Studio would yield the ideal solution, but increases computation time by an unreasonable large amount. In addition, purely relying on evaluation and minimization of wavefront aberrations at the system's focal plane neglects the asymmetry between both SHS arms, in particular, a shift between the two images of the individual SHS arms is not considered.

Fortunately, this shift is directly related to the interferogram fringe visibility and can be evaluated based on ZEMAX merit function operands as follows. Assume converging wavefronts propagating the SHS at a small angle of incidence. Split-up at the beam splitter, each wavefront passes the FWP at a different thickness, thus, converges at different positions relative to the grating center due to the non-telecentric front optics layout. Consequently, the images of the individual SHS arms obtained after dispersion at the grating and propagation through the camera optics appear shifted. Taking into account that waves converge to a focus of finite size, the PSF, a portion of both wavefronts still overlaps which causes either constructive or destructive interference based on their respective phase differences within the overlapping area. The ratio of the overlapping area and the spot size formed by each individual wavefront is now interpreted as a direct measure of interferogram fringe visibility whereby the non-modulated contribution is equal to the non-overlapping area. Thus, in order to maximize the interferogram visibility, either this ratio has to be at a maximum or the distance between the centroid of both images has to be at a minimum. The latter one is easily accessible by

merit function operands and used in the final optimization of AtmoLITE. Values of achieved minimal centroid displacements and evaluated at four different field positions are presented in Table 3.5. Moreover, the ratio between overlapping area and the geometric spot size is found to be a good proxy of interferogram fringe visibility. Compared to the simulations presented in section 3.5, the ratios are within ± 8 % of simulated visibility at a wavelength of $\lambda = 759.83$ nm, whereby ratios tend to underestimate visibility near the FOV centre and yield values above simulated visibility near the FOV edge. These differences are caused by the non-circular shape of the AtmoLITE spot size where coma and astigmatism cause an increasingly asymmetric spot shape towards the edges. For reference, spot sizes at nine different field points are appended in Figure A.1.

Table 3.5: Spot sizes and centroid mismatch after final optimization of AtmoLITE. Evaluated are four field points at the wavelength of $\lambda = 759.83$ nm. Based on the geometric spot size r_{geo} and the distance between the centroid positions of both SHS arms Δ_{centroid} , the area ratio overlapping between both spots to the individual arm spot size is estimated.

H_x	H_y	r_{geo} [μm]	Δ_{centroid} [μm]	A_{overlap} [μm^2]	ratio to spot size [%]
0.0	0.0	2.539	1.582	0.012	61.0
0.0	1.0	6.377	0.227	0.125	97.7
1.0	0.0	5.815	0.572	0.099	93.7
1.0	1.0	8.523	0.215	0.192	84.0

3.10 Expected O₂ A-band Radiances In-Orbit

A significant contribution to the overall temperature retrieval uncertainty is the signal-to-noise ratio on the detector currently limited by shot-noise. Therefore, an estimation is made of the expected O₂ A-band radiances as seen by the AtmoSHINE and AtmoLITE instruments. Afterwards, corresponding signal levels on the detector array are derived in dependence of observation altitude. The result is later used in section 5.4 to derive the temperature retrieval uncertainty of the AtmoLITE EM prototype based on measured instrumental line shapes.

The observed atmospheric scene is shown in Figure 3.22 as the projected detector area within the nominal field of view. Based on the different satellite orbit altitudes, the limb LOS increases from 2600 km up to 3600 km, thus, the expected scene width varies between 59.0 km and 81.6 km. In this configuration the solid angle Ω_{FOV} within the FOV is defined by the base of the volume enclosed between the instrument's entrance aperture and the observed scene. This is indicated by the red-framed pyramid. The collecting area $A_{aperture}$ is the full entrance aperture of the instrument perpendicular to the observed scene. Thus, the etendue E can be expressed as product of solid angle and entrance aperture area 3.6.

$$E = \Omega_{FOV} \times A_{aperture} \quad (3.6)$$

By design, the instrument's aperture stop is the free aperture at the first lens element of the instrument optics. It is estimated as the enclosed area of a circle which yields $A_{aperture} = 34.2 \text{ cm}^2$ and $A_{aperture} = 44.2 \text{ cm}^2$ for the AtmoSHINE and AtmoLITE optics, respectively. The solid angle Ω_{FOV} is analytically calculated based on Equation 3.7. The detailed derivation for the solid angle of a tetrahedron is given in Van Oosterom and Strackee [1983] which is used by Gossman et al. [2010] to derive an expression for pyramidally shaped solid angles. The pyramid base width a and height b are described geometrically by considering the tangent along the observer-scene distance d . Thus, a and b directly correspond to aforementioned width and height of the observed scene.

$$\begin{aligned} \Omega_{FOV} &= 4 \arcsin \left[a * b / [(d^2 + a^2) * (d^2 + b^2)]^{1/2} \right] \\ &= 0.00051 \text{ sr} \end{aligned} \quad (3.7)$$

Substituting Equation 3.7 into Equation 3.6 yields the nominal etendue of the satellite instruments which evaluates to $E = 0.018 \text{ cm}^2 \text{ sr}$ and $E = 0.023 \text{ cm}^2 \text{ sr}$ for AtmoSHINE and AtmoLITE, respectively. Similar values are obtained based on the numerical aperture in image space NA. In this case, the solid angle is defined

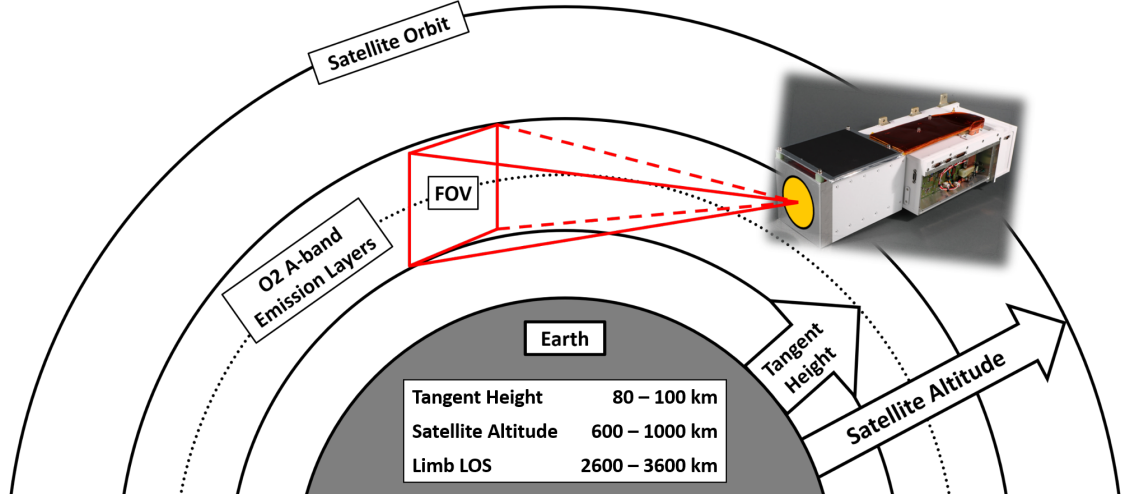


Figure 3.22: Limb viewing geometry of the AtmoSHINE and AtmoLITE missions. The nominal detector area corresponding to the full FOV is projected onto the atmospheric scene (red frame). Radiance estimations are considered over the circular instrument entrance aperture (yellow patch). The scene to observer distance (Limb LOS) changes in dependence on satellite altitude which causes a variable observed scene width and height between 59.0 km and 81.6 km.

by the cone of rays over the full aperture which illuminates the detector array at each field point. Thus, the solid angle is the integral over the surface element in spherical coordinates given by Equation 3.8.

$$\begin{aligned}
 \Omega_{\text{NA}} &= \int_0^{2\pi} d\phi \int_0^{\arcsin \text{NA}} \sin \theta \, d\theta \\
 &= 2\pi [1 - \cos(\arcsin(\text{NA}))] \\
 &= 4\pi \sin^2[0.5 * \arcsin(\text{NA})]
 \end{aligned} \tag{3.8}$$

Combining Equation 3.6 and 3.8 yields the etendue E_{NA} based on the image space numerical aperture which tends to be 6 % larger than the estimation based on FOV. The deviation is caused by the paraxial approximation utilised to estimate the numerical aperture. Values are given for the AtmoSHINE and AtmoLITE instruments separately in Equation 3.9 as the image sizes and numerical apertures in image space differ between both systems.

$$\begin{aligned}
 E_{\text{NA}} &= \Omega_{\text{NA}} * A_{\text{image}} \\
 E_{\text{NA, AtmoSHINE}} &= 0.126 \text{ sr} * 0.3953^2 \text{ cm}^2 \\
 &= 0.019 \text{ cm}^2 \text{ sr} \\
 E_{\text{NA, AtmoLITE}} &= 0.027 \text{ sr} * 0.9472^2 \text{ cm}^2 \\
 &= 0.024 \text{ cm}^2 \text{ sr}
 \end{aligned} \tag{3.9}$$

Next, in order to assess the expected O₂ A-band radiances in-orbit, two datasets are utilised. The first dataset consists of typical measured OSIRIS spectra during daytime observations. This dataset provides O₂ A-band spectra between 7 km and 110 km altitude at a spectral resolution of 1 nm [McLinden et al., 2012]. In addition, the spectra are already provided in terms of radiance $L_{\text{O}_2 \text{ A-band}}$. The second dataset is based on O₂ A-band simulations introduced in section 2.1. It provides the spectral radiance integrated along the LOS and was estimated for an orbit altitude of 600 km. The spectral radiance is calculated at single wavenumbers and convolved with a perfect Gaussian line-shape to simulate the nominal resolving power of $R = 9000$ of the AtmoLITE instrument. An overview of the two datasets is shown in Figure 3.23 which distinguishes the expected radiances by altitude.

In order to estimate the expected intensity I_{CMOS} expressed in photons per second at the detector array, the instrument's etendue E , the optical transmission T_{optics} and the interference filter are considered. The optical transmission is mostly limited by the beam splitter cube where effectively 50 % of the photons are back-reflected to the entrance aperture. In addition, typical silver-coated diffraction gratings have about 70 % efficiency in first order which results in another 30 % loss of photons [Edmund Optics, 2022a]. Further, each lens and prism surface is coated with an anti-reflective multi-layer coating to minimize transmission losses due to surface reflections. The corresponding worst-case effective transmission is 88.7 % based on the $R < 0.5$ % coating specification. Therefore, the minimum overall optical transmission is 31 % of the incoming photons. The interference filter mounted in front of the optics limits the wavelength range seen by the instrument. Its design differs between AtmoSHINE and AtmoLITE due to the extended bandpass of the latter system. At the time of writing, only the theoretical transmission curve is available for the AtmoLITE filter whereas the measured profile is utilised for the AtmoSHINE instrument. Both filter curves used in this work are shown in Figure 3.23. The expected intensity is now estimated as product of spectral radiance, etendue, optical and filter transmission T_{filter} and integrated over the full O₂ A-band emission spectrum as indicated in Equation 3.10.

$$I_{\text{CMOS}} [ph/s] = \int_{\lambda} L_{\text{O}_2 \text{ A-band}}(\lambda) * E * T_{\text{optics}} * T_{\text{filter}}(\lambda) d\lambda \quad (3.10)$$

The calculation is performed at each altitude layer individually while assuming a constant layer extent of 0.0325° as seen by the instrument. This corresponds to a division of the full FOV into 40 equally spaced altitude layers. Resulting profiles are presented in the bottom row of Figure 3.23. The main difference between the measured OSIRIS spectra and simulation results is apparent around an altitude of

70 km. Here, the neglected self-absorption of the O₂ A-band emission along the LOS yields a higher intensity by at least 50 % in the simulation. Thus, the following estimations are based on the measured OSIRIS spectra to provide the minimum number of photons expected in preparation of later SNR analysis.

Based on the angular extent of the considered altitude layers, the number of illuminated detector pixel may be estimated. By design, the AtmoSHINE instrument relies on the HWK1910 sensor whereas the AtmoLITE optics is compatible to either the HWK1910 or GSENSE440Bsi sensors. The main difference between those detectors is the pixel pitch of 5.4 μm of the HWK1910 and 11 μm of the GSENSE440Bsi. In addition, the area illuminated A_{illu} by aforementioned angular extent differs between both instruments. It is therefore necessary to scale the intensity at the detector to individual pixel before further S/N considerations may be made. The direct comparison is provided in Table 3.6 which is used in section 5.4 to relate the AtmoLITE temperature retrieval uncertainty to SNR.

Table 3.6: Expected in-orbit flux per detector pixel. Values are derived based on OSIRIS spectrograph daytime measurements at an altitude of 87 km. The layer thickness assumed here is 1.5 km in limb viewing geometry.

	unit	AtmoSHINE	AtmoLITE	
detector		HWK1910	HWK1910	GSENSE440Bsi
A_{illu} , full FOV	[cm ²]	0.3953 ²	0.9472 ²	
N_{pixel} , full FOV	—	784 ²	1754 ²	861 ²
A_{illu} , one layer	[cm ²]	0.0099 * 0.3953	0.0237 * 0.9472	
N_{pixel} , one layer	—	19 * 732	44 * 1754	22 * 861
I_{CMOS}	[ph/s/pixel]	216	91	370

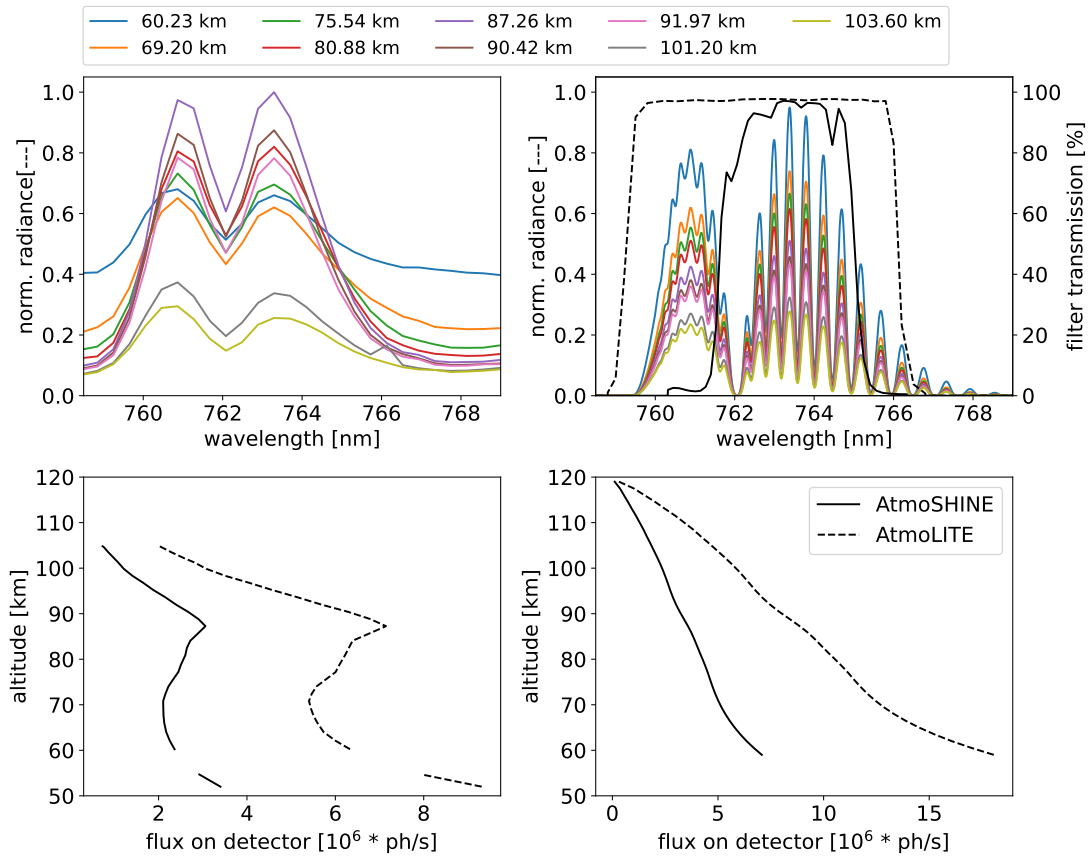


Figure 3.23: Simulated O₂ A-band radiance as seen by the satellite instrument. Estimated radiance data is shown based on measured OSIRIS spectra (top-left) and simulated O₂ A-band volume emission rates integrated along the expected LOS (top-right). Shown values are normalised to the radiance at 87.26 km. The corresponding total intensity is calculated at each altitude by integration over the full bandpass filter range (bottom). Bandpass filter transmission data is given based on measured profiles for the AtmoSHINE instrument and the designed bandpass of AtmoLITE. The modelled radiance data does not account for self-absorption along the LOS, thus, radiances below an altitude of 80 km are overestimated by at least 50 %.

Summary of instrument optics design

This chapter discussed the design changes which advanced the AtmoSHINE instrument towards the AtmoLITE instrument. Starting with the assessment of AtmoSHINE imaging performance, the mathematical framework of point-spread and modulation transfer function evaluation was demonstrated on measured wavefront aberration data. It was shown that this kind of evaluation is suitable for the instruments front optics, but rather limited for evaluation of the camera optics. Further, the stray light problem of AtmoSHINE due to double reflections within the optics was discussed which was the initial starting point towards the new AtmoLITE optical design.

Regarding the new AtmoLITE optical design adaptation to the new AtmoLITE SHS, compensation mechanisms in the front and camera optics to compensate manufacturing tolerances, and changes of effective focal length when the instrument is moved from environments at ambient pressure to vacuum were discussed. Most importantly, the analysis of the combined optical system of AtmoLITE optics and AtmoLITE SHS was extended to include simulations of the expected interferograms. The quantity of interest was the interferogram fringe visibility which is seen as a direct measure of instrument performance regarding temperature retrieval uncertainty. It was demonstrated that interferogram fringe visibility larger than $V > 50 \%$ is expected for all operational conditions of the instrument if the compensation mechanisms are properly applied. In preparation of the temperature retrieval uncertainty estimation of AtmoLITE following in chapter 5, the expected radiance levels of the O₂ A-band airglow as observed by AtmoLITE have been estimated as well.

4

The AtmoLITE Calibration Unit

Contents

4.1	AtmoLITE Calibration Unit - Design Concept	93
4.2	AtmoLITE Calibration Unit - Requirements	95
4.3	AtmoLITE Calibration Unit - Optical Design	100
4.4	AtmoLITE Calibration Unit - Mechanical Design	103
4.5	AtmoLITE Calibration Unit - Alignment	105
4.6	Verification of the ACU prototype(s)	119
4.7	Impact of a ACU non-uniformity on visibility	132

Calibration setups of SHS based optical systems have rarely been discussed in literature and approaches differ quite a lot. A first calibration setup based on a plane emitting source and an adjacent telescope which creates an image virtually at infinity when viewed by the SHS instrument was explored by Laubscher et al. [1999], Milligan et al. [1999] and Smith et al. [1999b]. Later studies by Patel [2012] and Langille et al. [2019b] relied on observation of a lambertian plane diffuser or integration spheres without additional optics between calibration source and SHS instrument, although the instruments under test featured imaging optics focused at infinity. Studies of non-imaging SHS instruments report about collimated point sources which are build up by a fibre and adjacent collimator [Waldron et al., 2020; Arellano et al., 2022; Foster et al., 2022]. The most ambitious calibration strategy was setup for the MIGHTI instrument which included an integrating sphere attached to a step-scanning Michelson interferometer. This setup allowed to derive pixel-to-pixel and spectral variations across the full image simultaneously Englert et al. [2017]. In all of these studies, evaluation of the measured interferograms

assumes the observed source to be uniform in angular extent and uniform in aperture illumination. Theoretical studies of SHS calibration rely on these assumptions as well [Englert et al., 2004; Englert and Harlander, 2006b; Perkins et al., 2013], and express the governing interferogram equation Equation 4.1 neglecting spatial modulation of the source which was first formulated by Harlander [1990]. The great advantage of these assumptions is the direct traceability with respect to spectral radiance [Englert et al., 2010, 2017]. Note that the main target of all SHS calibration approaches is to measure the relative systems response to different source intensities (linearity) and to derive a pixel-to-pixel matrix of relative spectral response (uniformity), in particular, if an absolute calibration expressed in units of radiance is not required. In addition, first efforts were made to compare spectra obtained by a conventional Bruker spectrometer and the SHIMCAD SHS instrument while observing the same source [Babcock, 2009]. Although qualitative agreement was demonstrated, a quantitative comparison was not possible due to different beam geometries and sample orientations of both setups.

In view of the AtmoLITE calibration, a dependence on source uniformity for the instrument discussed in the present study is expected. It is therefore suggested to include expected spatial modulation of the source in the interferogram description which yields Equation 4.1, and to setup a characterised calibration source with known uniformities accordingly. Note that Equation 4.1 already includes a separate description of the individual arm transmissions $t_{A|B}$ which is commonly referred to as the flat-field portion of the interferogram [Englert and Harlander, 2006b]. The phase distortion term $\Phi(x, \nu)$ allows to describe interferograms in all practical applications without the need of first order approximations used in Equation 2.19 [Englert et al., 2004]. In general, phase distortions are caused by refractive index non-uniformities of the FWP and beam splitter, imperfections of the grating surface or contamination and by the imaging quality of optics adjacent to the SHS, e.g. image distortion introduced by the camera optics, thus, need to be characterised for each individual SHS instrument.

$$I(x) = B(x, \nu) * (t_A^2 + t_B^2 + 2t_A t_B \cdot \cos(2\pi\nu x + \Phi(x, \nu))) \quad (4.1)$$

In the following, development of a setup with known source uniformity and suitable for the calibration of the AtmoLITE instrument is discussed. Design requirements and optical layout are covered in section 4.2 and section 4.3. Demonstration of a breadboard prototype is presented in section 4.5 and experimental verification of the as-build source uniformity follows in section 4.6. The first experimental results of the combined system of the developed calibration setup and the AtmoLITE

instrument are discussed later in chapter chapter 5. This further includes guidelines on how to proceed with the project as some experiments and verifications had to be delayed beyond the work presented here due to COVID-19.

4.1 **AtmoLITE Calibration Unit - Design Concept**

Development of the instrument visibility calibration concept involving the ACU was first started prior to the AtmoSHINE in-orbit demonstration. Its main purpose was to build a light stimulus similar to the nominal atmospheric scene observed by the instrument. The desired benefit compared to commonly used single axis collimation setups [e.g. Zettner et al., 2020], was a more deliberate control of the illumination distribution over different field angles and the entrance aperture. In particular, a device was required which could provide a uniform illumination during SHS assembly, wavelength calibration and flat-field estimations. However, two iterations of the ACU had to be developed before all design and performance requirements were identified and the final ACU alignment and characterisation strategy was developed. A schematic overview of those two designs is given in Figure 4.1.

The first iteration focused on a sharply defined intensity drop of the illumination source in angular space. The main purpose of such a top-hat illumination profile is to illuminate the instrument only within its FOV. Thereby, calibration data can be obtained without contributions of out-of-field radiation and, in particular, stray light contributions due to out-of-field sources can be separated from in-field data. A property that is not obtainable when relying on integration spheres only. The top-hat illumination profile was achieved by combination of a Koehler illumination system with a plane diffuser and adjacent collimation optics. Starting from the source, a tunable laser source was coupled into the setup. The spatial coherence of the laser source was broken up by refocusing the laser source onto a rotating ground glass diffuser [Stangner et al., 2017]. This setup suppressed and allowed to neglect the visible speckle observed during previous calibrations of the AtmoSHINE prototypes. Afterwards, a Koehler illumination setup consisting of two micro-lens arrays, collimation and collector optics was utilised to produce a rectangular top-hat illumination profile on the second ground glass diffuser. This was achieved by splitting the initial collimated beam into multiple divergent beamlets and overlapping them in a common plane. This transformed the initial Gaussian beam profile into a flat top-hat with sharply defined edges. The theoretical description of a general Koehler illumination setup is given by Voelkel and Weible

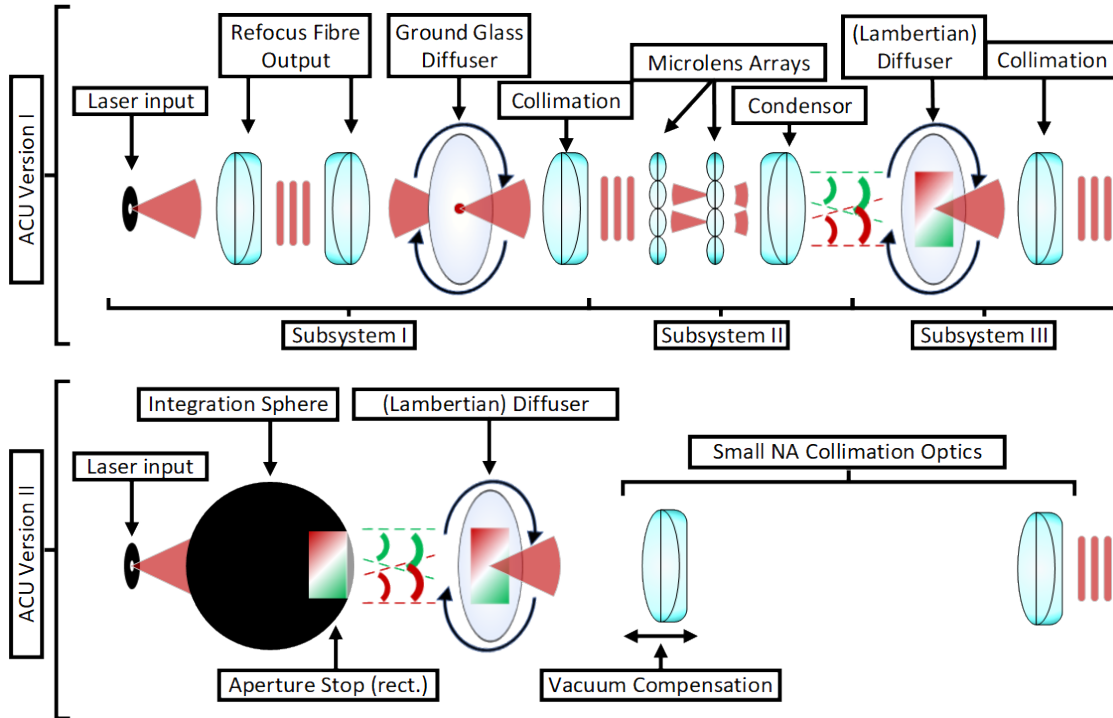


Figure 4.1: Conceptual design of the ACU. Starting from the source, each setup contained a tuneable laser source which was coupled via a fibre port into the system. Whereas the first version utilised two subsystems in order to reduce speckle noise and form a rectangular light stimulus on the last diffuser, the second version relied on a single integration sphere in close proximity to the diffuser. The saved space was taken up by a long focal length/ small NA collimation optics in the second version which allowed to include a vacuum compensator as well.

[2008] and simulations of the expected light stimulus' flatness were first published in Kaufmann et al. [2019]. A first experimental implementation utilised in the first ACU iteration was developed in the master thesis of Krichel [2019]. Finally, the adjacent collimation optics after the second diffuser were utilised to transform the now spatially rectangular light source into the desired angular field light stimulus matching the nominal FOV of the AtmoSHINE instrument.

Unfortunately, envisaged opal white glass diffusers turned out to be impractical during the ACU alignment processes as the shearogram measurement used to evaluate proper diffuser alignment yielded no fringe contrast. More precisely, the volumetric scattering of the opal white glass diffuser enlarged the transmitted focus size such that the shearogram contrast vanished. Instead, the fall back solution involving standard ground glass diffusers had to be utilised. Details of the alignment procedure and its evaluation follow in section 4.5. Consequently, the first ACU iteration could not provide a homogeneous aperture illumination but produced a sharp peak in illumination at the aperture centre. This sharp peak was caused by

the narrow scattering profiles of non-lambertian diffusers combined with a high numerical aperture/ short focal length optics. These optics effectively project the scattering profile subtended by the numerical aperture onto the exit aperture of the ACU, hence, more narrow profiles yielded a stronger drop in aperture illumination. In section 4.7 the impact of non-uniform aperture illumination on interferogram fringe visibility expected with AtmoLITE in front of the calibration source will be quantitatively investigated. Up-front, only the general result that measured interferogram fringe visibility is expected to increase if less than the full aperture is uniformly illuminated is used to motivate the design of a second ACU. In addition, the experimental Koehler illumination setup combined with the collimation optics yielded modulations across the light stimulus not seen in simulations and preliminary tests done by Krichel [2019]. These modulations were identified as potential source of uncertainty for the final instrument calibration.

Thus, a second ACU is designed as described in the following, in order to tackle the aforementioned problems and the corresponding design and performance requirements described in section 4.2 are updated. The new design includes two major changes. At first, the de-speckle and Koehler illumination setup are replaced by a single integration sphere. By placing the integration sphere in close proximity to a rotating diffuser and putting a rectangular aperture stop at the sphere's exit port, the spatially rectangular light stimulus is preserved. The new setup allows to adjust the top-hat illumination profile width more easily, as well, as it is only dependent on the aperture stop size placed at the exit port of the integration sphere. Continuous rotation of this diffuser preserves the de-speckling characteristic of the ACU. Secondly, the numerical aperture of the adjacent collimation optics is reduced to decrease the illumination drop across the aperture. Details about this design are presented in section 4.3 and the first experimental verification results are discussed in section 4.4 and section 4.6.

4.2 AtmoLITE Calibration Unit - Requirements

The ACU design is driven by two main considerations. At first, a light stimulus is required which closely resembles the atmospheric scene confined to the full instrument FOV, in particular provides uniform illumination within the instrument FOV and includes a sharp intensity drop down to zero near the transition of in-field to out-of-field observation. The sharp drop between in-field and out-of-field observation angles is expected to allow later stray light investigations to derive a separate impact of in-field and out-of-field stray light contributions to measured

interferogram fringe visibility. Thus, the designed angular coverage requires at least $\pm 0.7^\circ$ in angular field coordinates and the operational wavelength range shall be between 758 nm and 770 nm, exceeding the nominal instrument specifications and bandpass in both cases. In addition, the visibility simulations discussed in chapter 3 suggest that wavefront aberrations of the ACU have to be similar or smaller compared to the instruments wavefront aberrations as the simulated contrast is directly dependent on the incident wavefront quality. Moreover, wavefront RMS is seen as a critical component as well and shall be minimized by design.

At the time of starting the ACU design, only the interferogram simulation for the full AtmoLITE optical system is available to evaluate required performance of the calibration device in-front of the AtmoLITE instrument and its impact on interferogram fringe visibility. Hence, a test is made whether curvature of the assumed incident plane waves causes a change of simulated interferogram fringe visibility. The result of this test simulation is shown in Figure 4.2. It is apparent that at wavefront curvatures greater 1 km no change in interferogram fringe visibility is obtained. This corresponds to a wavefront PV and RMS allowed for the ACU of 0.76λ and 0.10λ , respectively, which is used as the baseline requirement for the ACU design. The strong drop in visibility occurring at smaller source-to-instrument distances indicates the current limitations of the visibility simulation. It is predominantly caused by the inaccurate mathematical description of the equations discussed in section 3.2 when applied to finite conjugates at source-to-instrument distances of less than 1 km. In particular, the simulation does not consider the overlapping images of multiple source points on the grating before imaging by the camera optics occurs. It is recommended to perform an experimental sensitivity study once the ACU and AtmoLITE instrument are available in order to verify the simulation results and to show how large the interferogram fringe visibility drop is for the as-build system in practice. In the following discussion, the necessary degrees of freedom to perform such study are included within the ACU design but, unfortunately, the experiment could not be conducted so far.

Spatial frequency components due to non-uniformities of the ACU in angular space are required to not exceed a 2.0 % threshold in magnitude relative to the source mean flux. This value is derived from the simulation results presented in Figure 4.3. Any inhomogeneities with a smaller amplitude and a spatial frequency of less than $2.0 \frac{\text{cycles}}{\text{cm}}$ fulfill RC.01 and RC.02 at a maximum expected relative spectral peak intensity change of less than 1.0 %, a necessary criterion to allow temperature retrieval at an uncertainty below $\Delta T = \pm 1.5 \text{ K}$ [Kaufmann et al., 2018]. Non-uniformities at larger spatial frequencies tend to have a negligible influence

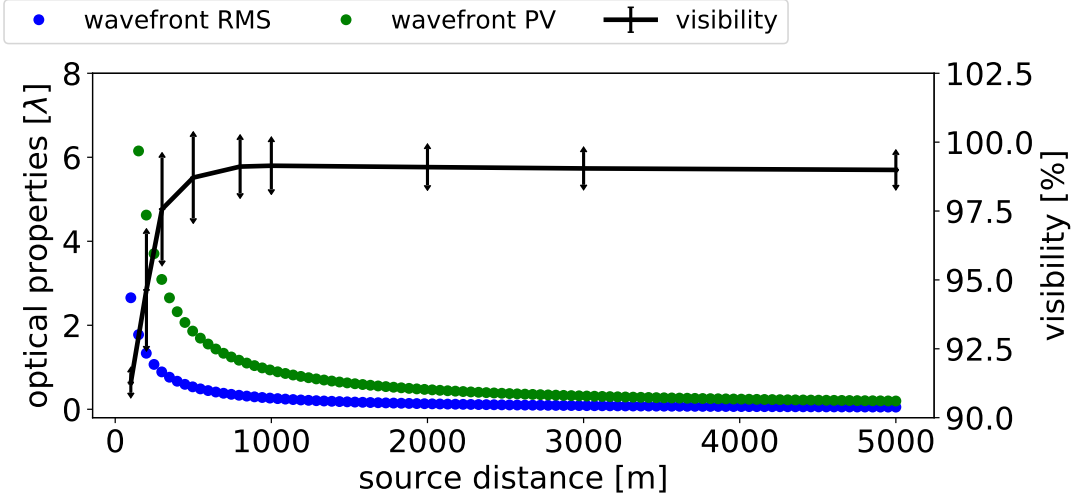


Figure 4.2: Nominal optical performance of the AtmoLITE instrument in dependence of the source-to-instrument distance and corresponding simulated interferogram visibility at 764.74 nm. The wavefront aberrations are generated by placing a perfect point source at finite distances in front of the instrument. Above a source-to-instrument distance of 800 m the interferogram visibility does not show significant variation. Error bars indicate the standard deviation of simulated mean visibility within one interferogram row.

on the recovered spectra. In the simulation, the combined interferogram including the reference signal and inhomogeneity is calculated based on Equation 4.2 where x denotes the detector position, f is the reference fringe frequency corresponding to $\nu = 13120 \text{ cm}^{-1}$ and an amplitude of $A = 1$ is assumed. I_0 describes the modulation of the ACU mean flux and is assumed to be a single frequency cosine with frequency f_{err} and amplitude A_{err} . The amplitude's magnitude is expressed relative to the ACU mean flux.

$$I(f, A, x) = I_0(f_{err}, A_{err}, x) * [1 + A * \cos(2\pi * f * x)] \quad (4.2)$$

Uniform aperture illumination is required to be better than 10 % regarding aforementioned problem of combining a narrow diffuser scattering profile and adjacent collimation optics (RO.05). This requirement is based on a sensitivity study presented later in section 4.7.

The second major design consideration is the necessity to perform the full instrument calibration under space conditions. Therefore, thermal-vacuum tests are taken into account for the instrument at varying instrument temperatures between -30°C to $+30^\circ\text{C}$ and pressures ranging from ambient levels down to less than 1 mbar. However, the ACU can be thermally decoupled from the instrument during such tests. This allows to design the ACU for operation at a single temperature of

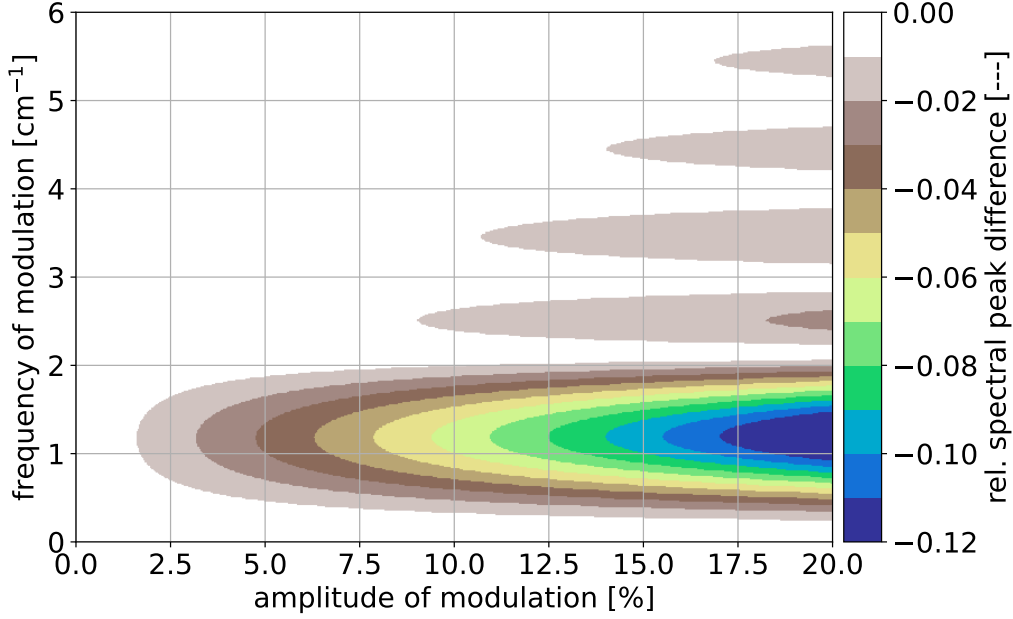


Figure 4.3: Relative spectral peak response to fixed frequency source non-uniformities along the spectral direction. Frequency values are expressed as projected onto the AtmoLITE detector. The estimation is performed at the centre of the O₂ A-band emission at $\nu = 13120 \text{ cm}^{-1}$ corresponding to a reference spatial frequency of 56.3 cm^{-1} . The non-uniformity modulation amplitude is chosen at a percentage level of the mean reference signal.

$T_{\text{ACU, op}} = 20^\circ\text{C}$, reducing design constraints to include a pressure compensation only which involves the shift of optical components and is discussed in section 4.3. The form factor of the full ACU is chosen to not exceed $1400 \times 400 \times 400 \text{ mm}^3$ which was the maximum allowed envelop fitting into available thermal-vacuum chambers alongside the instrument. For ease of transportation and dust protection, all components are required to be integrated inside an aluminium box. For instance, this allows to utilise thermal-vacuum chamber at external testing facilities during ACU characterisation or final instrument calibration. In addition, all optical components and alignment stages are required to be COTS components.

The summary of all requirements is given in Table 4.1. Each requirement is given a separate identifier which are divided into optical, mechanical and calibration requirements. They are sorted by importance within their category starting with the most important once.

Table 4.1: Optical and mechanical design requirements of the AtmoLITE Calibration Unit. Wavefront values are provided at the reference wavelength of $\lambda = 764$ nm.

ID	Type	Value	Unit
RO.01	Wavefront RMS	< 0.10	$[\lambda]$
RO.02	Wavefront PV	< 0.76	$[\lambda]$
RO.03	Clear aperture	75.00	[mm]
RO.04	Field of view coverage	± 0.70	$[\circ]$
RO.05	Aperture uniformity	< 10.0	[%]
RO.06	Uniformity across virtual scene	< 2.00	[%]
RO.07	Operational temperature $T_{ACU, op}$	20	$[\circ C]$
RO.08	Wavelength range covered	758 – 770	[nm]
RM.01	Form factor	$1400 \times 400 \times 400$	$[mm^3]$
RM.02	The system shall be insensitive to transportation.		
RM.03	The system shall be operational under vacuum.		
RM.04	The system shall be made out of COTS components.		
RC.01	Visibility reduction due to ACU	< 1.00	[%]
RC.02	Relative change of instrument line response	< 1.00	[%]

4.3 AtmoLITE Calibration Unit - Optical Design

The second ACU optical design starts with the collimation optics transforming the rectangular light stimulus into an angular illumination field. Given the requirements described in section 4.2 a triplet is chosen as the most simple baseline design that yields sufficient degrees of freedom to balance out spherical aberration and coma, commonly referred to as the two major aberrations in this kind of simple lens systems [cf. Smith, 2007]. In addition, all lenses have to be available in stock. Thus, two low power positive elements with one negative element in between are chosen of plano-convex (PCX) and plano-concav (PCC) type, respectively. N-BK7 and its equivalents are the most common material among stock optics, thus, are chosen as the starting material and kept for the positive elements. Running a global optimization in ZEMAX Optical Studio based on RMS wavefront optimization and limiting the aperture sizes at element two and three to less than 50 mm, the optimal power distribution is found to be 1.0 m^{-1} , -3.3 m^{-1} and 5.0 m^{-1} . Reducing the refractive index of the negative element yields significantly lower wavefront aberrations, thus, the material at element two is changed to fused silica. In the final step, each component is compared to and replaced by available stock lenses based on the lens catalogue provided within Zemax Optical Studio version 19.1. Replacing the third component with an achromatic lens instead of a simple PCX lens reduces aberrations even further during the selection of COTS lenses. The resulting final system layout is given in Figure 4.4 with the lens prescription data summarised in Table 4.2.

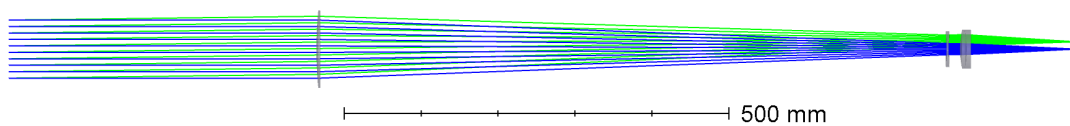


Figure 4.4: ACU optical layout in ZEMAX. The nominal system stop is 400 mm to the left of the first element’s vertex. Displayed are two fields between $+0.0^\circ$ and $+0.7^\circ$ incidence angle at the centre wavelength of 764 nm.

The final system has a nominal rectangular image height of $2 \times 9.48 \text{ mm} = 18.96 \text{ mm}$ at $\pm 0.70^\circ$ field angle. With the entrance aperture being defined by the

Table 4.2: Lens prescription data of finite-infinite AtmoX Calibration Unit optics.

ID	Type	f_{eff}	Material	Part-Nr.	Distributor
L1	PCX	1000 mm	S-BSL7	SLB-100-1000P	OptoSigma
L2	PCC	-300 mm	SILICA	SLSQ-50.8-300N	OptoSigma
L3	ACHR	200 mm	N-LAK22, N-SF6	47319	Edmund Optics

instrument under test, the ACU supports an instrument aperture of up to 75 mm. In addition, the distance between the instrument aperture and the vertex of L1 can lie between 200 mm and 500 mm with the optimized distance at 400 mm. At smaller distances the nominal RMS wavefront error at 758 nm exceeds 0.1λ which violates RO.01. Larger distances start to introduce vignetting of the full aperture which is already more than 1.0 % at a distance of 600 mm which directly impacts aperture and virtual scene uniformity. At small lateral misalignments between the optical axes of ACU and instrument under test of no more than ± 3 mm the nominal wavefront quality is in compliance with the design requirements. Therefore, this ACU design allows for relaxed manual alignment between instrument and ACU LOS in all degrees of freedom.

Evaluation of the wavefront quality of the final system including manufacturing and alignment tolerances as shown in Figure 4.5 yields compliance with RO.01 and RO.02. At first, all elements are assigned manufacturing uncertainties. Given values include uncertainties of surface figures, surface irregularities, centre thicknesses and centering errors stated by the corresponding manufacturers. Further, assumptions are made for element alignment and positioning perpendicular and along a common optical axis. Based on experience with the previous AtmoLITE Calibration Unit iteration, these tolerances are chosen at ± 0.2 mm and $\pm 0.1^\circ$ for lateral misalignment and element tilt, respectively. No tolerances are assumed for the positioning between element one and two and the focal plane adjustment and both distances are utilised as compensation along the optical axis. A compensator between those elements is necessary to offset the large radii uncertainty TM.01 and corresponding wavefront aberrations. The primary criterion of tolerance evaluation is the RMS wavefront across all field angles and wavelengths supported by the ACU. Additional constraints are the total track length (TOTR) of less than $\text{TOTR} < 1400$ mm already keeping in mind the AtmoLITE stray light baffle length, and a limit of the clear apertures at element two and three to $\emptyset < 47$ mm. A complete numerical summary of all tolerances is presented in Table 4.3. In total, two times 1000 Monte-Carlo simulations are conducted for the nominal system and a system with the entrance aperture displaced by +3.0 mm in both lateral directions perpendicular to the optical axis. Evaluation of the two compensators highlights the necessity to allow movement of L1 and the doublet L2 + L3 at a 1σ -level of 5.3 mm and 2.1 mm, respectively.

The vacuum compensation RM.03 is implemented by movement of the combined doublet L2 + L3 along the optical axis. When changed from an air to vacuum environment, this doublet has to be moved by +1.17 mm towards the focal plane to preserve the wavefront quality. In addition, the small numerical aperture $\text{NA} =$

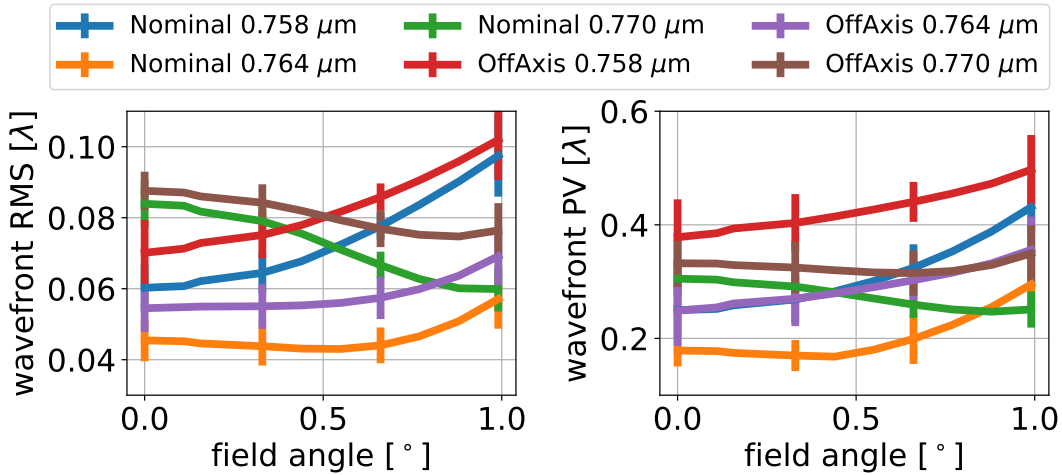


Figure 4.5: Mean RMS and PV wavefront aberrations including the 3σ tolerance budget of the final ACU design. Simulation runs are performed at the two extreme wavelengths and one centre wavelength. The statistical mean values are obtained based on 1000 simulation runs. Two aperture stop positions aligned nominally and shifted diagonally by 4.2 mm from the optical axis are considered.

0.048 is unaffected by a change between an air or vacuum environment and yields the required uniformity of the aperture illumination RO.05 when coupled with a Lambertian type diffuser. However, pre-testing the diffuser alignment process discussed in section 4.4 revealed that Lambertian type diffusers such as opal white glass diffusers and thin Zenith polymer based diffuser foils as provided by Edmund Optics [2022b] and SphereOptics GmbH [2022], respectively, are impractical as no shearograms can be obtained. It is assumed that their volumetric scattering properties broaden the focal point spot size within the diffuser during the alignment process which consequently decreases the shearogram contrast to zero. Therefore,

Table 4.3: Tolerance parameters utilised to verify the AtmoLITE Calibration Unit’s optics in an as-build scenario. Values given by manufacturers are indicated by TM.XX whereas values based on assumptions are marked TA.XX.

ID	Type	Value	Unit	ID	Type	Value	Unit
TM.01	Lens radii	± 1.00	[%]	TA.01	Positioning XYZ	± 0.20	[mm]
TM.02	Lens thickness	± 0.15	[mm]	TA.02	Lens orientation	± 0.10	[°]
TM.03	Lens diameter	-0.20	[mm]				
TM.04	Surface irregularity	± 1.00	[fringe]				
TM.05	Abbe number	± 1.00	[%]				
TM.06	Refractive Index	± 0.05	[%]				
TM.07	Surface centring	± 0.02	[°]				

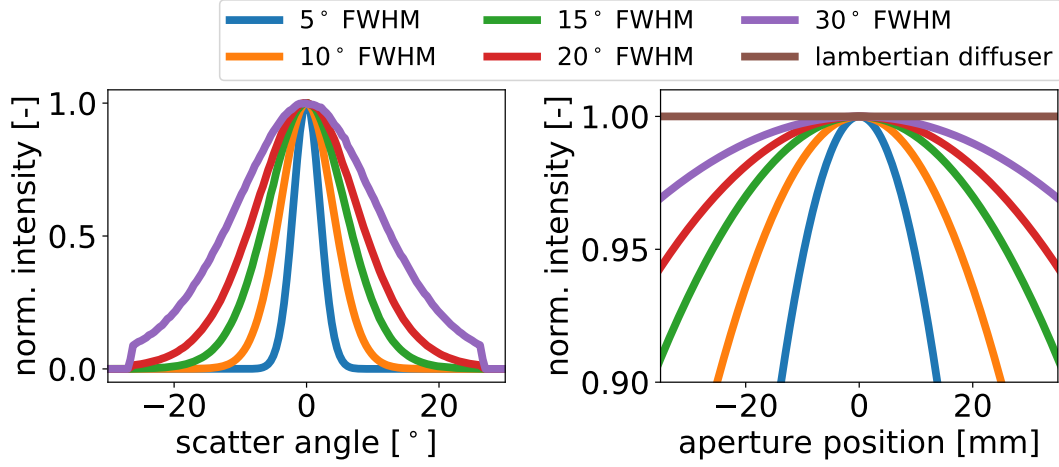


Figure 4.6: Normalised intensities of simulated diffuser scatter profiles (left) and aperture illumination (right). The simulation was conducted at $\lambda = 764$ nm for the on-axis field point at $(0^\circ, 0^\circ)$ field angle. The radiating source area was set to the nominal instrument RMS spot size of $\emptyset = 19$ μm .

ground glass diffusers are considered as an alternative. A ray-tracing simulation in Zemax Optical Studio is setup based on an empirical diffuser model [Ang and Tran, 2020] which allows to simulate different FWHM diffuser scattering patterns. These simulations suggest that commercially available ground glass diffusers with grit sizes between 120 to 220 yield a drop in aperture illumination between 5.6 % and 9.1 %. This is accepted for the first experimental verification discussed in section 4.6 because the simulated impact on measured interferogram fring visibility is in the sub-percent range as pointed out in section 4.7. The simulation results of expected diffuser scatter profiles are visualised in Figure 4.6 whereby the $\text{FWHM} = 20^\circ$ and $\text{FWHM} = 30^\circ$ simulations correspond to the grid sizes of 220 and 120, respectively.

4.4 AtmoLITE Calibration Unit - Mechanical Design

The full ACU including optics, lens mounts, alignment stages and integration sphere is integrated into a large aluminium box. A 3D illustration of this setup is provided in Figure 4.7. On top of its 1.45 m long baseplate four stages are mounted which secure the ACU optics in-place. A low-profile FLS 95 rail system from QIOPTIQ is utilised to mount lens element L1. Centred in a Thorlabs LMR100 metric mount and fixed to a X95 carrier the element L1 can be moved along the optical axis and be

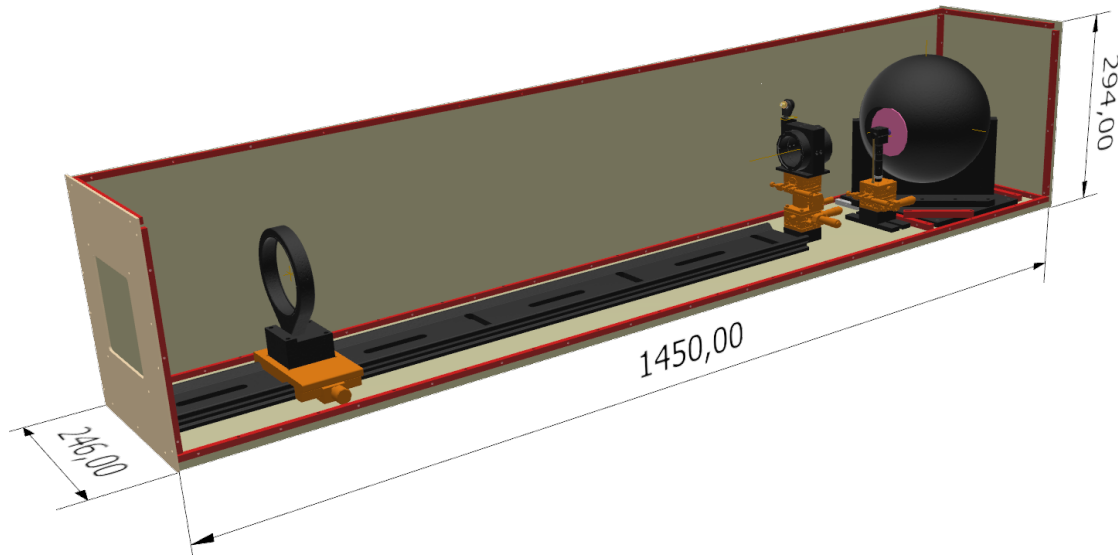


Figure 4.7: CAD illustration of the ACU mechanics without optics. All parts are coloured based on their utility: fixed mounts & integration sphere (black), alignment stages (orange), ground glass diffuser (pink) baseplate and walls (gray) and connecting aluminium bars (red). Lenses are not shown. Additional constructions strengthening and connecting the separated baseplate and side walls are excluded for clarity as well. The scales of the outer envelop are given in millimetres.

secured in its final position. This provides sufficient margin to implement the first compensator mentioned in section 4.3. The doublet L2 + L3 is mounted in a custom made aluminium barrel. The lens seats are each manufactured as tight fits which ensure accurate positioning with respect to TA.01 and TA.02 within the doublet. However, given the surface centring uncertainty TM.07 and the expected lens tilt TA.02 a lateral displacement to a common optical axis is expected between L1 and the doublet by up to 1.4 mm. Compensation of this displacement is achieved by adjustment of the doublet lens barrel on a five-axes alignment stage. The degrees of freedom include rotations around the two axes perpendicular to the optical axis and lateral shifts in XYZ-directions. The five-axes alignment stage is completely build utilising the 40 mm × 40 mm series of manual adjustment stages from OptoSigma, yielding a compact solution and avoiding additional interface plates. In addition, these stages provide a build-in way to secure the doublet lens barrel at the end of the alignment procedure. On top of the double lens barrel a photo diode of type SM05PD3A from Thorlabs is mounted. It allows to monitor the relative laser power change within the ACU during operation due to the direct measurement of the scattered radiation from the ground glass diffuser at a nominal scatter angle of 20°. A third stage is utilised to mount the ground glass diffuser disc. First, the diffuser disc is attached to a Faulhaber S1028 brushless DC motor, whereby a aluminium

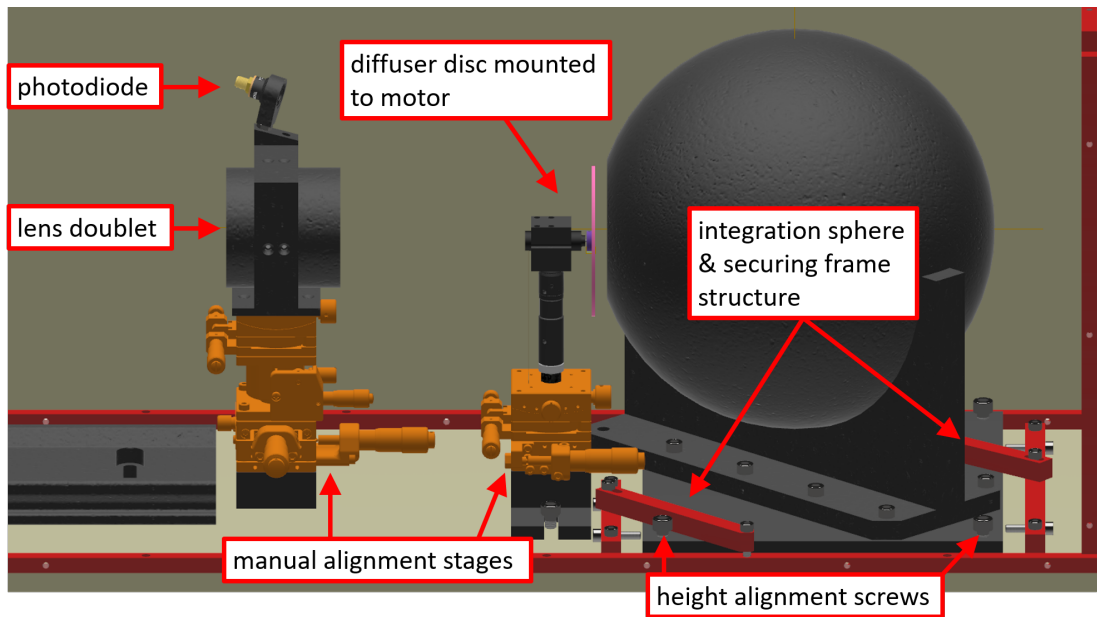


Figure 4.8: Detailed view of the ACU mechanics between lens doublet and integration sphere. All parts are coloured based on their utility: fixed mounts and integration sphere (black), alignment stages (orange), ground glass diffuser (pink) baseplate and walls (gray) and connecting aluminium bars (red).

annulus is glued between the diffuser and the motor shaft as connector. Similar to the doublet lens barrel, the diffuser disc is moveable in five axes. However, only the adjustment along the optical axis and the two rotations are tunable with adjustment screws. The two lateral shifts perpendicular to the optical axis are controlled by shims or by mounting the full assembly stage at different designated positions on the baseplate. Thus, the diffuser disc is selected with a minimum diameter of $\varnothing 75$ mm in order to accommodate the motor mount width, two times the nominal light stimulus width and additional 5 mm adjustment margin. The last stage carries the integration sphere. Mounted on top of an interface plate, the integration sphere's position can be freely moved in X-, Y- and Z-direction which allows precise positioning of the integration sphere's exit aperture towards the diffuser disc. A surrounding frame structure is utilised to secure the integration sphere assembly in place which is shown in Figure 4.8. The laser fibre input port is directly mounted to the integration sphere and no additional coupling optics are necessary.

4.5 AtmoLITE Calibration Unit - Alignment

First alignment of the ACU was done in three major steps separated in optics, diffuser and integration sphere alignment. At first, the lenses were aligned with

the help of a Zygo interferometer and corresponding reference sphere as follows. L1 and the lens doublet were setup in their nominal positions. This part of the ACU was moved in front of the Zygo interferometer which was setup for testing an infinite-finite conjugate setup as shown in Figure 4.9. The Zygo interferometer was switched on and set into the coarse alignment mode. Blocking the reference sphere and lens doublet with a sheet of paper allowed to only observe the direct back-reflections of L1 due to the non-zero reflection of the lens coating at the operational wavelength $\lambda = 632.8$ nm. The ACU and Zygo were aligned until the back-reflections overlapped with the nominal Zygo testing LOS by moving the ACU and/or the Zygo interferometer with respect to each other. This step effectively defined the optical test axis. Afterwards, this process was repeated for the lens doublet utilising the five-axes alignment stage. Lastly, the reference sphere was unblocked and adjusted to the cat-eye position until the test wavefront overlapped with the nominal Zygo LOS. At this point, the Zygo interferometer was switched into measurement mode and the reference sphere's tilt and lateral position were adjusted until a minimum wavefront error was measured. The measurement setup alignment was completed by moving the reference sphere backwards along the optical axis by two times its focal length. Once this step was completed, the lens doublet was carefully adjusted until a minimum wavefront aberration could be measured. In addition, care was taken that the back-reflections still overlapped when viewed in alignment mode to keep the overall lens alignment to a common optical axis. One example of the directly obtained wavefront measurement is shown in Figure 4.10 without applying the ISF. After scaling with the ISF = 0.5, the final ACU wavefront quality was obtained at a wavefront PV of 0.40λ and wavefront RMS of 0.07λ . Both values were well in agreement with the required wavefront quality RO.01 and RO.02. Note that the values reported here correspond to the measured maximum wavefront aberration in order to demonstrate the worst case of as-build performance. Mean values of measured wavefront PV were about 0.1λ smaller. No changes of wavefront aberrations in terms of the derived upper limit of PV and RMS values between $\lambda = 632.8$ nm and $\lambda \approx 764$ nm are expected if the focal plane position of the ACU is determined as presented in the following section. This is a direct consequence of the relatively large ACU effective focal length of 774.26 nm at small numerical aperture of NA=0.0484.

The second major step in the ACU alignment procedure was the diffuser alignment. Hereby, the exact knowledge about the focal plane position of the ACU near the lens doublet was critical. In order to determine the focal plane position a $\emptyset 20 \mu\text{m}$ pinhole was placed near the nominal focal plane position and

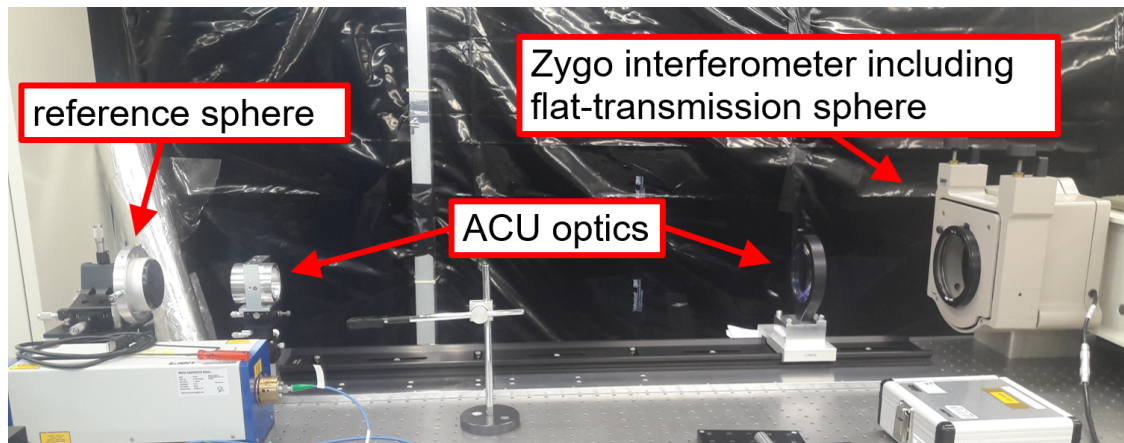


Figure 4.9: ACU lens alignment and wavefront measurement in front of Zygo interferometer.

backside-illuminated at 761 nm. The pinhole's height was set at the nominal optical axis height of $143 \text{ mm} \pm 1 \text{ mm}$ and a shearing plate collimation tester was utilised to measure the corresponding wavefront curvature exiting the ACU. This setup is indicated in Figure 4.11 including the first obtained shearogram.

A collimation tester consists of an extremely flat optical glass plate. Typically one side of this optical flat is wedged at a small angle of a few arc-seconds. For instance, the collimation tester used here has a nominal wedge of $10''$. If a plane wave from a collimated beam is incident on the optical flat, two reflections occur at the front and back side, respectively. If used at an incident angle larger zero, the reflected wavefronts can be observed at a distant screen. The finite thickness of the optical flat introduces a lateral displacement, so called shear, between the two wavefronts. Thus, a phase difference across the overlapping area of the two wavefronts on the screen manifests as an interference pattern. If the incident wave is perfectly flat, the interference pattern consists of equally spaced straight fringes oriented perpendicular to the direction of the wedge. Note that the collimation tester at time of recording could not be utilised in the nominal configuration due to a 90° turn of the wedged glass plate. Therefore, the wedged glass plate was mounted on a secondary stage and a large error budget was attributed to the angular alignment between ACU, collimation tester and visualising screen as discussed in the following.

When the pinhole was moved along the optical axis, a fringe tilt of up to $\pm 5^\circ$ was observed at a maximum displacement of the diffuser of $\pm 1 \text{ mm}$. However, based on the preliminary characterisation of the shearing plate, the required position tolerance in terms of shearogram fringe tilt was below 1.5° as discussed in section B.2. Thus, based on this first qualitative test, an alignment tolerance of better $\pm 300 \mu\text{m}$ was expected and a more deliberate positioning strategy was implemented where the

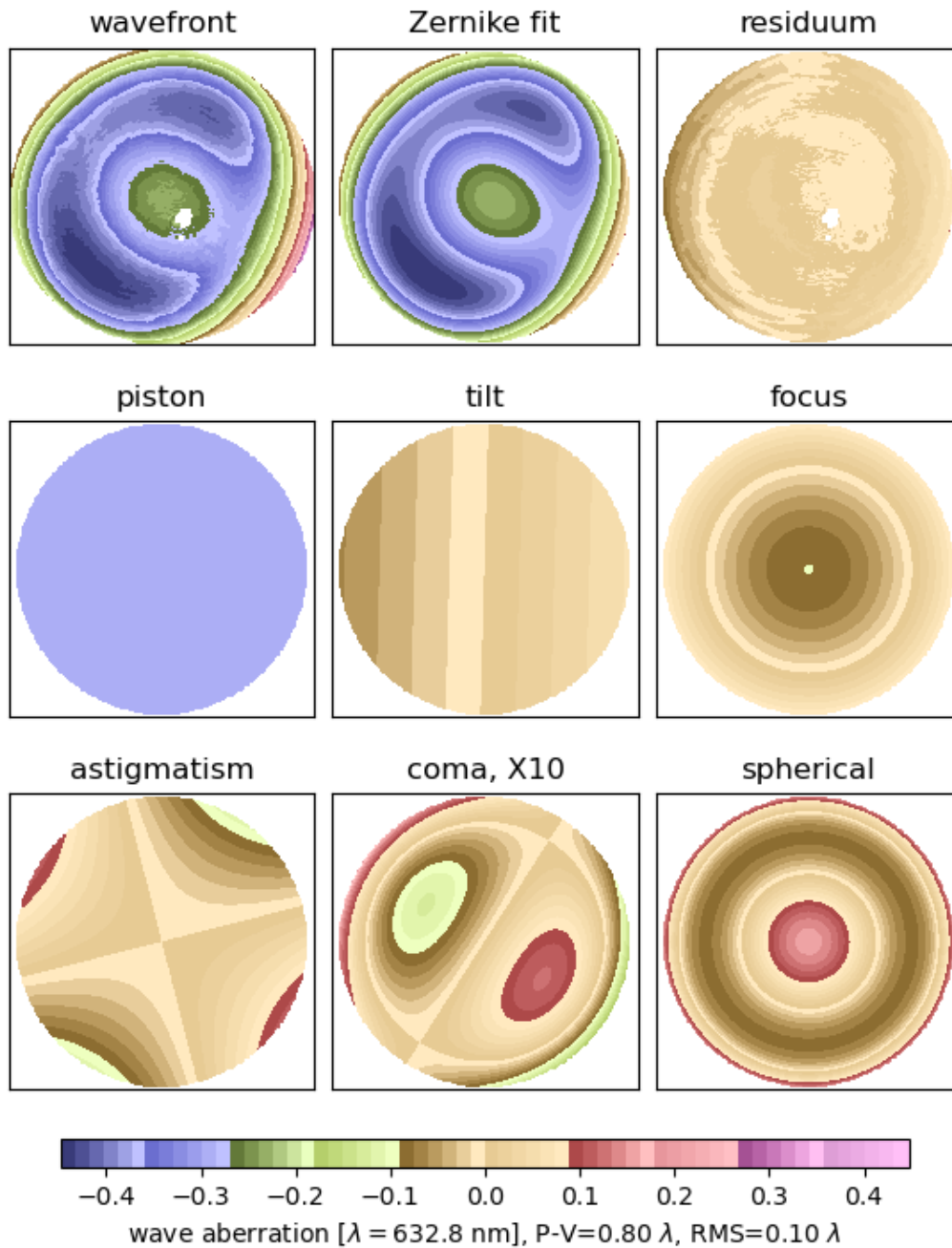


Figure 4.10: Measured ACU wavefront quality obtained in front of the Zygo interferometer. Measured wavefront aberrations were fitted based in the first 36 Zernike polynomials. The first 9 Zernike polynomials describing first order piston, tilt, focus, astigmatism, coma and spherical aberration were separately plotted which showed the dominant contribution of focus and spherical aberrations. Shown data did not consider the ISF.

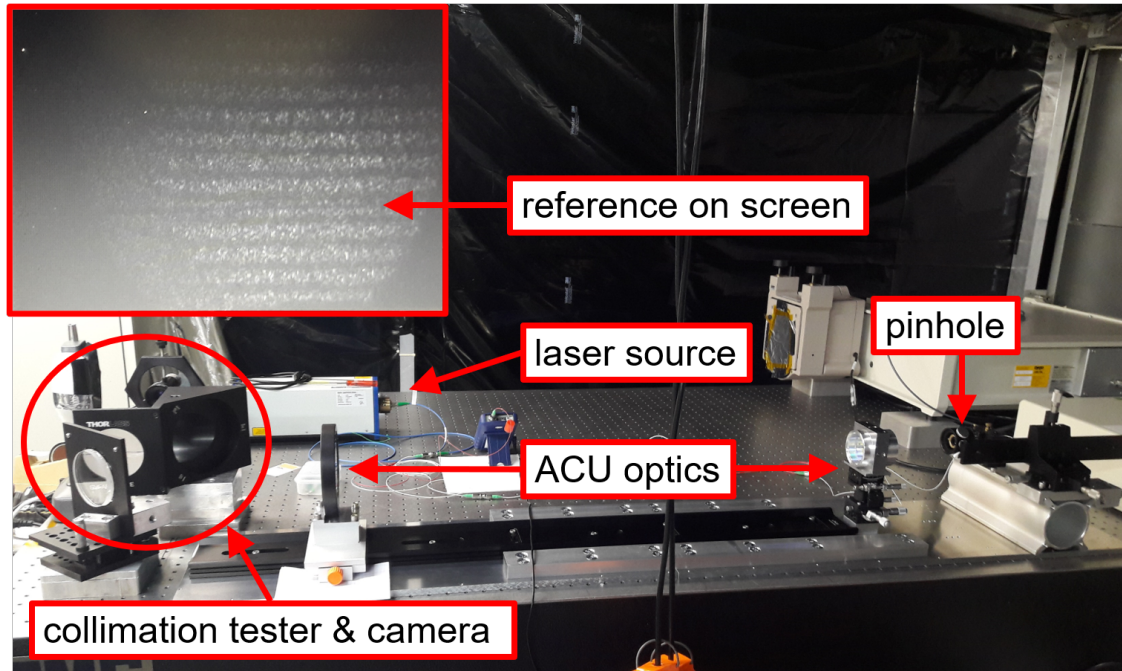


Figure 4.11: Setup during the ACU focal plane determination based on shearogram measurements of a point source.

displacement of the point source could be fine controlled with a precision of $10 \mu\text{m}$. At first, the pinhole was replaced with a microscope objective of $\text{NA} = 0.2$ which effectively formed a point source mid-air required for the latter diffuser alignment. In addition, the mounting stage of this assembly was secured on the ACU baseplate. The point source was moved along the optical axis in $50 \mu\text{m}$ steps and at each position a shearogram was recorded. The collected data was smoothed and an adaptive threshold applied in order to reduce the measurement noise as shown in Figure 4.12. Two regions of interest were selected above and below the integrated reference line on the collimation tester's screen in order to avoid biases to the fringe tilt estimation. A hough-line transform [Hough, 1959] was conducted and the median over the most-likely 5 % of detected lines in parameter space was taken as the final fringe tilt estimate. The obtained result is shown in Figure 4.13.

Estimation of the wavefront curvature was based on Riley and Gusinow [1977]. They derived analytical expressions for the shear and tilt of the overlapped wavefronts which are given in Equation 4.3 and Equation 4.4, respectively. These expressions depend only on the shearing plate's properties. The refractive index of fused silica was denoted $n = 1.454$ with the value taken from Malitson [1965] as no further reference was provided by the manufacturer. The 3σ refractive index error was chosen at $\delta n = 0.001$ which was based on the difference to values reported by the manufacturer SCHOTT AG [2022b]. The shearing plate orientation α relative

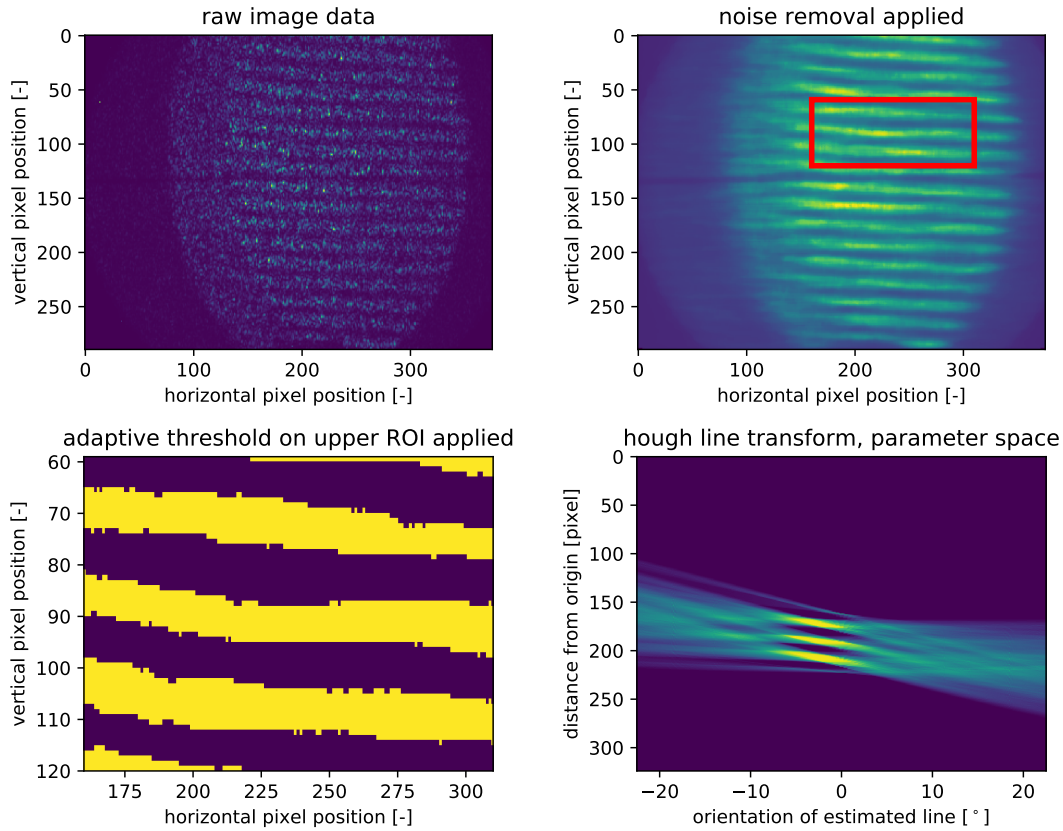


Figure 4.12: Processing of measured shearogram data. A median filter and adaptive threshold were applied to isolate the fringes and a hough-line transform was chosen for the estimation of the most likely fringe tilt.

to the ACU was aligned at $\alpha = 45^\circ \pm 15^\circ$ including a 3σ uncertainty. The wedge angle δ of the collimation tester was characterised as described in section B.2. Based on that shear and tilt estimation of the overlapped wavefronts, Riley and Gusinow derived expressions for the fringe spacing and fringe tilt in the shearogram plane given in Equation 4.5 and Equation 4.6. In the context presented here, the ratio of the screen to shearing plate distance L to the actual wavefront radius of curvature $R(L)$ could be neglected and was set to zero which introduced an wavefront curvature estimation error of less than 0.1 %.

$$s = t \times \sin 2\alpha \times (n^2 - \sin^2 \alpha)^{-1/2} \quad (4.3)$$

$$\theta = 2\delta(n^2 - \sin^2 \alpha)^{1/2} \quad (4.4)$$

$$\begin{aligned} d &= \lambda[\theta \times (1 - L/R(L))]^{-1} \\ &= \lambda/\theta \end{aligned} \quad (4.5)$$

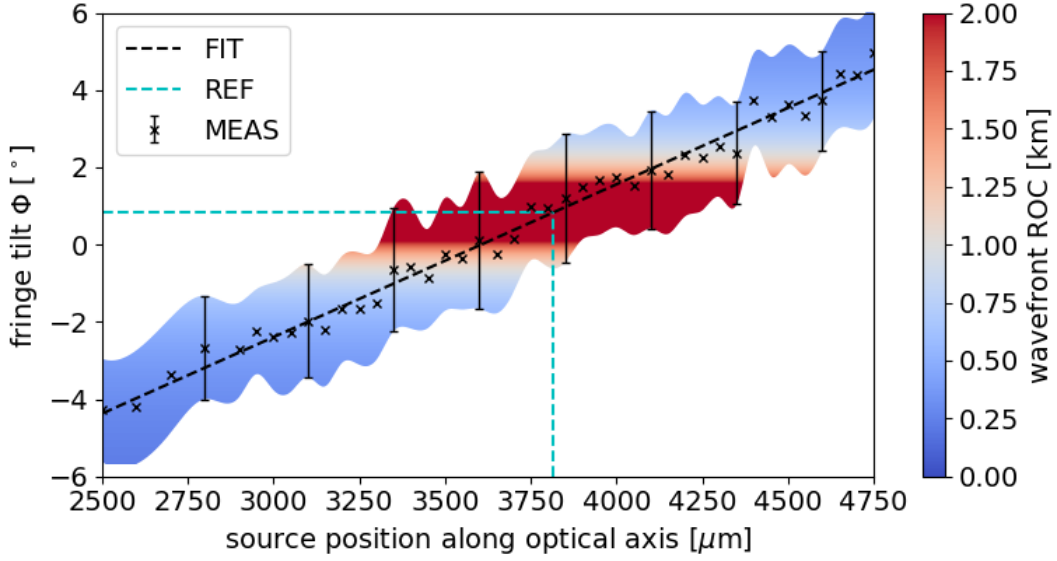


Figure 4.13: Estimated shearogram fringe tilt and corresponding wavefront curvature at different point source positions along the ACU optical axis. The source positions were obtained based on the micrometer scale. Shown uncertainties are based on the statistical standard deviation of the hough-line transform. The linear relation between fringe tilt and source position is indicated by the dashed black line (FIT). Inclination of the reference line is indicated by the blue dashed line (REF).

$$\tan \phi = sd \times (\lambda R(L))^{-1} \quad (4.6)$$

The reciprocal relation between the fringe tilt angle and the wavefront curvature in Equation 4.6 did not allow for a direct fitting to the measured data. In particular, no analytical relation between the source position along the optical axis and the wavefront curvature was available. Thus, a linear fit was chosen to approximate the measured data and to relate the fringe tilt to the measured source position. The reasoning behind a linear fit function is explained in section B.2. Next, the ideal source position SP was found at the intersection of the reference line tilt and the linear fit which corresponded to $SP = 3815 \mu\text{m} \pm 64 \mu\text{m}$ which includes the propagated statistical uncertainty of the reference line tilt estimation $\Delta\Phi = \pm 0.2^\circ$. The obtained linear fit was further substituted into Equation 4.6 to estimate the ACU wavefront curvature at all other source positions which is shown as colour-coded transition in Figure 4.13. Here, the transition from red to white confined the region of compliance with RO.01 and RO.02.

The uncertainty budget of the lower and upper limit of the achieved ACU wavefront curvature was estimated in a Monte Carlo simulation based on Equation 4.3 to Equation 4.6. The estimation considered uncertainties of the shear plate

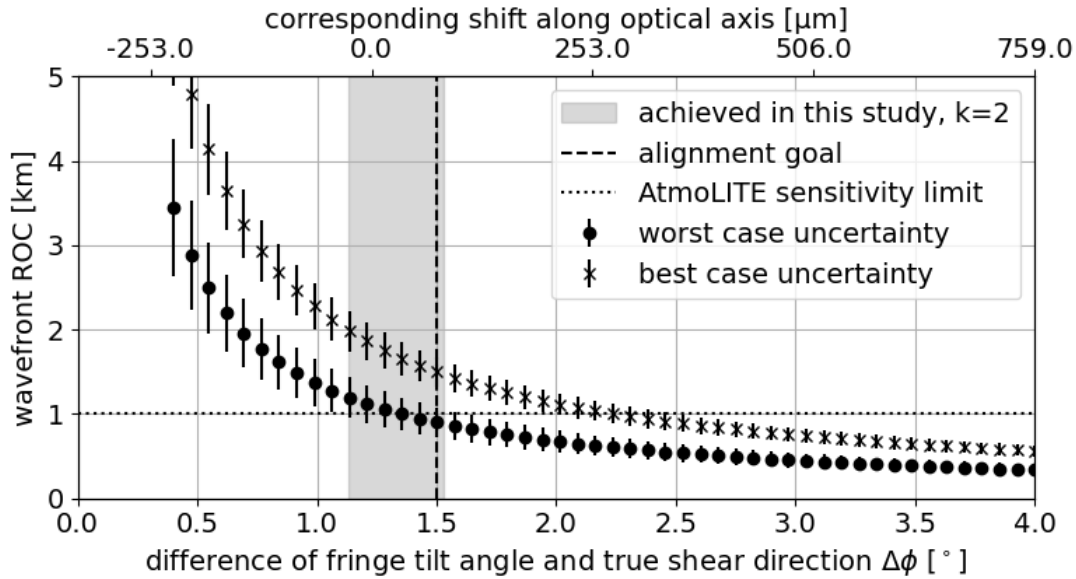


Figure 4.14: Uncertainty estimation of the ACU wavefront curvature. The AtmoLITE instrument’s sensitivity limit and the achieved lower alignment limit were indicated with horizontal and vertical lines, respectively. The worst and best case uncertainties were based on measured and theoretically expected fringe spacings, respectively. Error bars indicate the 1σ uncertainty of the corresponding Monte Carlo runs, in particular express the propagation of alignment and manufacturing uncertainties of the collimation tester’s shearing plate.

thickness, shear plate wedge, alignment between the screen containing the reference line and the shear plate, the refractive index of the shear plate, the measured shearing fringe distance and the relative alignment between shear cube and ACU. Considering the theoretically expected fringe spacing of $d = 2.0$ mm, the upper limit was estimated at $\text{ROC} = 1.5 \text{ km} \pm 0.3 \text{ km}$ based on Equation 4.6. Based on the measured fringe spacing of $d = 3.3 \text{ mm} \pm 0.1 \text{ mm}$, the lower limit was estimated at $\text{ROC} = 0.9 \text{ km} \pm 0.2 \text{ km}$. The full uncertainty range including all measurement uncertainties is shown in Figure 4.14. It is expected that re-alignments of the ACU in upcoming studies will provide even larger ROC and smaller uncertainties, and a new shearing plate has already been procured at the time of writing. The main drivers of the upper and lower limit presented here were the larger than envisaged wedge angle of the shear plate and additional alignment uncertainty due to the non-nominal mounting of the shear plate. In particular, a 2.6-times higher sensitivity with respect the shift along the optical axis indicated in Figure 4.14 is expected based on the shearogram fringe tilt thresholds estimated in section B.2.

Once the source position of best collimation was found and aligned, the diffuser disc alignment stage was installed. Best alignment between the diffuser and the

converging laser, in particular the smallest cross-section of the laser beam at the diffuser, was expected when a minimum number of speckle was observed [Goodman, 1976; Hu et al., 2020]. At first, the diffuser was centered near the focus mid-air and adjusted until the apparent visible spot size on the diffuser surface was minimised. Note that the shearogram fringes' visibility decreased to zero on the screen monitored during aforementioned measurements when the diffuser disc was installed. Therefore, a separate CCD detector was directly exposed to the reflected wavefronts behind the shearing plate in this study and multiple large-area speckle became visible after the focus shift introduced by the finite diffuser thickness was manually corrected based on the simulated expectation of $600\ \mu\text{m}$ (cf. Figure 4.19). Starting the disc rotation, a quick check of the shearogram fringes was possible. However, knowing the speckle pattern did neither show a single large speckle nor an overlapped fringe pattern, the disc rotation was stopped again. The diffuser tilt was fine-tuned and thereby the number of speckle was reduced until the shearogram fringes became visible with the stationary diffuser in place. At this point, the lateral alignment of the disc along the optical axis could be adjusted to maximize the fringe contrast. The corresponding measured shearograms are shown in Figure 4.15. Next, the focus' position on the diffuser was marked as the microscope objective had to be removed prior to the final alignment step.

The final alignment step was the implementation of the back-sided illumination of the diffuser disc. A small-sized integration sphere with an outer diameter of 34 cm was utilised. Its output port was fully covered by a Zenith polymer foil provided by SphereOptics. In addition, a $20\ \text{mm} \times 20\ \text{mm}$ rectangular field stop was glued on back and front side of the polymer foil in order to limit the illuminated area on the rotating diffuser disc. Note that the rectangular stop was slightly oversized with respect to the rectangular FOV of AtmoLITE as projected through the ACU. The nominal width of the projected FOV was 18.96 mm. Afterwards, the integration sphere assembly was placed in close proximity to the diffuser disc. To mitigate risk of mechanical failure, the design distance of $500\ \mu\text{m}$ was not yet established between diffuser and integration sphere output port due to the surprisingly large wobble of the diffuser disc during the start-up of diffuser rotation. Thus, an air gap of $\Delta_{\text{gap}} \approx 1.0\ \text{mm}$ was left open which effectively introduced a stronger than designed radial drop across the radiating source area as discussed in section 4.6. The aperture stop was centred to the aforementioned laser focus marker within an uncertainty of $\pm 1\ \text{mm}$ perpendicular to the optical axis.

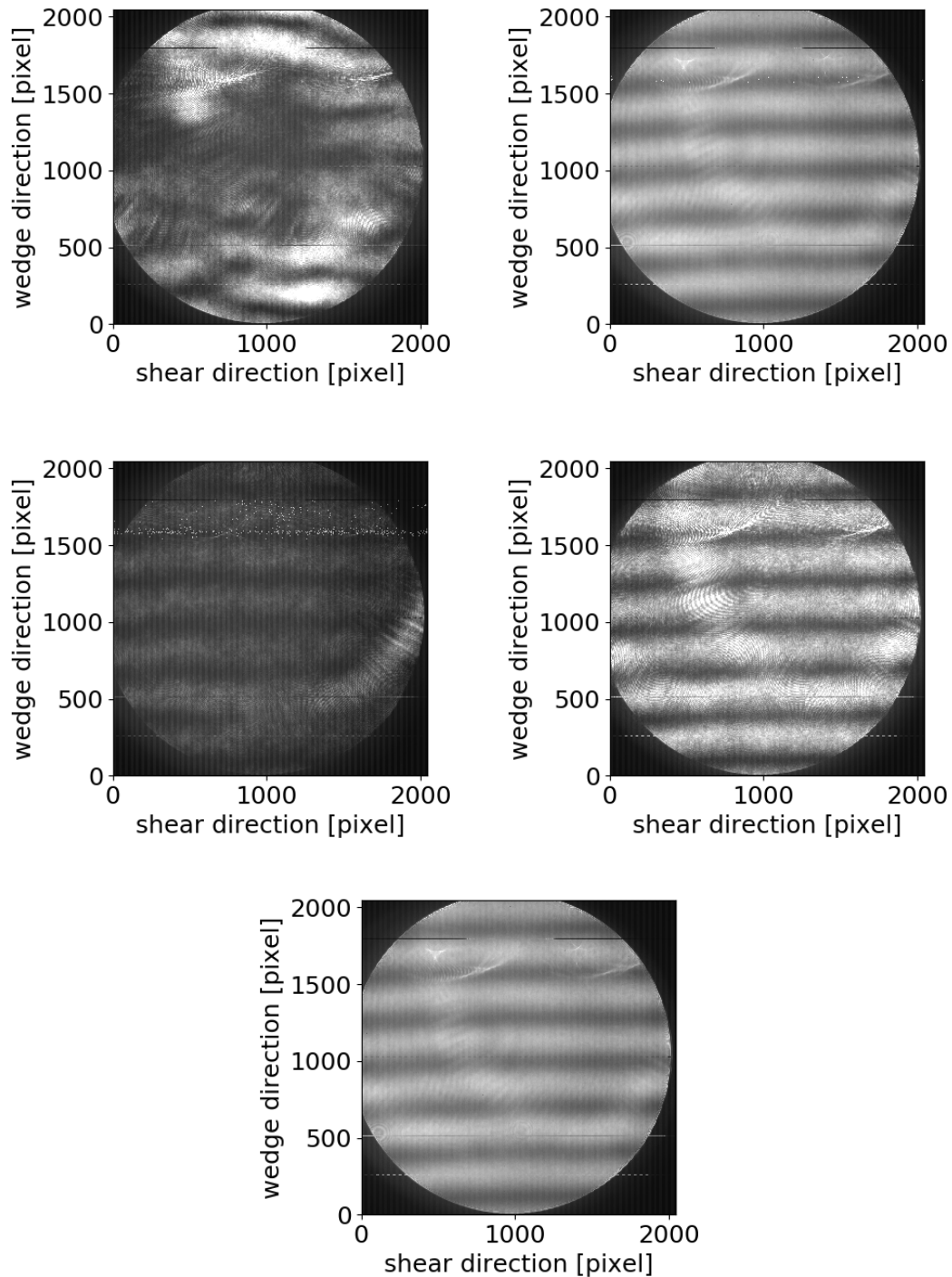


Figure 4.15: Measured shearograms during the diffuser disc alignment. Measurements with stationary and rotating diffuser before tilt correction (top), tilt correction and shift along optical axis towards best focus (middle) and final shearogram of rotating diffuser (bottom).

Remarks about expected diffuser illumination

The expected intensity distribution on the rotating diffuser disc is simulated based on the analytical description of radiative transfer between two parallel rectangular areas [Ehlert and Smith, 1993]. The simulated rectangular top-hat intensity profile is shown in Figure 4.16 and considers the ideal design and as-built scenarios. In the as-built scenario, a centre-to-edge drop of the top-hat intensity by $\Delta I = -9\%$ is expected within the nominal FOV of the AtmoLITE instrument indicated by the dashed outline. This effectively limited the angular range compliant to RO.04 and RO.06 to a FOV of $\pm 0.5^\circ$ during the first experimental verification.

Further, a simulation run is conducted to test the full calibration setup including the ACU alongside the AtmoLITE instrument. The instrument entrance aperture is positioned at the nominal ACU exit aperture position. A 8.1 mm wide radiating source region was defined on the rotating disc diffuser corresponding to an instrumental FOV of $\pm 0.6^\circ$ along one row, in particular, a slightly smaller FOV than the full AtmoLITE FOV of $\pm 0.65^\circ$ is used in the simulation so that results are not biased by the artifacts near the interferogram edges mentioned in section 3.5. The larger extend was considered along the dispersion direction of the SHS gratings within the instrument and two line pairs were considered at both edges of the O₂ A-band spectrum. For each wavelength, the simulated spectral line shape is

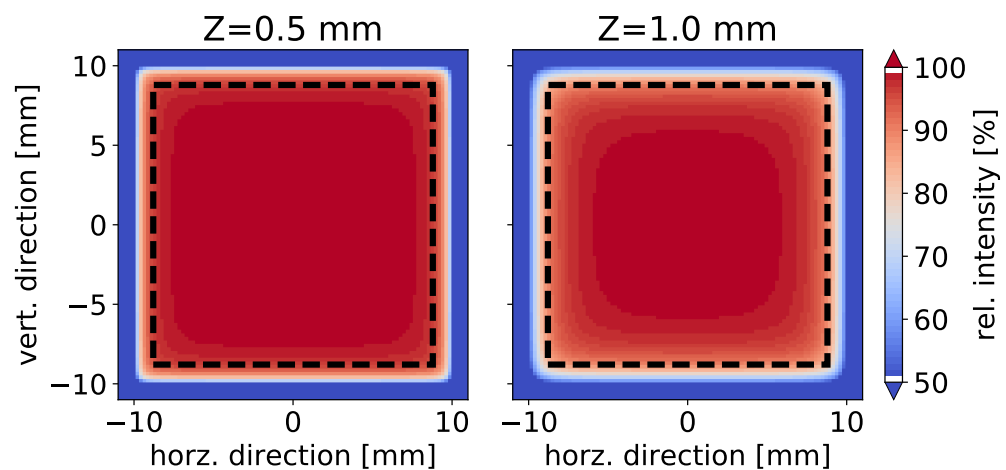


Figure 4.16: Results of the radiative transfer simulation between integration sphere assembly and rotating diffuser disc. Shown is the spatial intensity distribution on the rotating diffuser disc. The dashed outline included the nominal FOV as seen by the AtmoLITE instrument. Relative intensities were normalised to the centre and distinguished in 1 % bins.

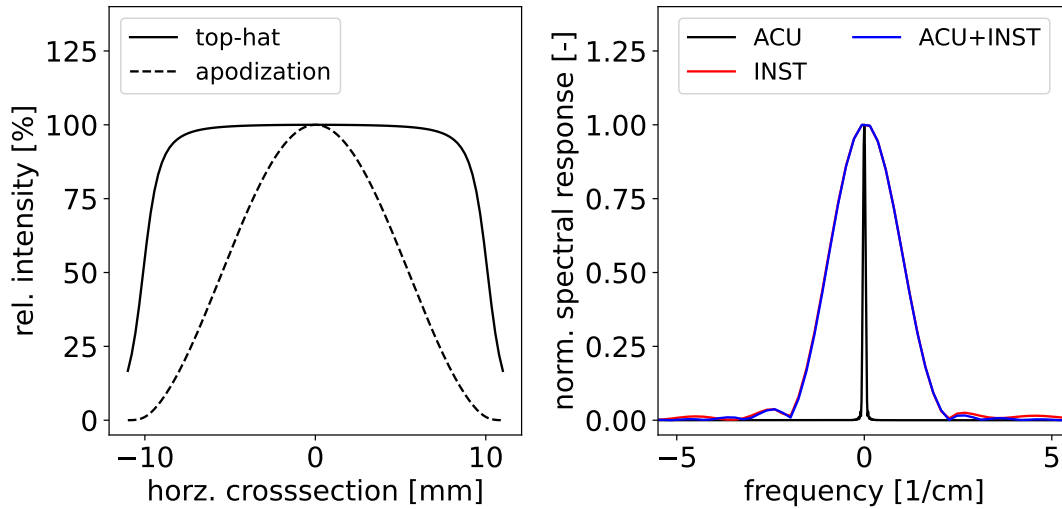


Figure 4.17: Crosssection through the centre of the expected spatial intensity distribution over the rotating disc diffuser in an as-built scenario (left). Including the shown blackman apodization, the top-hat’s spectral line shape was estimated by means of FFT (right). The two broader line shapes were acquired for the AtmoLITE instrument based on simulations of the sole instrument or in combination with the ACU at 764.74 nm.

integrated over a region of $\pm 10 \text{ cm}^{-1}$ centred on the simulated lines frequency and the ratios of the integrals are taken within each line pair. When comparing the nominal system’s ratio to the combined system’s ratio, a difference of -0.4% and -0.5% is found for the line pairs at (764.63, 764.74) nm and (759.83, 759.95) nm, respectively. These differences are caused by the spectral footprint introduced by the ACU as shown in Figure 4.17 and are caused by the centre-to-edge drop of the intensity profile over the rotating disc diffuser and non-zero wave aberrations. The absolute change itself is not critical as it does not impact the retrieved temperature. However, a spectral dependence of this change is apparent in the order of 0.1% .

Remarks about finite diffuser thickness

When inserting the diffuser disc into the setup, a rotation of the shearogram fringes is expected due to a shift of the intermediate focal point position. This shift along the optical axis is explained by a lateral narrowing of the converging beam profile within the diffuser as indicated by the ray trace in Figure 4.18. Passing through the diffuser disc, the rays are subject to a lateral shift perpendicular to the optical axis Δa which is related to the focal shift Δz by Equation 4.7. Note that for small angles and including Snell's law of refraction, Equation 4.7 can be simplified which allows to transform the equation into a more handy form valid for most practical applications [Greivenkamp, 2004].

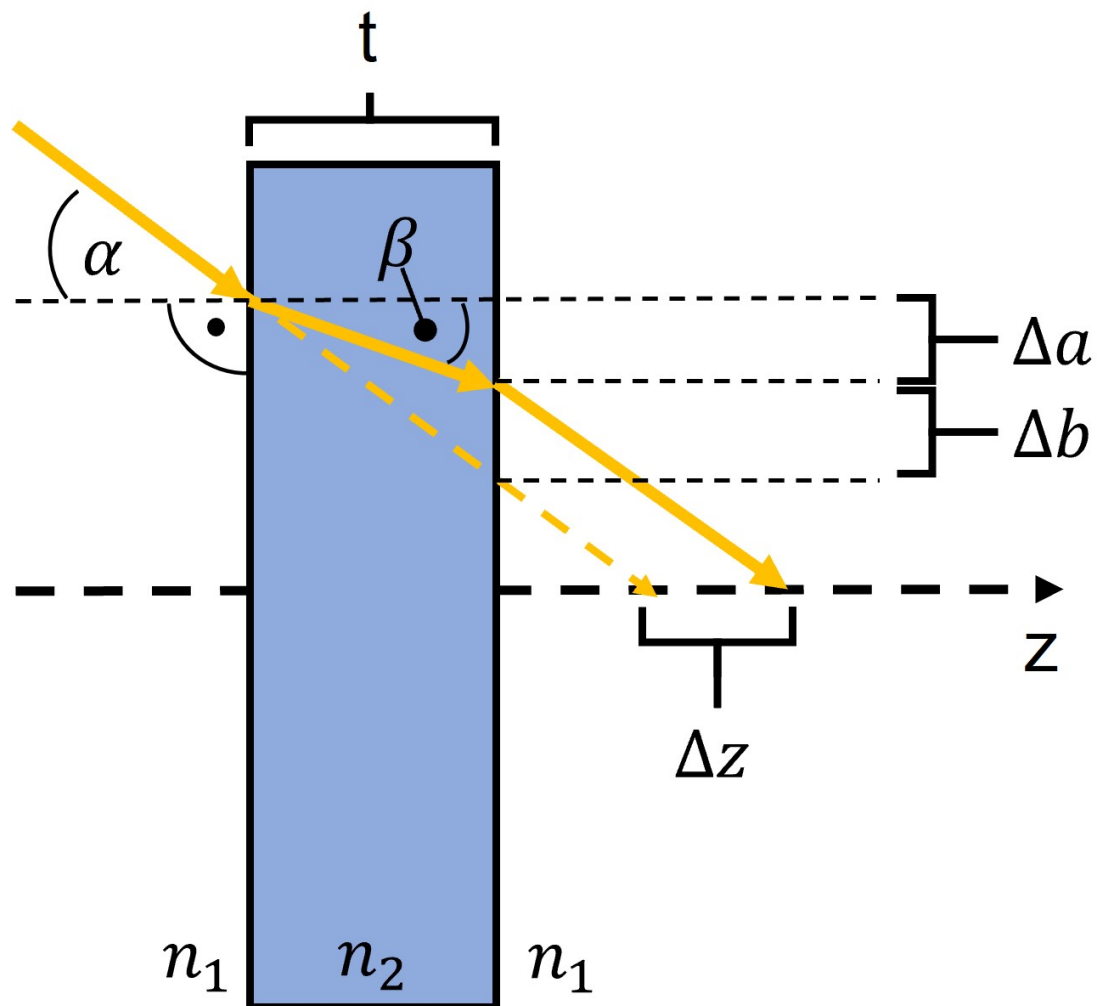


Figure 4.18: Impact of finite diffuser thickness on converging beam. Shown is the marginal ray trace in transmission through a slab of finite thickness t . The difference of refractive indices causes a deviation of the ray which effectively shifts the focus of the converging beam along the optical axis by Δz .

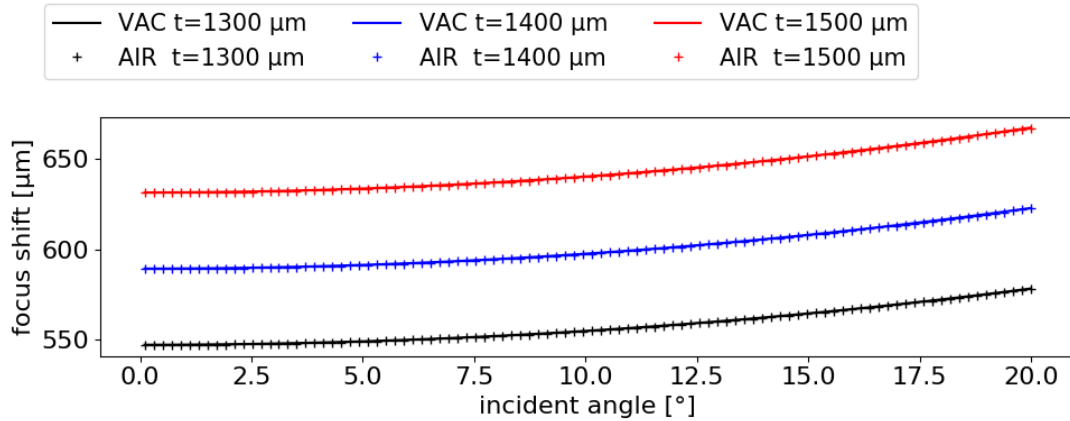


Figure 4.19: Expected shift of focal point along optical axis due to finite thickness of diffuser plate. Values are estimated for an air environment at ambient pressure and under vacuum. The difference in focal shift between both pressure environments is below $1.0 \mu\text{m}$.

$$\Delta z = t \cdot \left(1 - \frac{\tan \beta}{\tan \alpha}\right) \approx t \cdot \left(\frac{n_2 - n_1}{n_2}\right) \quad (4.7)$$

A graphical evaluation of the non-simplified Equation 4.7 is shown in Figure 4.19. The data shown is calculated for a typical ground glass diffuser of refractive index $n_2 = 1.73$ and a thickness t between 1.3 mm and 1.5 mm. Unfortunately, this focal shift and the corresponding additional shearogram fringe rotation could not be monitored precisely during the first experimental setup of the ACU discussed above because the detector and, thus, the angular reference had to be changed after including the diffuser disc. However, the experiment was repeated prior to the AtmoLITE calibration campaign including an improved shearogram acquisition setup which allowed to observe a focal shift of $\Delta z = 590 \mu\text{m}$ (personal communications, Marco Miebach, 2022), well within expectations.

4.6 Verification of the ACU prototype(s)

An experimental verification strategy was developed to measure the ACU illumination uniformity in spatial and angular extent over the exit aperture. The goal was to verify the expected properties discussed in section 4.2 and section 4.4. The focus was put on the illumination distribution across the ACU exit aperture and the illumination under different field angles as viewed by AtmoLITE. In this section, the developed equipment as utilised during the verification of the second ACU iteration is introduced. The different alignment steps and obtained measurements are discussed and a résumé is given about the ACU readiness for the AtmoLITE instrument calibration. Results obtained for the first ACU iteration are provided for reference only without detailed discussion.

Test setup - ACU scan head and aperture masks

The core of the test setup is the single aspheric collector lens of type ALL-100-200 provided by the German company asphericon GmbH. The attached aperture stop with a clear aperture of 75 mm allows to mount six smaller aperture masks on top in order to block specific parts of the aperture. By design, the mask openings are chosen as concentric annuli of equal area coverage placed at different radial positions. All openings add up to the full clear aperture of AtmoLITE. In the following, the masks are labelled from A_0 to A_5 starting with the outermost opening as shown in Figure 4.20. A mathematical description of these masks is appended in section B.4.

Four manually controlled alignment stages are stacked and utilised to align the lens-aperture assembly to the ACU. The first stage consists of two carriers which allow horizontal translation perpendicular to the optical axis. The lab jack of type L490M provided by Thorlabs is mounted on top of these carriers and ensures a stable height adjustment. Both lateral adjustment stages do not provide a built-in scale, thus, a measure is utilised to measure position changes relative to the table edge and top surface, respectively, which provides a lateral and height position uncertainty of ± 1 mm. The last two stages are the rotary table of type M-UTR80S provided by Newport and the goniometer of type GOH-60A115R provided by Sigmakoki. Both stages provide built-in scales and can be locked in any position which allows to perform independent angular scans in horizontal or vertical direction. Their readable angular measurement uncertainties are $\pm 0.08^\circ$ and $\pm 0.02^\circ$, respectively. A custom made aluminium spacer is utilised to adjust the lens vertex to the centre of rotation above the goniometer stage. In addition, the extension of this aluminium

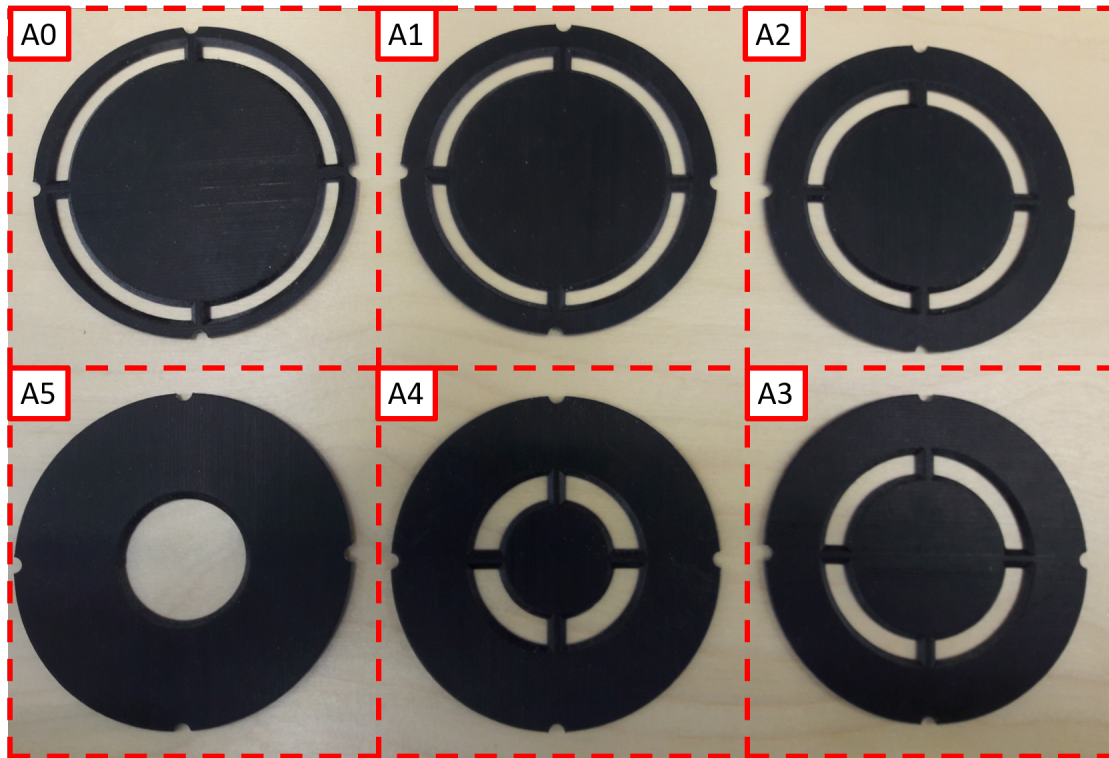


Figure 4.20: Different aperture masks utilised during the verification of the second ACU iteration. All openings cover an equal area of one sixth of the full aperture but start at different radial positions. The four notches at the outside are part of a clamping mechanism securing each aperture on top of the collector lens during measurements.

spacer carries the five-axis kinematic mount of type K5X1 and integrated photo-diode of type SM05PD3A, both provided by Thorlabs. An optional pinhole can be installed within the K5X1 in order to limit the divergence cone collected by the lens onto the photo-diode's active area which can increase the angular resolution of the scan head. A photograph of the fully assembled stage positioned in front of the second generation ACU is shown in Figure 4.21 and further design details of the ACU scan head are appended in section B.5. The distance between collector lens aperture and ACU is measured at $83 \text{ mm} \pm 1 \text{ mm}$. This corresponds to a distance of $265 \text{ mm} \pm 2 \text{ mm}$ between collimator lens aperture and the vertex of the ACU's last lens and is well within the margins discussed in section 4.3. The older setup utilised during the first generation ACU verification is shown in Figure 4.22 which featured motorised stages borrowed from partners within the MetEOC-3 project. Unfortunately, these stages are no longer available for the characterisation of the second ACU iteration.

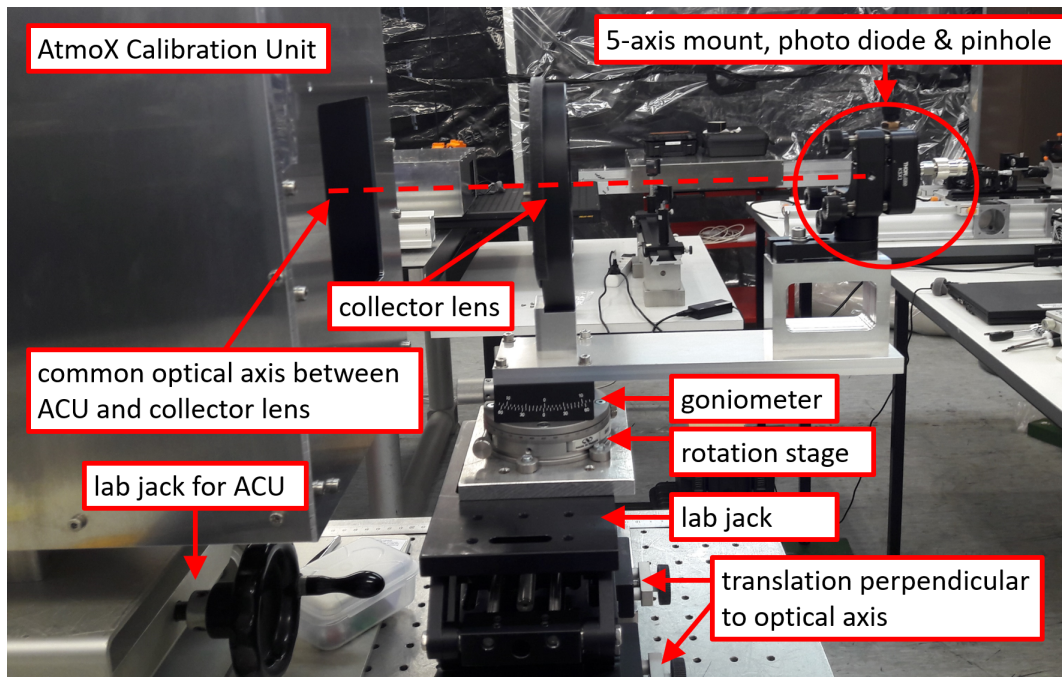


Figure 4.21: Manual test equipment during the ACU's illumination verification at BUW. All parts are shown in fully assembled and aligned position at the exit aperture of the second generation ACU. Note that the readout electronics were disconnected from the photodiode connector while the photo was taken.

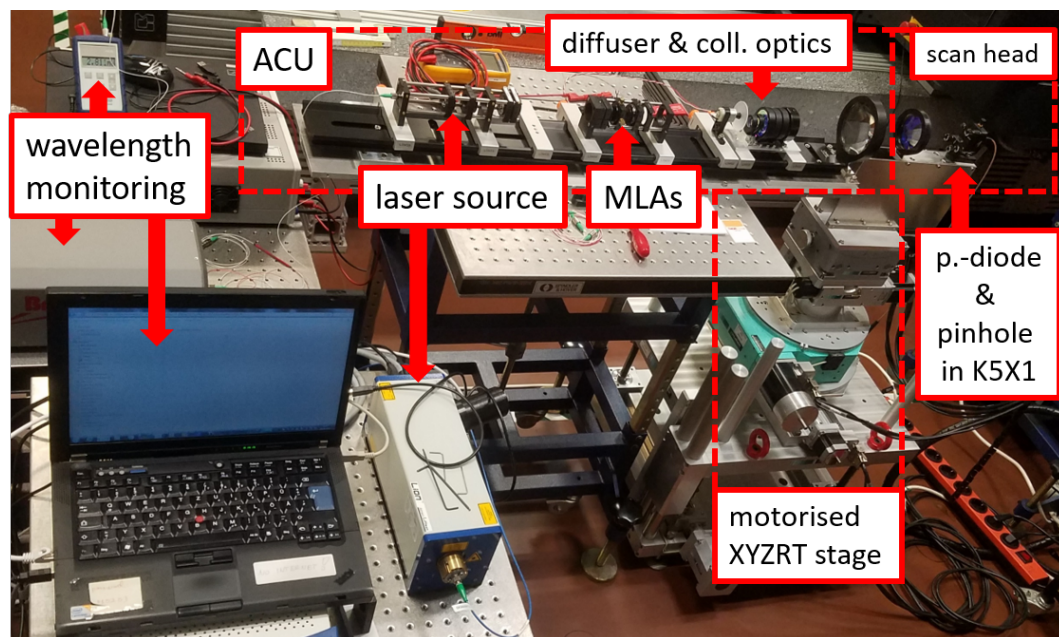


Figure 4.22: Motorised test equipment during the first generation ACU's illumination verification. All parts are shown in fully assembled and aligned position. Monitoring was included to measure relative laser intensity change and the laser wavelength used during the experiment.

Problems encountered with the first ACU iteration

At the beginning of February 2020, the relative intensity distributions across the 1st generation ACU exit aperture and field angles were measured. The goal was to get a first experimental verification of the overall ACU performance prior to AtmoLITE instrument characterisations. In the following, two measurements are presented for reference which highlighted the problems encountered with the 1st ACU.

Full field angular scans were performed at the wavelengths of $\lambda = 762$ nm and $\lambda = 765$ nm. The scan head was equipped with a $\emptyset 25$ μm pinhole which restricted the acceptance angle of the scan head to $\pm 0.005^\circ$, and a set of 120×120 measurement positions corresponding to an angular range of $\pm 1.5^\circ$ was obtained. This effectively prevented crosstalk between measurements under different angles. Note that the full clear aperture during the 1st ACU verification was set to $\emptyset 66$ mm, similar to the instrument entrance aperture size at that time. The result is presented in Figure 4.23.

A rectangular top-hat profile could be measured as expected. The full edge-to-edge extent was at least 2.7° in horizontal and vertical scan directions indicating a complete coverage of the required instrument FOV. However, multiple small and large scale inhomogeneities were observed which violated the requirements stated in section 4.2 as discussed in the following. A frame like structure centred at -1.0° and $+0.8^\circ$ in vertical scan direction, respectively, was found. It led to non-uniformities of up ± 6 % relative intensity along the full horizontal scan direction. In addition, the enclosed field at angles between -0.5° and $+0.8^\circ$ showed a linear decrease of -10 % relative intensity along the vertical scan direction.

In order to evaluate the uniformity of illumination across the ACU's exit aperture, the scan head was replaced by a trap detector. Its aperture of $\emptyset 8$ mm allowed to scan the aperture stepwise while simultaneously integrating over an $\text{FOV} > 10^\circ$ at each position. Thus, at each measurement position the full ACU angular range was integrated. A grid of 100×100 measurement positions was used with a step size between measurement positions of 1 mm. The measured intensity distribution is shown in Figure 4.24.

A clear maximum was observed in the centre of the ACU aperture. The measured intensity decreased over the innermost 66 mm by at least 55 %. Moreover, by comparison to values obtained near the edge of the ACU aperture where effectively stray radiation reflected by the ACU lens mount was measured, below -22 mm in vertical and at least 35 mm outside the horizontal centre, it was apparent that the intensity caused by direct illumination from the ACU actually dropped to almost zero and large parts of the ACU aperture were only illuminated by radiation from the surrounding laboratory. This was investigated by a more precise scan

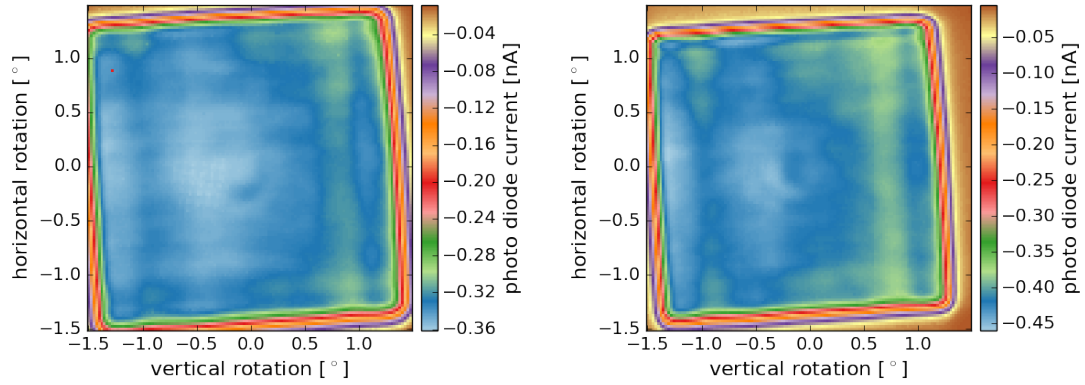


Figure 4.23: Angular field scans of the 1st generation ACU obtained with the motorised setup. Measurements were conducted at 762 nm and 765 nm. The measurement grid consisted of 120×120 equally spaced points. Clear non-uniformities are apparent with a modulations of up to $\pm 6\%$ relative intensity across the top-hat region.

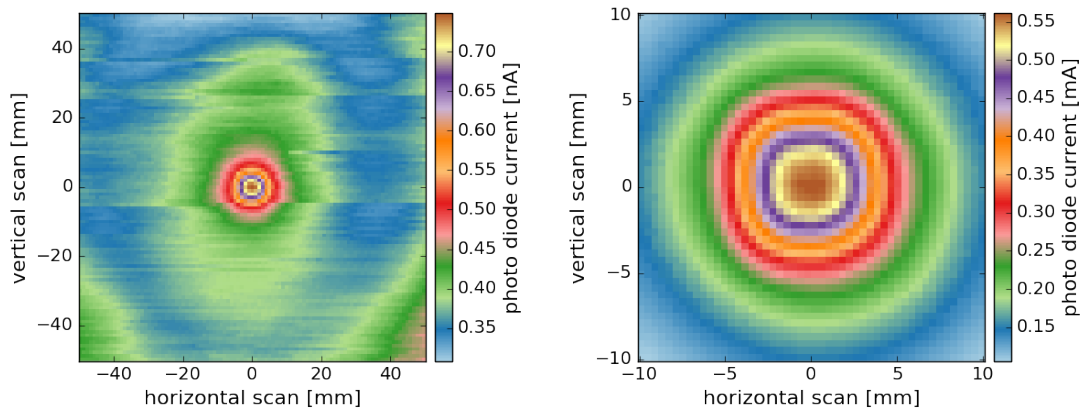


Figure 4.24: Aperture scans at the exit aperture of the 1st generation ACU. A trap detector was utilised to scan an area of $100 \times 100 \text{ mm}^2$ at the aperture centre of the ACU in steps of $\Delta = 1 \text{ mm}$. At each point the full angular range of the ACU was integrated over the $\varnothing = 8 \text{ mm}$ aperture of the trap detector (left). A scan with higher resolution was obtained near the centre of the ACU aperture in order to investigate the strong decrease of intensity across the aperture more precisely (right). The laser had to be restarted between measurements which resulted in the different absolute intensities recorded within the trap detector.

over the innermost $10 \times 10 \text{ mm}^2$ and showed an even more pronounced drop in intensity by over 80 % within the innermost 30 % of the aperture. The evaluated performance therefore showed a clear violation of RO.05 and the decision to re-design the ACU was made.

Uniformity obtained with the second ACU iteration

Verification of the second ACU iteration was conducted in November of 2021 at the BUW. No motorised stages were available, thus, all results presented in the following were obtained with the manually controlled scan head which only allowed to verify the ACU uniformity on a rather coarse grid with an angular resolution of 5 arcmin between measurement positions. In addition, to measure the much smaller absolute radiance emitted by the second ACU, the pinhole size within the scan head was increased to $\emptyset 50 \text{ }\mu\text{m}$. This increased the angular resolution of the scan head to 0.016° . In addition, the clear aperture of the test setup was increased to $\emptyset 75 \text{ mm}$ to accommodate the AtmoLITE aperture size. Available measurement time restricted the number of test wavelengths and the decision to perform the verification at $\lambda = 759.001 \text{ nm}$ and $\lambda = 764.091 \text{ nm}$ was made.

Alignment between ACU and the scan head was conducted as follows. Once positioned in front of the ACU exit aperture, scans were performed either using the rotation in horizontal and vertical or shifting the scan head laterally. After each individual scan, the position of highest flux was marked and used as the new nominal alignment position of the scan head with respect to the centre of the observed top-hat illumination profile expected from the ACU. After two iterations of all scan directions, significant local flux maxima were no longer observed and the centre of the top-hat profile measured in the two following iterations was estimated based on the positions of its FWHM. At this point, alignment was stopped because changes of the centre position regarding angular and lateral alignment were smaller than available manual controlled precisions of $\pm 5 \text{ arcmin}$ and $\pm 1 \text{ mm}$, respectively, and characterisation of the ACU was started.

At the wavelength of $\lambda = 759.001 \text{ nm}$, five angular scans (rotation) in horizontal and five angular scans in vertical direction were recorded. The goal was to verify the top-hat illumination profile at field angles of 0.0° , $\pm 0.33^\circ$ and $\pm 0.5^\circ$ offset to the top-hat centre and in both scan directions. One additional horizontal scan with the scan head laterally shifted by 4 mm, both vertically and horizontally, was conducted in order to evaluate changes of the illumination as seen by a non-properly aligned observer. To test spectral dependencies of the top-hat illumination profile, two scans at $\lambda = 764.091$ were performed through the centre of the top-hat.

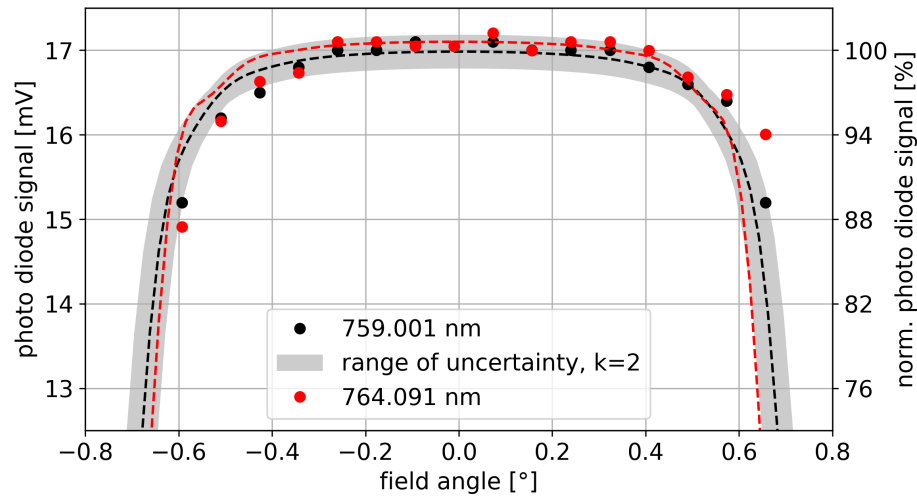


Figure 4.25: Results of the angular ACU scan in horizontal direction. Shown is the measured photo diode signal for different orientations of the ACU scan head at two different wavelengths of $\lambda = 759.001$ nm and 764.091 nm. The dashed curves indicate the best fit of the analytical top-hat description, Equation B.1. The range of uncertainty ($k=2$ at $\lambda = 759.001$ nm) is indicated by the shaded area which considers alignment accuracy of the rotation stage and precision of the photo diode digital readout.

Obtained crosssections are compared in Figure 4.25, Figure 4.26 and Figure 4.27 which correspond to the horizontal scans, vertical scans and the results obtained after laterally shifting the scan head. In an attempt to visualize the full top-hat

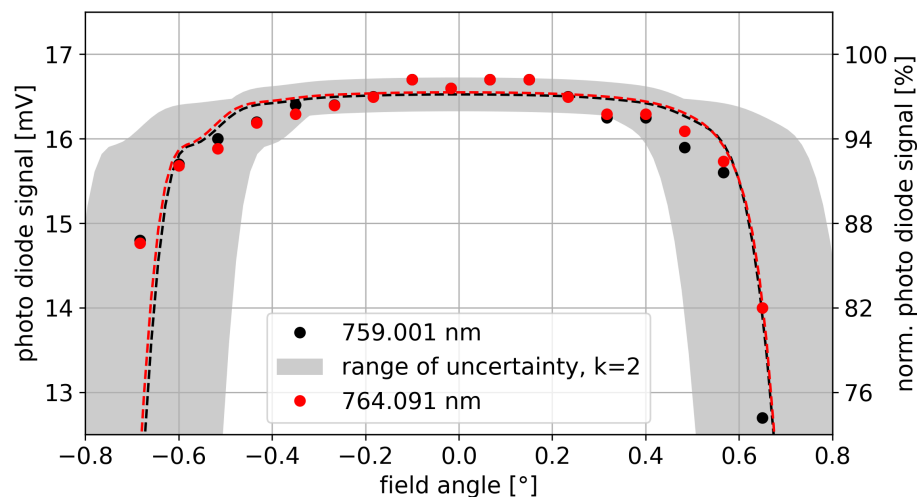


Figure 4.26: Results of the angular ACU scan in vertical direction. Shown is the measured photo diode signal for different orientations of the ACU scan head at two different wavelengths of $\lambda = 759.001$ nm and 764.091 nm similar to Figure 4.25. The larger uncertainty is caused by the goniometer stage which had a more coarse alignment accuracy than the rotation stage.

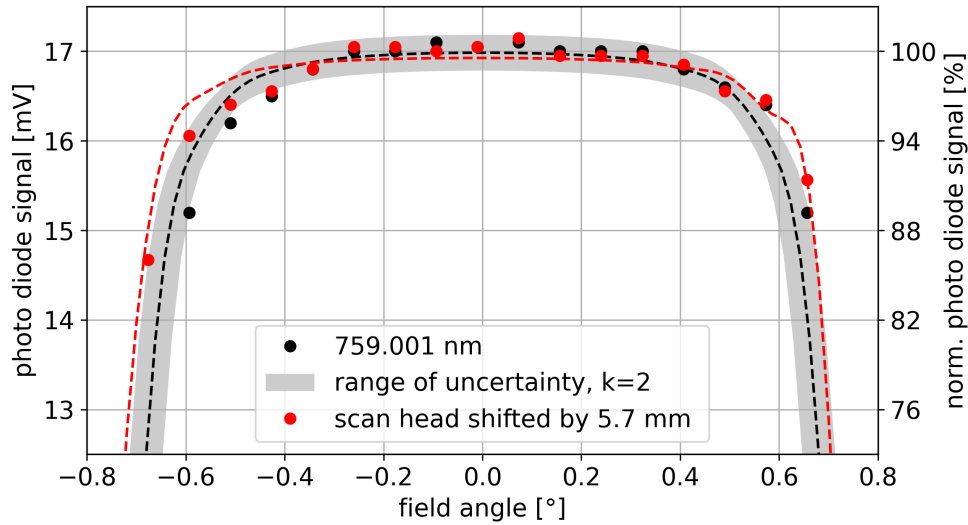


Figure 4.27: Results of the angular ACU scan with a laterally shifted ACU scan head. The shift corresponded to 4.0 mm in horizontal and vertical direction yielding a total lateral shift of 5.7 mm. Shown is the measured photo diode signal for different orientations of the ACU scan head at $\lambda = 759.001$ nm. The dashed curves indicate the best fit of the analytical top-hat description, Equation B.1. The range of uncertainty ($k=2$ at $\lambda = 759.001$ nm) is indicated by the shaded area which considers alignment accuracy of the rotation stage and precision of the photo diode digital readout.

illumination profile, a 2D linear interpolation of all measurements conducted at $\lambda = 759.001$ nm is presented in Figure 4.28. Note that the model fitted to the cross-section did not converge when applied to obtained 2D-data due to the coarse measurement grid and related large uncertainties of measurement positions.

Measurement uncertainties of the observed flux were based on the precision of the readout of the photo diode. The readout consisted of a sub femto ampere current amplifier of type DDCPA-300 manufactured by FEMTO coupled to a Fluke 115 digital multimeter. At the observed signal levels, the limiting component was the multimeter operated in *DC mV* mode at a resolution of ± 0.1 mV. According to the manufacturer, the accuracy was $\pm 0.5\%$ which at measured voltages of $V \approx 17$ mV was below the resolution of ± 0.1 mV. Hence, the following estimation was made in order to derive the measurement uncertainty based on signal stability (noise), background contributions (offset) and temporal drift of the signal. At an average signal level of 17.0 mV, the measurement noise was below ± 0.1 mV. Background contributions of stray radiation were measured at be below < 0.1 mV while the laser was turned off. Repeated measurements at the same measurement positions showed repeatability better than < 0.1 mV. Before start and after end of each scan a single measurement at the previously found top-hat centre was conducted. Results

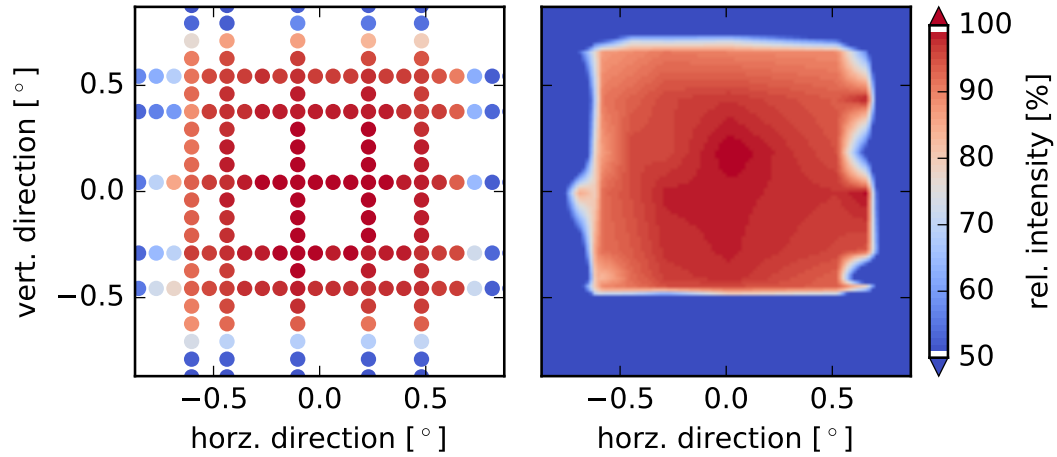


Figure 4.28: Results of the angular ACU scan at $\lambda = 759.001$ nm. Shown is the linear 2D-interpolation of all measurement points. The interpolation did not converge at angles below -0.2° in vertical direction, thus, no interpolated data is provided. The colorbar is given in steps of $\Delta = \pm 1$ %.

were only reported if no difference between these two measurements of more than ± 0.1 mV was observed which ensured that drifts of the laser power over time were negligible. Otherwise the scans were repeated. For direct comparison, measurements conducted at 764.091 nm showed a smaller mean flux due to the laser source non-constant power-to-wavelength relation and were up-scaled such that fluxes matched at the centre of the top-hat. Note that this linear scaling did not change the shape of the measured top-hat profiles. Including the recommended coverage factor of $k = 2$, the reported range of uncertainty was estimated at ± 0.2 mV which corresponded to ± 1.2 % relative measurement uncertainty at the centre of the top-hat illumination profile. In addition, angular accuracy of the alignment between ACU and scan head based on the readable scales of the goniometer and rotation stage was assumed to correspond to a range of 1σ , yielding $\pm 0.08^\circ$ and $\pm 0.02^\circ$ in horizontal and vertical scan direction, respectively. The model of radiative transfer between two rectangular plates discussed in section B.1 was used to fit the measured data and to indicate the combined range of uncertainty continuously in between measurement positions.

In the angular range of $\pm 0.5^\circ$ around the top-hat centre, the scans at $\lambda = 759.001$ and $\lambda = 764.091$ showed no significant difference and a continuous drop of up to

−4 % in relative flux from centre to edge was found. Significant differences larger than the measurement uncertainty of 1.2 % occurred at larger field angles only and increased towards the top-hat edges. These differences were most likely caused by the chromatic focal shift of the ACU (cf. section B.3 whereby the chromatic focal shift caused imaging of the diffuser disc at a different angular magnification. In turn, the different angular magnification caused a more narrow FWHM of the measured top-hat illumination profile with increasing wavelength. Preparations of a re-aligned and improved ACU were already started at the time of writing to increase the radiating source area of the integration sphere exit aperture and to decrease the nominal distance between radiating source area and diffuser disc such that the apparent edge of the top-hat illumination profile occurs outside the nominal AtmoLITE FOV. Although data of a second verification is still missing, it is expected that these improvements will yield the full required angular range of $\pm 0.7^\circ$ free of differences between the top-hat profiles at different wavelengths and to further reduce the centre-to-edge drop in relative flux below the required 2 %, RO.06.

One not expected effect was observed in Figure 4.26 by the comparison of the measured and modelled profiles in vertical direction only. The measured profile showed a steeper drop in flux around the top-hat centre than the model was able to explain. In particular, at the centre region between field angles of -0.08° and $+0.16^\circ$ a sudden increase of the measured flux of up to +1.1 % was observed compared to the model. Most likely, this effect was caused by a non-uniform illumination of the integration sphere exit aperture and has to be investigated once improvements are implemented. This effect is also apparent in Figure 4.28 by the oval-shaped regions of same relative intensity which had a greater extend in vertical than in horizontal direction.

Results obtained with the scan head laterally shifted and presented in Figure 4.27 showed no significant changes at field angles between -0.33° and $+0.50^\circ$. At larger field angles the top-hat profile obtained with the scan head shifted was apparently wider by up to +5 % (0.06°) at the FWHM.

Uniformity of the aperture illumination was verified by placing the aperture masks alternating between A_0 to A_5 in front of the ACU scan head. Measurements were conducted at both wavelengths, $\lambda = 759.001$ nm and $\lambda = 764.091$ nm, and at different field angles. Results are shown in Figure 4.29 and were obtained as follows.

For each of the aperture masks A_0 to A_4 a total of four measurements was conducted during which three of the four openings were blocked. A single measurement was conducted using aperture mask A_5 . Initial tests showed that background stray radiation, while the laser source was turned off, yielded up to ± 25 % relative

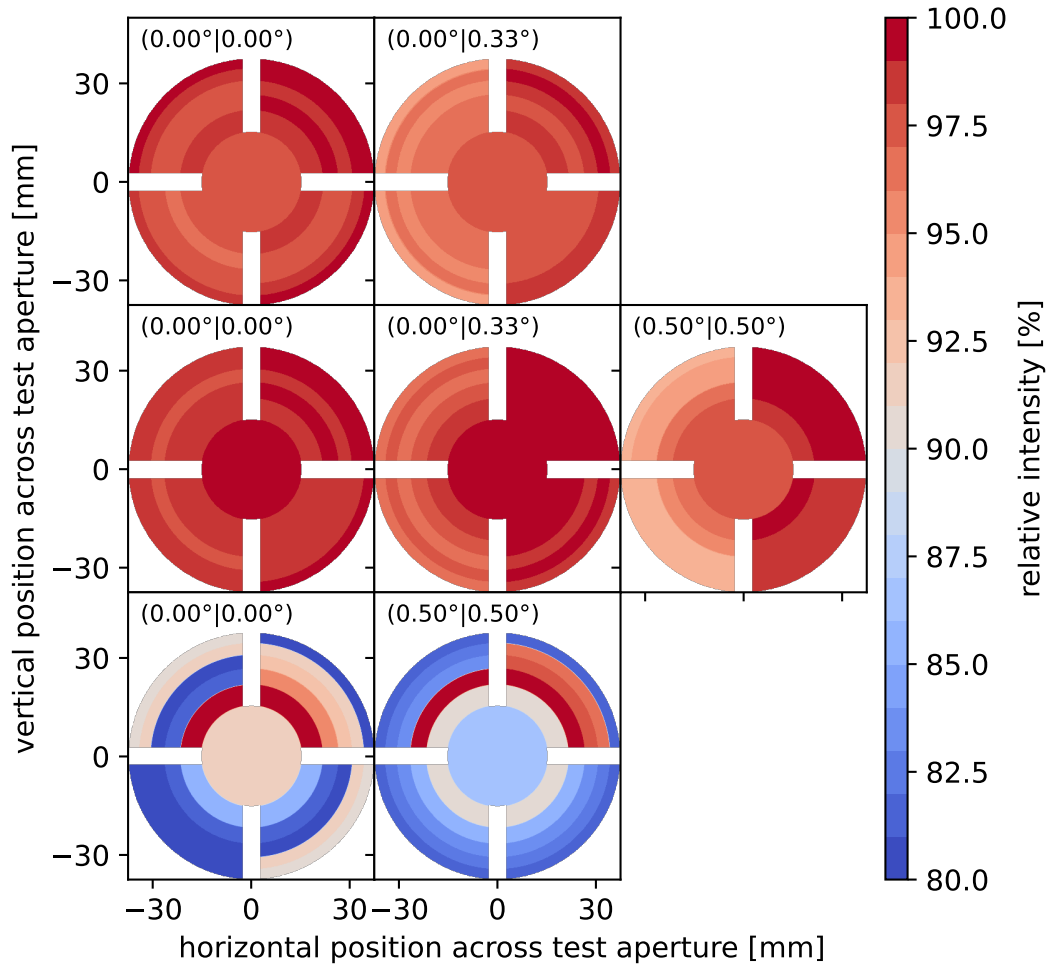


Figure 4.29: Results of the ACU aperture illumination measurements and uniformity estimation. Shown are the relative intensity distributions measured across the ACU exit aperture whereby the pinhole was removed from the ACU scan head. The colorbar is provided in steps of $\Delta = \pm 1\%$. Normalisation is done with respect to the highest measured intensity of each configuration. The tested configurations are from top left to bottom right: two on-axis and off-axis measurements at $\lambda = 764$ nm, three on-axis and off-axis measurements at $\lambda = 759$ nm and two measurements including the pinhole within the ACU scan head at $\lambda = 759$ nm are shown for reference only. White regions indicate the positions of the aperture mask bridges where no data was obtained. Angular orientation between ACU and scan head is indicated in brackets providing horizontal and vertical orientation, respectively.

contribution of the measured mean flux with the laser source turned on. In addition, measurement noise was as large as $\pm 14\%$ relative to the measured mean flux and the decision was made to remove the pinhole from the scan head in order to increase

the measured mean flux and correspondingly decrease the relative contributions of background and measurement noise. Including this change, the combined relative contributions of background stray radiation and noise amounted to $\pm 6\%$ ($k=2$) which was deemed sufficiently small to go ahead with the first verification of ACU aperture illumination uniformity. This also increased the acceptance angle of the scan head to a FOV of $\pm 0.16^\circ$.

Evaluation at $\lambda = 764.091$ nm showed that relative uniformity normalised to the maximum of each set of measurements was better than 3% and 5% at on-axis and off-axis field angles, respectively. The minimum occurred in the lower left compared to the maximum at the top right quadrant. Similar distributions were obtained at $\lambda = 759.001$ nm where the aperture illumination was uniform within 2% , 4% and 7% corresponding to the three angular field positions (H_x , H_y) of $(0.00^\circ, 0.00^\circ)$, $(0.00^\circ, 0.33^\circ)$ and $(0.50^\circ, 0.50^\circ)$, respectively. Expected was a radial drop in aperture illumination of up to 5.6% based on the selected diffuser. The two angular field positions (H_x , H_y) at $(0.00^\circ, 0.00^\circ)$ and $(0.00^\circ, 0.33^\circ)$ showed a lesser drop whereas an increase of up to $+1.4\%$ was measured at $(0.50^\circ, 0.50^\circ)$. Considering the measurement uncertainty of $\pm 6\%$ ($k=2$) all measurements without the pinhole therefore demonstrated compliance of the ACU aperture illumination uniformity with RO.05. Due to the large uncertainty of the measurements including the pinhole at $\lambda = 759.001$ nm, the results shown in the bottom row of Figure 4.29 were not used in this evaluation.

This measurement is further used to derive a first estimate of the relative tilt between the diffuser disc and the ACU optical axis. The assumption is that the scattering profile of the diffuser (cf. simulations in section 4.3) is the only cause of the radial drop in ACU aperture illumination uniformity because no vignetting is expected within the nominal FOV of the ACU. At small inclinations of the diffuser disc, the peak of the radial drop would then appear within the ACU aperture if on-axis measurements at ($H_x = 0.00^\circ$, $H_y = 0.00^\circ$) are considered. Off-axis measurements bias the peak position due to inclination of the optical axis. Based on the measured data shown in Figure 4.29 a clear peak was identified when using the pinhole within the ACU scan head at a radial distance between $r_5 = 15.31$ mm and $r_4 = 21.65$ mm and centered between the top quadrants. Considering the measurements with the pinhole removed, the peak appeared between $r_4 = 21.65$ mm and $r_0 = 37.5$ mm of the top right quadrant for the measurement conducted at $\lambda = 759.001$ nm. Results obtained at $\lambda = 764.091$ nm showed the peak shifted more towards the centre, but no clear maximum in the top right quadrant was apparent. Using the nominal numerical aperture of $NA = 0.0484$, the half cone opening angle

of the ACU over the full aperture becomes 2.77° . Assuming the scattering profile orientation is normal to the diffuser disc surface, the derived radial position are then proportional to the opening angle of the ACU. Thus, the estimate of the inclination of the diffuser disc becomes $\gamma_{\text{disc, min}} = 1.13^\circ$ based on the pinhole measurement. The upper limit is technically $\gamma_{\text{disc, max}} > 2.77^\circ$ because the peak extends towards the the edge of the evaluated aperture area, thus, cannot be accurately derived in this work.

This inclination is now compared to results shown in Figure 4.14. There, the ACU alignment goal was found to allow a shift of the diffuser of $\pm 380 \mu\text{m}$ away from its designed position if the current problem of unspecified tolerance of alignment between reference line and shear direction is not considered. Considering the image height of the ACU of 8.78 mm corresponding to the full AtmoLITE FOV of 0.65° and assuming the diffuser was aligned at the center of the ACU image, the allowed diffuser tilt then becomes $\gamma_{\text{disc, allowed}} = 2.48^\circ$. Thus, if the peak of the radial drop of the ACU aperture illumination uniformity lies outside the ACU aperture, proper alignment is not achieved. Aforementioned derivation of $\gamma_{\text{disc, min|max}}$ yields $\gamma_{\text{disc, min}} < \gamma_{\text{disc, allowed}} < \gamma_{\text{disc, max}}$, in particular no clear result is obtained. Therefore, it is recommended to repeat this characterisation once a more stable and accurate measurement setup is available in order to verify if required diffuser tilt is achieved.

4.7 Impact of a ACU non-uniformity on visibility

So far, the ACU concept is based on a sensitivity study of the interferogram fringe visibility simulation concerning the curvature of the incoming wavefront. The derived alignment goal corresponds to $ROC > 1000$ m. In addition, spatial modulations across the source shall be small to not introduce frequency components biasing the instrument calibration (RO.05). Concerning the calibration of AtmoLITE two further issues were raised: How much do non-uniform aperture illumination (1) or wavefront aberrations of the calibration source (2) impact the interferogram fringe visibility measured by AtmoLITE?

The first issue was addressed by interferogram simulations similar to those discussed in section 3.5. A radial drop-off in aperture illumination was introduced in front of the AtmoLITE entrance aperture and the resulting interferogram fringe visibility was compared to the results shown in Figure 3.19. The radial drop-off in aperture illumination was simulated by a cosine function whereby the amplitude is varied from 100 % down to 40 % relative to the flux between aperture centre and edge. The differences found on-axis and off-axis at a wavelength of 759.83 nm are plotted in dependence on the magnitude of the radial drop-off in aperture illumination as shown in Figure 4.30. The verification of the ACU discussed in section 4.6 showed a maximum radial drop-off of $7 \% \pm 6 \% (k = 2)$, thus, a positive visibility bias of up to $\Delta V = +0.6 \%$ was expected which was deemed sufficiently small to start prototyping of the instrument and calibration setup.

The impact of issue (2) was evaluated by simulations of the combined system of AtmoLITE and the ACU. Considered were the two wavelengths $\lambda = 764.74$ nm and $\lambda = 759.83$ nm at four different diffuser positions relative to the ACU optics and at the on-axis and off-axis field angles of $H_y = 0.0$ and $H_y = 0.9$. The ACU diffuser disc was considered as a plane emitting source and the interferogram fringe visibility was simulated based on the apparent wavefront aberrations introduced by ACU and AtmoLITE. In fact, this violates the assumption of incoming plane waves made in chapter 3 as wavefronts are traced from source points at the diffuser surface, thus, only the relative visibility change with respect to the designed diffuser disc position was evaluated and no absolute interferogram fringe visibility was estimated. This corresponded to the effective change in interferogram fringe visibility caused by additional wave aberrations introduced by a diffuser displacement. The following results are therefore seen as the upper limit of visibility change due to ACU misalignments, especially, because the relevant length scale is below the diffraction limited focal depth of the ACU of about $320 \mu\text{m}$, below which no changes of the

interferogram fringe visibility would be expected with an imaging system such as the AtmoLITE optics. In particular, it is below the acceptable diffuser displacement of $380 \mu\text{m}$ indicated in Figure 4.14 if current problems with the unknown tolerance between shear direction and reference line are neglected.

The simulation result is shown in Figure 4.31. The ACU focal plane defocus at $0 \mu\text{m}$ is taken as reference and denotes the designed diffuser position. Shifting the diffuser away from the ACU optics ($+100 \mu\text{m}$) is expected to change the interferogram fringe visibility by less than $< 1 \%$. In contrast, shifting the diffuser disc by $-200 \mu\text{m}$ towards the ACU optics is expected to decrease interferogram fringe visibility by up to -4.9% or to cause an increase of up to 2.0% at on-axis and off-axis field points, respectively.

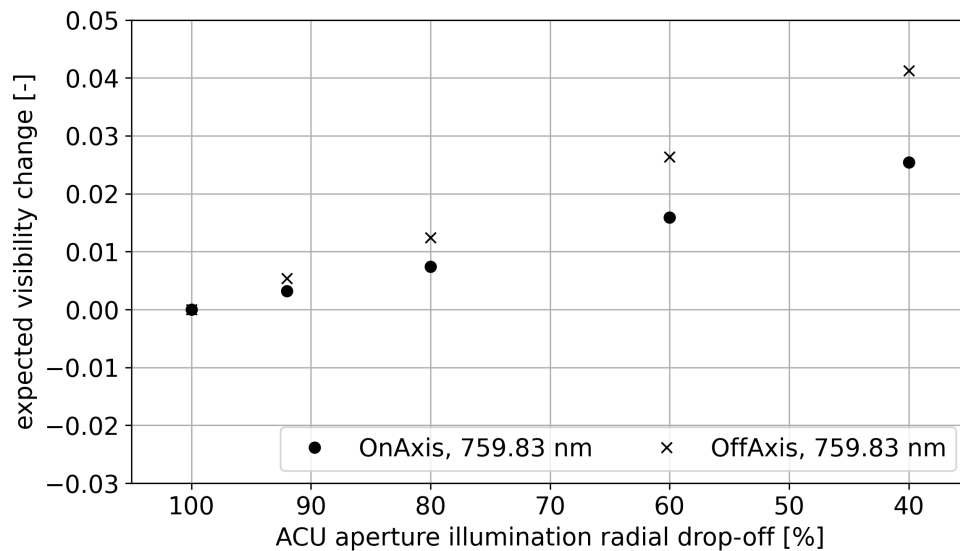


Figure 4.30: Expected change of visibility due to non-uniform aperture illumination. The non-uniform aperture illumination is simulated as a relative drop between centre and edge of the aperture. In general, visibility is expected to increase as less of the AtmoLITE entrance aperture is illuminated due to the decreasing amount of wavefront aberrations near the centre of the optical axis.

The discrepancy between the estimations used to design and align the ACU based on wavefront radius of curvature, and the sensitivity of interferogram fringe visibility to diffuser misalignment is currently seen as the most important theoretical issue which has to be resolved by experiment. The necessary DoFs to move the diffuser are already implemented in the ACU. However, delays due to COVID19 did not allow to perform the experiments, yet. Thus, the experimental verification of AtmoLITE instrument performance discussed in the following chapter only covers an introduction to the general interferogram description and instrument performance.

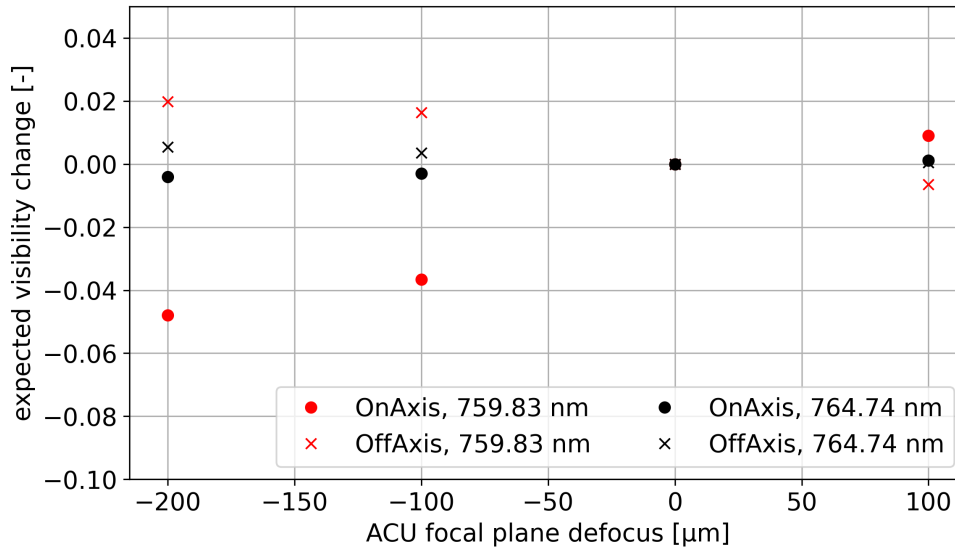


Figure 4.31: Interferogram fringe visibility change due to ACU misalignment. Shown is the expected change in interferogram fringe visibility if defocus is introduced between ACU optics and the radiating source area (diffuser disc). A defocus of $0 \mu\text{m}$ represents designed alignment and is used as the reference position. On- and off-axis refer to the field positions $H_y = 0.0$ and $H_y = 0.9$, respectively.

Thereby, the presented uncertainty budget considers the current discrepancy by artificially introducing a degradation of visibility into the retrieval scheme which yields a temperature bias towards lower temperatures.

Summary of ACU design and verification

This chapter introduced the novel calibration approach developed for the AtmoLITE instrument, in particular for characterisation of the AtmoLITE SHS spectral response. In addition, a first experimental verification of ACU performance was attempted. Regarding the ACU design, a baseline design was developed consisting of a tunable laser source, an integration sphere, a rotating disc diffuser and a dedicated collimation optics. Coupling of the tunable laser source to the integration sphere provides a uniform illumination of the diffuser. Rotation of the diffuser reduces overall speckle noise during calibration. The collimation optics images the illuminated diffuser surface to the AtmoLITE instrument which creates a light stimulus similar to the atmospheric scene. A noteworthy property of the ACU is the restriction of the illuminated angular FOV of AtmoLITE by inclusion of a field stop between integrating sphere and rotating diffuser. By design, this stop confines the illumination to field angles of about $\pm 0.7^\circ$, thus, enabling calibration of the in-field interferogram fringe visibility of AtmoLITE without contributions of potential out-of-field stray light.

Most importantly, two major milestones were demonstrated. At first, a concept to align the ACU collimation optics was developed and experimentally demonstrated. The goal was a wavefront radius of curvature larger than 1 km. The achieved result yielded a lower limit of $ROC = 0.9 \text{ km} \pm 0.2 \text{ km}$ and an upper limit of $ROC = 1.5 \text{ km} \pm 0.3 \text{ km}$. The major limitation was the shearing plate collimation tester used to evaluate the wavefront curvature which had an unspecified alignment tolerance between shear direction and reference line. Secondly, the ACU illumination uniformity was experimentally assessed. Achieved ACU aperture illumination was uniform by up to $7\% \pm 6\%$ and a uniform FOV coverage with a radial centre-to-edge drop of $-4.0\% \pm 1.2\%$ within a FOV of $\pm 0.5^\circ$ was observed.

In the following chapter, these results are now used to evaluate the combined performance of the AtmoLITE instrument in-front of the ACU with respect to the AtmoLITE temperature retrieval uncertainty.

5

The AtmoLITE Prototype - An experimental verification of performance

Contents

5.1 SHS assembly	138
5.2 Characterisation of PSF, MTF & FOV	139
5.3 First interferograms of AtmoLITE	149
5.4 Expected temperature retrieval uncertainty	158

In preparation of the upcoming AtmoLITE mission, two prototypes of the new SHS and optics were assembled and tested. The goal was to demonstrate the improved SHS alignment strategy, SHS integration to the opto-mechanics and to verify the new iterative optimization procedure used to align the front and camera optics with respect to the SHS. The first prototype was solely used to test the improved SHS assembly strategy, whereas the second prototype was used to demonstrate optics performance with respect to PSF, MTF and interferogram fringe visibility. In the following, both prototypes are referenced by AtmoLITE SHS prototype and AtmoLITE EM prototype, respectively.

Due to COVID-19, preparation of the test facility at the BUW and manufacturing of the as-designed opto-mechanics was delayed in parts beyond the works discussed here. In particular, performance verification was limited to tests under ambient conditions because the thermal-vacuum chamber was not yet procured. Hence, no temperature and pressure dependence of performance was investigated. Limited by the choice of available manufacturers, the opto-mechanics were manufactured from

aluminium instead of INVAR. The first compensator of the front optics had to be omitted and larger than required manufacturing tolerances were accepted.

In the following sections, achieved performance is reported which includes remarks about the SHS assembly in section 5.1 and the characterisation of overall imaging performance featuring PSF, MTF and a FOV scan in section 5.2. Guidelines for the alignment of SHS and optics are appended in Appendix C. Achieved interferogram fringe visibility is discussed in section 5.3 and section 5.4 summarises the current uncertainty budget with respect to expected temperature retrieval precision which, for the first time, includes parts of the calibration chain of the AtmoLITE instrument. Expected outcomes of postponed measurements and sensitivity studies are included based on simulations. The final temperature retrieval standard uncertainty reported in this study of ± 1.4 K is derived which represents the worst case performance expected for upcoming missions and studies. Based on assumptions made, currently a systematic temperature bias of -0.8 K is expected. Application of Equation 4.1 to measured interferograms is discussed which showed how spectral dependencies of the interferogram mean, modulation and phase distortion were evaluated. In particular, the wavelength dependence of the interferogram mean highlighted the need to include spectral and spatial dependence of the flat-field in upcoming studies.

5.1 SHS assembly

The assembly and alignment procedure of the SHS and its final integration between front and camera optics have been gradually improved since the AtmoSHINE integration in 2017. In contrast to assembly of the SHS under collimated illumination, while relying on optics different from the instrument optics and a subsequent second integration step to the instrument, the AtmoLITE SHS was assembled while simultaneously being integrated between the final front and camera optics as shown in Figure 5.1.

A single interface plate provided rigid support for the opto-mechanics and two alignment stages were used to align both SHS arms individually. Two grippers were attached to the alignment stages and protruded through the side-ports of the SHS housing which allowed adjustments of the individual SHS arms. As a result, a better alignment between the front optics focal, the SHS localisation and the camera optics object plane was expected compared to previous SHS assemblies. However, only 5-axes of the alignment stages were ready-to-use at the time of demonstration which resulted in values of achieved interferogram fringe visibility

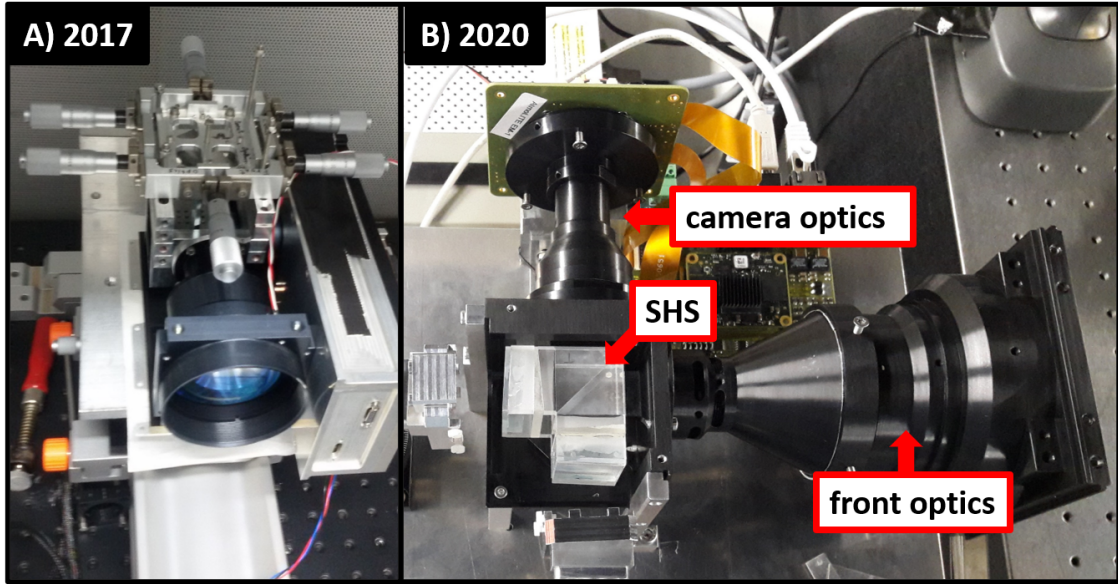


Figure 5.1: Improvements of the SHS assembly and alignment jig. While integration during AtmoSHINE required pre-assembly of the SHS outside the instrument optics and a final integration in 2017 (A), the new SHS assembly and alignment tool enabled assembly and alignment in a single integration step directly in-front of the ACU (B). Two 6-axis alignment stages shall enable a more precise relative grating orientation between both SHS arms before the UV curing adhesive is applied, although, only 5-axes were ready-to-use during the demonstration discussed in this work.

being below expectations as discussed in section 5.3. In particular, adjustment of the DoF corresponding to angle $\delta_{1|2}$ (cf. Figure C.1) was not yet implemented. During integration, a transparent acrylic glass plate was mounted on top of the SHS housing. Here, three plastic screws were inserted to clamp the SHS beam splitter cube between top and bottom of the SHS housing during integration.

Having the front optics attached to the SHS housing, the new approach also supported illumination of the instrument by the ACU during integration, thus, alignment of the SHS and the interferogram visibility could be directly optimized for observation of a light source virtually at infinity. A step-by-step guide on how to assemble and align the SHS is appended in section C.1 which includes a guideline of the iterative alignment procedure of front and camera optics as well.

5.2 Characterisation of PSF, MTF & FOV

In the following, an experimental approach is presented which was used to characterise PSF, MTF and FOV extent of the AtmoLITE EM prototype. In particular, the PSF extent during alignment of the front optics and at different field positions

were evaluated. A relation between observed field angle and pixel position was obtained. Based on a chequerboard target the system MTF was evaluated.

Experimental Setup during AtmoLITE Optics Alignment

All measurements were obtained in a single experimental setup which is shown in Figure 5.2. The setup comprised a point source virtually placed at infinity and the ACU. Both sources were arranged in an L-shaped setup around the instrument support stage which was mounted on an XYZRT-stage. With proper height adjustment and a single 90° rotation, the AtmoLITE instrument could either be illuminated by the point source or the ACU. Note that the center of rotation of the XYZRT-stage underneath the AtmoLITE EM instrument was aligned to the center of the instrument entrance aperture. Due to limited time available to setup the experiments and for a proof-of-concept demonstration only, the point source was build up using the back-side illuminated ACU scan head instead of assembling a second ACU. The pinhole was replaced by a $\emptyset 25 \mu\text{m}$ one. This effectively provided a point source with a nominal divergence angle of 0.007° which limited the achievable apparent spot sizes during alignment of the front (and camera) optics to $d_{\text{PSF, theo}} = 52 \mu\text{m} < 5 \text{ pixel}$. Here, spot sizes refers to the apparent footprint size on the detector, in particular the area of illuminated pixel.

Variation of PSF during optics alignment

During alignment of the front optics, substantial size variations of the observed PSF were expected. Following the recommended step-by-step procedure appended in section C.2, first experimental results were obtained based on the AtmoLITE EM prototype which are shown in Figure 5.3. At first, the instrument was aligned to the point source and saturation was observed across the full detector. Thus, the laser source power was reduced gradually until a single non-saturated spot remained. Orientation of the instrument towards the point source was adjusted such that the spot appeared centered on the detector. Next, adjustments were made to the compensator of L4 in steps of 30° (refer to section 3.6 for a description of the compensator). This resulted in a decrease of the apparent spot size. Note that a lateral displacement of the spot centre by up to 33 pixel ($\approx 360 \mu\text{m}$) in vertical or horizontal direction was observed between rotations of the compensator which was not expected for a compensator affecting effective focal length only! This indicated that the rotational DoF of the compensator was not independent from lateral shifts or tilt within its outer threading. Tighter tolerance requirements and fittings with respect to the optics barrel are expected to minimize this issue in

upcoming instrument assemblies, once the mechanics are manufactured according to the requirements specified in section 3.6. After the compensator position of minimum spot size was identified, all locking mechanisms surrounding L4 were secured. Afterwards the minimum spot size achieved was investigated quantitatively at different field positions which is discussed in the next section. Note that the Airy discs surrounding the central PSF maximum were no longer resolved after alignment was finalised (cf. Figure 5.3D) due to the pixel pitch of $11\ \mu\text{m}$. In particular, the expected diameter of the Airy disc, if the optics were aligned perfectly and neglecting the source divergence, corresponds to $\approx 10\ \mu\text{m}$.

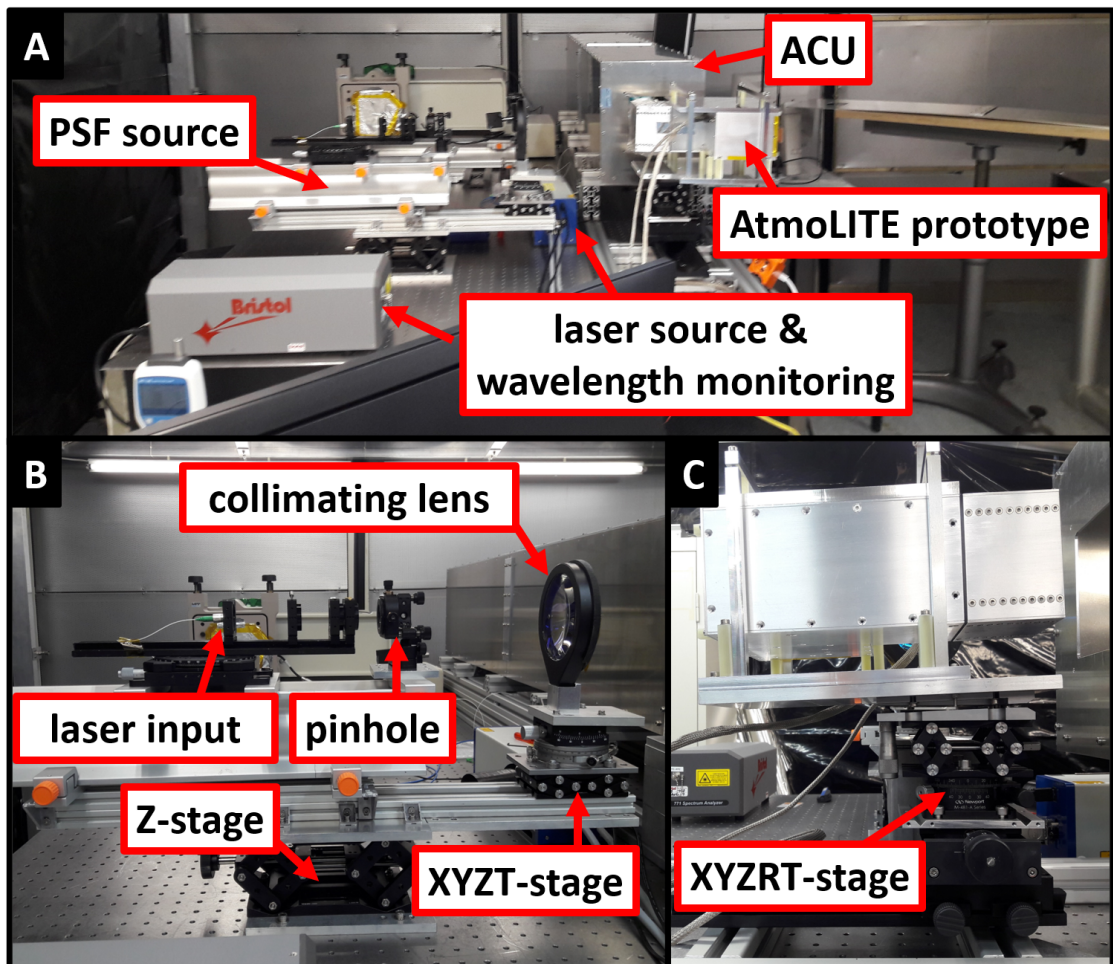


Figure 5.2: Experimental setup during PSF, MTF and FOV measurements of the AtmoLITE instrument. The point source, instrument and ACU are arranged in an L-shaped angle (A). This allows to either image the point source or look into the ACU illumination field. A close-up view of the point source setup and the AtmoLITE instrument mount are provided in (B) and (C).

Verification of AtmoLITE EM PSF across the full FOV

In order to assess the AtmoLITE EM PSF performance across the full FOV, the orientation between the AtmoLITE EM and the point source was gradually changed. A total of 10×10 measurements was conducted spanning an almost equi-distant grid over the full FOV. At each position, a single image was acquired. An overview of these measurements is shown in Figure 5.4 which features a stitched image of all 100 measurements, an inset of the bottom-left corner, an example of 2D Gaussian approximations used to evaluate the FWHM spot size and the obtained statistics over all approximated spot sizes. Individual SHS arms were not blocked during the measurements, thus, individual PSF spots appeared with varying intensities due to the overlapped interference pattern of the spectrometer. A 2D Gaussian

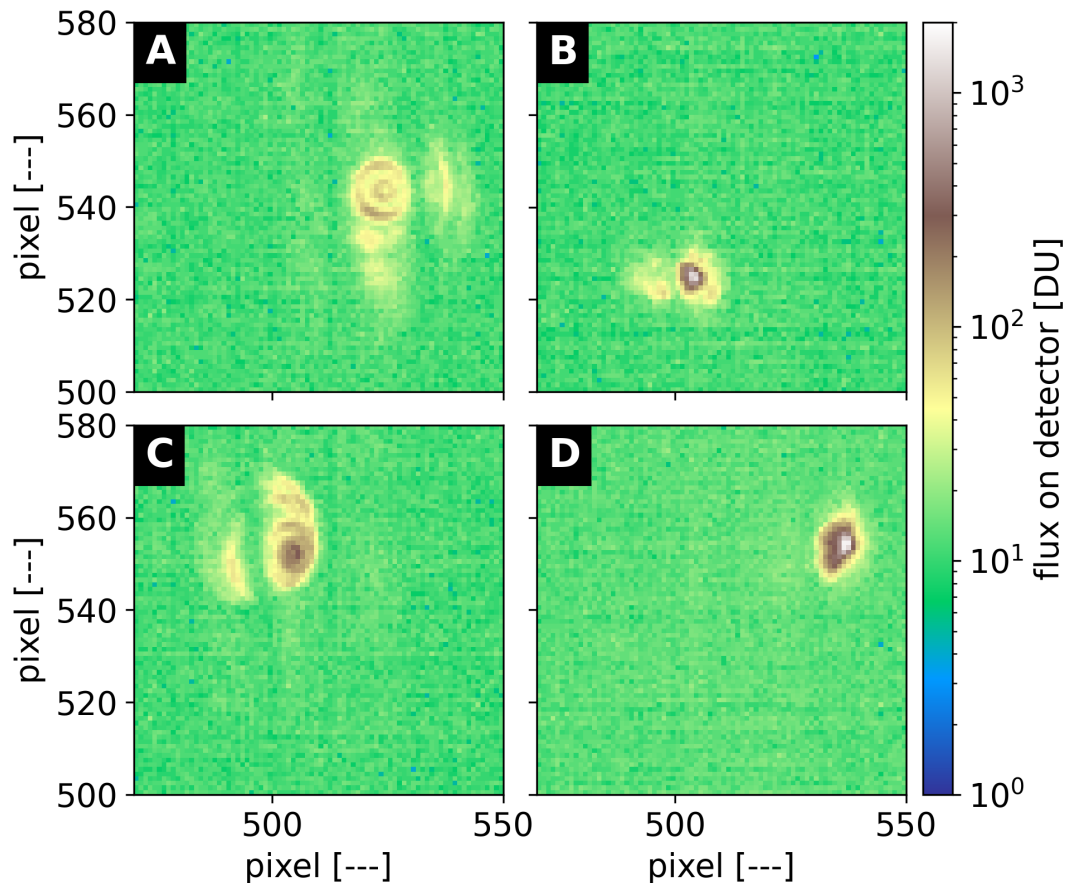


Figure 5.3: AtmoLITE EM PSF during front optics alignment. By rotation of the compensator at L4 in steps of 30° (A-C), the position of minimum apparent spot size was identified. The final achieved apparent spot size after the compensator was locked in position is shown in (D).

approximations to each PSF measurement was used and normalized to unity which allowed to estimate FWHM PSF spot size extent along the horizontal and vertical axis of the detector, separately at all field positions. The parametrised Equation 5.1 was used whereby (x, y) denoted the pixel along rows and columns of the detector, θ was the clockwise rotation of the Gaussian approximation, and σ_x^2 and σ_y^2 were the variance along rows and columns.

$$g(x, y) = A \exp(-[a(x - x_0)^2 + 2b(x - x_0)(y - y_0) + c(y - y_0)^2]) \quad (5.1)$$

$$\begin{aligned} a &= \frac{\cos^2 \theta}{2\sigma_x^2} + \frac{\sin^2 \theta}{2\sigma_y^2} \\ b &= -\frac{\sin 2\theta}{4\sigma_x^2} + \frac{\sin 2\theta}{4\sigma_y^2} \\ c &= \frac{\sin^2 \theta}{2\sigma_x^2} + \frac{\cos^2 \theta}{2\sigma_y^2} \end{aligned} \quad (5.2)$$

The resulting FWHM distribution was centered around a mean FWHM PSF spot size of $x_{\text{mean}} = 4.5$ pixel and $y_{\text{mean}} = 5.2$ pixel. The corresponding standard uncertainties were $\sigma_x = 2.1$ and $\sigma_y = 1.7$ based on the Gaussian approximation. Due to the spatial filtering of the source (pinhole) and the paraxial approximation used to estimate $d_{\text{PSF, theo}}$, it was assumed that $\approx 99\%$ of the incoming flux at the detector fell within the apparent spot size. Therefore, the FWHM estimated from the Gaussian approximation was multiplied by 2.58 according to Equation 5.3, in order to compare spot sizes of the Gaussian approximation to $d_{\text{PSF, theo}}$. The factor 2.58 was estimated by numerical evaluation of Equation 5.1. The results corresponded to full widths of 11.6 pixel and 13.3 pixel along directions of x and y , respectively. Compared to $d_{\text{PSF, theo}}$ this was a 2.4-fold to 2.8-fold increase between expectation and measurement. This indicated that as-designed imaging performance could not be achieved during assembly of the AtmoLITE EM prototype which was quantitatively confirmed by an MTF measurement as discussed in the next section.

$$d_{\text{width at 1\% of maximum}} = 2.58 \cdot \text{FWHM} \quad (5.3)$$

These measurements also allowed to relate a change in field angle to a change of pixel position on the detector. The first order distortion division model, Equation 5.4, which has already been tested on AtmoSHINE data by Liu [2019], was applied to all 100 measurements. In addition, the ratio between FOV angle and pixel r_{optics} is included to relate measured pixel coordinates to corresponding angular alignment obtained from the goniometer and rotation stage underneath the instrument. The distortion parameter was denoted K . The distortion model also allowed to estimate

the image centre x_c . Here, r denotes the distance between individual PSF spot centres and the image centre.

$$x_u = r_{\text{optics}} \cdot \left(x_c + \frac{x_d - x_c}{1 + K \cdot r^2} \right) \quad (5.4)$$

The designed optical system imaged the full FOV of 1.3° onto 861 pixel which corresponded to $r_{\text{optics, theo}} = 0.001557^\circ/\text{pixel}$ including a distortion parameter $K = 8.95 \times 10^{-8}$. Based on the measured PSF spot positions, a larger $r_{\text{optics, meas}} = (0.001639 \pm 0.000031)^\circ/\text{pixel}$ was observed corresponding to a FOV of 1.3° across

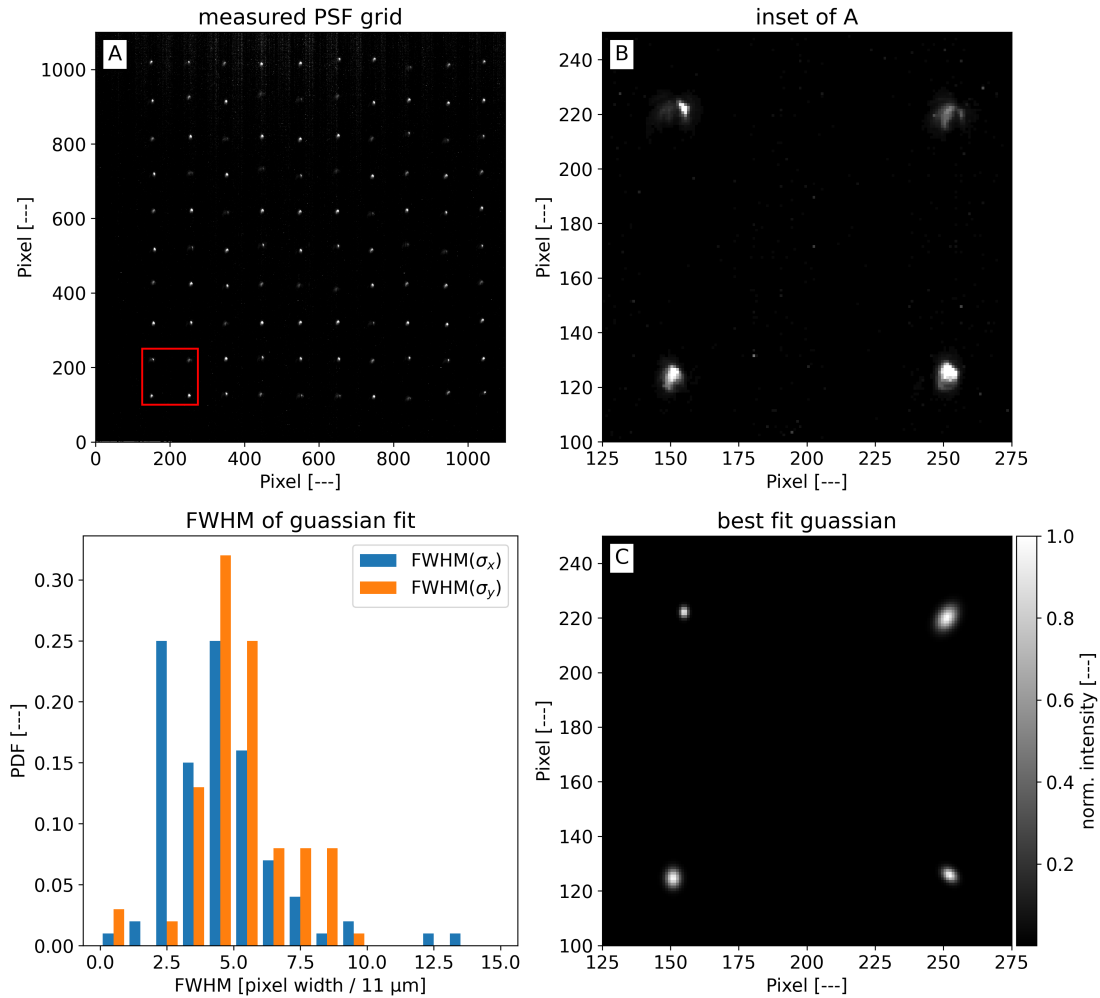


Figure 5.4: AtmoLITE EM PSF scan across full field of view. A total of 100×100 measurements was conducted (A). A comparison of normalised 2D-Gaussian approximations used to fit all PSF spots is provided for the inset of (A) in (B) and (C). The probability density function of derived PSF FWHM is separately shown for the horizontal (blue bars) and vertical direction (orange bars). It was expressed normalised to the pixel size of the GSENSE440Bsi sensor.

828 pixel at an estimated distortion parameter of $K = 2.53 \times 10^{-8}$. The uncertainty of $r_{\text{optics, meas}}$ corresponded to the accuracy of the goniometer stage used to incline the instrument. This deviation between designed and as-build performance was critical in view of the comparison between ACU field scans and instrument performance discussed in section 5.3. If upcoming instrument calibrations involve measurements of a calibrated radiance source, e.g. a black body source, this characterisation of the relation between FOV and image size will become even more important in order to estimate the as-build instrument's etendue in dependence on evaluated ROI over the detector.

Note that no distortion test target was used here. Typical test targets require an additional supplementary optics to virtually place the test target at infinity as required for the AtmoLITE optics. This inevitably introduces additional distortion of the supplementary optics. If the ACU were used for such a measurement, the expected impact of the ACU is an underestimation of the overall distortion by about -0.47% . This corresponds to 4 pixel over the full image. Moreover, one does not get information about the relation between FOV and pixel positions, $r_{\text{optics, meas}}$, because the distortion model using distortion test targets reduces to Equation 5.5.

$$x_u = \left(x_c + \frac{x_d - x_c}{1 + K \cdot r^2} \right) \quad (5.5)$$

Verification of AtmoLITE EM MTF

The tolerance estimations and compensation mechanisms mentioned in chapter 3 were analysed with respect to a diffraction limited optical design goal. However, the scientific purpose to derive temperature distributions with an altitude resolution of at least 1.5 km does not require a diffraction limited optical performance. In the following, the first experimental verification of the overall optics MTF is discussed. Obtained results indicated that the required altitude resolution was achieved, even though compensators in the front optics were partially omitted.

The experimental setup included a chequered pattern placed on top of the diffuser disc of the ACU. Pointing the AtmoLITE EM prototype at the ACU and using a white-light source LED source instead of the tunable laser, the chequerboard pattern was imaged by the AtmoLITE EM prototype. The resulting image is presented in the top left of Figure 5.5. Due to the non-homogeneous illumination, only a small ROI marked by the red frame was chosen for the demonstration only.

Similar to the method presented by Mooney [1995], a sum of Fermi functions were used to approximate the edge spread function (ESF) occurring at the transition between dark and bright areas. Consequently, the line spread function (LSF) was computed by analytically differentiating the ESF, Equation 5.7, whereby D , a_i , b_i and c_i were constant fit parameters. The LSF is the one-dimensional equivalent to the PSF, thus, the AtmoLITE EM MTF curve was obtained by taking the Fourier transform of the LSF and averaging over all rows within the ROI.

$$F(x) = D + \sum_{i=0}^2 \frac{a_i}{\exp[(x - b_i)/c_i] + 1} \quad (5.6)$$

$$\text{LSF} = \left| \frac{dF(x)}{dx} \right| = \left| \sum_{i=0}^2 \frac{a_i \exp[(x - b_i)/c_i]}{[\exp[(x - b_i)/c_i] + 1]^2} \right| \quad (5.7)$$

In order to compare the measured MTF to expectations and to separate contributions of ACU and AtmoLITE, three simulations were considered and their results are shown in Figure 5.5 (B) alongside the measured MTF. Displayed are the MTF curves expected by design, including a shift $\Delta\text{ACU} = 700 \mu\text{m}$ of the ACU focal plane representing a combination of the finite thickness of the chequered pattern foil and alignment uncertainties within the ACU, including an additional shift $\Delta\text{Optics} = 20 \mu\text{m}$ of the lens doublet $L2 + L3$ along the optical axis and the measured MTF. The frequency of evaluation $f_{\text{MTF}} = 4.23 \text{ mm}^{-1}$ was chosen corresponding to the required 1.5 km altitude resolution. Simulated defocus near

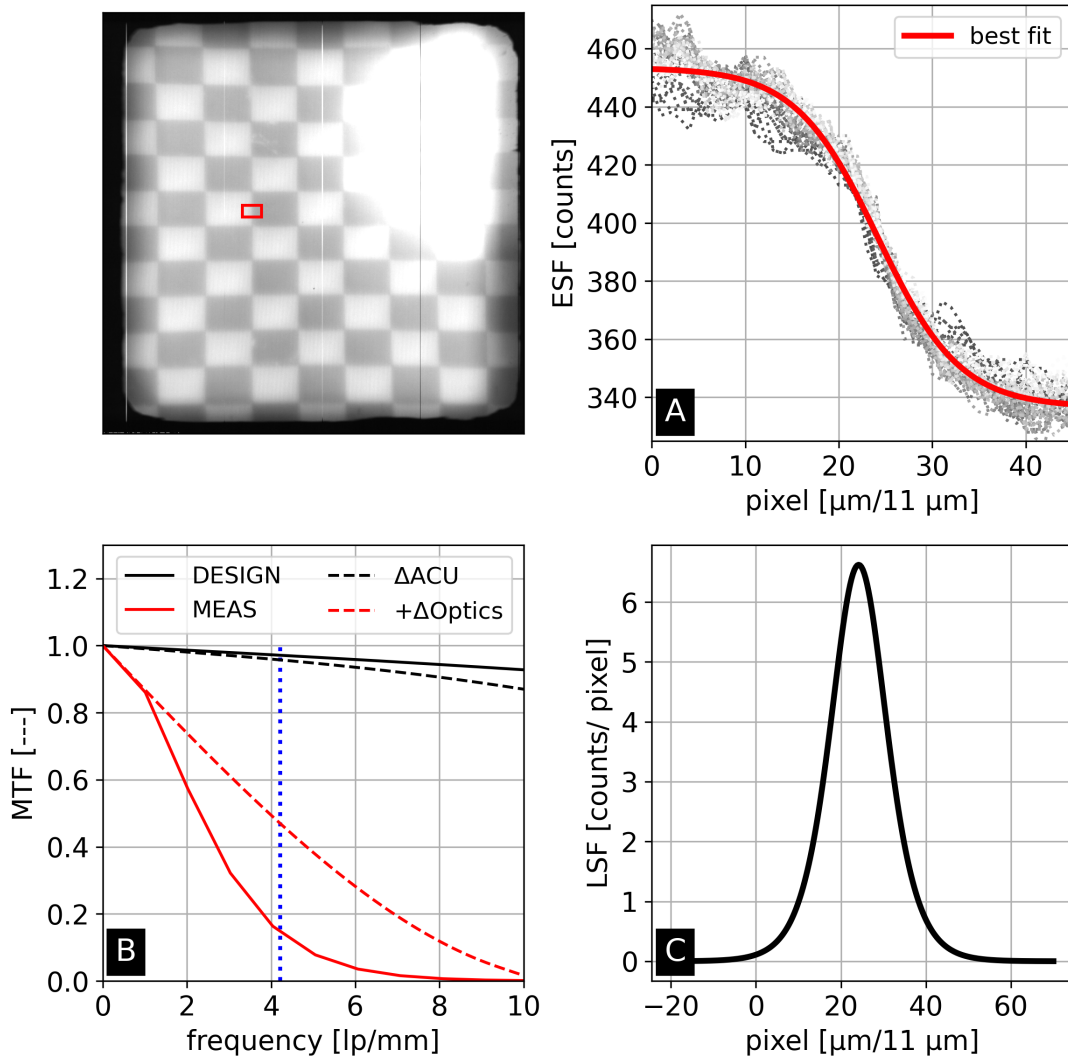


Figure 5.5: Experimentally derived MTF curve for the AtmoLITE EM prototype. A chequerboard pattern was placed near the ACU diffuser disc and imaged by the combined system of ACU and AtmoLITE instrument optics. At a single edge the ESF was derived (A) and transformed by differentiation into the LSF (C). By Fourier transformation the MTF was estimated and compared to values expected by design (B). For reference, the frequency corresponding to 40 altitude layers was indicated as blue dashed line.

the ACU focal plane did show negligible MTF changes of $\Delta\text{MTF} = -1\%$ of the combined systems which was a direct consequence of the small NA of the ACU. On the contrary, a single non-compensated deviation from design within the AtmoLITE front optics sufficed to reduce the MTF by at least $\Delta\text{MTF} = -50\%$ down to $\text{MTF}_{4.23} = 45\%$. In particular, this highlighted the sensitivity of the AtmoLITE optics imaging performance to manufacturing tolerances as the compensator around L2+L3 was not adjusted to compensate for deviations from design. Considering the

simulated deviation was chosen at $\Delta\text{Optics} = 20 \mu\text{m}$, thus, much lower than the tolerances of $\Delta\text{Optics} = 150 \mu\text{m}$ specified by the manufacturer of the AtmoLITE EM prototype opto-mechanics, an additional MTF degradation for the as-build system was expected. Indeed, the measured MTF was found to be as low as $\text{MTF}_{4.23} = 17\%$ at the frequency of evaluation $f_{\text{MTF}} = 4.23 \text{ mm}^{-1}$. Technically, these MTF values above zero allow to resolve different altitude layers up to the required 1.5 km separation but studies of the required deconvolution algorithms and related uncertainties introduced to the temperature retrieval scheme are still ongoing.

5.3 First interferograms of AtmoLITE

Two sets of interferograms were recorded with both instruments aligned to the ACU. Data for the AtmoLITE SHS prototype was acquired with the SHS aligned to smallest apparent fringe rotation but not glued. In case of the AtmoLITE EM prototype the SHS was fully procured including the cured adhesive. An overview of both measurement sets is provided in Figure 5.6 and Figure 5.7. In the following, properties of the recorded interferograms are discussed in order to demonstrate construction of the calibration matrix based on Equation 4.1.

Littrow wavenumber

Interferograms were evaluated over a region of interest (ROI) of 900×900 pixel. The integration time was set to $t_{\text{int}} = 300$ ms at a frame time of $t_{\text{frame}} = 1$ sec. Interferograms were recorded with the laser wavelength continuously modulated between 758 nm and 768 nm. Equation 5.8 was used to relate the observed interferogram fringe frequency $\nu(\lambda)$ and the wavenumber of observation σ to θ_L and G . Note that $\sigma = \lambda^{-1}$ and $\theta_L = G/2 \cdot \sigma_L$ yielded an almost linear relation between $\nu(\lambda)$ and λ where the magnification M and σ_L were the remaining fit parameters. $G = 300$ lp/mm was taken from the specifications of the gratings. Recall that the desired Littrow vacuum-wavenumber for the AtmoLITE SHS in air corresponded to $\sigma_L = 13048.86 \text{ cm}^{-1}$ (766.35 nm-vac).

$$\begin{aligned} \nu(\lambda) &= 4 \times \tan(\theta_L) \times (\sigma - \sigma_L) \times M \\ &= 4 \times \tan(\arcsin[G/2 \cdot \sigma_L]) \times (\lambda^{-1} - \sigma_L) \times M \end{aligned} \quad (5.8)$$

Evaluation was performed at the centre row (index 450). An FFT of the interferograms was performed and the peak position in spectral domain $\nu(\lambda)_{\text{peak}}$ was estimated. Substitution into Equation 5.8 allowed to derive the Littrow wavenumbers for both instruments. The results were $\sigma_{L, SHS} = 13054.33 \text{ cm}^{-1} \pm 0.07 \text{ cm}^{-1}$ and $\sigma_{L, EM} = 13048.28 \text{ cm}^{-1} \pm 0.14 \text{ cm}^{-1}$ for the AtmoLITE SHS and EM prototypes under ambient conditions, respectively.

The difference $\sigma_{L, SHS} - \sigma_L = 5.47 \text{ cm}^{-1}$ between as-build and designed system indicated that minimization of the fringe rotation, while relying on five degrees of freedom during alignment, was compensated by a change of the Littrow wavenumber towards larger wavenumbers for the AtmoLITE SHS prototype. A much smaller difference $\sigma_L - \sigma_{L, EM} = 0.6 \text{ cm}^{-1}$ was achieved for the AtmoSHINE EM prototype. However, due to the missing sixth degree of freedom during alignment and the corresponding gap between FWP and spacer in one SHS arm, non-controlled contractions of the SHS during curing of the adhesive caused a slight rotation of the interferogram fringes.

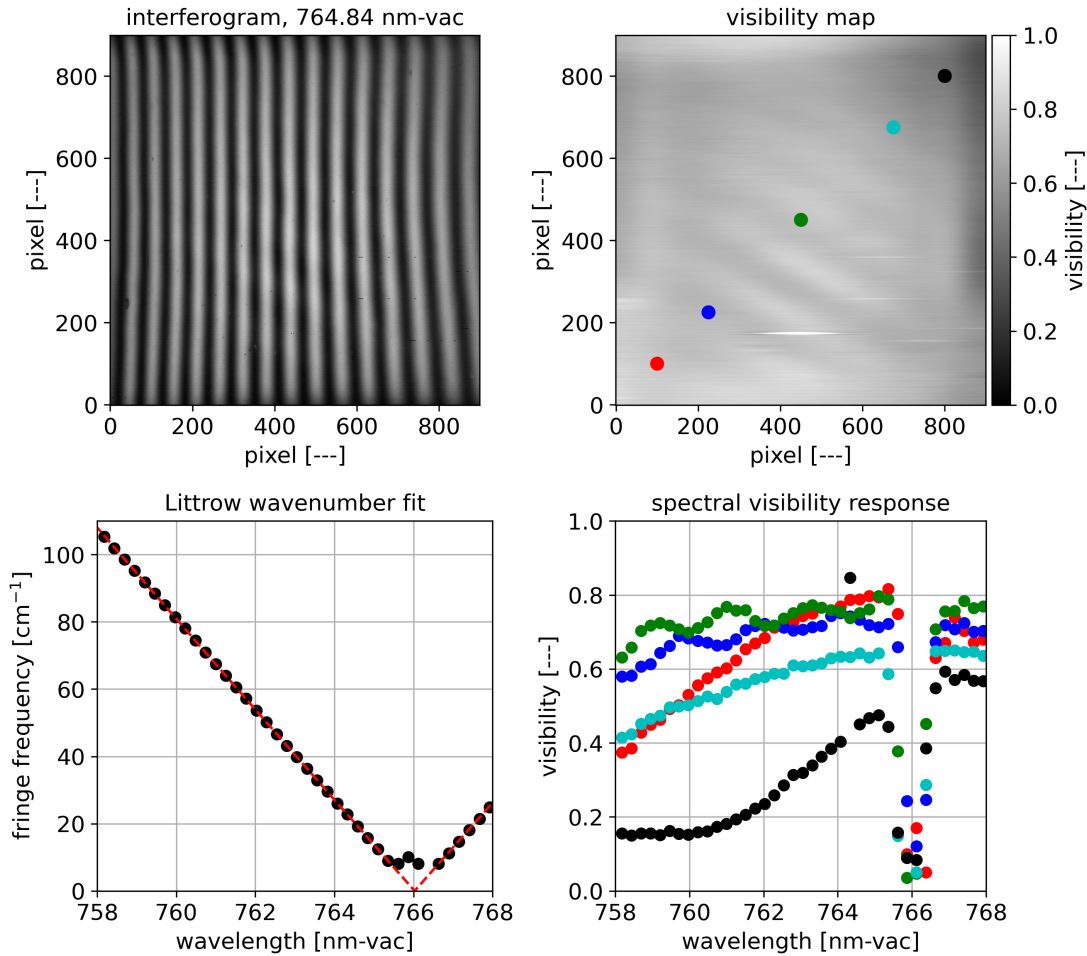


Figure 5.6: Demonstration of AtmoLITE SHS performance. The as-build visibility and Littrow wavenumber were evaluated within the full AtmoLITE bandpass. A region of interest of 900×900 pixel was chosen corresponding to a slightly larger than designed area on the detector. Comparison of interferogram visibility obtained at different wavelengths allowed to derive the spectral response expressed in terms of the visibility. Due to missing AR coatings and corresponding double-reflections within the SHS, the visibility maps exhibited a wavelength dependent modulation perpendicular to the dispersion direction. A Littrow wavenumber of $\sigma_L = 13054.33 \pm 0.07 \text{ cm}^{-1}$ was derived in good agreement with expectations. All data were obtained on 09.11.2020.

Interferogram fringe visibility

The interferogram fringe visibility was estimated by the algorithm already applied in section 3.5 to analyse simulated interferograms including necessary corrections of background and defect pixel as follows. Background measurement was subtracted from all interferograms which was obtained by the average of 20 measurements with the laser source turned off. Rows and columns containing defect pixel were interpolated based on the median values of neighbouring pixel. A low pass Savitzky-

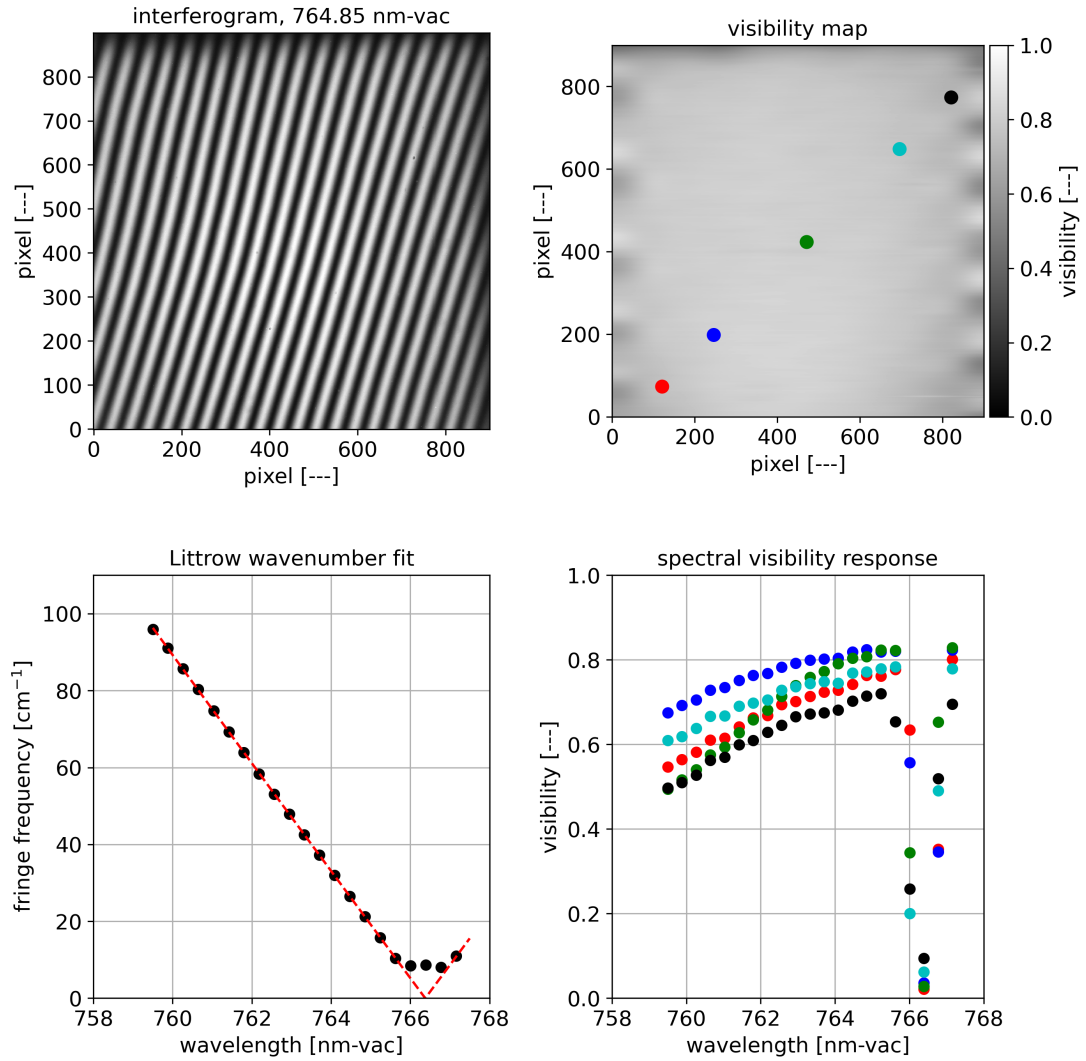


Figure 5.7: Evaluation of AtmoLITE EM visibility similar to Figure 5.6 including coated SHS components. Aforementioned modulation due to ghosting is no longer observed in the spectral visibility response. A lower than expected Littrow wavenumber of $\sigma_L = 13048.28 \pm 0.14 \text{ cm}^{-1}$ is derived. The expected on-axis visibility drop at high frequencies/ small wavelengths while maintaining overall high visibility near the interferogram edges is observed after fine adjustments of the camera optics was completed. All data were obtained on 31.03.2021.

Golay filter was applied to estimate the interferogram mean. Afterwards, the interferogram mean was corrected by the flat-fielding approach proposed by [Englert and Harlander, 2006b] whereby the assumption was made that interferogram mean and flat-field were related based on Equation 5.9. The envelop of the remaining modulated interferogram was estimated by a Hilbert transformation similar to the method proposed by Liu [2019]. One can further transform the modulated

interferogram part $\epsilon(x, \nu)$ by an FFT to visualize the change of relative spectral response of the instrument, though, one has to be careful when interpreting this response and to not confuse it with the absolute spectral response of the instrument! Recalling $V = 2 \cdot t_A t_B \cdot \epsilon(x, \nu) / (t_A^2 + t_B^2)$, the normalisation of $\epsilon(x, \nu)$ was similar to that of visibility up to contributions of the flat-field, thus, provided an effective spectral weighting which indicated how many of the collected photons (absolute spectral responsivity) at a given wavelength contributed to measured spectra. For instance, 68 % of photons measured at 765.36 nm were modulated whereas only 45 % of measured photons at 759.50 nm contributed to observed spectra. An example of this calculation is shown in Figure 5.8 and Figure 5.9 for interferogram crosssections obtained with the AtmoLITE EM prototype. The last step was the estimation of the phase and phase distortion of the interferograms. Here, the method proposed by Englert et al. [2004] was used. The method relied on a forward and backward FFT of the modulated interferogram part whereby a high-pass was used after forward FFT in order to exclude low frequency components. Here, frequencies between 0 cm^{-1} and 5 cm^{-1} were excluded and the estimated phase distortion is shown in Figure 5.10. The set of equations governing aforementioned interferogram properties is appended in Equation A.13 to Equation A.18.

$$I(x)_{mean} = t_A^2 + t_B^2 \quad (5.9)$$

A closer look on polychromatic flat field data is provided in Figure 5.11. For reference, a single interpolated ACU angular scan obtained at $\lambda = 759.001 \text{ nm}$ was overlaid (cf. Figure 4.26). The overlaid ACU scan is provided with and without distortion correction as seen by the AtmoLITE EM prototype. The comparison showed the great importance to characterise the FOV angle to pixel relation and distortion ahead of visibility and flat-field characterisations as the nominal field of AtmoLITE corresponded to 848 pixel instead of the designed 861 pixel. Thus, the ACU profile had to be considered less far along the detector whereby the projection was obtained by applying an inverse distortion to the ACU profile data. The inverse distortion was based on the parameters $r_{optics, meas}$ and K experimentally obtained for the AtmoLITE EM instrument. The shown data further relied on the assumption that angular ACU scan measurements and AtmoLITE instrument alignment to the ACU yielded the same FOV centre. In addition, with the sparse data set of angular ACU scans a rotation around the optical axis between the rectangular FOV of AtmoLITE with respect to the rectangular ACU top-hat profile could not be investigated. When looking at a cross-section such as Figure 5.11, the apparent

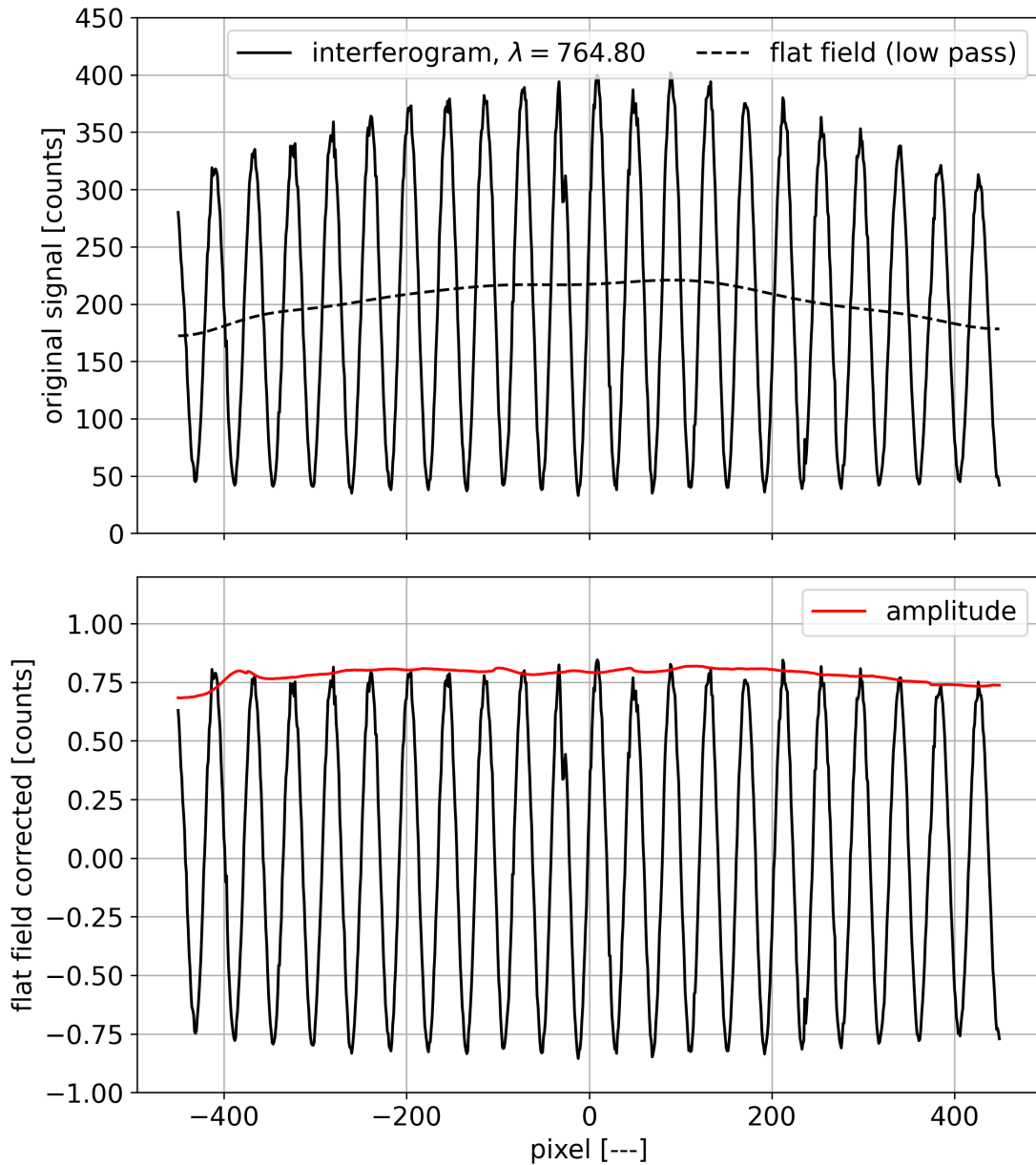


Figure 5.8: Interferogram crosssection at 764.80 nm obtained with the AtmoLITE EM prototype. A low pass Savitzky-Golay filter was applied to the data which yielded a smooth approximation of the flat field description (top). The modulated interferogram part was isolated after flat field correction (bottom). A Hilbert transformation was used to estimate the amplitude envelope of the flat-field corrected interferogram.

ACU profile width would need to be stretched. Missing this correction of the ACU profile width, the corrected flat field started to diverge towards the edge of the ROI.

Data sets were normalised to the centre of the interferogram which revealed that the AtmoLITE EM prototype flat-field had a slight wavelength dependence. This was best seen by a shift of the maximum of the flat-field occurring at different positions

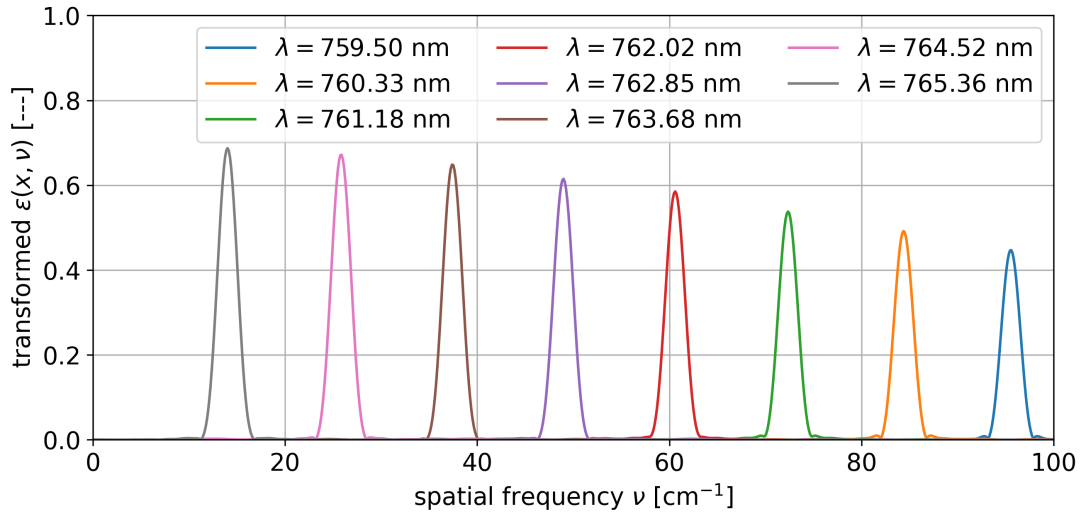


Figure 5.9: Derived AtmoLITE EM modulation efficiency. Shown is the AtmoLITE EM spectral response in terms of the Fourier transformed modulation efficiency. The smooth line-shapes and low side-lobe contributions were obtained after flat field and phase correction.

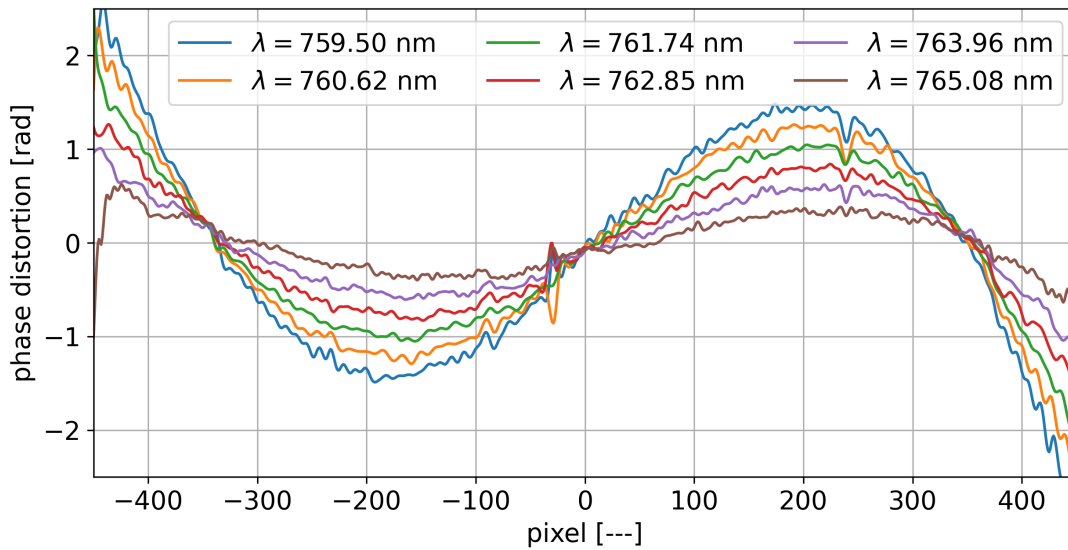


Figure 5.10: Derived phase distortion of the AtmoLITE EM. Shown is the monochromatic phase distortion obtained within the AtmoLITE bandpass. An overall increase of the phase distortion in dependence on wavelength was observed from low to high fringe frequencies. Near pixel index -30 and 230 detector artefacts were not fully corrected, thus, the phase distortion was locally disturbed.

along the spectral direction. Comparing the outermost maxima at wavelengths of $\lambda = 759.5$ nm and $\lambda = 761.18$ nm, the shift was as large as $\Delta x = 210$ pixel. As the data shown here relied on the approximation of the interferogram mean by

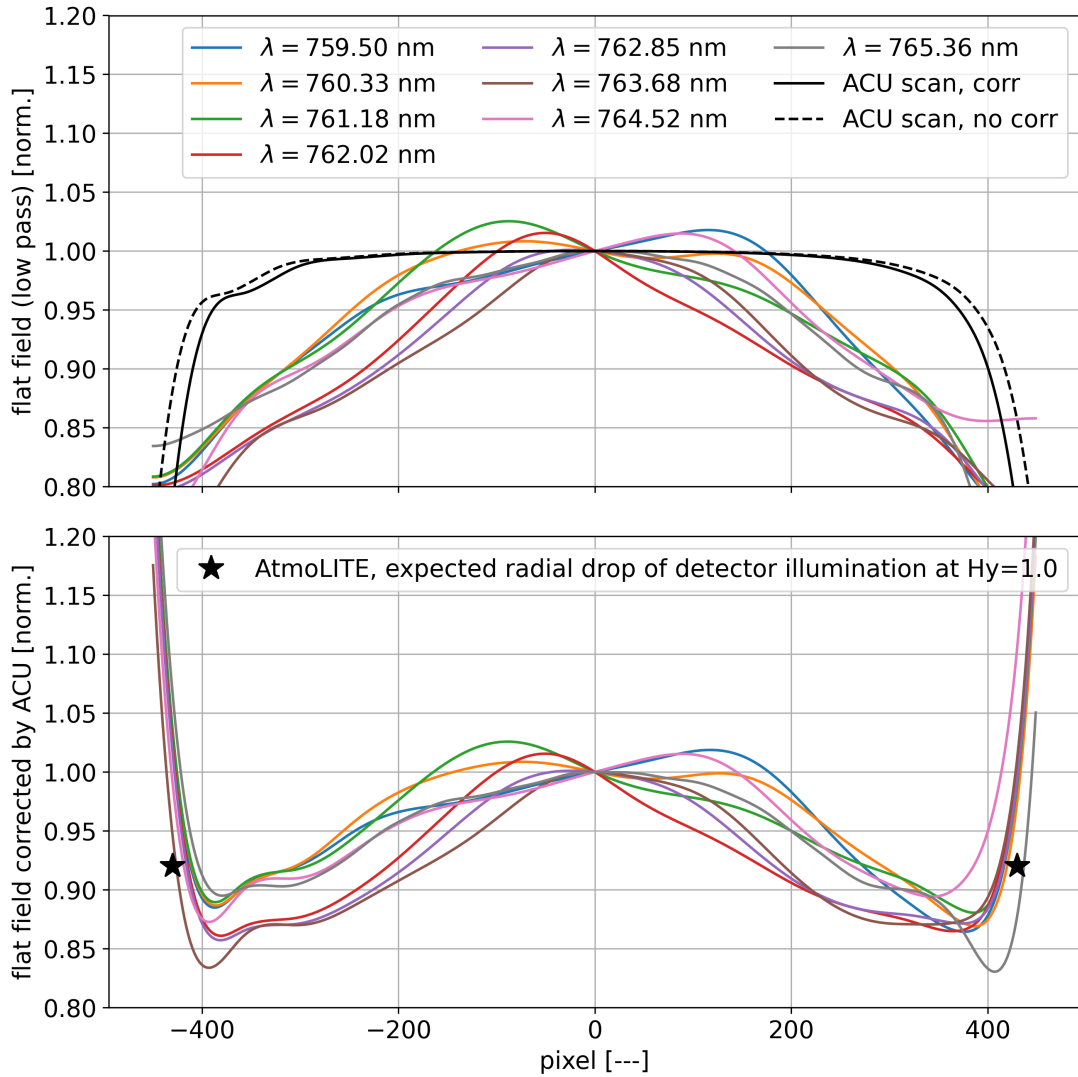


Figure 5.11: AtmoLITE EM polychromatic flat field description at different wavelengths (top). Assuming ideal alignment between AtmoLITE and the ACU, the radial drop of the source radiance was corrected (bottom). The expected radial drop of detector illumination due to transmission losses of the AtmoLITE optics is indicated by a star. Further details are discussed in the text.

means of a Savitzky-Golay filter, it is recommended to verify this approximation once flat field measurements become available. The wavelength dependence could then be directly included in the instrumental line shape description by substitution of $t_{A|B}^2 \rightarrow t_{A|B}^2(x, \nu)$. Note that the radial drop in relative detector illumination remaining after correction by the ACU profile is expected by design of the AtmoLITE optics. This drop was expected to be as large as 8 % at a field angle of 0.65° relative to the centre of the FOV. After correction of the ACU radial drop, the apparent drop in relative illumination was still twice as large as expected. The difference

could be caused by vignetting of the as-built instrument aperture if lens mounts and retaining rings are not perfectly centred on the optical axis.

A direct impact on visibility is not expected because visibility is equivalent to the ratio of the modulation amplitude and the flat-field. In particular, visibility is given by $V = 2 \cdot t_A t_B \cdot \epsilon(x, \nu) / (t_A^2 t_B^2)$ where the radial drop of relative detector illumination is cancelled out. Therefore, the visibility is also not affected by aforementioned correction of the ACU profile relative illumination drop. This allowed a full analysis of the achieved AtmoLITE EM interferogram fringe visibility while missing a precise full field description of the ACU. The ACU profile correction is still important to consider, if one were to analyse the spectral resolution of AtmoLITE because the radial drop of the ACU top-hat profile effectively broadens the AtmoLITE line-shape, in particular reduces the apparent spectral resolution.

For direct comparison of visibility, five points were chosen across the detector as indicated in Figure 5.7. The corresponding pixel coordinates (X, Y) were (121, 73) for red, (246, 198) for dark blue, (471, 423) for green, (696, 648) for light blue, and (821, 773) for black dots. X and Y corresponded to the horizontal (dispersion) and vertical (altitude) direction of the detector. The green dot was centred to the distortion centre, in particular marking the FOV center. The red and black dots are at a field angle corresponding to 0.78° (0.55° in both dispersion and altitude direction). The derived visibilities at $\lambda = 764.85$ nm were $V_{\text{red}} = 0.76$ %, $V_{\text{d. blue}} = 0.83$ %, $V_{\text{green}} = 0.81$ %, $V_{\text{l. blue}} = 0.77$ % and $V_{\text{black}} = 0.71$ %. At $\lambda = 759.83$ nm the visibilities were $V_{\text{red}} = 0.56$ %, $V_{\text{d. blue}} = 0.69$ %, $V_{\text{green}} = 0.52$ %, $V_{\text{l. blue}} = 0.62$ % and $V_{\text{black}} = 0.51$ %. This demonstrated that near the FOV center a drop in visibility occurred towards higher interferogram fringe frequencies, as expected by simulated results shown in Figure 3.19. However, measured visibility was about 10 % to 15 % lower than expected at wavelengths ranging from $\lambda = 759.83$ nm to $\lambda = 764.85$ nm. The difference increased towards smaller wavelengths/ higher interferogram fringe frequencies. Near the Littrow wavenumber, in particular below wavenumbers of $\sigma = 13061$ cm^{-1} the algorithm did not accurately determine the visibility and the instrumental line shape fit failed.

Lastly, a remark about a potential source of stray light due to multiple reflections within the AtmoLITE SHS is discussed based on interferograms obtained with the AtmoLITE SHS prototype. The field-widening prisms of the AtmoLITE SHS prototype were not anti-reflection coated, giving rise to multiple reflections within the field-widening prisms, similar to a Fabry-Perot etalon. The measured interferograms therefore showed an additional interference pattern perpendicular to the dispersion direction. The main impact was an oscillation of the derived visibility in dependence

on wavelength. The effect was best seen at the two pixel positions marked in green and blue in Figure 5.6). Over a spectral range of $\lambda = 1$ nm the observed impact on visibility was as large as ± 4 %. However, not observing this interference in the AtmoLITE EM prototype indicated that proper anti-reflection coatings could suppress this interference and no impact on upcoming instruments is expected. If the interference pattern of these multiple reflections always occurs perpendicular to the dispersion direction could not be investigated.

All in all, this experimental verification of performance demonstrated that the AtmoLITE EM instrument prototype behaved as expected. In particular, the iterative alignment procedure of front and camera optics has been successfully been conducted such that overall system imaging capabilities and interferogram fringe visibility could be assessed. The effective FOV extent was measured by a PSF scan across the FOV. The result was further used to estimate the distortion without additional optics between instrument and source (target). A preliminary result for overall system MTF was derived which showed that a vertical resolution of 1.5 km is feasible at a reduced contrast. In particular, $MTF_{4.23} = 17$ % was found in contrast to expected values of $MTF > 95$ %. Tighter manufacturing tolerances and inclusion of all compensation mechanisms in upcoming instrument assemblies are expected to improve the MTF towards expected values. Visibility was found to be slightly below expected values with differences of up to 15 % at a wavelength of $\lambda = 759.83$ nm, but was overall above $V > 50$ % under ambient conditions. Derivation of the instrumental line shape description was also demonstrated. In the following section the derived instrumental line shape is finally used to derive a first estimate of the AtmoLITE EM prototype temperature retrieval uncertainty.

5.4 Expected temperature retrieval uncertainty

In the following, an uncertainty estimate is derived for the AtmoLITE EM prototype regarding temperature retrieval based on measured interferograms. The estimate is provided based on the derived instrumental line-shape function (ILS) only. In particular, modelling of the atmosphere including satellite orbit, temperature gradients across the FOV caused by atmospheric dynamics or uncertainties related to retrieval algorithms and image manipulations such as distortion correction are not considered. Included are measured interferogram phase and flat-field/baseline, shot noise, all emission lines between 13047 cm^{-1} and 13160 cm^{-1} with a relative contribution of more than $> 1 \%$ with respect to O_2 A-band peak radiances at $T_{rot} = 180 \text{ K}$, integration time, number of images per averaged interferogram, measured spectral modulation efficiency and the impact of uncertainties encountered during characterisation of the ACU. Data sets concerning detector defects such as hot pixel, a non-uniform or non-linear detector responsivity and stray light are not yet available, thus, these effects are not corrected and remain as potential artefacts. The goal is to express the uncertainty in terms of temperature differences based on a comparison of ideal input spectra before and after modulation by instrument noise and calibration uncertainties.

The starting point is a list of the known emission lines of the atmospheric O_2 A-band emission which is taken from the HITRAN database and appended in Table A.5. For each emission wavelength a single interferogram is generated based on a smoothed linear interpolation of the measured instrumental line shape discussed in section 5.3. The interpolation is performed separately for interferogram phase, modulation efficiency and flat-field, and the full interferogram is obtained based on Equation A.13 where each interferogram is scaled by the corresponding radiance $B(x, \nu)$. The radiance is calculated based on Equation 2.11. All interferograms corresponding to individual emission lines are summed up and an FFT is applied to obtain the spectrum. An example of the interferogram and different spectra is provided in Figure 5.12 for a rotational temperature of $T_{ref} = 180 \text{ K}$. The spectral axis is provided in units of interferogram fringe frequency and demonstrates that the full O_2 A-band spectrum can be measured by the AtmoLITE instrument well below the designed fringe frequency limit of $\nu = 150 \text{ lp/cm}$. Note that the ILS discussed here was obtained without the bandpass filter in-front of the optics, hence, one additional pair of emission lines between 13047 cm^{-1} and 13057 cm^{-1} contributes at fringe frequencies of 4.4 lp/cm and 5.7 lp/cm .

In order to evaluate the impact of uncertainties contained in interferogram domain but propagated into spectral domain or to include noise in the temperature

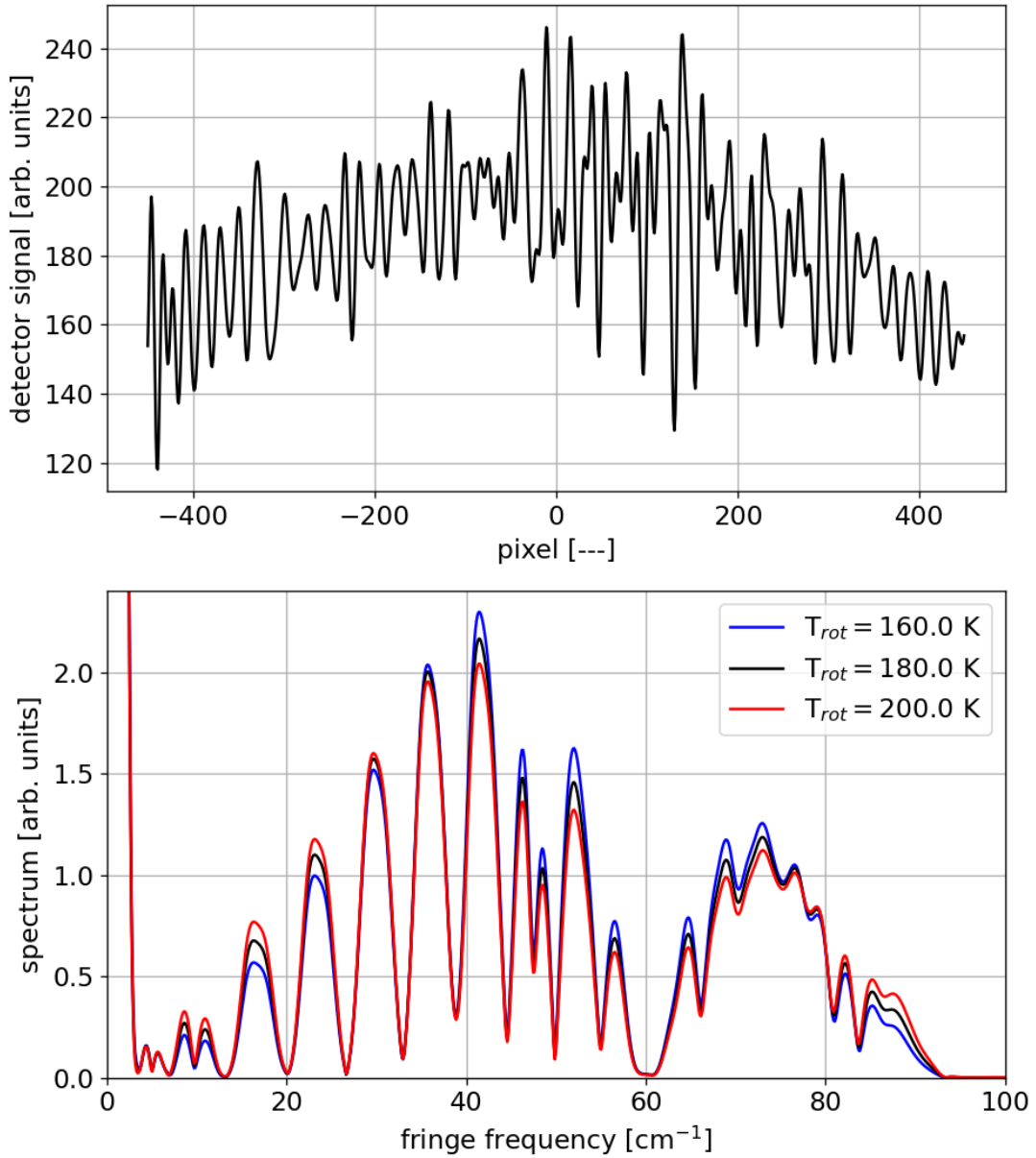


Figure 5.12: Expected atmospheric spectrum based on the measured AtmoLITE EM instrumental line-shape. The monochromatic instrumental line-shape data is interpolated and weighted according to expected relative atmospheric radiance levels. Starting in interferogram domain (top) atmospheric spectra are derived by Fourier transformation (bottom). Note that the first two emission lines at 4.4 lp/cm and 5.7 lp/cm will be suppressed below the noise level once the AtmoLITE bandpass filter is available.

retrieval, a Monte Carlo ansatz is used. Spectral variations of t_A , t_B , $\epsilon(x, \nu)$ and $\Phi(x, \nu)$ are simulated by applying a small, random wavelength shift to the wavelength axis used during interpolation of the ILS. This is equivalent to reading errors by the operator and/or calibration uncertainties of the spectrum analyser used

during acquisition of the measured data. A standard uncertainty of $u_\lambda = 0.001$ nm is assumed which is at least one order of magnitude larger than the spectrum analysers precision used during the acquisition of the ILS data. The corresponding ILS description of the individual interferograms transforms according to Equation 5.10, in particular, $B(x, \nu)$ is not evaluated at different wavelengths! For clarity, the wavelength and pixel dependence of the flat-fields $t_{A|B}(x, \nu) \rightarrow t_{A|B}(x, \lambda + u_\lambda)$ is not shown and the abbreviation $\nu(\lambda + u_\lambda) = \nu_{u_\lambda}$ is used.

$$\begin{aligned}
I(x, \nu) &= B(x, \nu) \cdot \left\{ t_A^2 + t_B^2 + 2t_A t_B \cdot \epsilon(x, \nu) \cdot \cos [2\pi\nu x + \Phi(x, \nu)] \right\} & (5.10) \\
&= B(x, \nu(\lambda)) \cdot \left\{ t_A^2 + t_B^2 + 2t_A t_B \cdot \epsilon(x, \nu(\lambda)) \cdot \right. \\
&\quad \left. \cos [2\pi\nu(\lambda)x + \Phi(x, \nu(\lambda))] \right\} \\
&\rightarrow B(x, \nu(\lambda)) \cdot \left\{ t_A^2 + t_B^2 + 2t_A t_B \cdot \epsilon(x, \nu(\lambda + u_\lambda)) \cdot \right. \\
&\quad \left. \cos [2\pi\nu(\lambda + u_\lambda)x + \Phi(x, \nu(\lambda + u_\lambda))] \right\} \\
&= B(x, \nu) \cdot \left\{ t_A^2 + t_B^2 + 2t_A t_B \cdot \epsilon(x, \nu_{u_\lambda}) \cdot \right. \\
&\quad \left. \cos [2\pi\nu_{u_\lambda}x + \Phi(x, \nu_{u_\lambda})] \right\} \\
&= I(x, \nu_{u_\lambda}) & (5.11)
\end{aligned}$$

In section 4.7 two uncertainties regarding uniform aperture illumination and defocus within the ACU are discussed based on interferogram simulations. These are denoted u_{aper} and u_{theo} and may be replaced by more accurate estimates in upcoming studies once experimental data becomes available. Both uncertainties impact the modulation efficiency of the SHS, hence, are included as a weighting factor of the modulation efficiency $\epsilon(x, \nu_{u_\lambda}) \rightarrow \epsilon(x, \nu_{u_\lambda}) \cdot u_{aper} \cdot u_{theo} = \epsilon_u(x, \nu_{u_\lambda})$. Based on the largest measured ACU aperture illumination non-uniformity of $7\% \pm 6\%$ and referring to Figure 4.30, a positive visibility bias is expected distributed around $u_{aper} = +0.6\% \pm 0.2\%$ in the Monte Carlo ansatz. In contrast, u_{theo} has to be scaled by wavelength in accordance to Equation 5.12 and yields a negative visibility bias. The magnitude considered in the Monte Carlo ansatz is given in Equation 5.12 whereby $\Delta\lambda = \lambda_L - 759.83$ nm ≈ 6.63 nm is used. It corresponds to the expected visibility decrease (cf. Figure 4.31) at an ACU defocus of 64 μ m (cf. section 4.5). Note that u_{theo} is used here as the expected upper limit due to limitations of the interferogram simulation of the combined system of ACU and AtmoLITE instrument, and expectations based on first principles, e.g. the ACU diffraction limited depth of focus of $d_{ACU, focus} \approx 320$ μ m, would yield negligible impact on visibility ($u_{theo} \rightarrow 0$). Hence, the following results are a conservative estimation of expected temperature retrieval uncertainty.

$$u_{theo}(\lambda) = 1 + \frac{-0.03}{\Delta\lambda} \cdot (\lambda_L - \lambda) \quad (5.12)$$

The ACU flat-field correction yields an uncertainty u_{meas} which is based on the accuracy of the ACU angular scans discussed in section 4.6. Dividing the measured flat-field by the ACU top-hat illumination profile propagates this relative uncertainty directly into the interferogram, hence, u_{meas} is considered as a scaling factor to the flat-field $t_{A|B} \rightarrow t_{A|B} \cdot u_{meas}$. Based on the discussion in section 4.6, u_{meas} is chosen distributed around unity with a standard uncertainty of 0.6 %, $u_{meas} = 1 \pm 0.006$, and the interferogram transform as follows:

$$I(x, \nu_{u_\lambda}) \rightarrow I(x, \nu_{u_\lambda}) \cdot u_{meas} \quad (5.13)$$

Similar to u_{meas} , an uncertainty is attributed to each interferogram measurement used for estimation of the ILS. This uncertainty is denoted u_{power} and refers to the precision either of the irradiance monitoring photo-diode within the ACU or the laser source power monitoring by a fibre optic power meter. A typical fibre optic power meter of type PM20 manufactured by Thorlabs provides an accuracy of $u_{meas} = \pm 0.25$ dB (± 5.6 %) whereas the combination of a DDCPA-300 and Fluke 115 digital multimeter already used during the ACU characterisation provides an uncertainty of $u_{meas} = 0.5$ % relative to the measured signal. In upcoming studies, the latter option is recommended and used in the following discussion. Because noise levels at the photo-diode were typically not resolved by the multimeter, a slightly higher value $u_{meas} = \pm 0.5$ % is used, similar to the discussion in section 4.6 where the same photo-diode and readout was used during the ACU characterisation.

$$I(x, \nu_{u_\lambda}) \rightarrow I(x, \nu_{u_\lambda}) \cdot u_{meas} \cdot u_{power} \quad (5.14)$$

Finally, all noise modulated interferograms are summed up and the corresponding reference spectrum S_{ref} is obtained by FFT.

$$\mathcal{F}[I_{tot}] = \mathcal{F}[I_{tot}] \quad (5.15)$$

$$= \mathcal{F}\left[\sum_{\lambda} I(x, \nu_{u_\lambda})\right] \quad (5.16)$$

$$= S_{ref} \quad (5.17)$$

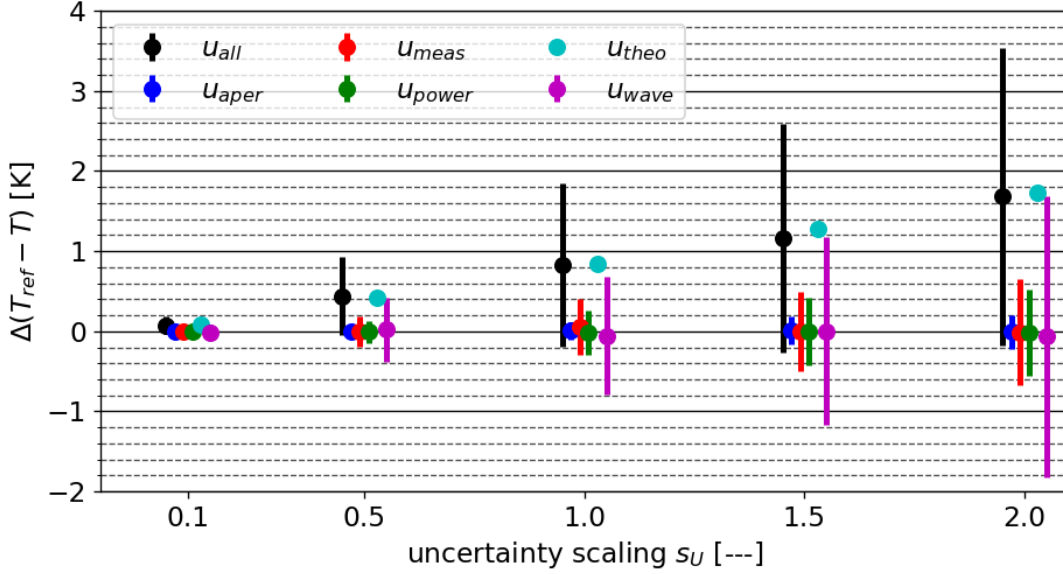


Figure 5.13: Expected AtmoLITE temperature retrieval uncertainty due to calibration of the ILS. The overall temperature retrieval uncertainty u_{all} is shown separated into uncertainties related to characterisation of the ACU top-hat profile u_{meas} , ACU aperture illumination uniformity u_{aper} , limitations of current interferogram fringe visibility simulations u_{theo} , laser power monitoring during interferogram acquisition u_{power} , and traceability of the laser wavelength during interferogram acquisition u_{wave} .

A spectral fit based on the noise free ILS is performed where the rotational temperature T_{rot} , a scaling parameter s and offset o are used as variable parameters. The fit is optimized in order to find a new temperature T_2 corresponding to the best fit ILS whereby ILS(λ) refers to the interferogram without weighting of the radiance.

$$\min \{S_{ref} - S\} = \min \{S_{ref} - s \cdot \mathcal{F}[I_{tot}] + o\} \quad (5.18)$$

$$= \min \left\{ S_{ref} - s \cdot \mathcal{F} \left[\sum_{\lambda} I(x, \nu(\lambda)) \right] + o \right\} \quad (5.19)$$

$$= \min \{S_{ref} - s \cdot [\text{ILS}(x, \nu(\lambda)) * B(x, \nu(\lambda))] + o\} \quad (5.20)$$

$$\rightarrow \min \{S_{ref} - s \cdot [\text{ILS}(x, \nu(\lambda)) * B(T_2)] + o\} \quad (5.21)$$

Repeating the calculation $N = 200$ times and calculating the temperature differences $\Delta(T_{ref} - T_2)$ yields the distributions shown in Figure 5.13. In addition, the full Monte Carlo simulation is repeated four more times with the individual uncertainties u_i scaled by the parameter s_u , $u_i \rightarrow u_i \cdot s_u$. $s_u = 1$ corresponds to aforementioned magnitudes of u_i .

The overall uncertainty at $s_u = 1$ is $u_{all} = 0.8 \text{ K} \pm 1.0 \text{ K}$ whereby a bias of -0.8 K with respect to T_{ref} is apparent and the real (random) uncertainty is

± 1.0 K. This bias is solely caused by u_{theo} and shall be investigated experimentally in upcoming studies. The most direct approach would be to continuously monitor the interferogram visibility while simultaneously shifting the diffuser disc along the optical axis of the ACU. The obtained visibility change in dependence on diffuser shift would then provide a direct measure of u_{theo} , in particular verifying if current conservative simulation results accurately predict as-build performance.

Individual uncertainties are $u_{aper} = 0.0$ K \pm 0.1 K, $u_{meas} = 0.1$ K \pm 0.3 K, $u_{power} = 0.0$ K \pm 0.3 K and $u_{wave} = -0.1$ K \pm 0.7 K. The bias contributed by u_{meas} and u_{wave} is a numerical artefact caused by rounding errors and the small number of Monte Carlo runs (N=200). It is apparent that u_{wave} has the largest uncertainty contribution to $\Delta(T_{ref} - T)$. Hence, it is recommended to make use of the smallest accuracy of $\Delta\lambda = \pm 0.0001$ nm reported for the 771 Series Laser Spectrum Analyzer available at the BUW for the final AtmoLITE calibration which reduces expected contribution to $u_{wave} \rightarrow \pm 0.1$ K.

In addition to aforementioned uncertainties, inherent to the calibration of the ILS, contributions by noise are important. Based on preliminary tests results of the chosen GSENSE400bsi detector, the overall noise is dominated by shot noise and the contributions to consider are readout noise $u_{read} = 3.5$ e⁻, dark current $u_{dc} = 1.5$ e⁻/s at $T_{GSENSE} = 0^\circ\text{C}$ as expected nominal operational temperature in-orbit, fixed pattern noise $u_{fp} = 2$ e⁻ and the number of incoming photons $I_{CMOS} = 370$ ph/s/pixel derived for day-time observations at a tangent altitude of 87 km in section 3.10. Here, $I_{CMOS} \cdot t_{int}$ is denoted n_{ph} to avoid confusion with the interferogram. The shot noise is then given by $u_{shot} = \sqrt{n_{ph}}$. Considering the quantum efficiency $QE = 0.7$ and the conversion rate $\alpha = 1.9$ DN/e⁻ from electrons to digital counts for the GSENSE400bsi when operated in gain mode $x7.25$, the overall signal to noise ratio is given by Equation 5.22.

$$\text{SNR} = \frac{\alpha \cdot QE \cdot n_{ph}}{\sqrt{\alpha^2 \cdot QE^2 \cdot n_{ph} + \alpha^2 \cdot (u_{read}^2 + [u_{dc} \cdot t_{int}]^2 + u_{fp}^2)}} \quad (5.22)$$

A set of simulations is conducted based on Equation 5.22 in order to assess the temperature retrieval uncertainty in dependence on SNR. Input signal levels range from 150 ph/s/pixel to 500 ph/s/pixel whereby the integration time is varied between $t_{int} = 1$ sec and $t_{int} = 8$ sec, in particular covering all expected radiance levels and foreseen integration times as presented in Figure 3.23. The result is presented in Figure 5.14 for a binning of 20 rows corresponding to 43 resolved altitude layers within the nominal FOV. An exponential fit is used as shown in

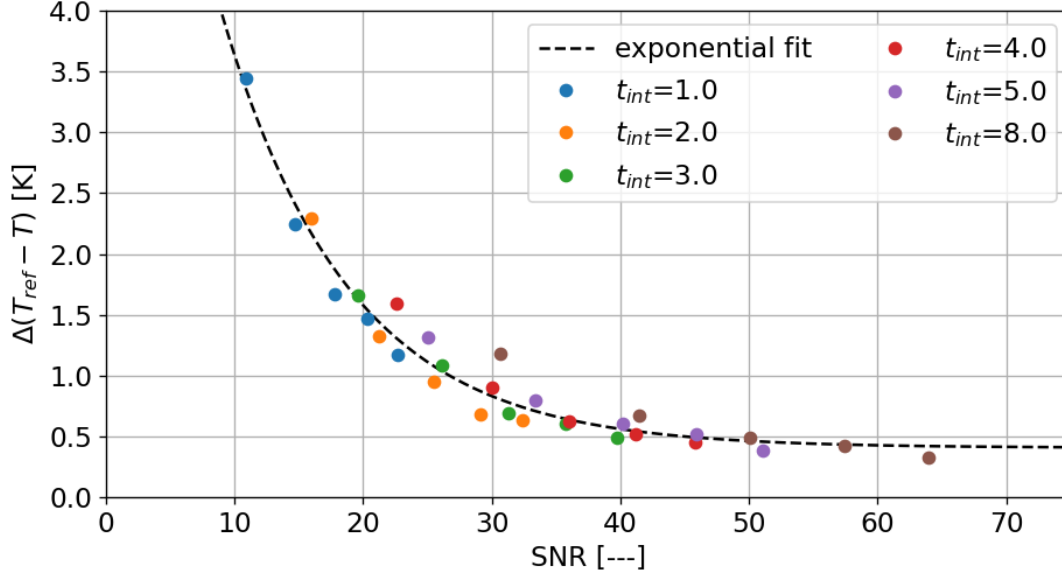


Figure 5.14: AtmoLITE EM noise contribution to temperature retrieval uncertainty.

Equation 5.23 in order to derive an analytical relation between SNR and $\Delta(T_{ref} - T)$ which corresponds to the expected asymptotic limit if a large number of Monte Carlo runs is conducted.

$$\Delta(T_{ref} - T)(\text{SNR}) = 8.9 \cdot \exp\left\{-\frac{\text{SNR}}{9.9}\right\} + 0.4 \text{ [K]} \quad (5.23)$$

It is apparent that the desired threshold of $\Delta(T_{ref} - T) = \pm 1.5$ K is achieved at integration times longer than $t_{int} > 4$ s. However, including the noise contribution by calibration u_{all} , the combined standard uncertainty becomes $u_{\text{AtmoLITE}} = \sqrt{u_{all}^2 + u_{noise}^2}$. Hence, either a reduction of the uncertainties during calibration from $s_u = 1$ down to $s_u = 0.5$ or an increase of integration time in-orbit to $t_{int} = 8$ sec is recommended to maintain $u_{\text{AtmoLITE}} < \pm 1.5$ K. It is noteworthy that a reduction of the calibration uncertainties down to $s_u = 0.1$ could enable integration times as small as $t_{int} = 2$ sec while maintaining $u_{\text{AtmoLITE}} < 1.5$ K.

6

Summary and final remarks

In this work, a redesign of the limb-sounding instrument AtmoSHINE towards the AtmoLITE instrument and its first experimental verification of performance have successfully been conducted. In addition, a novel calibration light source called AtmoLITE Calibration Unit (ACU) tailored to characterise the AtmoLITE spectral response has been developed. Critical performance requirements of the ACU regarding uniform aperture illumination and uniform FOV coverage during calibration of the AtmoLITE instrument were identified, characterised by experiment and their expected impact on the AtmoLITE temperature retrieval uncertainty estimated.

Regarding the design of the AtmoLITE instrument, the first milestone was the development of a new spatial heterodyne spectrometer (SHS) design. The new design now allows observation of the O₂ A-band spectrum over an extended spectral range compared to AtmoSHINE, in particular covering the full spectral range between 13047.0 cm⁻¹ and 13160.8 cm⁻¹. Necessary design changes included an increase of the illuminated grating width from 7.1 mm to 15.2 mm, a reduction of the grating groove density from 1200 lp/mm down to 300 lp/mm and a shift of the Littrow wavenumber from 13127 cm⁻¹ towards 13047 cm⁻¹. In combination, these changes reduced the overall resolving power of the SHS from 16800 down to 9000 while still maintaining the desired temperature retrieval accuracy of below $\Delta T = \pm 1.5$ K. No changes were made to the selection of glass materials within the SHS in order to keep the minimization of thermal drifts within the SHS.

The second milestone was the adaptation of the new optics of the AtmoLITE instrument to the developed SHS. Apart from increases to the effective focal lengths of front and camera optics, necessary to match the larger illuminated grating area,

the new optical system includes multiple compensation mechanism to compensate manufacturing tolerances. In particular, compensation mechanisms in the front optics are used to adjust overall optics resolution whereas compensation mechanisms in the camera optics are primarily used to enhance interferogram fringe visibility. These mechanisms further allow to compensate changes of effective focal length when the instrument is moved from environments at ambient pressure to vacuum. A corresponding iterative alignment procedure was proposed but could only be verified under ambient conditions in this work. The analysis of the combined optical system of AtmoLITE optics and AtmoLITE SHS was further extended to include simulations of the expected interferograms. The quantity of interest was the interferogram fringe visibility which is seen as a direct measure of instrument performance regarding temperature retrieval uncertainty. Interferogram fringe visibility was analysed with respect to varying instrument temperature, surrounding pressure, manufacturing tolerances of the optics and alignment of the SHS. All simulations indicated that interferogram fringe visibility larger $V > 50\%$ is feasible over the full spectral range of AtmoLITE.

The third milestone was the development of the ACU which is build up from three core components as follows. At first, an integration sphere coupled to a tunable laser is used to uniformly illuminate a rotating diffuser disc. Secondly, the rotating diffuser disc breaks the spatial coherence of the laser source, thus, minimizing the impact of speckle noise during calibration. Lastly, a collimation optics is used to image the illuminated diffuser surface to the AtmoLITE instrument which creates a light stimulus similar to the atmospheric scene. A noteworthy property of the ACU is the restriction of the illuminated angular FOV of AtmoLITE by inclusion of a field stop between integrating sphere and rotating diffuser. By design, this stop confines the illumination to field angles of about $\pm 0.7^\circ$, thus, enabling calibration of the in-field interferogram fringe visibility of AtmoLITE without contributions of potential out-of-field stray light.

The last milestone was an experimental verification of performance of all optical systems: the isolated ACU, and the combined system of AtmoLITE optics and SHS in-front of the ACU. Achieved ACU aperture illumination was uniform by up to $7\% \pm 6\%$ and a uniform FOV coverage with a radial centre-to-edge drop of $-4.0\% \pm 1.2\%$ within a FOV of $\pm 0.5^\circ$ was observed. The expected impacts on the derived AtmoLITE temperature retrieval uncertainty were $u_{aper} = \pm 0.1$ K and $u_{meas} = \pm 0.3$ K, respectively. Including standard uncertainties related to the stability and monitoring accuracy of wavelength and laser source power during interferogram acquisition, in particular $u_{wave} = \pm 0.7$ K and $u_{power} = \pm 0.3$ K, the

total standard uncertainty estimate yielded $u_{all} = \pm 1.0$ K. It is expected that especially the contribution of u_{wave} can be reduced down to $u_{wave} = \pm 0.4$ K if wavelength monitoring with an increased precision of $\Delta\lambda = 0.5$ pm is used. In this case, the standard uncertainty is expected to decrease down to $u_{all} = \pm 0.6$ K. Additional uncertainty is expected due to noise contained in recorded AtmoLITE interferograms. At an integration time of $t_{int} > 8$ sec the expected impact of noise on the temperature retrieval uncertainty is better than $u_{noise} < 1.2$ K during daytime and limb-observation at a tangent altitude of 87 km. Therefore, the combined standard uncertainty expected for the AtmoLITE instrument in nominal operation becomes $u_{AtmoLITE} = 1.4$ K in this work. Imaging capabilities of the new AtmoLITE optics were evaluated based on evaluation of measured point-spread and modulation transfer function. Although, one compensating mechanism within the AtmoLITE front optics was omitted, the target resolution corresponding to an altitude separation of 1.5 km could be achieved. The measurements also allowed to demonstrate estimation of the overall AtmoLITE optics distortion characterisation. This showed that the assembled system imaged an angular FOV of $\pm 0.65^\circ$ onto 828 pixel instead of the designed 861 pixel.

Ongoing projects at the University of Wuppertal and the Research Centre Jülich and in preparation of the next in-orbit demonstration of AtmoLITE on INSPIRESat-4, already work on improving the ACU further in order to reduce the AtmoLITE temperature retrieval uncertainty presented here. These studies will address sources of uncertainty currently not addressed in this work. The three most important issues are as follows.

First of all, simulations discussed in section 4.7 show reduced interferogram fringe visibility obtained in the combined system which is expected to cause a bias in the retrieved temperature by up to $u_{theo} = -0.8$ K in dependence on defocus between ACU optics and the contained diffuser disc. Here, it is recommended to experimentally quantify the change of interferogram fringe visibility in dependence on an ACU through focus scan. The required DoFs are already build into the ACU which allow to shift the diffuser disc along the optical axis. This experiment is further expected to clarify which of the two simulation approaches is more appropriate to predict impacts on interferogram fringe visibility: (1) a combined simulation of ACU and AtmoLITE or (2) the impact of the incoming wavefront curvature which is expected to cause no significant change of interferogram fringe visibility if optics are aligned within the diffraction limited focal depth of the ACU $d_{ACU, focus} \approx 320 \mu\text{m}$. This test shall also be extended to include the dependence of measured interferogram fringe visibility on the relative tilt between diffuser surface and ACU optical axis.

So far, no clear verification of the diffuser tilt impact is derived as the upper limit of the diffuser tilt could not be determined. The inequality derived in this work is $\gamma_{\text{disc, min}} < \gamma_{\text{disc, allowed}} < \gamma_{\text{disc, max}}$ with values of 1.13° , 2.48° and 2.77° , respectively.

Secondly, expected changes of interferogram fringe visibility with the instrument in vacuum and during thermal cycling have not been verified in this work. Current simulations predict a thermal drift of the Littrow wavenumber of $\sigma_L = 13047 \text{ cm}^{-1} \pm 1.0 \text{ cm}^{-1}/50 \text{ K}$ and an interferogram fringe visibility of at least $V > 52 \%$ for operation under space conditions at all instrument temperatures between $T = -30^\circ\text{C}$ and $T = +20^\circ\text{C}$.

Lastly, repeated alignment between AtmoLITE instrument optics to the ACU and its impact on the repeatability of measured interferogram fringe visibility could not be tested. Whereas alignment in this work relied on maximizing the interferogram mean, a more precise ACU angular scan and mapped out non-uniformities could yield alternative alignment marks for upcoming studies. Further, if those studies show a significant impact of alignment on recorded interferogram fringe visibility, it is recommended to include a target in front of the ACU diffuser disc and near the AtmoLITE FOV edge as an additional alignment mark.

The next in-orbit demonstration of the new AtmoLITE design and including calibrated optics is currently expected to launch in late 2023. Based on the results presented in this work and ongoing improvements of the ACU and instrument setups, this mission is expected to be the first demonstrator within the AtmoX-family of CubeSat sized instruments to deliver atmospheric temperature data within the mesosphere.

References

- Abbe Hon., E. (1881). Vii.—on the estimation of aperture in the microscope. *Journal of the Royal Microscopical Society*, 1(3):388–423.
- Alexander, M. J., Geller, M., McLandress, C., Polavarapu, S., Preusse, P., Sassi, F., Sato, K., Eckermann, S., Ern, M., Hertzog, A., Kawatani, Y., Pulido, M., Shaw, T. A., Sigmond, M., Vincent, R., and Watanabe, S. (2010). Recent developments in gravity-wave effects in climate models and the global distribution of gravity-wave momentum flux from observations and models. *Quarterly Journal of the Royal Meteorological Society*, 136(650):1103–1124.
- Alexander, M. J., Gille, J., Cavanaugh, C., Coffey, M., Craig, C., Eden, T., Francis, G., Halvorson, C., Hannigan, J., Khosravi, R., Kinnison, D., Lee, H., Massie, S., Nardi, B., Barnett, J., Hepplewhite, C., Lambert, A., and Dean, V. (2008). Global estimates of gravity wave momentum flux from high resolution dynamics limb sounder observations. *Journal of Geophysical Research*, 113(D15).
- Ang, A. and Tran, J. (2020). *How to Use the Luminit LSD Scatter Model*. Luminit LLC.
- Arellano, F. J., Yoshinuma, M., and Ida, K. (2022). Charge exchange spectroscopy using spatial heterodyne spectrometer in the large helical device. *Review of Scientific Instruments*, 93(3):033503.
- Atkinson, R., Baulch, D. L., Cox, R. A., Hampson, R. F., Kerr, J. A., and Troe, J. (1992). Evaluated kinetic and photochemical data for atmospheric chemistry: Supplement IV: IUPAC subcommittee on gas kinetic data evaluation for atmospheric chemistry. *Atmospheric Environment. Part A. General Topics*, 26(7):1187–1230.
- Babcock, D. D. (2009). Spatial heterodyne spectroscopy for long-wave infrared: first measurements of broadband spectra. *Optical Engineering*, 48(10):105602.
- Ball, S. M., Hancock, G., and Winterbottom, F. (1995). Product channels in the near-UV photodissociation of ozone. *Faraday Discussions*, 100(0):215–227. Publisher: The Royal Society of Chemistry.
- Barth, C. A. and Hildebrandt, A. F. (1961). The 5577 Å airglow emission mechanism. *Journal of Geophysical Research (1896-1977)*, 66(3):985–986. _eprint: <https://onlinelibrary.wiley.com/doi/pdf/10.1029/JZ066i003p00985>.
- Basilio, R. R., Pollock, H. R., and Hunyadi-Lay, S. L. (2014). OCO-2 (Orbiting Carbon Observatory-2) mission operations planning and initial operations experiences. page 924105, Amsterdam, Netherlands.
- Becker, E. (2011). Dynamical control of the middle atmosphere. *Space Science Reviews*, 168(1-4):283–314.
- Becker, E. and Vadas, S. L. (2018). Secondary gravity waves in the winter mesosphere: Results from a high-resolution global circulation model. *Journal of Geophysical Research: Atmospheres*, 123(5):2605–2627.
- Beig, G. (2011). Long-term trends in the temperature of the mesosphere/lower thermosphere region: 1. anthropogenic influences. *Journal of Geophysical Research: Space Physics*, 116(A2):n/a–n/a.

- Beig, G., Keckhut, P., Lowe, R. P., Roble, R. G., Mlynczak, M. G., Scheer, J., Fomichev, V. I., Offermann, D., French, W. J. R., Shepherd, M. G., Semenov, A. I., Remsberg, E. E., She, C. Y., Lübken, F. J., Bremer, J., Clemesha, B. R., Stegman, J., Sigernes, F., and Fadnavis, S. (2003). Review of mesospheric temperature trends. *Reviews of Geophysics*, 41(4).
- Bittner, M., Offermann, D., Graef, H.-H., Donner, M., and Hamilton, K. (2002). An 18-year time series of OH rotational temperatures and middle atmosphere decadal variations. *Journal of Atmospheric and Solar-Terrestrial Physics*, 64(8):1147–1166. PSMOS 2000 Workshop - Planetary Scale Mesopause Observing System.
- Blackman, R. B., Tukey, J. W., and Teichmann, T. (1960). The measurement of power spectra. *Physics Today*, 13(2):52–54.
- Bovensmann, H., Burrows, J. P., Buchwitz, M., Frerick, J., Noël, S., Rozanov, V. V., Chance, K. V., and Goede, A. P. H. (1999). SCIAMACHY: Mission objectives and measurement modes. *Journal of the Atmospheric Sciences*, 56(2):127–150.
- Bremer, J. (1998). Trends in the ionospheric e and f regions over Europe. *Annales Geophysicae*, 16(8):986–996.
- Bucholtz, A., Skinner, W. R., Abreu, V. J., and Hays, P. B. (1986). The dayglow of the O₂ atmospheric band system. *Planetary and Space Science*, 34(11):1031–1035.
- California Polytechnic State University (2022). Cubesat design specification. <https://www.cubesat.org/cubesatinfo>, last checked 05.01.2022.
- Campbell, I. M. and Gray, C. N. (1973). Rate constants for O(3P) recombination and association with N(4S). *Chemical Physics Letters*, 18:607–609. ADS Bibcode: 1973CPL....18..607C.
- Campbell, J. B. (1987). Introduction to remote sensing. *Geocarto International*, 2:64–64.
- Chandran, A., Selvadurai, S., Srivastava, S., Naren Athreyas, K., Kaufmann, M., Olschewski, F., Boyajian, S., Sullivan, T., Chang, L., Chao, C.-K., Priyadarshan, H., Kumar, A., Palo, A., Rongen, H., and Neubert, T. (2019). A Very Low Altitude Satellite for Equatorial Ionosphere Measurements. 27th Annual AIAA/USU Conference on Small Satellites.
- Chen, Q. (2020). *Retrieval of atmospheric quantities from remote sensing measurements of nightglow emissions in the MLT region*. PhD. thesis, University of Wuppertal.
- Chen, Q., Ntokas, K., Linder, B., Krasauskas, L., Ern, M., Preusse, P., Ungermann, J., Becker, E., Kaufmann, M., and Riese, M. (2022). Satellite observations of gravity wave momentum flux in the mesosphere and lower thermosphere (mlt): feasibility and requirements. *Atmospheric Measurement Techniques*, 15(23):7071–7103.
- Connes, P. (1958). Spectromètre interférentiel à sélection par l’amplitude de Modulation. *J. phys. radium*, 19:215–222.
- Contreras, J. W. and Lightsey, P. A. (2004). Optical design and analysis of the James Webb Space Telescope: optical telescope element. In Sasian, J. M., Koshel, R. J., Manhart, P. K., and Juergens, R. C., editors, *Novel Optical Systems Design and Optimization VII*, volume 5524, pages 30 – 41. International Society for Optics and Photonics, SPIE.

- Cooley, J. W. and Tukey, J. W. (1965). An algorithm for the machine calculation of complex fourier series. *Mathematics of Computation*, 19(90):297–301.
- Deiml, M. (2017). Development of a small satellite remote sensing payload for passive limb sounding of the atmospheric oxygen emission. PhD. thesis, University of Wuppertal.
- Deiml, M., Kaufmann, M., Knieling, P., Olschewski, F., Toumpas, P., Langer, M., Ern, M., Koppmann, R., and Riese, M. (2014). *DiSSECT – Development of a small satellite for climate research*, volume 6. Journal Abbreviation: Proceedings of the International Astronautical Congress, IAC Publication Title: Proceedings of the International Astronautical Congress, IAC.
- Deiml, M., Song, R., Fröhlich, D., Rottland, B., Wagner, F., Liu, J., Wroblowski, O., Chen, Q., Loosen, F., Kaufmann, M., Rongen, H., Neubert, T., Schneider, H., Olschewski, F., Knieling, P., Mantel, K., Solheim, B., Shepherd, G., Koppmann, R., and Riese, M. (2017). Test of a remote sensing michelson-interferometer for temperature measurements in the mesosphere on a reus rocket. Proceedings of the 23. ESA symposium on European Rocket and Ballon Programmes and related Research.
- Ditto, T. D., Hsieh, M.-L., Newberg, H. J., Swordy, L., Hoyt, R., and Cushing, J. (2020). Optical space telescope without mirrors. In Lystrup, M., Perrin, M. D., Batalha, N., Siegler, N., and Tong, E. C., editors, *Space Telescopes and Instrumentation 2020: Optical, Infrared, and Millimeter Wave*, volume 11443, page 114431B. International Society for Optics and Photonics, SPIE.
- Edmund Optics (2022a). Richardson gratings 300 grooves, 25x25 mm, 760nm, plane ruled reflection grating. <https://www.edmundoptics.com/p/300-grooves-25-x-25mm-760nm-high-performance-reflection-grating/37287/>, last checked 15.02.2022.
- Edmund Optics (2022b). White diffusing glass. <https://www.edmundoptics.com/f/white-diffusing-glass/15084/>, last checked 15.02.2022.
- Ehlert, J. R. and Smith, T. F. (1993). View factors for perpendicular and parallel rectangular plates. *Journal of Thermophysics and Heat Transfer*, 7(1):173–175.
- Englert, C. R., Cardon, J. G., Harlander, J. M., and Roesler, F. L. (2005). Correction of Phase Distortion in Spatial Heterodyne Spectroscopy (SHS). In *Fourier Transform Spectroscopy/ Hyperspectral Imaging and Sounding of the Environment (2005)*, paper FTuB2, page FTuB2. Optica Publishing Group.
- Englert, C. R. and Harlander, J. M. (2006a). Flatfielding in spatial heterodyne spectroscopy. *Applied Optics*, 45(19):4583–4590.
- Englert, C. R. and Harlander, J. M. (2006b). Flatfielding in spatial heterodyne spectroscopy. *Applied Optics*, 45(19):4583.
- Englert, C. R., Harlander, J. M., Brown, C. M., Marr, K. D., Miller, I. J., Stump, J. E., Hancock, J., Peterson, J. Q., Kumler, J., Morrow, W. H., Mooney, T. A., Ellis, S., Mende, S. B., Harris, S. E., Stevens, M. H., Makela, J. J., Harding, B. J., and Immel, T. J. (2017). Michelson interferometer for global high-resolution thermospheric imaging (MIGHTI): Instrument design and calibration. *Space Science Reviews*, 212(1-2):553–584.

- Englert, C. R., Harlander, J. M., Cardon, J. G., and Roesler, F. L. (2004). Correction of phase distortion in spatial heterodyne spectroscopy. *Applied Optics*, 43(36):6680.
- Englert, C. R., Stevens, M. H., Siskind, D. E., Harlander, J. M., and Roesler, F. L. (2010). Spatial heterodyne imager for mesospheric radicals on STPSat-1. *Journal of Geophysical Research*, 115(D20).
- Ern, M. (2004). Absolute values of gravity wave momentum flux derived from satellite data. *Journal of Geophysical Research*, 109(D20).
- Ern, M., Preusse, P., Gille, J. C., Hepplewhite, C. L., Mlynczak, M. G., Russell, J. M., and Riese, M. (2011). Implications for atmospheric dynamics derived from global observations of gravity wave momentum flux in stratosphere and mesosphere. *Journal of Geophysical Research*, 116(D19).
- Ern, M., Trinh, Q. T., Kaufmann, M., Krisch, I., Preusse, P., Ungermann, J., Zhu, Y., Gille, J. C., Mlynczak, M. G., III, J. M. R., Schwartz, M. J., and Riese, M. (2016). Satellite observations of middle atmosphere gravity wave absolute momentum flux and of its vertical gradient during recent stratospheric warmings. *Atmospheric Chemistry and Physics*, 16(15):9983–10019.
- Fellgett, P. (2006). The nature and origin of multiplex Fourier spectrometry. *Notes and Records of the Royal Society*, 60(1):91–93. Publisher: Royal Society.
- Forbes, J. M., Bruinsma, S. L., Doornbos, E., and Zhang, X. (2016). Gravity wave-induced variability of the middle thermosphere. *Journal of Geophysical Research: Space Physics*, 121(7):6914–6923.
- Foster, M., Brooks, W., Jahn, P., Hedberg, J., Andersson, A., , and Ashton, L. (2022). Demonstration of a compact deep uv raman spatial heterodyne spectrometer for biologics analysis. *Journal of Biophotonics*, 15(7).
- Frisk, U., Hagström, M., Ala-Laurinaho, J., Andersson, S., Berges, J. C., Chabaud, J. P., Dahlgren, M., Emrich, A., Florén, H. G., Florin, G., Fredrixon, M., Gaier, T., Haas, R., Hirvonen, T., Hjalmarsson, Å., Jakobsson, B., Jukkala, P., Kildal, P. S., Kollberg, E., Lassing, J., Lecacheux, A., Lehikoinen, P., Lehto, A., Mallat, J., Marty, C., Michet, D., Narbonne, J., Nexon, M., Olberg, M., Olofsson, A. O. H., Olofsson, G., Origné, A., Petersson, M., Piironen, P., Pons, R., Pouliquen, D., Ristorcelli, I., Rosolen, C., Rouaix, G., Räisänen, A. V., Serra, G., Sjöberg, F., Stenmark, L., Torchinsky, S., Tuovinen, J., Ullberg, C., Vinterhav, E., Wade Falk, N., Zirath, H., Zimmermann, P., and Zimmermann, R. (2003). The Odin satellite. I. Radiometer design and test. *Canadian Journal of Physics*, 402:L27–L34.
- Fritts, D. C. and Alexander, M. J. (2003). Gravity wave dynamics and effects in the middle atmosphere. *Reviews of Geophysics*, 41(1).
- Gilmore, D. G. (2002). *Spacecraft thermal control handbook*. Aerospace Press, El Segundo, CA, 2 edition.
- Gomer, N. R., Gordon, C. M., Lucey, P., Sharma, S. K., Carter, J. C., and Angel, S. M. (2011). Raman Spectroscopy Using a Spatial Heterodyne Spectrometer: Proof of Concept. *Applied Spectroscopy*, 65(8):849–857. Publisher: SAGE Publications Ltd STM.
- Goodman, J. (2005). *Introduction to Fourier Optics*. McGraw-Hill physical and quantum electronics series. W. H. Freeman.

- Goodman, J. W. (1976). Some fundamental properties of speckle. *Journal of the Optical Society of America (1917-1983)*, 66:1145–1150.
- Gornushkin, I. B., Smith, B. W., Panne, U., and Omenetto, N. (2014). Laser-Induced Breakdown Spectroscopy Combined with Spatial Heterodyne Spectroscopy. *Applied Spectroscopy*, 68(9):1076–1084. Publisher: SAGE Publications Ltd STM.
- Gossman, M. S., Pahikkala, A. J., Rising, M. B., and McGinley, P. H. (2010). Providing solid angle formalism for skyshine calculations. *Journal of Applied Clinical Medical Physics*, 11(4):278–282.
- Green, J. G., Shi, J., and Barker, J. R. (2000). Photochemical Kinetics of Vibrationally Excited Ozone Produced in the 248 nm Photolysis of O₂/O₃ Mixtures. *The Journal of Physical Chemistry A*, 104(26):6218–6226. Publisher: American Chemical Society.
- Greivenkamp, J. E. (2004). *Field Guide to Geometrical Optics* -. Society of Photo Optical, Bellingham, Washington USA.
- Gumbel, J., Megner, L., Christensen, O. M., Ivchenko, N., Murtagh, D. P., Chang, S., Dillner, J., Ekebrand, T., Giono, G., Hammar, A., Hedin, J., Karlsson, B., Krus, M., Li, A., McCallion, S., Olentsenko, G., Pak, S., Park, W., Rouse, J., Stegman, J., and Witt, G. (2020). The MATS satellite mission – gravity wave studies by Mesospheric Airglow/Aerosol Tomography and Spectroscopy. *Atmospheric Chemistry and Physics*, 20(1):431–455. Publisher: Copernicus GmbH.
- Hadj-Ziane, S., Held, B., Pignolet, P., Peyrous, R., and Coste, C. (1992). Ozone generation in an oxygen-fed wire-to-cylinder ozonizer at atmospheric pressure. *Journal of Physics D: Applied Physics*, 25(4):677–685. Publisher: IOP Publishing.
- Harlander, J. (1990). Spatial heterodyne spectroscopy: interferometric performance at any wavelength without scanning. Ph.D. thesis, University of Wisconsin-Madison.
- Harlander, J. M., Englert, C. R., Babcock, D. D., and Roesler, F. L. (2010). Design and laboratory tests of a Doppler Asymmetric Spatial Heterodyne (DASH) interferometer for upper atmospheric wind and temperature observations. *Optics Express*, 18(25):26430–26440. Publisher: Optica Publishing Group.
- Harlander, J. M., Roesler, F. L., Cardon, J. G., Englert, C. R., and Conway, R. R. (2002). Shimmer: a spatial heterodyne spectrometer for remote sensing of earth's middle atmosphere. *Appl. Opt.*, 41(7):1343–1352.
- Harlander, J. M., Roesler, F. L., Englert, C. R., Cardon, J. G., Conway, R. R., Brown, C. M., and Wimperis, J. (2003). Robust monolithic ultraviolet interferometer for the SHIMMER instrument on STPSat-1. *Applied Optics*, 42(15):2829–2834. Publisher: Optica Publishing Group.
- Harlander, J. M., Roesler, F. L., Englert, C. R., Cardon, J. G., and Wimperis, J. (2004). Spatial Heterodyne Spectroscopy For High Spectral Resolution Space-Based Remote Sensing. *Optics and Photonics News*, 15(1):46–51. Publisher: Optica Publishing Group.
- Harlander, J. M., Tran, H., Roesler, F. L., Jaehnig, K. P., Watchorn, S., Sanders III, W. T., and Reynolds, R. J. (1995). Sounding rocket payload designed for investigations of the distribution and dynamics of the hot component of the

- interstellar medium using a field-widened spatial heterodyne spectrometer. pages 132–140, San Diego, CA.
- He, W., Wu, K., Feng, Y., Fu, D., Chen, Z., and Li, F. (2019). The Radiative Transfer Characteristics of the O₂ Infrared Atmospheric Band in Limb-Viewing Geometry. *Remote Sensing*, 11(22):2702. Number: 22 Publisher: Multidisciplinary Digital Publishing Institute.
- Holton, J. R. (1982). The role of gravity wave induced drag and diffusion in the momentum budget of the mesosphere. *Journal of the Atmospheric Sciences*, 39(4):791–799.
- Holton, J. R. (1984). The generation of mesospheric planetary waves by zonally asymmetric gravity wave breaking. *Journal of the Atmospheric Sciences*, 41(23):3427–3430.
- Hoogeveen, R. W. M., Goede, A. P. H., Slijkhuis, S., Selig, A., and Burrows, J. P. (1994). Scanning imaging absorption spectrometer for atmospheric cartography (SCIAMACHY) development. In Cerutti-Maori, G. and Roussel, P., editors, *Space Optics 1994: Earth Observation and Astronomy*, volume 2209, pages 78 – 85. International Society for Optics and Photonics, SPIE.
- Hough, P. V. C. (1959). Machine Analysis of Bubble Chamber Pictures. *Conf. Proc. C*, 590914:554–558.
- Howell, J. R., Daun, K., Siegel, R., and Menguc, M. P. (2020). *Thermal Radiation Heat Transfer*. CRC Press, London, England, 7 edition.
- Hu, X.-B., Dong, M.-X., Zhu, Z.-H., Gao, W., and Rosales-Guzmán, C. (2020). Does the structure of light influence the speckle size? *Scientific Reports*, 10(1).
- Kalicinsky, C., Knieling, P., Koppmann, R., Offermann, D., Steinbrecht, W., and Wintel, J. (2016). Long-term dynamics of OH* temperatures over central Europe: trends and solar correlations. *Atmospheric Chemistry and Physics*, 16(23):15033–15047.
- Kalisch, S., Preusse, P., Ern, M., Eckermann, S. D., and Riese, M. (2014). Differences in gravity wave drag between realistic oblique and assumed vertical propagation. *Journal of Geophysical Research: Atmospheres*, 119(17):10,081–10,099.
- Kalogerakis, K. S. (2019). A previously unrecognized source of the O₂ atmospheric band emission in earth’s nightglow. *Science Advances*, 5(3).
- Kaufman, M. I., Frayer, D. K., Corredor, A., Malone, R. M., and Light, B. B. (2017). Design guidelines for predicting stress in cemented doublets undergoing temperature change. In *Optical Design and Fabrication 2017 (Freeform, IODC, OFT)*, page ITh3A.6. Optical Society of America.
- Kaufmann, M., Olschewski, F., Mantel, K., Solheim, B., Shepherd, G., Deiml, M., Liu, J., Song, R., Chen, Q., Wroblowski, O., Wei, D., Zhu, Y., Wagner, F., Loosen, F., Froehlich, D., Neubert, T., Rongen, H., Knieling, P., Toumpas, P., Shan, J., Tang, G., Koppmann, R., and Riese, M. (2018). A highly miniaturized satellite payload based on a spatial heterodyne spectrometer for atmospheric temperature measurements in the mesosphere and lower thermosphere. *Atmospheric Measurement Techniques*, 11(7):3861–3870.

- Kaufmann, M., Olschewski, F., Mantel, K., Wroblowski, O., Chen, Q., Liu, J., Gong, Q., Wei, D., Zhu, Y., Neubert, T., Rongen, H., Koppmann, R., and Riese, M. (2019). On the assembly and calibration of a spatial heterodyne interferometer for limb sounding of the middle atmosphere. *CEAS Space Journal*, 11(4):525–531.
- Klais, O., Laufer, A. H., and Kurylo, M. J. (1980). Atmospheric quenching of vibrationally excited $O_2(1\Delta)$. *The Journal of Chemical Physics*, 73(6):2696–2699. Publisher: American Institute of Physics.
- Klingshirn, H. and Maier, M. (1985). Quenching of the $1\Sigma+g$ state in liquid oxygen isotopes. *The Journal of Chemical Physics*, 82(2):714–719. Publisher: American Institute of Physics.
- Kokin, G. and Lysenko, E. (1994). On temperature trends of the atmosphere from rocket and radiosonde data. *Journal of Atmospheric and Terrestrial Physics*, 56(9):1035–1040. Middle Atmosphere Science.
- Krichel, M. (2019). Aufbau und Charakterisierung einer Kalibrationseinheit für das AtmoLITE Satelliten-Instrument. Master thesis, University of Wuppertal.
- Lamontagne, F., Desnoyers, N., Doucet, M., Cote, P., Gauvin, J., Anctil, G., and Tremblay, M. (2015). Lens auto-centering. In Mazuray, L., Wartmann, R., and Wood, A. P., editors, *Optical Systems Design 2015: Optical Design and Engineering VI*, volume 9626, page 962619. International Society for Optics and Photonics, SPIE.
- Langille, J., Letros, D., Bourassa, A., Solheim, B., Degenstein, D., Dupont, F., Zawada, D., and Lloyd, N. D. (2019a). Spatial heterodyne observations of water (SHOW) from a high-altitude airplane: characterization, performance, and first results. *Atmospheric Measurement Techniques*, 12(1):431–455. Publisher: Copernicus GmbH.
- Langille, J., Letros, D., Bourassa, A., Solheim, B., Degenstein, D., Dupont, F., Zawada, D., and Lloyd, N. D. (2019b). Spatial heterodyne observations of water (SHOW) from a high-altitude airplane: characterization, performance, and first results. *Atmospheric Measurement Techniques*, 12(1):431–455.
- Laubscher, B. E., Smith, B. W., Cooke, B. J., LaDelfe, P. C., Berggren, R. R., Villeneuve, P. V., Goeller, R. M., Obbink, G. M., Milligan, S., Howard, J. W., Norton, P. R., Stegall, M., Burgett, C. B., Harlander, J. M., and Horton, R. F. (1999). Infrared imaging spatial heterodyne spectrometer (IRISHS) experiment effort. In Holst, G. C., editor, *SPIE Proceedings*. SPIE.
- Lee, L. C. and Slinger, T. G. (1978). Observations on $O(1D\rightarrow 3P)$ and $O_2(b\ 1\Sigma+\rightarrow X\ 3\Sigma-)$ following O_2 photodissociation. *The Journal of Chemical Physics*, 69(9):4053–4060. Publisher: American Institute of Physics.
- Lindzen, R. S. (1981). Turbulence and stress owing to gravity wave and tidal breakdown. *Journal of Geophysical Research*, 86(C10):9707.
- Liu, J. (2019). Study on a miniaturized satellite payload for atmospheric temperature measurements. Ph.D. thesis, University of Wuppertal.
- Liu, J., Wei, D., Zhu, Y., Kaufmann, M., Olschewski, F., Mantel, K., Xu, J., and Riese, M. (2018). Effective wind and temperature retrieval from doppler asymmetric spatial heterodyne spectrometer interferograms. *Appl. Opt.*, 57(30):8829–8835.

- Llewellyn, E., Lloyd, N. D., Degenstein, D. A., Gattinger, R. L., Petelina, S. V., Bourassa, A. E., Wiensz, J. T., Ivanov, E. V., McDade, I. C., Solheim, B. H., McConnell, J. C., Haley, C. S., von Savigny, C., Sioris, C. E., McLinden, C. A., Griffioen, E., Kaminski, J., Evans, W. F. J., Puckrin, E., Strong, K., Wehrle, V., Hum, R. H., Kendall, D. J. W., Matsushita, J., Murtagh, D. P., Brohede, S., Stegman, J., Witt, G., Barnes, G., Payne, W. F., Piché, L., Smith, K., Warshaw, G., Deslauniers, D. L., Marchand, P., Richardson, E. H., King, R. A., Wevers, I., McCreath, W., Kyrölä, E., Oikarinen, L., Leppelmeier, G. W., Auvinen, H., Megie, G., Hauchecorne, A., Lefevre, F., de La Nöe, J., Ricaud, P., Frisk, U., Sjöberg, F., von Schéele, F., and Nordh, L. (2004). The OSIRIS instrument on the Odin spacecraft. *Canadian Journal of Physics*, 82:411–422.
- Malitson, I. H. (1965). Interspecimen comparison of the refractive index of fused silica*,†. *J. Opt. Soc. Am.*, 55(10):1205–1209.
- McDade, I. C., Murtagh, D. P., Greer, R. G. H., Dickinson, P. H. G., Witt, G., Stegman, J., Llewellyn, E. J., Thomas, L., and Jenkins, D. B. (1986). ETON 2: Quenching parameters for the proposed precursors of O₂(b¹Σ_g⁺) and O(1S) in the terrestrial nightglow. *Planetary and Space Science*, 34(9):789–800.
- McLinden, C. A., Bourassa, A. E., Brohede, S., Cooper, M., Degenstein, D. A., Evans, W. J. F., Gattinger, R. L., Haley, C. S., Llewellyn, E. J., Lloyd, N. D., Loewen, P., Martin, R. V., McConnell, J. C., McDade, I. C., Murtagh, D., Rieger, L., von Savigny, C., Sheese, P. E., Sioris, C. E., Solheim, B., and Strong, K. (01 Dec. 2012). Osiris: A decade of scattered light. *Bulletin of the American Meteorological Society*, 93(12):1845 – 1863.
- Michelsen, H. A., Salawitch, R. J., Wennberg, P. O., and Anderson, J. G. (1994). Production of O(¹D) from photolysis of O₃. *Geophysical Research Letters*, 21(20):2227–2230. _eprint: <https://onlinelibrary.wiley.com/doi/pdf/10.1029/94GL02052>.
- Milligan, S., Howard, J. W., Laubscher, B. E., Smith, B. W., Berggren, R. R., and Harlander, J. M. (1999). Optical design of an imaging spatial heterodyne infrared spectrometer. In Andresen, B. F. and Strojnik, M., editors, *SPIE Proceedings*. SPIE.
- Mooney, J. M. (1995). Measurement of the modulation transfer function of infrared cameras. *Optical Engineering*, 34(6):1808.
- Offermann, D., Grossmann, K.-U., Barthol, P., Knieling, P., Riese, M., and Trant, R. (1999). Cryogenic infrared spectrometers and telescopes for the atmosphere (CRISTA) experiment and middle atmosphere variability. *Journal of Geophysical Research: Atmospheres*, 104(D13):16311–16325.
- Offermann, D., Hoffmann, P., Knieling, P., Koppmann, R., Oberheide, J., and Steinbrecht, W. (2010). Long-term trends and solar cycle variations of mesospheric temperature and dynamics. *Journal of Geophysical Research: Atmospheres*, 115(D18).
- Ohara Corp. (2022). Optical glass information. <http://www.oharacorp.com/catalog.html>, last checked 11.02.2022.
- Olberg, M., Frisk, U., Lecacheux, A., Olofsson, A. O. H., Baron, P., Bergman, P., Florin, G., Hjalmarsen, Å. ., Larsson, B., Murtagh, D., Olofsson, G., Pagani, L., Sandqvist, A., Teyssier, D., Torchinsky, S. A., and Volk, K. (2003). The Odin satellite. II. Radiometer data processing and calibration. *Canadian Journal of Physics*, 402:L35–L38.

- Park, J., Lühr, H., Lee, C., Kim, Y. H., Jee, G., and Kim, J.-H. (2014). A climatology of medium-scale gravity wave activity in the midlatitude/low-latitude daytime upper thermosphere as observed by CHAMP. *Journal of Geophysical Research: Space Physics*, 119(3):2187–2196.
- Patel, A. (2012). Spatial heterodyne observations of water (show) instrument characterization. Master thesis, York University.
- Perkins, C. P., Kerekes, J. P., and Gartley, M. G. (2013). Spatial heterodyne spectrometer: modeling and interferogram processing for calibrated spectral radiance measurements. In Mouroulis, P. and Pagano, T. S., editors, *SPIE Proceedings*. SPIE.
- Pollock, R., Haring, R. E., Holden, J. R., Johnson, D. L., Kapitanoff, A., Mohlman, D., Phillips, C., Randall, D., Rechsteiner, D., Rivera, J., Rodriguez, J. I., Schwochert, M. A., and Sutin, B. M. (2010). The Orbiting Carbon Observatory instrument: performance of the OCO instrument and plans for the OCO-2 instrument. page 78260W, Toulouse, France.
- Preusse, P., Ern, M., Bechtold, P., Eckermann, S. D., Kalisch, S., Trinh, Q. T., and Riese, M. (2014). Characteristics of gravity waves resolved by ECMWF. *Atmospheric Chemistry and Physics*, 14(19):10483–10508.
- Preusse, P., Ern, M., Eckermann, S. D., Warner, C. D., Picard, R. H., Knieling, P., Krebsbach, M., Russell, J. M., Mlynczak, M. G., Mertens, C. J., and Riese, M. (2006). Tropopause to mesopause gravity waves in august: Measurement and modeling. *Journal of Atmospheric and Solar-Terrestrial Physics*, 68(15):1730–1751.
- Preusse, P., Schroeder, S., Hoffmann, L., Ern, M., Friedl-Vallon, F., Ungermann, J., Oelhaf, H., Fischer, H., and Riese, M. (2009). New perspectives on gravity wave remote sensing by spaceborne infrared limb imaging. *Atmospheric Measurement Techniques*, 2(1):299–311.
- Reisin, E. and Scheer, J. (2002). Searching for trends in mesopause region airglow intensities and temperatures at el Leoncito. *Physics and Chemistry of the Earth, Parts A/B/C*, 27(6):563–569.
- Remsberg, E. E., Marshall, B. T., Garcia-Comas, M., Krueger, D., Lingenfelter, G. S., Martin-Torres, J., Mlynczak, M. G., Russell, J. M., Smith, A. K., Zhao, Y., Brown, C., Gordley, L. L., Lopez-Gonzalez, M. J., Lopez-Puertas, M., She, C.-Y., Taylor, M. J., and Thompson, R. E. (2008). Assessment of the quality of the version 1.07 temperature-versus-pressure profiles of the middle atmosphere from TIMED/SABER. *Journal of Geophysical Research*, 113(D17).
- Riley, M. E. and Gusinow, M. A. (1977). Laser beam divergence utilizing a lateral shearing interferometer. *Appl. Opt.*, 16(10):2753–2756.
- Rodrigo, R., Lopez-Moreno, J. J., Lopez-Puertas, M., Moreno, F., and Molina, A. (1986). Neutral atmospheric composition between 60 and 220 km: A theoretical model for mid-latitudes. *Planetary and Space Science*, 34(8):723–743.
- Sato, K. and Nomoto, M. (2015). Gravity wave-induced anomalous potential vorticity gradient generating planetary waves in the winter mesosphere. *Journal of the Atmospheric Sciences*, 72(9):3609–3624.

- Sato, K., Watanabe, S., Kawatani, Y., Tomikawa, Y., Miyazaki, K., and Takahashi, M. (2009). On the origins of mesospheric gravity waves. *Geophysical Research Letters*, 36(19).
- Scheer, J., Reisin, E., Gusev, O., French, W., Hernandez, G., Huppi, R., Ammosov, P., Gavrilyeva, G., and Offermann, D. (2006). Use of CRISTA mesopause region temperatures for the intercalibration of ground-based instruments. *Journal of Atmospheric and Solar-Terrestrial Physics*, 68(15):1698–1708.
- SCHOTT AG (2022a). Mechanical and thermal properties of optical glass. <https://www.schott.com/en-us/products/optical-glass-p1000267/downloads/TIE31-Technical-Information-US.pdf>, last checked 11.02.2022.
- SCHOTT AG (2022b). Properties of optical glass. <https://www.schott.com/en-us/products/optical-glass-p1000267/technical-details>, last checked 11.02.2022.
- Serafimov, K. and Serafimova, M. (1992). Possible radioindications of anthropogenic influences on the mesosphere and lower thermosphere. *Journal of Atmospheric and Terrestrial Physics*, 54(7):847–850.
- Sheese, P. (2011). *Mesospheric ozone densities retrieved from OSIRIS observations of the O₂ A-band dayglow*. PhD. thesis, Library and Archives Canada, Bibliotheque et Archives Canada, Ottawa.
- Shepherd, G. G., Thuillier, G., Gault, W. A., Solheim, B. H., Hersom, C., Alunni, J. M., Brun, J.-F., Brune, S., Charlot, P., Cogger, L. L., Desaulniers, D.-L., Evans, W. F. J., Gattinger, R. L., Girod, F., Harvie, D., Hum, R. H., Kendall, D. J. W., Llewellyn, E. J., Lowe, R. P., Ohrt, J., Pasternak, F., Peillet, O., Powell, I., Rochon, Y., Ward, W. E., Wiens, R. H., and Wimperis, J. (1993). WINDII, the wind imaging interferometer on the upper atmosphere research satellite. *Journal of Geophysical Research*, 98(D6):10725.
- Siskind, D. E., Drob, D. P., Emmert, J. T., Stevens, M. H., Sheese, P. E., Llewellyn, E. J., Hervig, M. E., Niciejewski, R., and Kochenash, A. J. (2012). Linkages between the cold summer mesopause and thermospheric zonal mean circulation. *Geophysical Research Letters*, 39(1):n/a–n/a.
- Slanger, T. G. and Black, G. (1977). O(1S) in the lower thermosphere—Chapman vs Barth. *Planetary and Space Science*, 25(1):79–88.
- Smith, B. W., Laubscher, B. E., Cooke, B. J., LaDelfe, P. C., Harlander, J. M., Howard, J. W., and Milligan, S. (1999a). IRISHS: the infrared imaging spatial heterodyne spectrometer: a new pushbroom Fourier transform ultraspectral imager with no moving parts. page 501, Orlando, FL.
- Smith, B. W., Laubscher, B. E., Cooke, B. J., LaDelfe, P. C., Harlander, J. M., Howard, J. W., and Milligan, S. (1999b). IRISHS: the infrared imaging spatial heterodyne spectrometer: a new pushbroom fourier transform ultraspectral imager with no moving parts. In Andresen, B. F. and Strojnik, M., editors, *SPIE Proceedings*. SPIE.
- Smith, W. J. (2007). *Modern Optical Engineering, 4th Ed.* -. McGraw Hill Professional, Madison.

- Snell, R., Atkins, C., Schnetler, H., Todd, I., Hernández-Nava, E., Lyle, A. R., Maddison, G., Morris, K., Miller, C., Roulet, M., Hugot, E., Sanginés, F. T., Vega-Moreno, A., van de Vorst, L. T. G. B., Dufils, J., Brouwers, L., Farkas, S., Mezö, G., Beardsley, M., and Harris, M. (2020). An additive manufactured CubeSat mirror incorporating a novel circular lattice. In Navarro, R. and Geyl, R., editors, *Advances in Optical and Mechanical Technologies for Telescopes and Instrumentation IV*, volume 11451, page 114510C. International Society for Optics and Photonics, SPIE.
- Song, R. (2018). *Tomographic reconstruction of gravity wave parameters from satellite-borne airglow observations*. PhD. thesis, University of Wuppertal.
- Song, R., Kaufmann, M., Ern, M., Ungermann, J., Liu, G., and Riese, M. (2018). Three-dimensional tomographic reconstruction of atmospheric gravity waves in the mesosphere and lower thermosphere (mlt). *Atmospheric Measurement Techniques*, 11(5):3161–3175.
- Sparks, R. K., Carlson, L. R., Shobatake, K., Kowalczyk, M. L., and Lee, Y. T. (1980). Ozone photolysis: A determination of the electronic and vibrational state distributions of primary products. *The Journal of Chemical Physics*, 72(2):1401–1402. Publisher: American Institute of Physics.
- SphereOptics GmbH (2022). Zenith polymer diffusers. <https://sphereoptics.de/en/product/zenith-polymer-diffusers/>, last checked 15.02.2022.
- Stangner, T., Zhang, H., Dahlberg, T., Wiklund, K., and Andersson, M. (2017). Step-by-step guide to reduce spatial coherence of laser light using a rotating ground glass diffuser. *Applied Optics*, 56(19):5427.
- Streit, G. E., Howard, C. J., Schmeltekopf, A. L., Davidson, J. A., and Schiff, H. I. (1976). Temperature dependence of O(1D) rate constants for reactions with O₂, N₂, CO₂, O₃, and H₂O. *The Journal of Chemical Physics*, 65(11):4761–4764. Publisher: American Institute of Physics.
- Svanberg, M., Pettersson, J. B. C., and Murtagh, D. (1995). Ozone photodissociation in the Hartley band: A statistical description of the ground state decomposition channel. *The Journal of Chemical Physics*, 102(22):8887–8896. Publisher: American Institute of Physics.
- Taubenheim, J., von Cossart, G., and Entzian, G. (1990). Evidence of co₂-induced progressive cooling of the middle atmosphere derived from radio observations. *Advances in Space Research*, 10(10):171–174.
- Thurairajah, B., Bailey, S. M., Cullens, C. Y., Hervig, M. E., and Russell, J. M. (2014). Gravity wave activity during recent stratospheric sudden warming events from SOFIE temperature measurements. *Journal of Geophysical Research: Atmospheres*, 119(13):8091–8103.
- Toth, C. and Józków, G. (2016). Remote sensing platforms and sensors: A survey. *ISPRS Journal of Photogrammetry and Remote Sensing*, 115:22–36. Theme issue 'State-of-the-art in photogrammetry, remote sensing and spatial information science'.
- Trinh, Q. T., Ern, M., Doornbos, E., Preusse, P., and Riese, M. (2018). Satellite observations of middle atmosphere–thermosphere vertical coupling by gravity waves. *Annales Geophysicae*, 36(2):425–444.

- Ungermann, J., Hoffmann, L., Preusse, P., Kaufmann, M., and Riese, M. (2010). Tomographic retrieval approach for mesoscale gravity wave observations by the PREMIER infrared limb-sounder. *Atmospheric Measurement Techniques*, 3(2):339–354.
- Vadas, S. L., Fritts, D. C., and Alexander, M. J. (2003). Mechanism for the generation of secondary waves in wave breaking regions. *Journal of the Atmospheric Sciences*, 60(1):194–214.
- Valentini, J. J., Gerrity, D. P., Phillips, D. L., Nieh, J., and Tabor, K. D. (1987). CARS spectroscopy of O₂(1Δ_g) from the Hartley band photodissociation of O₃: Dynamics of the dissociation. *The Journal of Chemical Physics*, 86(12):6745–6756. Publisher: American Institute of Physics.
- Van Oosterom, A. and Strackee, J. (1983). The solid angle of a plane triangle. *IEEE Transactions on Biomedical Engineering*, BME-30(2):125–126.
- Voelkel, R. and Weible, K. J. (2008). Laser beam homogenizing: limitations and constraints. In Duparré, A. and Geyl, R., editors, *Optical Fabrication, Testing, and Metrology III*, volume 7102, pages 222 – 233. International Society for Optics and Photonics, SPIE.
- von Savigny, C. (2004). First near-global retrievals of OH rotational temperatures from satellite-based meinel band emission measurements. *Geophysical Research Letters*, 31(15).
- Waldron, A., Allen, A., Colon, A., Carter, J. C., and Angel, S. M. (2020). A monolithic spatial heterodyne raman spectrometer: Initial tests. *Applied Spectroscopy*, 75(1):57–69.
- Wallace, L. and Hunten, D. M. (1968). Dayglow of the oxygen A band. *Journal of Geophysical Research*, 73:4813–4834. ADS Bibcode: 1968JGR....73.4813W.
- Wang, J. Y. and Silva, D. E. (1980). Wave-front interpretation with zernike polynomials. *Appl. Opt.*, 19(9):1510–1518.
- Watanabe, S., Sato, K., Kawatani, Y., and Takahashi, M. (2015). Vertical resolution dependence of gravity wave momentum flux simulated by an atmospheric general circulation model. *Geoscientific Model Development*, 8(6):1637–1644.
- Watchorn, S., Roesler, F. L., Harlander, J., Jaehnig, K. P., Reynolds, R. J., and Sanders, W. T. (2010). Evaluation of payload performance for a sounding rocket vacuum ultraviolet spatial heterodyne spectrometer to observe C IV 1550 emissions from the Cygnus Loop. *Applied Optics*, 49(17):3265–3273. Publisher: Optica Publishing Group.
- Watchorn, S., Roesler, F. L., Harlander, J. M., Jaehnig, K. P., Reynolds, R. J., and Sanders III, W. T. (2001). Development of the spatial heterodyne spectrometer for VUV remote sensing of the interstellar medium. pages 284–295, San Diego, CA.
- Woodward, P. and Davies, I. (1952). Information theory and inverse probability in telecommunication. *Proceedings of the IEE - Part III: Radio and Communication Engineering*, 99(58):37–44.

- Yankovsky, V. (1991). Electronically-vibrationally relaxation of $\text{o}_2(\text{b } 1\Sigma\text{g}^- \nu = 1, 2)$ molecules in collisions with ozone, oxygen molecules and atoms. *Soviet journal of chemical physics*, 10:291–306.
- Yankovsky, V. and Manuilova, R. O. (2006). Model of daytime emissions of electronically-vibrationally excited products of o_3 and o_2 photolysis: application to ozone retrieval. *Annales Geophysicae*, 24:2823–2839.
- Yoder, P. R. (2008). *Mounting Optics in Optical Instruments*. SPIE.
- Zettner, A., Gojani, A. B., Schmid, T., and Gornushkin, I. B. (2020). Evaluation of a spatial heterodyne spectrometer for raman spectroscopy of minerals. *Minerals*, 10(2):202.
- Zhou, X. (2002). Forcing of secondary waves by breaking of gravity waves in the mesosphere. *Journal of Geophysical Research*, 107(D7).

Appendices



AtmoSHINE & AtmoLITE addon

Contents

A.1	Zernike Polynomials	186
A.2	LOS Calibration - Propagation of Uncertainties	188
A.3	Characterisation of PSF and spot size - continued	189
A.4	Instrument and ACU Info Sheets	191
A.5	Oxygen A-band emission lines	193
A.6	AtmoLITE - Simulated Spectra continued	194
A.7	AtmoLITE - ILS formulas	195

A.1 Zernike Polynomials

The evaluation and description of wavefront aberration measurements presented in section 3.2 and section 4.5 are based on Zernike polynomials. These polynomials are typically written as the product of a radial function $f(r)$ of degree $2n$ containing no power less than m and an angular contribution $g(\theta)$. The normalisation is chosen over the unit circle such that $f(1) = 1$ and by requiring the orthogonality relation A.1 [Wang and Silva, 1980].

$$\int_0^1 f \cdot g(n, m, r) \times f \cdot g(n', m, r) r dr = \frac{1}{2(n+1)} \delta(n - n') \quad (\text{A.1})$$

Each radial function may be written explicitly by Equation A.2 and practical implementation of the angular contribution is a sum of sines and cosines as shown in Equation A.3 known as Zernike fringe polynomials. Note that the sums in A.3 represent a linear system of equations over the unit circle where the coefficients $a(n)$, $b(n, m)$ and $c(n, m)$ may be used to fit experimental data. For further reference, the first 36 Zernike Fringe polynomials utilised in the description of wavefront aberration measurements are given in Table A.1.

$$f(r)_{n,m} = r^m \cdot \sum_{s=0}^{n-m} (-1)^s \frac{(2n-m-s)!}{s!(n-s)!(n-m-s)!} r^{2(n-s-m)} \quad (\text{A.2})$$

$$ZP(r, \theta) = \text{const.} + \sum_{n=1}^N \left(a(n) f(r)_{n,0} + \sum_{m=1}^n f(r)_{n,m} [b(n, m) \cos(m\theta) + c(n, m) \sin(m\theta)] \right) \quad (\text{A.3})$$

Evaluation of wavefront aberration is predominantly based on estimates of the P-V and RMS wavefront aberration. When Zernike fringe polynomials are fitted to measured or simulated wavefront data, the P-V value corresponds to the difference between minimum and maximum values of the wavefront and the RMS value can be easily obtained based on Equation A.4.

$$\sigma^2 = \sum_{n=1}^N \left[\frac{A(n)^2}{2n+1} + \frac{1}{2} \sum_{m=1}^n \frac{B(n, m)^2 + C(n, m)^2}{2n+1-m} \right] \quad (\text{A.4})$$

For further details the reader is referred to Wang and Silva [1980] and references cited therein.

Table A.1: First 36 Zernike polynomials in polar coordinates r and θ . They are sorted by radial degree n , azimuthal degree m and a global index ID.

ID	n	m	type	polynomial
0	0	0	piston	1
1	1	1	tilt in x-direction	$r \cos \theta$
2	1	1	tilt in y-direction	$r \sin \theta$
3	1	0	focus	$2r^2 - 1$
4	2	2	astigmatism in x-direction	$r^2 \cos 2\theta$
5	2	2	astigmatism in y-direction	$r^2 \sin 2\theta$
6	2	1	coma in x-direction	$(3r^2 - 2)r \cos \theta$
7	2	1	coma in y-direction	$(3r^2 - 2)r \sin \theta$
8	2	0	spherical aberration	$6r^4 - 6r^2 + 1$
9	3	3	trefoil in x-direction	$r^3 \cos 3\theta$
10	3	3	trefoil in y-direction	$r^3 \sin 3\theta$
11	3	2	secondary astigmatism	$(4r^2 - 3)r^2 \cos 2\theta$
12	3	2		$(4r^2 - 3)r^2 \sin 2\theta$
13	3	1	secondary coma	$(10r^4 - 12r^2 + 3)r \cos \theta$
14	3	1		$(10r^4 - 12r^2 + 3)r \sin \theta$
15	3	0	secondary spherical	$20r^6 - 30r^4 + 12r^2 - 1$
16	4	4	tetrafoil	$r^4 \cos 4\theta$
17	4	4		$r^4 \sin 4\theta$
18	4	3	secondary trefoil	$(5r^2 - 4)r^3 \cos 3\theta$
19	4	3		$(5r^2 - 4)r^3 \sin 3\theta$
20	4	2	tertiary astigmatism	$(15r^4 - 20r^2 + 6)r^2 \cos 2\theta$
21	4	2		$(15r^4 - 20r^2 + 6)r^2 \sin 2\theta$
22	4	1	tertiary coma	$(35r^6 - 60r^4 + 30r^2 - 4)r \cos \theta$
23	4	1		$(35r^6 - 60r^4 + 30r^2 - 4)r \sin \theta$
24	4	0	tertiary spherical	$70r^8 - 140r^6 + 90r^4 - 20r^2 + 1$
25	5	5	pentafoil	$r^5 \cos 5\theta$
26	5	5		$r^5 \sin 5\theta$
27	5	4	secondary tetrafoil	$(6r^2 - 5)r^4 \cos 4\theta$
28	5	4		$(6r^2 - 5)r^4 \sin 4\theta$
29	5	3	tertiary trefoil	$(21r^4 - 30r^2 + 10)r^3 \cos 3\theta$
30	5	3		$(21r^4 - 30r^2 + 10)r^3 \sin 3\theta$
31	5	2	quaternary astigmatism	$(56r^6 - 105r^4 + 60r^2 - 10)r^2 \cos 2\theta$
32	5	2		$(56r^6 - 105r^4 + 60r^2 - 10)r^2 \sin 2\theta$
33	5	1	quaternary coma	$(126r^8 - 280r^6 + 210r^4 - 60r^2 + 5)r \cos \theta$
34	5	1		$(126r^8 - 280r^6 + 210r^4 - 60r^2 + 5)r \sin \theta$
35	5	0	quaternary spherical	$252r^{10} - 630r^8 + 560r^6 - 210r^4 + 30r^2 - 1$

A.2 LOS Calibration - Propagation of Uncertainties

The discussion in section 3.3 defines the coordinate system of points \vec{P}_i and introduces the angular difference $\Delta\theta$ between LOS and reference mirror surface normal evaluated during the AtmoSHINE LOS calibration. Here, simplified formulas of the uncertainty propagation are given.

The measurements are performed in a spherical coordinate system but differences between vectors and coordinate points are evaluated in Cartesian coordinates. Therefore, each coordinate transformation introduces an additional uncertainty. Based on the Gaussian formulation of propagation of uncertainties, the transformation from Cartesian to spherical coordinates introduces the uncertainties δx , δy and δz governed by equation A.5, A.6 and A.7. Uncertainties introduced by the backwards transformation are governed by equation A.8, A.9 and A.10 where $\hat{r} = \sqrt{x^2 + y^2 + z^2}$.

$$\delta x = \sqrt{(\sin \theta \cdot \cos \phi \cdot \delta r)^2 + (r \cos \theta \cdot \cos \phi \cdot \delta \phi)^2 + (r \sin \theta \cdot \sin \phi \cdot \delta \phi)^2} \quad (\text{A.5})$$

$$\delta y = \sqrt{(\sin \theta \cdot \sin \phi \cdot \delta r)^2 + (r \cos \theta \cdot \sin \phi \cdot \delta \phi)^2 + (r \sin \theta \cdot \cos \phi \cdot \delta \phi)^2} \quad (\text{A.6})$$

$$\delta z = \sqrt{(\cos \theta \cdot \delta r)^2 + (\sin \theta \cdot r \cdot \delta \theta)^2} \quad (\text{A.7})$$

$$\delta r = \sqrt{\left(\delta x \cdot \frac{x}{\hat{r}}\right)^2 + \left(\delta y \cdot \frac{y}{\hat{r}}\right)^2 + \left(\delta z \cdot \frac{z}{\hat{r}}\right)^2} \quad (\text{A.8})$$

$$\delta \theta = \sqrt{\left(\frac{\delta z}{\hat{r} \sqrt{1 - (z/\hat{r})^2}}\right)^2 + \left(\frac{z \cdot \delta r}{\hat{r}^2 \sqrt{1 - (z/\hat{r})^2}}\right)^2} \quad (\text{A.9})$$

$$\delta \phi = \sqrt{\left(\frac{\delta y}{x \cdot (1 + (y/x)^2)}\right)^2 + \left(\frac{y \cdot \delta x}{x^2 \cdot (1 + (y/x)^2)}\right)^2} \quad (\text{A.10})$$

Given the definition of $\vec{\text{LOS}}$ and $\vec{\text{N}}_{\text{mirror}}$, separate uncertainty contributions to each vector component j are estimated by Equation A.11 and Equation A.12, respectively.

$$\delta \vec{\text{LOS}}_j = \sqrt{\delta P_{762,j}^2 + \delta P_{B,j}^2} \quad (\text{A.11})$$

$$\vec{\text{N}}_{\text{mirror},j} = \sqrt{\frac{1}{2} \left(\delta P_{S,j}^2 + \delta P_{HeNe,j}^2 + 2 \cdot \delta P_{R,j}^2 \right)} \quad (\text{A.12})$$

A.3 Characterisation of PSF and spot size - continued

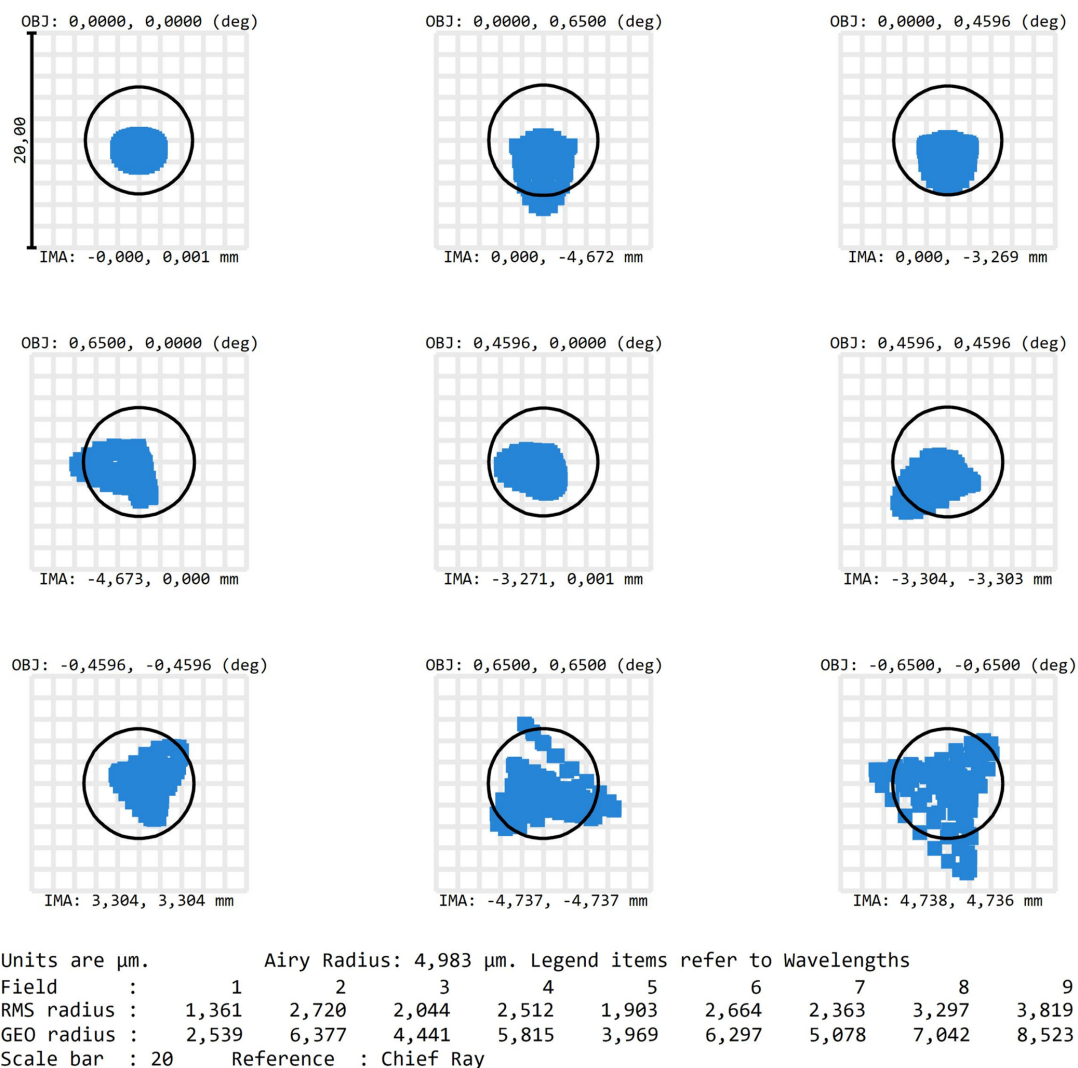


Figure A.1: AtmoLITE spot sizes at 759.83 nm. Shown are the intersections of ray traces through the AtmoLITE optics with the detector array. Nine different field angles covering the range of $\pm 0.65^\circ$ along dispersion and altitude direction are considered. The resulting spot sizes are provided as RMS and GEO radius simulated in Zemax Optical Studio. The location of intersection at the detector is provided in units of mm underneath each plot (IMA) and is computed with respect to the image centre.

Table A.2: AtmosHINE PSF measurements at different field points. Given are the fit parameters of the Gaussian approximation to each measured PSF distribution as discussed in section 3.4. Where possible ghost spots were identified and an additional Gaussian approximation was fitted. Statistical errors representing the width of the Gaussian approximations were mostly less than the first significant digit which is indicated by ± 0.0 . The definition of the 2D Gaussian function is given in Equation 5.1 and 5.2. All data was obtained on 20.02.0218.

Main Spot										Ghost Spot									
A [1/s]	X [-]	Y [-]	σ_x [-]	σ_y [-]	θ [rad]	Δ [1/s]	A [1/s]	X [-]	Y [-]	σ_x [-]	σ_y [-]	θ [rad]	Δ [1/s]	ratio $\frac{I_{ghost}}{I_{main}}$					
4107.7±32.0	1666.3±0.0	203.7±0.0	1.6±0.0	4.1±0.0	4.8±0.0	12.9±2.8	-	-	-	-	-	-	-	-					
3152.7±36.3	1648.7±0.1	399.4±0.0	5.0±0.1	2.0±0.0	0.1±0.0	41.0±6.5	-	-	-	-	-	-	-	-					
2718.1±23.2	1641.4±0.0	582.6±0.0	5.3±0.0	2.6±0.0	0.0±0.0	5.2±4.2	-	-	-	-	-	-	-	-					
2112.2±17.0	1648.1±0.0	768.0±0.0	5.5±0.0	3.2±0.0	6.1±0.0	0.0±4.0	-	-	-	-	-	-	-	-					
2657.0±18.3	1673.9±0.0	1050.2±0.0	3.1±0.0	2.6±0.0	6.2±0.0	13.6±2.8	-	-	-	-	-	-	-	-					
5373.4±62.4	1485.4±0.0	62.5±0.0	3.7±0.0	1.6±0.0	0.4±0.0	51.0±8.8	-	-	-	-	-	-	-	-					
6540.4±73.2	1473.8±0.0	273.5±0.0	3.9±0.0	1.9±0.0	0.5±0.0	51.7±8.8	-	-	-	-	-	-	-	-					
5824.7±54.1	1466.3±0.0	579.6±0.0	2.5±0.0	3.8±0.0	1.9±0.0	16.1±6.6	-	-	-	-	-	-	-	-					
4814.4±48.6	1470.4±0.0	800.7±0.0	3.0±0.0	4.2±0.0	1.2±0.0	0.0±9.0	-	-	-	-	-	-	-	-					
3562.8±26.4	1480.6±0.0	1019.1±0.0	2.6±0.0	4.9±0.0	0.8±0.0	13.3±4.3	-	-	-	-	-	-	-	-					
15155.0±171.4	1165.3±0.0	170.7±0.0	1.4±0.0	3.0±0.0	2.7±0.0	216.4±21.3	83.9±1.9	918.7±0.1	1026.6±0.2	5.6±0.1	6.9±0.2	5.9±0.1	3.0±0.5	0.05±0.00					
17143.8±285.7	1160.4±0.0	345.5±0.0	2.8±0.1	1.8±0.0	1.0±0.0	173.7±58.4	305.5±5.2	927.8±0.1	852.6±0.1	5.8±0.1	4.7±0.1	6.1±0.1	8.4±1.2	0.10±0.00					
18758.3±319.6	1158.5±0.0	585.4±0.0	2.7±0.0	1.8±0.0	0.8±0.0	180.1±40.0	395.8±6.0	929.9±0.1	614.5±0.1	5.0±0.1	7.4±0.1	1.4±0.0	7.1±1.4	0.16±0.00					
14500.8±239.0	1158.7±0.0	808.0±0.0	2.0±0.0	2.5±0.0	0.0±0.1	126.1±29.6	178.9±2.4	929.6±0.1	394.5±0.1	5.2±0.1	4.9±0.1	1.1±0.2	7.8±0.4	0.06±0.00					
5401.3±98.4	1158.8±0.0	1029.9±0.1	2.1±0.0	3.5±0.1	6.3±0.0	94.5±16.6	-	-	-	-	-	-	-	-					
11273.6±147.7	984.5±0.0	183.9±0.0	1.9±0.0	3.0±0.0	5.7±0.0	135.1±23.5	167.8±3.9	1100.5±0.1	1009.1±0.1	5.9±0.1	4.4±0.1	1.5±0.1	8.1±0.8	0.07±0.00					
18433.9±286.2	987.0±0.0	422.9±0.0	1.7±0.0	2.7±0.0	2.5±0.0	282.0±46.1	473.8±6.6	1097.6±0.1	774.4±0.1	7.9±0.1	4.6±0.1	0.2±0.0	1.3±1.2	0.20±0.01					
20325.2±340.4	987.3±0.0	592.3±0.0	1.8±0.0	2.6±0.0	2.4±0.0	214.2±46.9	692.4±6.4	1098.9±0.1	607.0±0.0	5.2±0.0	7.0±0.1	1.5±0.0	5.8±0.8	0.27±0.00					
12504.4±187.5	984.2±0.0	876.5±0.0	2.7±0.0	2.0±0.0	1.3±0.0	158.9±28.2	204.7±1.8	1100.9±0.1	330.2±0.1	6.4±0.1	5.9±0.1	0.5±0.1	3.9±0.3	0.11±0.00					
6246.4±82.9	981.3±0.0	1050.9±0.1	1.9±0.0	3.9±0.1	0.0±0.0	95.3±12.0	-	-	-	-	-	-	-	-					
10084.2±91.6	459.3±0.0	49.1±0.0	1.4±0.0	1.9±0.0	2.0±0.0	54.5±10.4	-	-	-	-	-	-	-	-					
20219.9±251.2	485.4±0.0	334.6±0.0	1.4±0.0	2.0±0.0	2.0±0.0	337.7±34.0	38.0±1.2	1566.2±0.4	855.1±0.2	15.7±0.7	7.1±0.4	3.0±0.0	0.0±1.3	0.08±0.01					
19607.9±218.7	490.7±0.0	649.7±0.0	1.6±0.0	2.2±0.0	5.3±0.0	293.6±28.6	63.1±1.1	1562.3±0.2	555.6±0.1	7.3±0.2	13.9±0.4	4.8±0.0	1.0±0.6	0.09±0.00					
19688.8±216.0	484.6±0.0	791.5±0.0	2.0±0.0	1.7±0.0	0.8±0.0	274.4±27.4	48.7±0.9	1566.5±0.2	421.9±0.1	12.8±0.4	7.7±0.2	3.4±0.0	0.0±0.9	0.08±0.00					

A.4 Instrument and ACU Info Sheets

Table A.3: Summary of ACU design parameters and properties.

AtmoLITE Calibration Unit		
optics		
eff. focal length	774.26	[mm]
image space NA	0.0484	[—]
field of view	non-vignetted > ± 0.65	[°]
image height	± 8.778	[mm]
image distortion	-0.47	[%]
total track length	988.0	[mm]
operational temp.	20.0	[°C]

Table A.4: Summary of instrument design parameters and properties. Given are the final values for the AtmoSHINE and AtmoLITE design separated by front-, camera optics and combined system where applicable.

	AtmoSHINE			AtmoLITE			
	front	camera	combined	front	camera	combined	
optics							
eff. focal length	272.86	16.38	162.60	653.22	85.74	403.06	[mm]
object space NA	—	0.134	—	—	0.061	—	[—]
image space NA	0.1201	0.220	0.1989	0.0573	0.0937	0.0926	[—]
field of view			± 0.65			± 0.65	[°]
image height			1.977			4.736	[mm]
magnification		0.559			0.625		[mm]
image distortion	0.41	1.96	7.12	1.09	0.15	1.38	[%]
operational temp.	[−30; +30]			[−30; +30]			[K]
spectrometer							
littrow wavenumber σ_L	13127.0			13047.0			[cm ^{−1}]
littrow angle θ_L	27.1984			6.6018			[°]
prism apex angle α	22.4318			5.470			[°]
entrance angle β	16.6332			4.8375			[°]
grating angle η	3.5598			1.7643			[°]
groove density G	12000			3000.0			[cm ^{−1}]
bandpass filter							
central wavelength	763.6 + 0.3			762.8 ± 0.3			[nm]
thermal drift	< 0.005			< 0.005			[nm K ^{−1}]
covered wave numbers	[13078; 13113]			[13057; 13160]			[cm ^{−1}]
FWHM	4.0			6.5			[nm]
detector array							
detector type	HWK1910			GSENSE400Bsi			
pixel number	784			861			[—]
pixel size	5.4			11.0			[μm]
quantum yield	0.4			0.7			[—]

A.5 Oxygen A-band emission lines

Table A.5: Listed are all HITRAN O₂ A-band emission lines used in simulations. To estimate the rotational distribution of the O₂ A-band emission the following quantities are used: wavenumber, Einstein coefficient of spontaneous emission A0, lower state energy LSE and the upper state degeneracy USD.

Wavenumber [cm ⁻¹]	Wavelength [nm]	Line strength [$\frac{\text{cm}^{-1}}{\text{molec} \times \text{cm}^{-2}}$]	A0 [s ⁻¹]	LSE [cm ⁻¹]	USD
13041.12	766.81	1.372e - 24	2.347e - 02	664.2596	41
13042.95	766.70	1.301e - 24	2.207e - 02	662.4360	41
13050.48	766.26	2.207e - 24	2.366e - 02	546.7042	37
13052.32	766.15	2.079e - 24	2.210e - 02	544.8622	37
13059.47	765.73	3.324e - 24	2.389e - 02	440.5617	33
13061.33	765.62	3.108e - 24	2.214e - 02	438.7010	33
13068.08	765.22	4.679e - 24	2.418e - 02	345.8494	29
13069.96	765.11	4.332e - 24	2.219e - 02	343.9694	29
13076.33	764.74	6.131e - 24	2.455e - 02	262.5826	25
13078.23	764.63	5.605e - 24	2.224e - 02	260.6824	25
13084.20	764.28	7.445e - 24	2.506e - 02	190.7748	21
13086.13	764.17	6.690e - 24	2.232e - 02	188.8530	21
13091.71	763.84	8.312e - 24	2.581e - 02	130.4375	17
13093.66	763.73	7.287e - 24	2.242e - 02	128.4920	17
13098.85	763.43	8.426e - 24	2.701e - 02	81.5805	13
13100.82	763.31	7.110e - 24	2.258e - 02	79.6069	13
13105.62	763.03	7.573e - 24	2.927e - 02	44.2117	9
13107.63	762.91	5.974e - 24	2.287e - 02	42.2001	9
13112.02	762.66	5.721e - 24	3.513e - 02	18.3371	5
13114.10	762.54	3.888e - 24	2.364e - 02	16.2528	5
13118.04	762.31	3.066e - 24	8.786e - 02	3.9610	1
13126.39	761.82	1.531e - 24	8.786e - 03	3.9610	5
13128.27	761.72	3.566e - 24	2.028e - 02	2.0842	5
13131.49	761.53	4.282e - 24	1.465e - 02	18.3371	9
13133.44	761.42	6.209e - 24	2.105e - 02	16.3876	9
13136.22	761.25	6.289e - 24	1.691e - 02	44.2117	13
13138.20	761.14	8.013e - 24	2.134e - 02	42.2239	13
13140.57	761.00	7.338e - 24	1.810e - 02	81.5805	17
13142.58	760.89	8.797e - 24	2.149e - 02	79.5646	17
13144.54	760.77	7.437e - 24	1.884e - 02	130.4375	21
13146.58	760.65	8.603e - 24	2.159e - 02	128.3977	21
13148.14	760.56	6.776e - 24	1.935e - 02	190.7748	25
13150.20	760.44	7.658e - 24	2.165e - 02	188.7133	25
13151.35	760.38	5.646e - 24	1.971e - 02	262.5826	29
13153.43	760.26	6.277e - 24	2.170e - 02	260.5008	29
13154.18	760.21	4.344e - 24	1.998e - 02	345.8494	33
13156.28	760.09	4.772e - 24	2.174e - 02	343.7481	33
13156.62	760.07	3.105e - 24	2.020e - 02	440.5617	37
13158.68	759.95	2.071e - 24	2.037e - 02	546.7042	41
13158.74	759.95	3.379e - 24	2.176e - 02	438.4413	37
13160.82	759.83	2.237e - 24	2.178e - 02	544.5651	41

A.6 AtmoLITE - Simulated Spectra continued

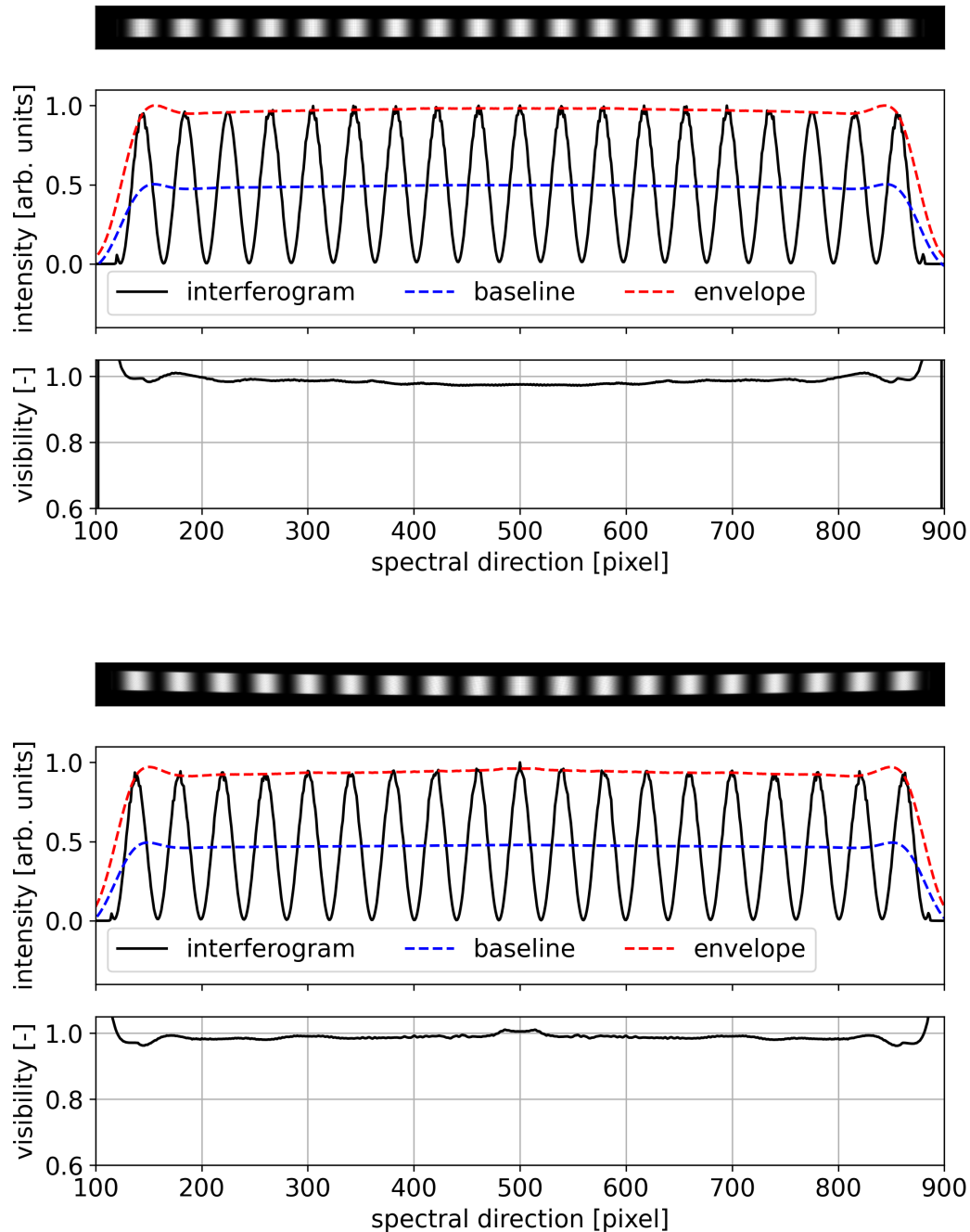


Figure A.2: Example of a single simulated interferogram at 764.74 nm. Shown are the simulated detector response and the cross-section along the centre row (top) and at the off-axis field point $H_y = 0.9$ (bottom). The estimated visibility was calculated based on a fitted baseline and envelope indicated by dashed lines. Noise and detector artefacts were not simulated.

A.7 AtmoLITE - ILS formulas

Recall the basic description of a monochromatic AtmoLITE interferogram:

$$I(x, \nu) = B(x, \nu) \cdot [t_A^2 + t_B^2 + 2t_A t_B \cdot \epsilon(x, \nu) \cdot \cos(2\pi x\nu + \Phi(x, \nu))] \quad (\text{A.13})$$

At first, to obtain the calibrated ILS description, each monochromatic interferogram is divided by the source radiance $B(x, \nu)$ and normalised to the interferogram mean. In case of calibration data, $B(x, \nu)$ is equal to results of the ACU angular scans.

$$\frac{I(x, \nu)}{B(x, \nu)} \cdot \frac{1}{t_A^2 + t_B^2} = res + 2 \cdot \frac{t_A t_B}{t_A^2 + t_B^2} \cdot \epsilon(x, \nu) \cdot \cos(2\pi x\nu + \Phi(x, \nu)) \quad (\text{A.14})$$

The residuum res for a perfect noise-free interferogram is equal to unity. However, measurement uncertainties of the interferogram mean and noise yield deviations of about $\pm 2\%$ from unity in all practical applications. The normalised interferogram is obtained by subtraction of res :

$$\begin{aligned} \frac{I(x, \nu)}{B(x, \nu)} \cdot \frac{1}{t_A^2 + t_B^2} - res &= 2 \cdot \frac{t_A t_B}{t_A^2 + t_B^2} \cdot \epsilon(x, \nu) \cdot \cos(2\pi x\nu + \Phi(x, \nu)) \\ &= I_{norm} \end{aligned} \quad (\text{A.15})$$

The modulated or flat-field corrected interferogram part is isolated as follows:

$$\begin{aligned} I_{norm} \cdot \frac{t_A^2 + t_B^2}{2 \cdot t_A t_B} &= \epsilon(x, \nu) \cdot \cos(2\pi x\nu + \Phi(x, \nu)) \\ &= I_{mod} \end{aligned} \quad (\text{A.16})$$

The amplitude $\epsilon(x, \nu)$ is obtained by a Hilbert transform of I_{mod} whereas the phase

low frequency contributions could bias the phase estimation, a spectral filter is applied whereby ν_1 and ν_2 enclose the spectral range of interest and all frequency contributions outside this range are set to zero. Here, \mathcal{F} denotes the complex Fourier transform.

$$\tilde{I}_{mod} = \mathcal{F}^{-1} \left[\mathcal{F}_{\nu_1}^{\nu_2} [\epsilon(x, \nu) \cdot \cos(2\pi x\nu + \Phi(x, \nu))] \right] \quad (\text{A.17})$$

Here, the complex Fourier transform is performed without apodization. For all other results presented in this work the blackman apodization window is used. The phase is then directly obtained from the ratio of real and complex part of the filtered interferogram:

$$2\pi x\nu + \Phi(x, \nu) = \tan^{-1} \frac{\text{Im}[\tilde{I}_{mod}]}{\text{Re}[\tilde{I}_{mod}]} \quad (\text{A.18})$$

, and a two-dimensional linear interpolation in x and ν is applied to isolate the phase distortion $\Phi(x, \nu)$. This comprises the full description of the AtmoLITE ILS separated into interferogram mean (or flat-field) t_A^2 and t_B^2 , the modulation efficiency $\epsilon(x, \nu)$, the linear phase $2\pi x\nu$ and the phase distortion $\Phi(x, \nu)$.

B

Additional information about ACU characterisation

Contents

B.1	View factor between two rectangular, parallel plates .	198
B.2	Preparations of ACU Wavefront Curvature Estimation	199
B.3	Impact of ACU chromatic focal shift	202
B.4	Aperture stop design of test equipment	204
B.5	ACU scan head design details	206
B.6	Power monitoring of ACU	212

B.1 View factor between two rectangular, parallel plates

In the second ACU iteration the top-hat illumination profile on the rotating disc diffuser is produced by a direct radiation transfer between a rectangular aperture stop and the diffuser surface in close proximity. The computation of view factors within this geometric configuration is a standard problem in radiative heat transfer and an analytical expression for the view factor has already been derived [Ehlert and Smith, 1993]. This section merely documents the coordinate system's definition and governing equation for fast access in later studies.

$$F_{1-2} = \frac{1}{2\pi(x_2-x_1)(y_2-y_1)} \sum_{l=1}^2 \sum_{k=1}^2 \sum_{j=1}^2 \sum_{i=1}^2 (-1)^{(l+k+j+i)} G(x_i, y_j, b_k, a_l) \quad (\text{B.1})$$

$$\begin{aligned} G = & (y-b) [(x-a)^2 + z^2]^{1/2} \tan^{-1} \frac{y-b}{[(x-a)^2 + z^2]^{1/2}} \\ & + (x-a) [(y-b)^2 + z^2]^{1/2} \tan^{-1} \frac{x-a}{[(y-b)^2 + z^2]^{1/2}} \quad (\text{B.2}) \\ & - \frac{z^2}{2} \ln [(x-a)^2 + (y-b)^2 + z^2] \end{aligned}$$

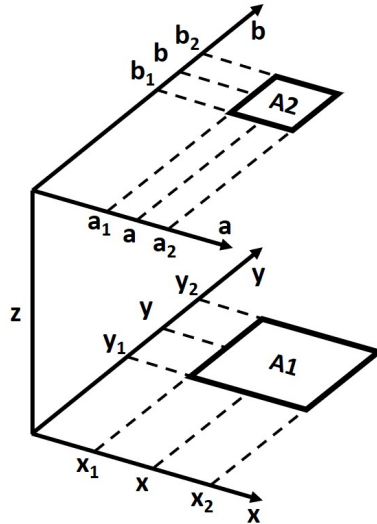


Figure B.1: View factor geometry of two plane parallel rectangles adapted from Howell et al. [2020]. For clarity, Cartesian coordinates are specified for each rectangle separately.

B.2 Preparations of ACU Wavefront Curvature Estimation

During the alignment of the ACU described in section 4.4 the shearing plate collimation tester's wedge angle was a critical unknown parameter. A simple test was implemented to evaluate this wedge angle. It was mounted on a six-axis alignment stage and positioned within the Zygo interferometer test beam. By carefully tuning vertical and horizontal tilt of the shearing plate with respect to the test beam, the front- and backside reflected wavefronts were overlapped. The corresponding interferogram is shown in Figure B.2 and a total of 32 fringes was observed over the full shearing plate aperture. The operational wavelength was at $\lambda = 632.8$ nm. Including the nominal shearing plate aperture of $D = 74.93$ mm, Equation B.3 was utilised to estimate the shearing plate wedge angle. The final result was $\alpha = (27.0 \pm 0.2)$ arcsec including measurement and manufacturing uncertainties.

$$\sin \alpha = \frac{(N - 1) * \lambda}{2 * D} \quad (\text{B.3})$$

Limitations of the Shearing Plate Method

In addition to aforementioned wedge angle uncertainty, the fringe tilt has to be evaluated against a given reference. During the measurements discussed in

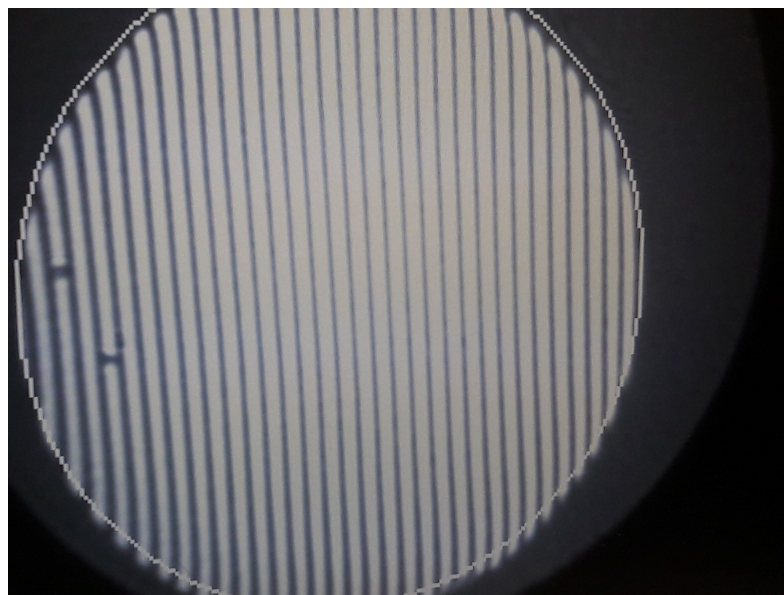


Figure B.2: Interferogram obtained during the shearing plate collimation tester's wedge estimation.

section 4.4 the reference is provided as a line directly included within the monitoring screen. However, the manufacturer does not specify tolerances regarding alignment between this reference line and the shearing plate's wedge angle itself. Therefore, the following tolerance estimations rely on a priori assumptions about potential misalignment between reference screen and shearing plate. Here, the medium tolerance class according to DIN-2768-1-m is considered which specifies a linear deviation of 0.3 mm for part sizes between 30 mm and 120 mm. The corresponding expected maximum angular deviation is $20'$. Considering that both the shearing plate and the reference screen are misaligned to a common mounting interface and attributing an additional tolerance to the mounting interface the total angular misalignment becomes $60'$. Further, the shearing plate and reference screen are glued to their respective frames during manufacturing. Thus, the tolerance is added one more time yielding an overall tolerance of 1.33° .

By estimation of the expected shearogram fringe tilt and comparison to the corresponding expected wavefront curvature, the suitability of different shearing plates is evaluated. An example of three shearing plate configurations with different wedge angles is shown in Figure B.3. The expected shear and wavefront curvature are plotted along the expected shearogram fringe tilt. The wedge angles chosen for the simulation are $28''$, $10''$ and $4.4''$. These angles correspond to the measured wedge angle of the first experimental setup, the original wedge angle as specified by the manufacture which the ACU verification concept is based on and a potential candidate to further improve the setup. The dashed black line indicates the expected shear during the experiment.

Based on section 4.2 a wavefront radius of curvature of the source above 1000 m is desirable. The corresponding shearogram fringe tilt thresholds are $1.5 \pm^\circ$, $4.0 \pm^\circ$ and $6.4 \pm^\circ$. Compared to the estimated uncertainty of 1.33° , setup one as used in this work is just sufficient to allow alignment to wavefronts better $ROC > 1000$ m. For upcoming studies, a new shearogram cube corresponding to the second setup is already prepared at which point the manufacturing tolerances of the shearing cube may be neglected.

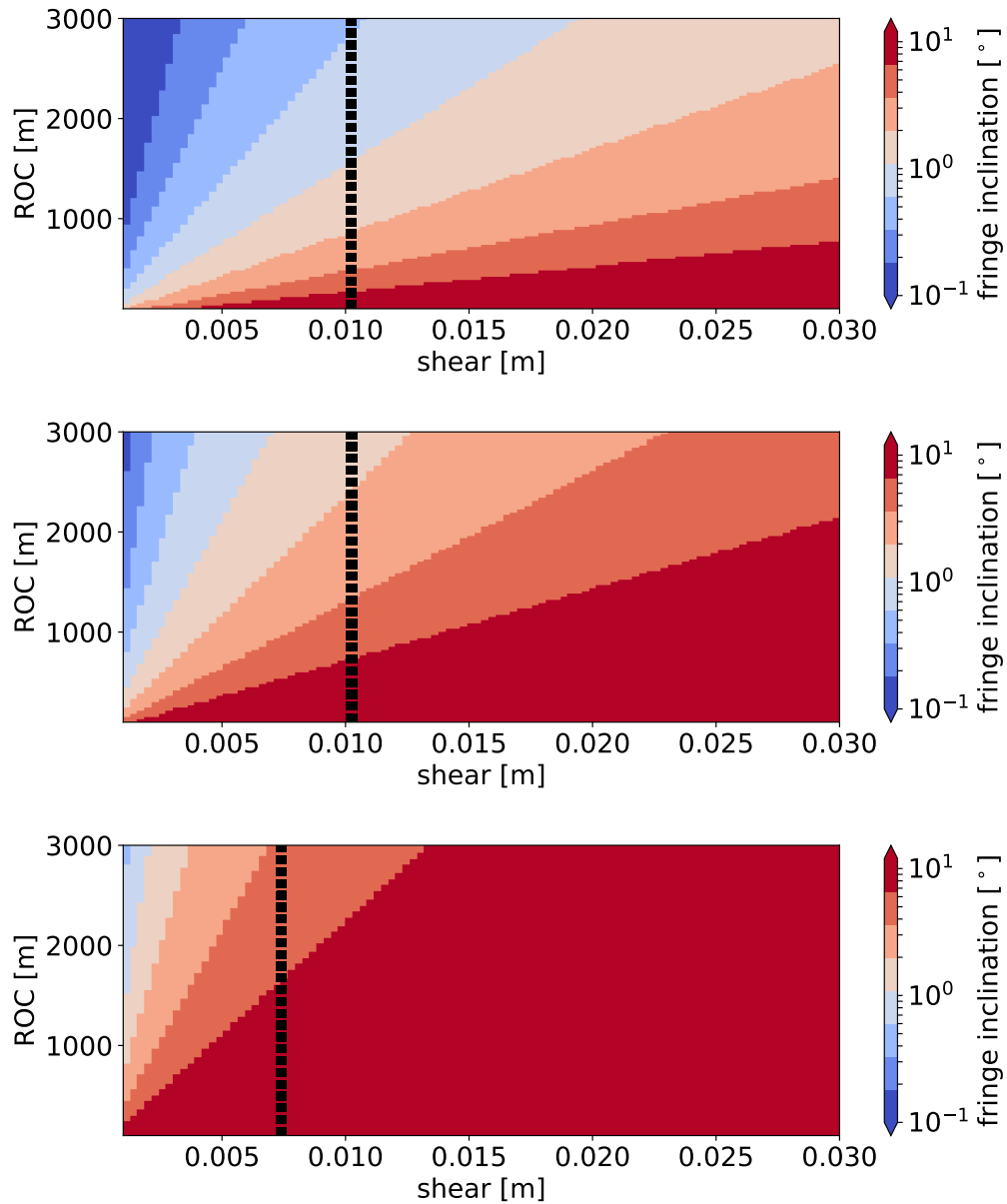


Figure B.3: Expected shearogram fringe tilt at different shears and wavefront radii of curvature. On top, results of the shearing plate utilised during the first experimental setup discussed in section 4.4 are shown which had a wedge angle of $28''$ and a plate thickness of 13 mm. The middle plot shows results after changing the wedge angle to the original wedge angle of $10''$ specified by the manufacturer. Example of expected shearogram fringe tilts if an even smaller wedge angle of $4.4''$ could be utilised which corresponds to the shearing plate 20QS20 available from Newport (bottom). The dashed line indicates the expected shear for each shearing plate, respectively.

B.3 Impact of ACU chromatic focal shift

The ACU optics is not achromatic by design and the focal plane shifts by $22 \mu\text{m}/\text{nm}$ in dependence on wavelength. The small image space numerical aperture of $\text{NA} = 0.0484$ yields the diffraction limited focal depth corresponding to approx. $320 \mu\text{m}$, in particular, much larger than the chromatic focal shift. Nevertheless, shearogram measurements are sufficiently sensitive to detect either the change of wavelength or change of focus at distances below $320 \mu\text{m}$. This raises the issue if ACU alignment at a single wavelength would degrade wavefront quality to below the desired $\text{ROC} > 1000 \text{ m}$ when used at other wavelengths during calibration. Assuming ACU alignment at $\lambda = 764 \text{ nm}$, shearogram simulations are performed at different wavelengths as shown in Figure B.5. It is apparent that a fringe tilt change of less than $\pm 1.0^\circ$ is expected between different wavelengths at a fixed position along the optical axis of the ACU. Thus, compared to the previously mentioned threshold of $\pm 1.5^\circ$, alignment at $\lambda = 764 \text{ nm}$ ensures proper wavefront radius of curvature at all wavelengths considered during later ACU operation. Note that the shearogram simulations predict a linear relation between adjusted defocus at the ACU focal plane and observed fringe tilt.

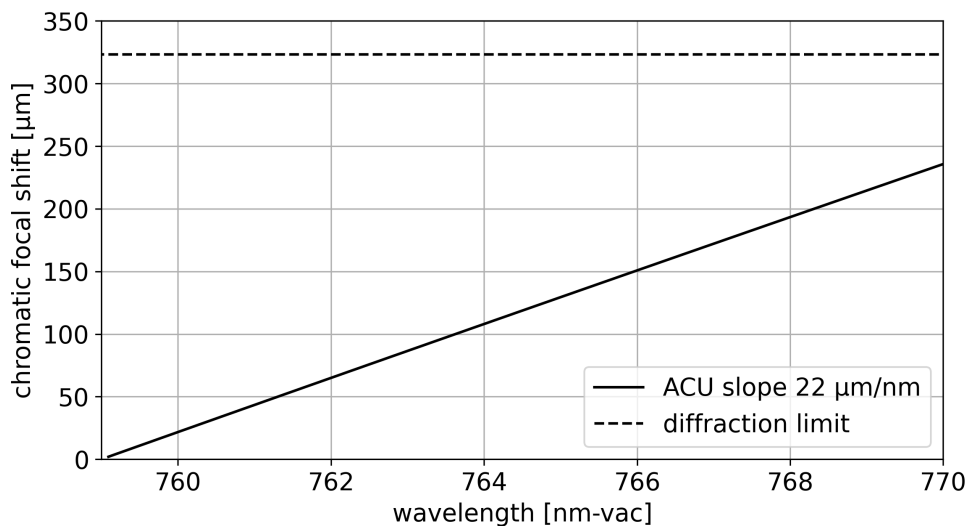


Figure B.4: ACU chromatic focal shift.

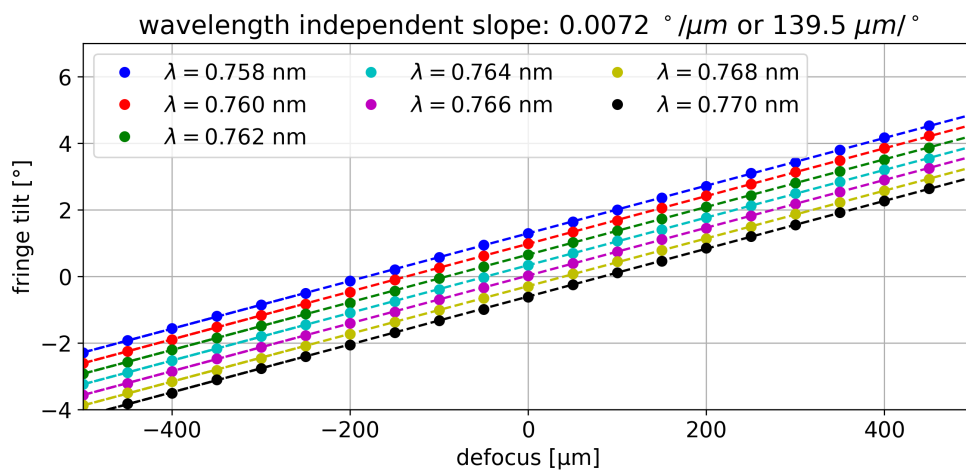


Figure B.5: Simulated shearogram tilt at different wavelengths.

B.4 Aperture stop design of test equipment

The aperture stops shown in Figure 4.20 were utilised during the verification of the illumination distribution across the ACU aperture. To ease the design, each aperture opening was chosen to cover an equal area of one sixth of the full aperture starting at different radial positions. Based on the nominal radius $r_0 = 37.5$ mm of the full aperture and the desired number of apertures $n = 6$, each subsequent radius was recursively defined by Equation B.4.

$$r_{i+1} = \sqrt{r_i^2 - r_0^2/n} \quad (\text{B.4})$$

Afterwards, four bridges were included in the design in order to connect the outer and inner frame around the aperture openings. Each bridge was chosen at a non-zero thickness of $t = 5$ mm which required consideration of a correction factor as the effective opening area was reduced. The correction factors $c_{corr, i}$ were estimated considering the geometrical cross sections indicated in Figure B.6 between the bridges and circular openings. Hereby, each cross section was divided into two circular and one rectangular section. The height of each circular section h_i was estimated by Equation B.5 where the central angle α_i was defined by Equation B.6. By combining h_i and the inner and outer radius of one opening, the length of the rectangular section $l_{i, i+1}$ was estimated based on Equation B.7. Adding the outer circular segment A_i and subtracting the inner one A_{i+1} , yielded the total cross section A_{bridge} . All radii, correction factors and effective areas were summarised in Table B.1.

$$h_i = r_i * (1 - \cos \alpha_i/2) \quad (\text{B.5})$$

$$\alpha_i = 2 * \arcsin \frac{t}{2*r_i} \quad (\text{B.6})$$

$$l_{i, i+1} = (r_i - h_i) - (r_{i+1} - h_{i+1}) \quad (\text{B.7})$$

$$A_i = r_i^2/2 * (\alpha_i - \sin \alpha_i) \quad (\text{B.8})$$

$$A_{\text{bridge}} = l_i * t + A_i - A_{i+1} \quad (\text{B.9})$$

$$c_{corr, i} = 1 - 4 * A_{\text{bridge}}/(\pi * (r_i^2 - r_{i+1}^2)) \quad (\text{B.10})$$

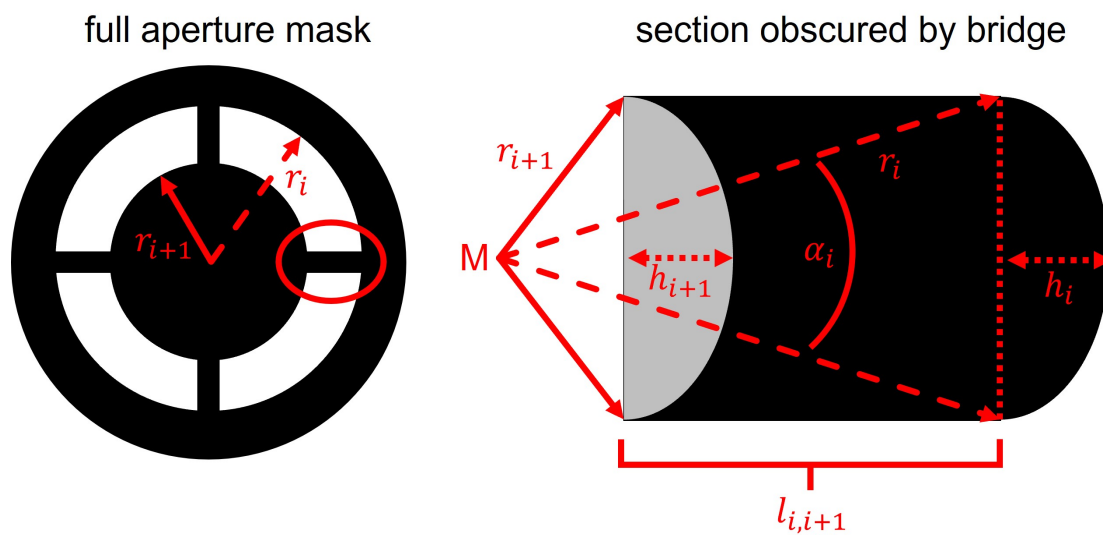


Figure B.6: ACU aperture mask and definition of correction factors.

Table B.1: Radii and correction factors utilised during the ACU aperture illumination characterisation.

ID	r_i [mm]	r_{i+1} [mm]	c_{corr} [%]	$A_{i, corr}$ [mm ²]
A0	37.5	34.23	91.1	670.43
A1	34.23	30.62	90.1	663.31
A2	30.62	26.52	88.7	653.22
A3	26.52	21.65	86.5	637.23
A4	21.65	15.31	82.2	605.51
A5	15.31	0.00	100.0	736.31

B.5 ACU scan head design details

Evaluation of the as-build ACU requires a dedicated scanning setup. The main goal is to evaluate the uniformity with respect to aperture illumination and angular distribution of irradiance at the ACU exit aperture. Further, to allow direct comparison of ACU characterisation measurements to later AtmoLITE measurements in front of the ACU, the setup used during ACU evaluation is required to have an aperture size and field angle coverage identical to the AtmoLITE optics. All components of the final setup can be grouped according to their function. Group one comprises a lens, aperture stop, pinhole and photo-diode. An $f_{\text{eff}} = 200$ mm aspheric lens with a clear aperture of $\emptyset > 90$ mm is used. The attached aperture stop of $\emptyset = 75$ mm matches the effective aperture to the nominal AtmoLITE entrance aperture. A pinhole of either $\emptyset = 25 \mu\text{m}$ or $\emptyset = 50 \mu\text{m}$ is placed at the on-axis focal point as a field stop. The photo-diode's active area is mounted at a distance of 1.5 mm behind the pinhole and is used as detector during ACU characterisation. An overview of group one is shown in Figure B.8. The second group is a set of three alignment stages which allow movement of group one. A rotation and goniometer stage are used to align the orientation of group one in horizontal or vertical direction with respect to the ACU. A Z-stage allows for height adjustment to a common optical axis of ACU and scanning setup. A CAD-view of this configuration is provided in Figure B.7. Further, this group is placed on a rail which allows for lateral movement perpendicular to the optical axis. The last group is the set of aperture masks discussed in section 4.6. These masks allow to block parts of the aperture and are used during the evaluation of aperture uniformity. A locking interface is provided at the aperture stop of group one which secures the masks in-place.

Limitations of ACU Scan Head

Two limitations of the ACU scan head are considered here. During the ACU characterisation, several wavelengths between 758 nm and 770 nm are used which can require a correction of the measured photo-diode current in case of a wavelength-dependent photo-diode responsivity. To account for a wavelength-dependent responsivity of the photo-diode, its characteristic current to power ratio in dependence on incident wavelengths can be used. Exemplary data for a photo-diode of type SM05PD3A is shown in Figure B.11 as provided by Thorlabs. The necessary relative, linear correction expected between 758 nm and 770 nm evaluates to 0.08 % per nm. In addition, the ACU always provides a divergent light cone

covering at least 1.3° in horizontal and vertical angular direction. This causes diffraction at the pinhole aperture which acts as the field stop and restricts the FOV of the ACU scan head to much smaller full cone angles of either 0.007° or 0.015° for the $\emptyset = 25 \mu\text{m}$ or $\emptyset = 50 \mu\text{m}$ pinhole apertures, respectively. This diffraction spreads part of the detected irradiance beyond the photo-diode's active area of $1.1 \times 1.1 \text{ mm}^2$, thus, causes a loss of total detected power and an unknown FOV cut-off angle if not considered.

In order to evaluate the effects of diffraction occurring within the ACU scan head, three simulations are considered which are based on the $50 \mu\text{m}$ pinhole aperture case. At first, the cut-off FOV angle of the field stop is determined in paraxial approximation by means of the relative illumination of the photo-diode with respect to observed field angle when the ACU scan head is pointed at an ideal Lambertian source. The results are shown in Figure B.11. The nominal system yields a cut-off angle of 0.007° . Introducing a shift of the pinhole aperture away from the nominal field stop position and along the optical axis by $\Delta = 250 \mu\text{m}$, allows to simulate expected misalignment and yields a larger cut-off angle of 0.021° . This cut-off angle is equivalent to the smallest step size used during ACU scans which allows to separate two measurements without overlap. Note that this cut-off angle is the half cone acceptance angle of the ACU scan head, thus, the smallest step size recommended during ACU scans including expected misalignment is about 0.04° . Next, a ray-trace is used to determine the fraction of enclosed energy passing the pinhole and impinging onto the photo-diode and to determine the corresponding expected illuminated area on the photo-diode. The two cases of nominal alignment and after a shift of the pinhole by $250 \mu\text{m}$ are evaluated on-axis and at a single off-axis field angle. The off-axis angle is chosen slightly above aforementioned cut-off angle at 0.008° in order to simulate the largest expected illuminated area on the photo-diode. The results are displayed in Figure B.11 where the enclosed energy is estimated by the number of rays impinging onto the photo-diode at a radial distance around the centroid of all rays. Evaluation of the on-axis simulation yields an expected illuminated area with a radial extent of $r_{\text{centroid}} = 294 \mu\text{m}$. Contributions due to off-axis illumination under an angle of 0.008° yield an increased expected illuminated area with a radial extent of up to $r_{\text{centroid}} = 440 \mu\text{m}$ in the worst case. Values of r_{centroid} are given at a fraction of enclosed energy of 99.9 %. Lastly, the physical optical propagation tool of ZEMAX is used. It allows to perform a physical trace of a full wavefront through the ACU scan head which allows to visualize the expected diffraction patterns on the photo-diode. The simulation considers a plane wavefront with a spatial extent of $80 \text{ mm} \times 80 \text{ mm}$ starting in front of the

ACU scan head's aperture stop at an initial total power of 1 W. The resulting flux distributions onto the photo-diode are shown separately for the on-axis and off-axis case in Figure B.9. On-axis evaluation yields good agreement with the paraxial simulations whereby the flux is concentrated in a circular region of $\emptyset \approx 0.6$ mm. The diffraction pattern drops by more than four orders of magnitude within the active area of the photo-diode, thus, no losses are expected due to diffraction under on-axis illumination. However, considering the active area of a photo-diode of type SM05PD3A of $1.1 \text{ mm} \times 1.1 \text{ mm}$, a small portion of the diffracted power is not captured on the active area in case of the off-axis illumination. This effect is best seen near the top edge of Figure B.9B. Here, an upper limit is estimated outside the active area by integration which yields up to 0.5 % loss of total detected power relative to the total power detected on-axis.

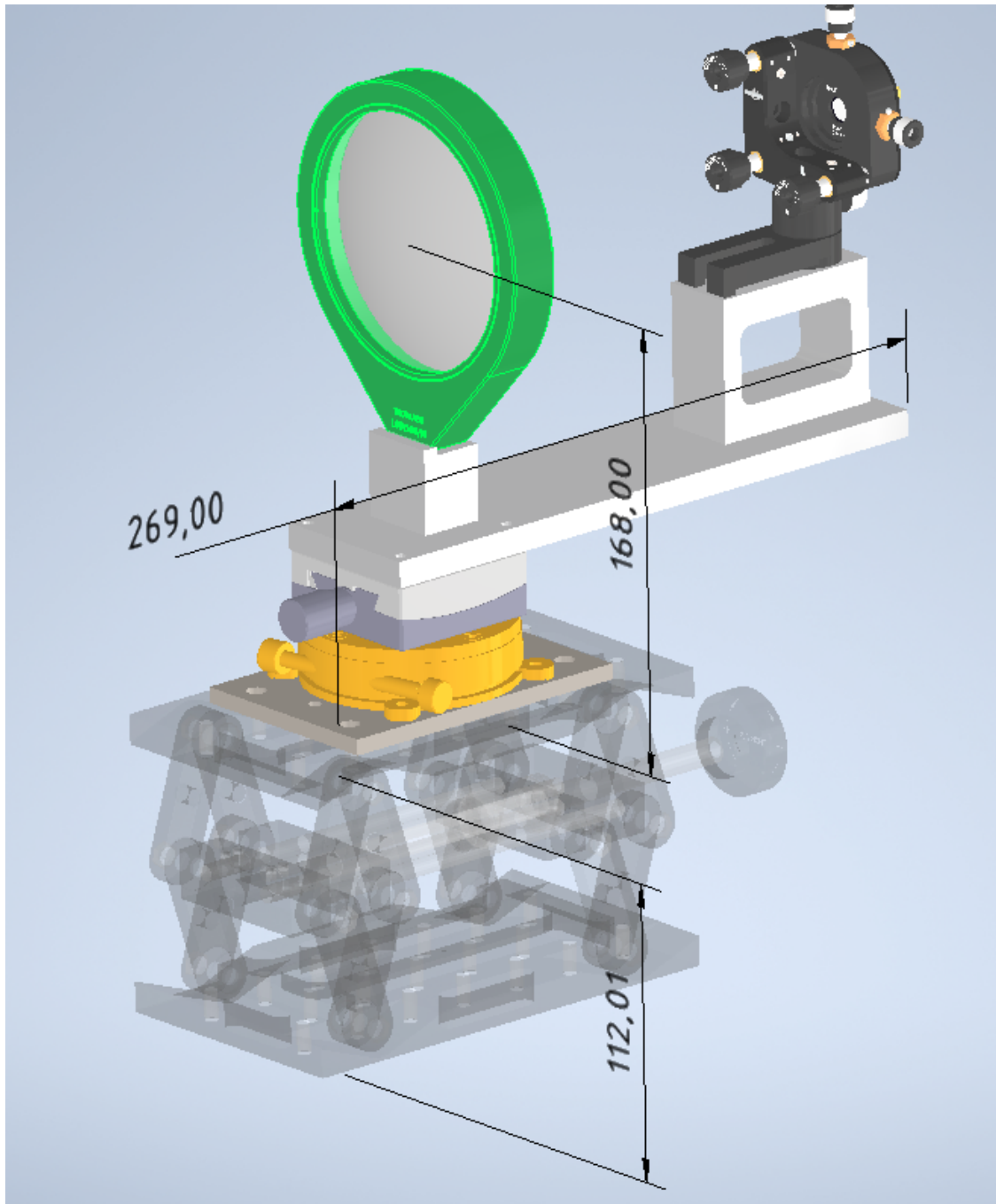


Figure B.7: CAD view of the ACU scan head setup.

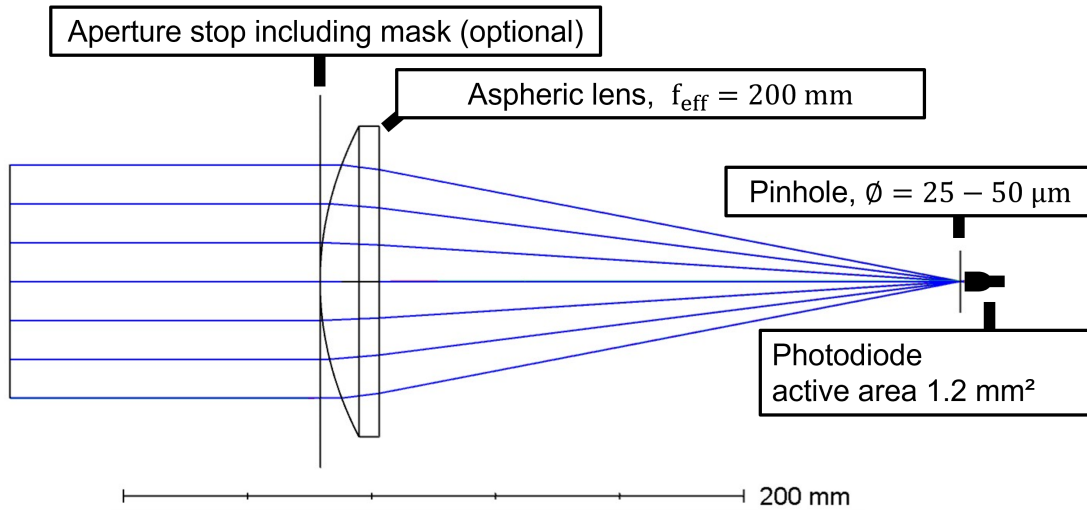


Figure B.8: On-axis raytrace of a collimated wavefront through the ACU scan head.

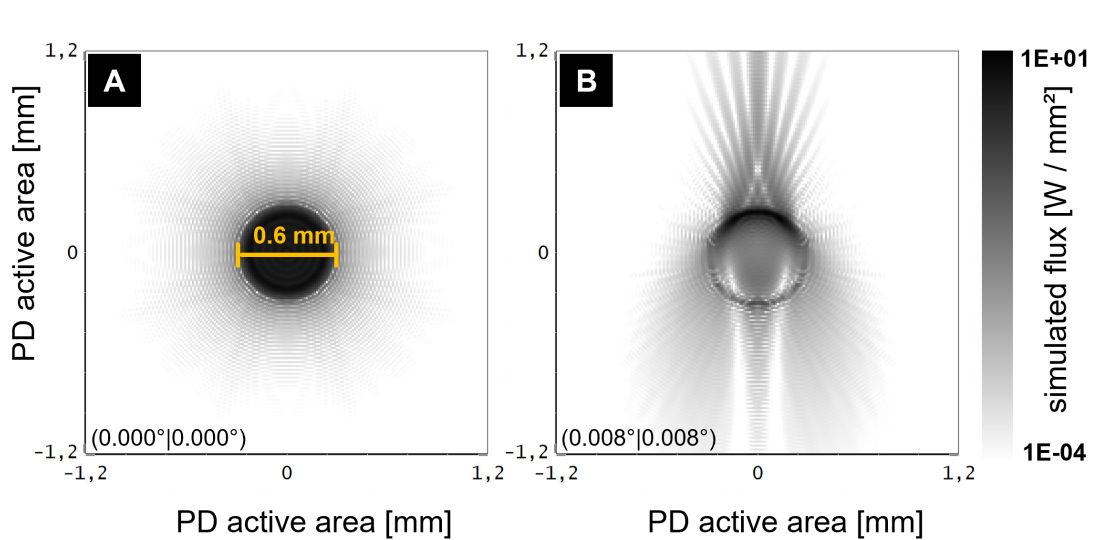


Figure B.9: Simulation of the pinhole aperture diffraction pattern as seen by the photodiode. Two cases are considered in which the wavefront is incident at an angle of 0.000° (A) or 0.011° (B) with respect to the aperture mask surface normal.

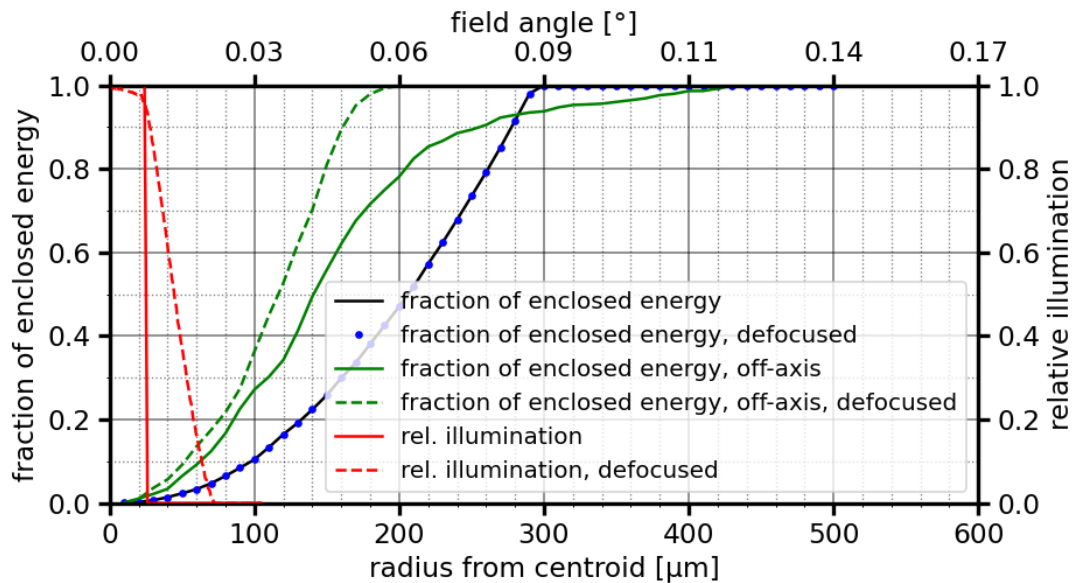


Figure B.10: Vignetting expected within the ACU scan head due to the finite aperture size of the pinhole. The pinhole acts as a field stop which effectively limits the acceptance angle of observed field angles. This is expressed as relative illumination per field angle normalised to normal incident. In addition, aperture diffraction at the pinhole causes a spread of the incident energy across the photo diode. In paraxial approximation, the fraction of enclosed energy is provided as a function of the radial distance around the expected centroid.

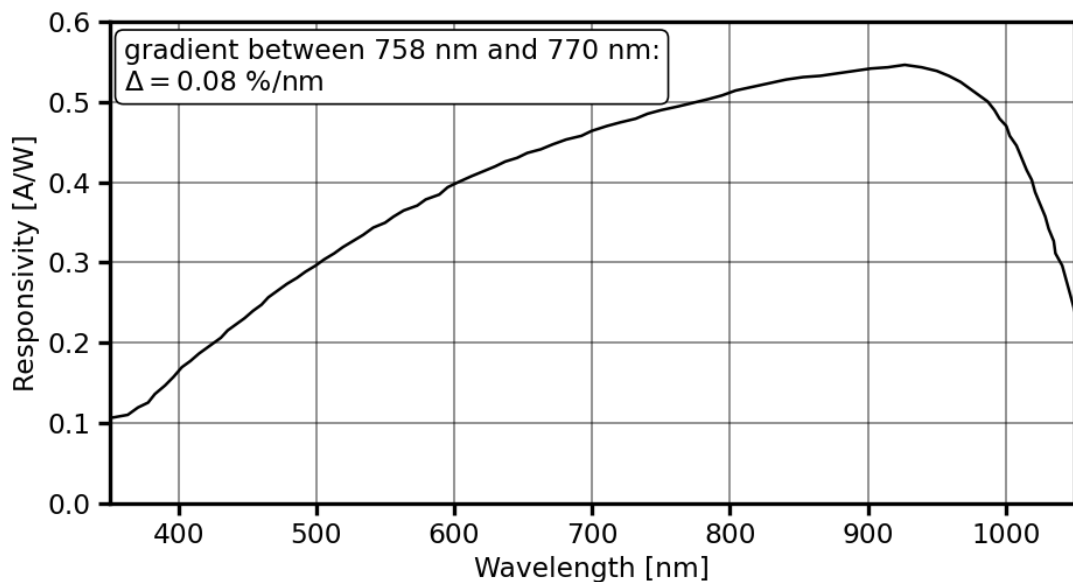


Figure B.11: Spectral responsivity of a typical photo-diode of type SM05PD3A as provided by Thorlabs. In the spectral range of interest between $\lambda = 758$ nm and $\lambda = 770$ nm the responsivity changes by 0.08 %/nm.

B.6 Power monitoring of ACU

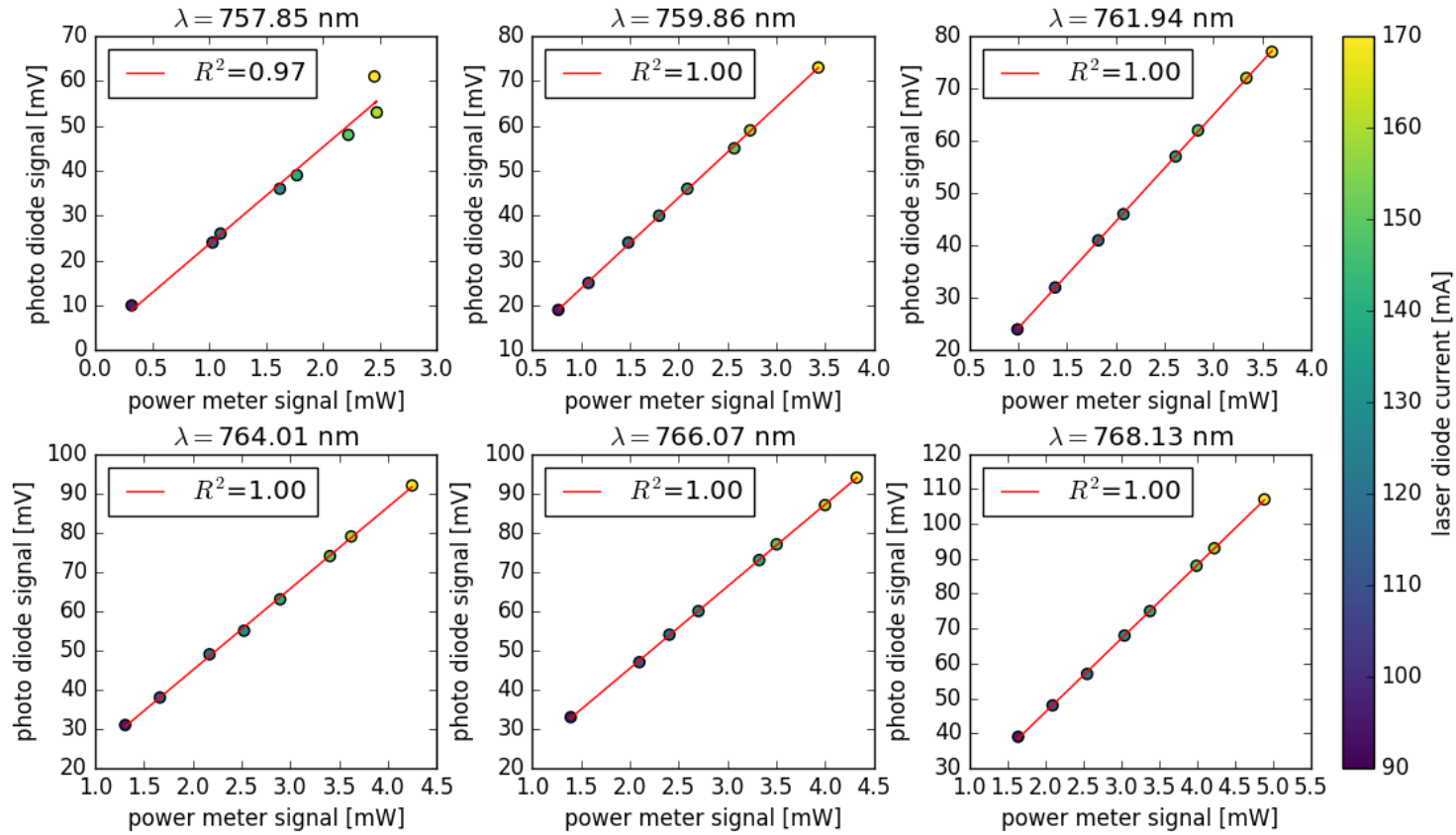


Figure B.12: Correlation of measured laser power by internal photo-diode and external powermeter. The laser diode current was varied between 90 mA and 170 mA. Simultaneously, the resulting laser output power was monitored via a power meter in front of the ACU integration sphere and behind the rotating diffuser disc by the internal photo diode. Both signals were found to correlate within less than $< 1\%$ for the wavelength range between 759.86 nm and 768.13 nm. Note, in dependence on wavelength, different slopes were found for the linear relation between power meter and photo diode signals.



AtmoLITE alignment guide

Contents

C.1 Step-By-Step guide to SHS alignment	215
C.2 Step-by-Step Alignment of Front and Camera Optics .	219

Since the first SHS and optics assemblies during the AtmoHIT activities at the BUW and Research Centre Jülich, a lot of improvements have been made to the SHS and optics assembly and alignment strategies. To complement the first experimental verification of the AtmoLITE prototypes, the following sections summarize the latest alignment strategies of the SHS and optics which were developed with the goal to simultaneously improve interferogram fringe visibility and overall imaging quality. These guidelines are quite general and, apart from values concerning the Littrow configuration, are not limited to the AtmoLITE SHS in particular.

C.1 Step-By-Step guide to SHS alignment

Based on the new alignment strategy for the AtmoLITE and following instruments, all SHS components (one beamsplitter cube, two of each support plate, spacer plate, FWP and four spacers) are no longer assembled in one step. Each grating forms a sub-assembly attached to a support plate and two spacers. The third sub-assembly is formed by the beam splitter, two spacer plates and the field-widening prisms (FWPs). Following, the six steps used in an iterative approach to combine all three sub-assemblies are discussed. The alignment process of the individual sub-assemblies and involved stages is not disclosed within this work.

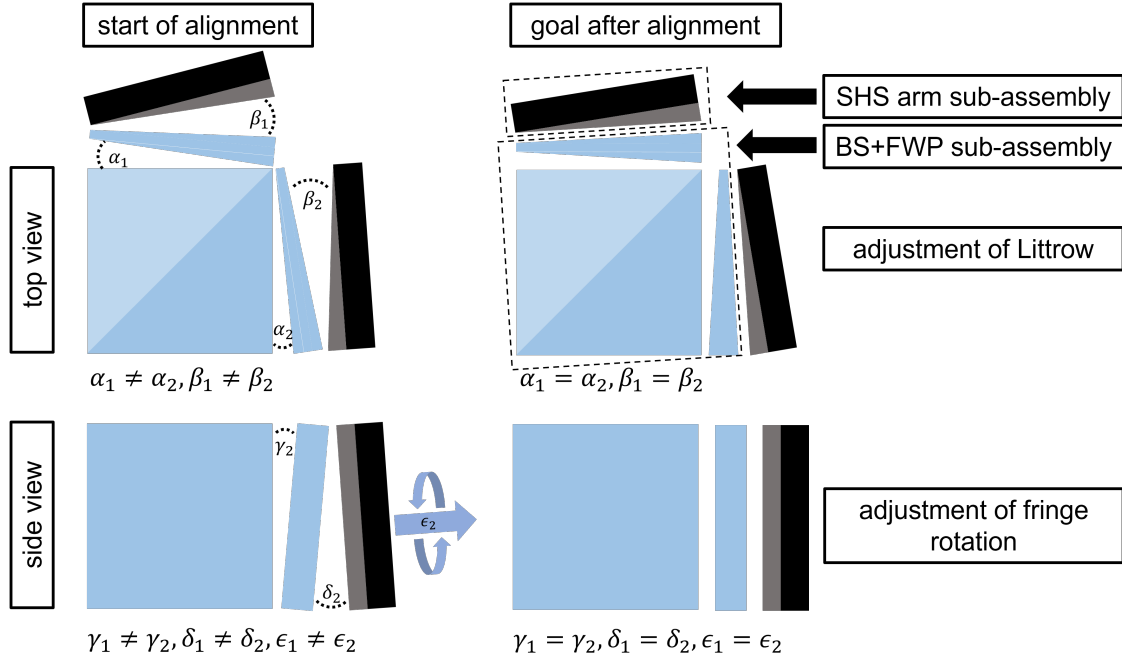


Figure C.1: Overview of DoFs during SHS assembly. Shown are the DoFs introduced due to the finite glue thickness at different bonding surfaces. Note that the angles α and γ are not controlled during the step-by-step process and rely on manufacturing tolerances and the procurement process of the sub-assemblies. The final goal is a reduction of arm imbalances corresponding to a near parallel alignment of all bonding surfaces. Top and side view of the SHS alignment jig are indicated as apparent to the jig-operator.

The overall goal is to optimize the following four criteria in descending order of importance:

- Maximize the interferogram fringe visibility at frequencies corresponding to $\lambda = 759.83 \text{ nm}$
- Adjust the SHS as close as possible to the nominal Littrow configuration corresponding to $\sigma_L = 13047 \text{ cm}^{-1}$ under vacuum
- Minimize the wavelength dependent interferogram fringe tilt caused by a non-ideal SHS assembly
- Minimize the glue thickness at bonding surfaces

Before diving into the detailed step-by-step alignment procedure, one may recall the following general relations between available DoFs and aforementioned goals:

- Direct control of the Littrow wave number is given by tilt of the SHS arm sub-assemblies along the dispersion direction.

- Rotation of the grating around the dispersion direction or around the grating surface normal changes interferogram fringe rotation. In practice, these two DoFs are not independent from tilt along the grating grooves and cause small contributions to a Littrow wave number change due to an imperfect alignment between SHS arm sub-assemblies and the alignment jig.
- Lateral shifts of the SHS arm sub-assemblies with respect to the optical axis cause negligible change in either Littrow wave number or fringe rotation as long as no contact is made between bonding surfaces. This is applicable in both cases w/ and w/o adhesive applied.
- The shift along the optical axis provides the largest direct feedback on interferogram fringe contrast as the virtual localisation plane moves in- or out-of focus of the camera optics.
- By (im-)proper adjustment of the camera optics focal length, the position of the localisation plane may be shifted by multiple millimetres away from the beam splitter/ field-widening prisms. Thus, enabling SHS configurations without mechanical contact between the sub-assemblies. This is a critical and important property of the system with respect to the minimization of glue thicknesses.

These general relations are only valid for a perfect alignment between the sub-assemblies orientation and the manual stages' centre of rotation. In practice, a mismatch is always expected which causes cross-talk between the DoFs. For instance, the Littrow wave number may be altered based on rotations around the grating surface normal and around the dispersion direction instead of a tilt along the dispersion direction. Thus, the following iterative alignment procedure is recommended.

STEP I - coarse alignment of camera optics focal length

At the beginning of the alignment process, the position of the localisation plane formed by the beam splitter and field-widening prisms sub-assembly with respect to the camera optics has to be determined. This position is the ideal position of the gratings for best interferogram contrast. Consequently, a line target can be placed in one arm (at the nominal position of the grating surface) and the camera optics focal length is adjusted until best image contrast is found. Next, the line target is removed and both SHS arm sub-assemblies are installed. In general, positioning the grating surface close to aforementioned line target position

yields a first interferogram without further adjustments. It is handy to start with a slight offset of the grating position from its nominal position, in particular, to start with a slight offset from the ideal localisation plane position. This introduces an air gap between the field-widening prisms and the spacers of the SHS arm sub-assemblies which can be used to familiarize oneself with the following steps in handling the SHS alignment jig. The gap further reduces the risk of damaging glass pieces or chip-off edges by accidentally contacting surfaces and applying too much pressure early in the alignment process.

STEP II - adjustment towards Littrow wave number

The Littrow wave number is determined by scanning through the (entire) wavelength range transmitted by the bandpass filter. It corresponds to the zero fringe frequency in dispersion direction. Based on the determined Littrow wave number and its deviation to expectation the grating tilt along dispersion direction has to be altered. If a live processing of the data and automated evaluation of fringe frequency is not available, these adjustments can be introduced at apparent fringe frequencies of about 10 lp/cm (offset from the Littrow wave number) where manual counting of fringes is possible. Next, the tilt and laser source wavelength are iteratively tuned in steps of about ± 3 lp/cm until the apparent fringe frequency matches expectations. If the difference between expectation and as-aligned Littrow wavelength is still larger than ± 1 nm, the tilt is equally adjusted in both SHS arm sub-assemblies. Otherwise, adjustments are made at a single sub-assembly.

STEP III - adjustment of the wavelength dependent fringe rotation

Scanning through the (entire) wavelength range of the bandpass may reveal a strong rotation of the interferogram fringes. This is minimized by rotation of the grating around its surface normal or the direction perpendicular to the dispersion direction. Once more, adjustments are introduced equally distributed to both SHS arms and at apparent fringe frequencies of about 10 lp/cm. Without a live processing of the interferogram, the detector (vertical) pixel orientation may be taken as a reference to evaluate the fringe inclination. Alternatively, one may estimate the ideal reference orientation by the mean of the fringe inclinations found at equal frequencies corresponding to two different wave numbers above and below the Littrow wave number. Note that the fringe rotation changes sign when crossing of the Littrow wave number occurs!

STEP IV - closing the remaining air gaps between bonding surfaces

At this point, the Littrow wave number shall be matched with expectations by about a few wave numbers with a fringe rotation below $< 5^\circ$. However, the air gap introduced in STEP I may still be present and the individual arms may show different inclinations with respect to the field-widening prisms in all three rotational DoFs. The air gap is reduced by shifting both SHS arm sub-assemblies towards the field-widening prisms until contact at either the upper or lower spacer is made. At the same time, the camera optics focal length has to be adjusted in order to maintain high interferogram contrast.

STEP V - final iteration of STEP II-IV

Once first contact at one edge of the spacer is made to the FWP, the steps II-IV are repeated iteratively until all SHS characteristics are matched to expectations. Hereby, care shall be taken to further reduce the imbalances between both arm inclinations which are indicated in Figure C.1. The general approach is to adjust one SHS arm sub-assembly at a time per iteration starting in the arm with largest apparent deviation from an ideal alignment.

STEP VI - application and curing of adhesive

Once acceptable alignment is achieved in steps I-V, both arm sub-assemblies are retracted. Next, a thin layer of adhesive is applied to the spacers of the SHS arm sub-assemblies. Afterwards, the alignment process of step I-V is repeated. Alignment is terminated once a strong increase in resistance while turning the micrometer in step IV is noticed by the operator. Future setups may include a pressure gauge at this point for more precise alignment. Care shall be taken to not withdraw the SHS arm sub-assemblies at any time during this last iteration, especially after the glue made first contact to the FWP, in order to avoid the inclusion of air bubbles. Final curing of the adhesive is started by placing two UV light sources around the alignment jig.

C.2 Step-by-Step Alignment of Front and Camera Optics

The two major goals of the step-by-step alignment of front and camera optics with respect to the SHS and adjacent detector are summarized as follows:

- The interferogram fringe visibility shall be optimized for observations of high spatial frequencies. In particular, frequencies observed at a wavelength of $\lambda = 759.83$ nm shall be obtained at visibilities $V > 0.5$.
- The overall imaging quality of a distant object expressed in terms of MTF shall be sufficient to resolve 40 altitude layers of the atmospheric scene. This limit corresponds to a spatial frequency of 4.23 lp/mm on the detector. From an optics point of view, any MTF value larger than zero is sufficient, but efforts shall be made to get close to the target value of $MTF > 80\%$, RO.06.

If the camera optics is already well aligned to the SHS and optics were not taken apart after SHS assembly, the procedure starts in STEP I. Otherwise and if no interferograms or a low interferogram fringe visibility is apparent while the instrument is illuminated by the ACU, optics alignment starts in STEP II.

STEP I - Alignment Optimization of Front Optics

The instrument is aligned to a point source such that the image of the point source appears near the detector centre. Next, the locking mechanisms of the compensators within the front optics are loosened in turns. Adjustments are made at either compensator to reduce the apparent image size of the point source to the smallest possible. A small inclination between instrument and point source allows to verify the point source response at off-axis field points. If no further improvements can be made, all locking mechanisms within the front optics are tightened and the alignment continues at the camera optics in STEP II. If live data processing is available, the as-measured MTF curve along a cross-section through the centre of the apparent point source image shall be used as performance criterion of evaluation. In paraxial approximation, the smallest achievable image size of the point source is limited either by the pixel size of 11 μm or the angular divergence of the source. In the latter case, and if the optics is aligned such that diffraction limited imaging is obtained, the smallest image size corresponds to $7.3 \text{ mm}/^\circ$ times the angular divergence of the source. For instance, the setup discussed in section 5.2 uses a $\emptyset 25 \mu\text{m}$ pinhole placed at the focal point of an $f = 200 \text{ mm}$ lens, thus, yields a source of 0.007° divergence and smallest achievable image sizes of about $\emptyset 52 \mu\text{m}$ are expected. First alignment test of the AtmoLITE prototypes discussed in section 5.2 demonstrated that such small image sizes are achievable in practice.

STEP II - Alignment Optimization of Camera Optics

The instrument is aligned to the ACU. It is recommended to either use alignment marks along the radiating source area of the ACU or to rely on the readable scales of the XYZRT-stages used to turn the instrument in order to ensure repeatability of alignment when iterating between STEP I and STEP II. Once aligned, the locking mechanisms of the compensators within the camera optics are loosened. In turns, both compensators are adjusted as necessary while the interferogram fringe visibility at an input laser wavelength of 759.83 nm is monitored. Best instrument performance is expected when the following criteria are met:

- Interferogram cross-sections at positions corresponding to off-axis field angles near $\pm 0.59^\circ$ exhibit an almost constant visibility (cf. simulations shown in fig 4.18).
- Near the interferogram centre a strong drop in visibility of up to $\Delta V = -0.2$ with respect to aforementioned off-axis field points is obtained.
- The visibility at the FOV centre is above $V > 0.5$ at a wavelength of 759.83 nm. Within a region of at least 860×860 pixel around the FOV centre the visibility does not drop below $V > 0.5$.

If no further improvements can be made, all locking mechanisms within the camera optics are tightened and the alignment continues with STEP III.

STEP III - Final Iteration of STEP I-II

STEP I and II have to be iterated several times until satisfactory results are obtained. Adjustments of the camera optics in STEP II may worsen system MTF and because MTF cannot be improved by other means but during alignment, it is recommended to finalise optics alignment in STEP I. In particular, degradation of interferogram fringe visibility due to adjustments of the front optics are expected to be small and related losses in SNR can be compensated by an increased integration time during in-orbit operation.